

# Shapes and Dynamics of Blood Cells in Poiseuille and Shear Flows

Inaugural-Dissertation

zur  
Erlangung des Doktorgrades  
der Mathematisch-Naturwissenschaftlichen Fakultät  
der Universität zu Köln  
vorgelegt von

Johannes Mauer  
aus Koblenz

Jülich  
2016

Berichterstatter (Gutachter):  
**Prof. Dr. Gerhard Gompper**  
**Prof. Dr. Andreas Schadschneider**

Tag der mündlichen Prüfung: 15. April 2016





# Kurzzusammenfassung

Die Dynamik, Form, Verformung und Ausrichtung roter Blutzellen in der Mikrozirkulation beeinflussen Rheologie, Fließwiderstand und Transporteigenschaften des Blutes. Dies führt zu wichtigen Zusammenhängen der zellulären und Kontinuums-Skalen. Des Weiteren ist die Dynamik roter Blutzellen, die verschiedenen Strömungen und Gefäßgeometrien unterliegen, relevant für sowohl Grundlagenforschung als auch biomedizinische Anwendungen (z.B. Medikamentenzuführung).

In dieser Arbeit wird das Verhalten roter Blutzellen für verschiedene Strömungen mittels Computersimulationen untersucht. Wir benutzen eine Kombination zweier mesoskopischer teilchenbasierter Simulationstechniken, Dissipative Particle Dynamics und Smoothed Dissipative Particle Dynamics. Wir konzentrieren uns auf die mikropillarisierende Skala von einigen  $\mu\text{m}$ . Auf dieser Skala kann Blut nicht auf der Kontinuums-Skala betrachtet, sondern muss auf der zellulären Skala untersucht werden. Die Verknüpfung zwischen zellulärer Bewegung und Blut-Rheologie wird untersucht.

Rote Blutzellen werden als viskoelastische Objekte modelliert, die mit einer viskosen flüssigen Umgebung wechselwirken. Die Membraneigenschaften, wie Biegesteifigkeit oder Scherfestigkeit, sind so gewählt, dass sie experimentellen Werten entsprechen. Des Weiteren werden thermische Fluktuationen mittels Zufallskräften betrachtet.

Analysen, die Lichtstreuungsmessungen entsprechen, werden durchgeführt, um mit Experimenten zu vergleichen und nahezulegen, für welche Situationen diese Methode geeignet ist. Statische Lichtstreuung von roten Blutzellen charakterisiert deren Form und erlaubt Vergleiche mit Objekten wie Kugeln oder Zylindern, deren Lichtstreuungssignale analytisch lösbar sind, im Gegensatz zu denen roter Blutzellen. Dynamische Lichtstreuung roter Blutzellen wird hinsichtlich seiner Eignung, Bewegungen, Verformungen und Membranfluktuationen nachzuweisen und zu analysieren, untersucht. Analysen zur dynamischen Lichtstreuung werden sowohl für diffundierende als auch fließende Zellen durchgeführt. Streusignale hängen von den Zelleigenschaften ab und erlauben daher, verschiedene Zellen voneinander abzugrenzen. Die Streuung diffundierender Zellen lässt mittels des effektiven Diffusionskoeffizienten Rückschlüsse auf ihre Biegesteifigkeit zu. Die Streuung fließender Zellen lässt mittels der Streuamplitudenkorrelation Rückschlüsse auf die Scherrate zu.

Im Fluss weist eine rote Blutzelle verschiedene Formen und dynamische Zustände auf, abhängig von Bedingungen wie eingeschränkter Geometrie, physiologischen/pathologischen Zuständen und Zellalter. In dieser Arbeit werden zwei wesentliche Strömungen untersucht: einfacher Scherfluss und Fluss durch eine zylindrische Röhre.

Einfacher Scherfluss als eine grundlegende Strömung ist Teil jeder komplexeren Strömung. Das Geschwindigkeitsprofil ist linear und die Scherspannung ist homogen. In einfachem Scherfluss finden wir eine Abfolge verschiedener Zellformen, wenn die Scherrate erhöht wird. Mit steigender Scherrate finden wir rollende Zellen in Schalenform, Trilobe- und

Quadrulobe-Formen. Dies stimmt mit aktuellen Experimenten überein. Des Weiteren wird der Einfluss der anfänglichen Ausrichtung auf die Dynamik untersucht. Um Verdrängungs- und kollektive Effekte zu untersuchen, werden Systeme mit höherem Hämatokrit aufgesetzt.

Die Strömung durch eine Röhre dient als idealisiertes Modell für die Strömung durch annähernd zylinderförmige Mikrogefäße. Ohne Zelle liegt ein parabolisches Geschwindigkeitsprofil vor. Eine einzelne rote Blutzelle wird in der Röhre platziert und einem Poiseuille-Profil ausgesetzt. Bei der Rohr-Strömung finden wir verschiedene Zellformen und -dynamiken, abhängig von der Einschränkung durch Geometrie (hier der Rohrdurchmesser), Scherrate und Zelleigenschaften. Für enge Röhren und hohe Scherraten finden wir Fallschirm-förmige Zellen. Obwohl nicht perfekt symmetrisch, sind sie dem Flussprofil angepasst und behalten eine stationäre Form und Ausrichtung. Für weite Röhren und niedrige Scherraten finden wir taumelnde Slipper-Formen, die sich drehen und ihre Form moderat ändern. Für weite Röhren und hohe Scherraten finden wir Slippers mit sogenannter Panzerketten-Membranrotation, die ihren Anstellwinkel leicht oszillieren und periodisch ihre Form stark ändern. Für die niedrigsten Scherraten finden wir Zellen, die eine Schlangelbewegung ausführen. Aufgrund der Zelleigenschaften und sich daraus ergebender Verformungen unterscheiden sich alle Formen von bisherigen Beschreibungen in der Literatur, wie z.B. stationäre Panzerketten-Membranrotation oder symmetrische Fallschirmformen. Wir führen Phasendiagramme ein, um die Parameterbereiche verschiedener Formen und Dynamiken zu identifizieren. Verändert man die Zelleigenschaften, ändern sich auch die Grenzen dieser Bereiche in den Phasendiagrammen.

In beiden Strömungstypen sind sowohl der Viskositätskontrast als auch die Wahl der spannungsfreien Form wichtig. Bei *in vitro* Experimenten war die Viskosität des Lösungsmittels bisher oft höher als die des Cytosols, was zu anderen Bewegungsformen führt, wie z.B. stationäre Panzerketten-Membranrotation. Die spannungsfreie Form einer roten Blutzelle, die den Zustand bei verschwindender Scherbelastung darstellt, ist noch umstritten, und Computersimulationen ermöglichen direkte Vergleiche möglicher Kandidaten bei ansonsten gleichen Strömungsbedingungen.

# Abstract

The dynamics, shape, deformation, and orientation of red blood cells in microcirculation affect the rheology, flow resistance and transport properties of whole blood. This leads to important correlations of cellular and continuum scales. Furthermore, the dynamics of RBCs subject to different flow conditions and vessel geometries is relevant for both fundamental research and biomedical applications (e.g drug delivery).

In this thesis, the behaviour of RBCs is investigated for different flow conditions via computer simulations. We use a combination of two mesoscopic particle-based simulation techniques, dissipative particle dynamics and smoothed dissipative particle dynamics. We focus on the microcapillary scale of several  $\mu m$ . At this scale, blood cannot be considered at the continuum but has to be studied at the cellular level. The connection between cellular motion and overall blood rheology will be investigated.

Red blood cells are modelled as viscoelastic objects interacting hydrodynamically with a viscous fluid environment. The properties of the membrane, such as resistance against bending or shearing, are set to correspond to experimental values. Furthermore, thermal fluctuations are considered via random forces.

Analyses corresponding to light scattering measurements are performed in order to compare to experiments and suggest for which situations this method is suitable. Static light scattering by red blood cells characterises their shape and allows comparison to objects such as spheres or cylinders, whose scattering signals have analytical solutions, in contrast to those of red blood cells. Dynamic light scattering by red blood cells is studied concerning its suitability to detect and analyse motion, deformation and membrane fluctuations. Dynamic light scattering analysis is performed for both diffusing and flowing cells. We find that scattering signals depend on various cell properties, thus allowing to distinguish different cells. The scattering of diffusing cells allows to draw conclusions on their bending rigidity via the effective diffusion coefficient. The scattering of flowing cells allows to draw conclusions on the shear rate via the scattering amplitude correlation.

In flow, a RBC shows different shapes and dynamic states, depending on conditions such as confinement, physiological/pathological state and cell age. Here, two essential flow conditions are studied: simple shear flow and tube flow.

Simple shear flow as a basic flow condition is part of any more complex flow. The velocity profile is linear and shear stress is homogeneous. In simple shear flow, we find a sequence of different cell shapes by increasing the shear rate. With increasing shear rate, we find rolling cells with cup shapes, trilobe shapes and quadrulobe shapes. This agrees with recent experiments. Furthermore, the impact of the initial orientation on the dynamics is studied. To study crowding and collective effects, systems with higher haematocrit are set up.

Tube flow is an idealised model for the flow through cylindrical microvessels. Without cell, a parabolic flow profile prevails. A single red blood cell is placed into the tube and subject to

a Poiseuille profile. In tube flow, we find different cell shapes and dynamics depending on confinement, shear rate and cell properties. For strong confinements and high shear rates, we find parachute-like shapes. Although not perfectly symmetric, they are adjusted to the flow profile and maintain a stationary shape and orientation. For weak confinements and low shear rates, we find tumbling slippers that rotate and moderately change their shape. For weak confinements and high shear rates, we find tank-treading slippers that oscillate in a limited range of inclination angles and strongly change their shape. For the lowest shear rates, we find cells performing a snaking motion. Due to cell properties and resultant deformations, all shapes differ from hitherto descriptions, such as steady tank-treading or symmetric parachutes. We introduce phase diagrams to identify flow regimes for the different shapes and dynamics. Changing cell properties, the regime borders in the phase diagrams change.

In both flow types, both the viscosity contrast and the choice of stress-free shape are important. For *in vitro* experiments, the solvent viscosity has often been higher than the cytosol viscosity, leading to a different pattern of dynamics, such as steady tank-treading. The stress-free state of a RBC, which is the state at zero shear stress, is still controversial, and computer simulations enable direct comparisons of possible candidates in equivalent flow conditions.



# Contents

<b>List of Figures</b>	<b>xiii</b>
<b>1 Introduction</b>	<b>1</b>
1.1 Blood as a Cell Suspension . . . . .	1
1.1.1 Red Blood Cells . . . . .	1
1.1.2 White Blood Cells . . . . .	3
1.1.3 Platelets . . . . .	4
1.2 Physical Aspects of Blood Cells and Blood Flow . . . . .	4
1.3 Physical Aspects of the Cardiovascular System . . . . .	5
1.4 Models for Blood-Related Phenomena . . . . .	6
1.4.1 Haemorheology . . . . .	6
1.4.2 Haemolysis . . . . .	8
1.4.3 Haemodynamic Quantities . . . . .	9
1.5 Thermodynamics of Lipid Membranes . . . . .	10
1.5.1 General Considerations . . . . .	10
1.5.2 Elasticity and Curvature . . . . .	12
1.5.3 Response Functions of a Membrane . . . . .	14
1.5.4 Shapes and Deformations of Vesicles . . . . .	14
1.6 Blood Flow: Previous Numerical Approaches and Results . . . . .	15
<b>2 Numerical Methods</b>	<b>19</b>
2.1 Simulation Framework . . . . .	19
2.1.1 Smoothed Particle Hydrodynamics . . . . .	19
2.1.2 Dissipative Particle Dynamics . . . . .	21
2.1.3 Smoothed Dissipative Particle Dynamics . . . . .	22
2.1.4 Integration of Equations of Motion . . . . .	23
2.2 Present RBC Models . . . . .	23
2.2.1 Vesicle Model . . . . .	24
2.2.2 Hyperelastic Model . . . . .	25
2.2.3 Combined Immersed Boundary LB & FEM . . . . .	26
2.2.4 Multiscale Model . . . . .	28
2.3 Red Blood Cell Model of this Thesis . . . . .	30
2.3.1 Membrane Triangulation . . . . .	31
2.3.2 Membrane Potentials . . . . .	31
2.4 Choices about the Rheological Properties of RBCs . . . . .	33
2.5 Simulation Units of Measurement . . . . .	35

2.6	Boundary Conditions in Flow . . . . .	35
2.6.1	Impermeability of Membranes and Walls . . . . .	35
2.6.2	No-Slip Boundary Conditions and Adaptive Shear Force . . . . .	36
<b>3</b>	<b>Light Scattering by a RBC</b>	<b>39</b>
3.1	Introduction . . . . .	39
3.2	Characteristic Quantities . . . . .	40
3.2.1	Form Factor . . . . .	41
3.2.2	Structure Factor . . . . .	41
3.2.3	Dynamic Scattering Function . . . . .	42
3.3	Light Scattering by Simple Objects . . . . .	43
3.3.1	Light Scattering by Spheres . . . . .	43
3.3.2	Light Scattering by Cylinders . . . . .	45
3.4	Light Scattering by Red Blood Cells . . . . .	46
3.4.1	Introduction . . . . .	46
3.4.2	Index of Refraction of Blood and Choice of Wavelength . . . . .	47
3.4.3	Static Light Scattering by a RBC . . . . .	48
3.4.4	Dynamic Light Scattering by a Diffusing RBC . . . . .	50
3.4.5	Diffusion Coefficient from Hydropro . . . . .	55
3.4.6	Multiple Scattering . . . . .	56
3.4.7	Red Blood Cells in Shear Flow . . . . .	56
3.5	Comparison with Polymers in Shear Flow . . . . .	70
3.6	Conclusion . . . . .	70
<b>4</b>	<b>Dynamics of a RBC in Simple Shear Flow</b>	<b>73</b>
4.1	Introduction . . . . .	73
4.2	Models & Methods . . . . .	74
4.2.1	Numerical Method . . . . .	74
4.2.2	Measured Quantities . . . . .	74
4.2.3	Single Cell in a Couette-Flow Setup with Walls . . . . .	75
4.2.4	Multiple Cells in Shear Flow . . . . .	75
4.3	Results . . . . .	76
4.3.1	Single Cell in Couette-Flow Setup with walls . . . . .	76
4.3.2	Multiple Cells in Shear Flow . . . . .	84
4.4	Conclusion . . . . .	96
<b>5</b>	<b>Dynamics of a RBC in Tube Flow</b>	<b>99</b>
5.1	Introduction . . . . .	99
5.2	Models & Methods . . . . .	100
5.2.1	Numerical interaction model . . . . .	100
5.2.2	Simulated Scenario . . . . .	100
5.2.3	Simulation Parameters and Scaling Equations . . . . .	101
5.2.4	Red Blood Cell Model . . . . .	101
5.2.5	Vessel Model . . . . .	102
5.3	Distinguishing Different Shapes and Dynamics . . . . .	102
5.4	Domains of Shapes and Dynamics . . . . .	105
5.4.1	Phase Diagram . . . . .	105

5.4.2	Representative Examples . . . . .	106
5.5	Comparative Parameter Set-Ups . . . . .	112
5.5.1	Viscosity Contrast of One . . . . .	112
5.5.2	Viscosity Contrast of Three . . . . .	113
5.5.3	Less Deformable . . . . .	114
5.5.4	Spontaneous Curvature . . . . .	115
5.6	A Closer Look at the Transition near the Border . . . . .	116
5.7	Conclusion . . . . .	117
<b>6</b>	<b>Conclusion and Outlook</b>	<b>119</b>
<b>7</b>	<b>Thanks &amp; Acknowledgements</b>	<b>123</b>
	<b>Bibliography</b>	<b>125</b>



# List of Figures

1.1	Erythropoiesis . . . . .	3
1.2	Whole Blood . . . . .	5
1.3	Sickle Cell Anaemia . . . . .	5
1.4	Viscosity as a Function of Vessel Diameter . . . . .	7
1.5	Viscosity as a Function of Shear Rate . . . . .	8
1.6	Lipid, Head Group and Tail Structure . . . . .	10
1.7	Lipid Bilayer . . . . .	11
1.8	Lipid Bilayer Embedding Proteins . . . . .	11
1.9	Lipid Melting . . . . .	12
1.10	RBC Membrane Composition . . . . .	13
1.11	Temperature-Induced Endocytosis . . . . .	15
1.12	RBC Aspirated in a Micropipette . . . . .	16
1.13	Velocity Profiles for Different Haematocrit . . . . .	17
2.1	IBM: membrane mesh and fluid grid . . . . .	28
2.2	Multiscale Model by Peng . . . . .	29
2.3	Triangulated RBC . . . . .	31
2.4	Stress-Free Shapes . . . . .	34
2.5	Erythroblasts . . . . .	34
2.6	Viscosity Contrast . . . . .	35
2.7	Simple Shear Velocity Profile . . . . .	36
2.8	Sphere of Interaction . . . . .	37
3.1	Light Scattering: Experimental Setup . . . . .	40
3.2	Form Factor of a Sphere . . . . .	43
3.3	$D_{\text{eff}}(q)$ of a Sphere . . . . .	44
3.4	Form Factor of a Cylinder; Axial $\vec{q}$ . . . . .	45
3.5	Form Factor of a Cylinder; Lateral $\vec{q}$ . . . . .	46
3.6	Light Scattering: RBC Alignment . . . . .	48
3.7	Form Factor of a RBC; Different $\vec{q}$ . . . . .	49
3.8	Scattering Amplitude of a RBC . . . . .	49
3.9	Time Averaged Intensity of a RBC . . . . .	50
3.10	Intermediate Scattering Function of a RBC with $\kappa_B = 10k_B T$ and Different $q$ . . . . .	52
3.11	Intermediate Scattering Function of a RBC for $q = 0.5/\mu m$ and Different $\kappa_B$ . . . . .	52
3.12	$D_{\text{eff}}(q)$ of a RBC . . . . .	53
3.13	$D_{\text{eff}}(q)$ : Different Simulations . . . . .	54

3.14	$D_{\text{eff}}(q)$ of a RBC with $N_v = 500$ . . . . .	55
3.15	DLS in Shear Setup . . . . .	58
3.16	Correlation Functions $S(q, t)$ for Different Shear Rates; Flow Direction . . . . .	62
3.17	Correlation Functions $S(q, t)$ for Different Shear Rates; Vorticity Direction . . . . .	63
3.18	Correlation Functions $S(q, t)$ for Different Shear Rates; Gradient Direction . . . . .	64
3.19	Average Intensity in Flow Direction . . . . .	65
3.20	Average Intensity in Vorticity Direction . . . . .	66
3.21	Average Intensity in Gradient Direction . . . . .	66
3.22	Correlation Decay Time in Flow Direction . . . . .	67
3.23	Correlation Decay Time in Vorticity Direction . . . . .	67
3.24	Correlation Decay Time in Gradient Direction . . . . .	68
3.25	Correlation Decay Frequency in Flow Direction . . . . .	68
3.26	Correlation Decay Frequency in Vorticity Direction . . . . .	69
3.27	Correlation Decay Frequency in Gradient Direction . . . . .	69
4.1	Simple Shear Flow Setup . . . . .	75
4.2	Cell Extensions at $\bar{\dot{\gamma}} = 57s^{-1}$ . . . . .	77
4.3	Cell Extensions at $\bar{\dot{\gamma}} = 573s^{-1}$ . . . . .	78
4.4	Quadrulobe at $\bar{\dot{\gamma}} = 2005s^{-1}$ . . . . .	78
4.5	Orientation Angle of Initially Upright Cells . . . . .	79
4.6	Membrane and Shape Motion at $\bar{\dot{\gamma}} = 57s^{-1}$ . . . . .	80
4.7	Membrane and Shape Motion at $\bar{\dot{\gamma}} = 286s^{-1}$ . . . . .	80
4.8	Orientation Angle at $\bar{\dot{\gamma}} = 57s^{-1}$ . . . . .	81
4.9	Asphericity at Shear Rates $57s^{-1}$ and $2005s^{-1}$ . . . . .	81
4.10	Asphericity at Shear Rates $286s^{-1}$ and $573s^{-1}$ . . . . .	82
4.11	Extensions of Cells with Different Internal Viscosity . . . . .	83
4.12	Aspect Ratio of Cells with Different Internal Viscosity . . . . .	84
4.13	Histogram of Eigenvalues . . . . .	85
4.14	Histogram of Smallest Eigenvalue . . . . .	85
4.15	Histogram of the Cell Extensions in Different Directions . . . . .	86
4.16	Histogram of the Cell Extensions in Flow Direction . . . . .	87
4.17	Histogram of the Acylindricity . . . . .	87
4.18	Histogram of the Angle in Flow Direction (Ensemble) . . . . .	88
4.19	Histogram of the Angle in Flow Direction (Single Cell) . . . . .	89
4.20	Histogram of the Angle in Gradient Direction (Ensemble) . . . . .	89
4.21	Histogram of the Angle in Gradient Direction (Single Cell) . . . . .	90
4.22	Asphericity at Different Shear Rates . . . . .	91
4.23	Asphericity at Comparable Shear Rates . . . . .	91
4.24	Shear Thinning of RBC Suspension . . . . .	93
4.25	Extension in Flow Direction at $\dot{\gamma} = 2000s^{-1}$ . . . . .	93
4.26	Extension in Gradient Direction at $\dot{\gamma} = 2000s^{-1}$ . . . . .	94
4.27	Extension in Vorticity Direction at $\dot{\gamma} = 2000s^{-1}$ . . . . .	94
4.28	Extension in Flow Direction Phase Diagram . . . . .	95
4.29	Extension in Gradient Direction Phase Diagram . . . . .	95
4.30	Extension in Vorticity Direction Phase Diagram . . . . .	96
5.1	Tube Flow Setup . . . . .	100

5.2	Angle to the Flow Direction; Phase Diagram . . . . .	103
5.3	Variation in the Angle to the Flow Direction; Phase Diagram . . . . .	103
5.4	Distance to the Centre Line; Phase Diagram . . . . .	104
5.5	Asphericity; Phase Diagram . . . . .	104
5.6	Bending Energy; Phase Diagram . . . . .	105
5.8	Phase Diagram for a Viscosity Contrast of Five . . . . .	105
5.9	Angle to the Flow Direction; Representative Shapes . . . . .	108
5.10	Distance to the Centre Line; Representative Shapes . . . . .	108
5.11	Asphericity; Representative Shapes . . . . .	108
5.12	Histogram of Angles; Representative Shapes . . . . .	109
5.13	Orientation Dynamics of a Tumbling Slipper . . . . .	109
5.7	Four Different Shapes/Dynamics Found in Tube Flow . . . . .	111
5.14	Phase Diagram for a Viscosity Contrast of One . . . . .	113
5.15	Phase Diagram for a Viscosity Contrast of Three . . . . .	114
5.16	Phase Diagram for a Less Deformable Cell . . . . .	115
5.17	Phase Diagram for a Cell with Spontaneous Curvature . . . . .	115





# Chapter 1

## Introduction

### 1.1 Blood as a Cell Suspension

Blood is a suspension of red and white blood cells, platelets and plasma. The latter makes up about 55% of blood volume and contains mostly water and dissolved proteins, electrolytes and smaller constituents such as neurotransmitters and hormones. Blood transports nutrients, metabolic waste products and oxygen to muscles and organs in living organisms [106]. The shape of red blood cells (RBCs) is intimately coupled to the ambient plasma, leading to a variety of RBC morphologies in the blood circulation [82]. Thus, blood is a complex fluid and its flow cannot be described by traditional laws for Newtonian fluids [82]. In the following, blood components are described as in reference [1].

#### 1.1.1 Red Blood Cells

In one microlitre of blood, there are 4.2 - 6.1 million red blood cells [126]. Red blood cells (RBCs) supply tissues and organs with oxygen. RBCs can react to changes in their environment. For example, under shear stress in constricted vessels, they release ATP (adenosine triphosphate), relaxing and dilating the vessel walls, thus promoting normal blood flow [180].

With a volume fraction (haematocrit) of 45%, RBCs make up the major part of whole blood. With a cellular volume of about  $92\mu\text{m}^3$ , in one litre of blood, there are around  $5 \cdot 10^{12}$  RBCs. Thereby, their dynamics, shape, deformation, and orientation in microcirculation affect the rheology, flow resistance and transport properties of whole blood [32, 46], leading to non-trivial correlations of cellular and continuum scale. For example, the viscosity of whole blood is not simply the weighted sum of the viscosities of its plasma and the cell cytosol.

Erythropoiesis, the formation of RBCs is described according to reference [139].

Mature blood cells have a relatively short lifespan on the order of 10 hours (eosinophils) to 120 days (RBCs). Thus, they have to be renewed continuously (haematopoiesis). To replace senescent or dead RBCs, around  $25 \cdot 10^{11}$  new RBCs are required daily.

In early embryos, blood cells arise from the mesoderm of the yolk sac. Later, the liver and spleen, and finally, the red bone marrow act as haematopoietic tissue. In adults, the red bone marrow at the ends of the long bones (particularly humerus and femur) and the flat bones (pelvis, ribs, sternum, vertebrae, clavicles, scapulae, and skull) produce blood cells. The bone marrow is enclosed by bone, thus, small arteries must penetrate the bone casing to

provide its blood supply. Small arterial branches communicate directly (without intervening capillaries) with venous sinuses, which are thin-walled vessels (diameters of 50-75 $\mu\text{m}$ ).

RBCs develop in association with macrophages near the wall of the sinuses before diapedesis (being delivered to the circulation). Most red cells enter the circulation in an immature state. Although blood contains many different cells with different functions, all of them originate from haematopoietic stem cells in the bone marrow. These cells are self renewing and multipotent: through a series of cell divisions, they can give rise to all of the different blood cells. Stem cells divide to form progenitor cells, which, in turn, give rise to precursor cells, committed to form the various types of blood cells.

Haematopoietic growth factors control the cell formation. These growth factors come from the bone marrow stroma, the liver, the kidneys, and WBCs. These growth factors are local signalling molecules called cytokines which are supplemented by two hormones. One of them is erythropoietin (EPO), balancing the rate of erythropoiesis to the prevailing need in the circulation. RBC production is accelerated due to for instance haemorrhage, donation of blood, and chronic hypoxia. Secretion of EPO is probably stimulated by a fall in tissue oxygenation, and its concentration in plasma is inversely related to the partial pressure of oxygen in the arterial blood. EPO accelerates the differentiation of progenitor cells into erythroblasts. Further essential components for RBC production are iron, folic acid, vitamin  $B_{12}$  and the glycoprotein intrinsic factor. If there is a lack in these components, RBC development is impaired resulting in pernicious anaemia.

The formation of RBCs is depicted in figure 1.1. Apparently, this is a stepwise process involving different mechanisms such as division, growth factors and mechanical changes. Once a RBC has entered the circulation, it lives around 120 days. Eventually, it is destroyed in the spleen, the liver, or lymph nodes by macrophages.

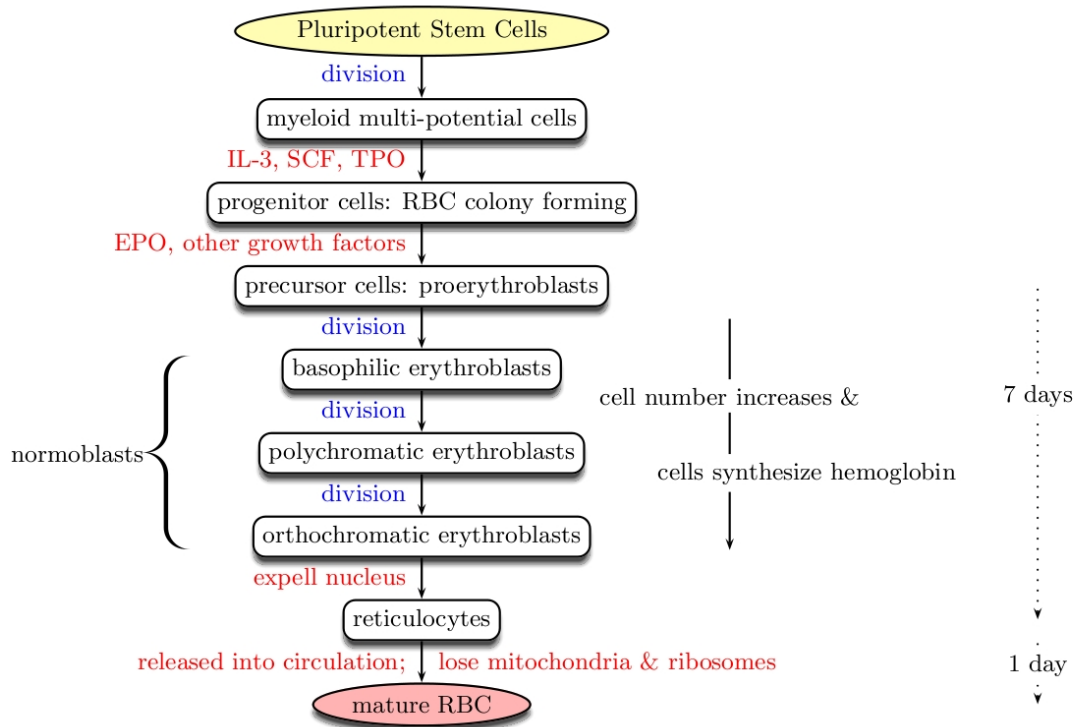


Figure 1.1: Erythropoiesis: shown are the growth factors interleukin-3 (IL-3), stem cell factor (SCF), and thrombopoietin (TPO). EPO is the hormone erythropoietin. After losing their mitochondria and ribosomes, RBCs cannot synthesise haemoglobin or generate ATP by oxidative metabolism anymore. Thus, they rely on glucose and the glycolytic pathway for their metabolic needs. This pathway can produce a glycerate that reduces the oxygen affinity of haemoglobin, thus facilitating oxygen release to the tissues. Information taken from reference [139].

### 1.1.2 White Blood Cells

In one microlitre of blood, there are 4000-11000 white blood cells [56]. White blood cells (WBCs) or leukocytes are the key players in the immune response. Out of many different WBC types, two are briefly described here as in reference [1].

Neutrophils fight bacteria and fungi. As the body's first response, they dominate early stages of acute inflammation. They live for about five days and make up 60-70% of the total WBC count. Neutrophils destroy bacteria via phagocytosis (devouring a particle by engulfing) to defend the body against infection. To digest microbes, lysosomes are required. These are organelles containing enzymes that can degrade and recycle cellular waste [152]. Neutrophils are unable to renew lysosomes, thus, after phagocytosing a few bacterial cells, they die.

Monocytes live for several hours to days and make up 5% of the total WBC count. Their first task is to present pathogene pieces to T-cells in order to start an antibody response and to memorise the pathogene. Their second task is to assist neutrophils with phagocytosis. Both task are performed in the bloodstream. Monocytes eventually leave the blood stream through the vascular wall to the underlying tissue. There, they become macrophages and phagocytose dead cell debris and microorganisms.

Phagocytosis starts through the binding of the receptors on the WBC surface to ligands on the particle. Then, the WBC deforms, surrounds and engulfs the particle. Thus, cell deformability is important. Furthermore, if bacteria have to be destroyed within the tissue, monocytes will have to deform to squeeze through small openings in the vessel wall. Phagocytability increases with shear stress [147]. Thus, it is worthwhile to study the influence of shear rate on cell deformability.

### 1.1.3 Platelets

In one microlitre of blood, there are 200000-500000 platelets [56]. Platelets have a discoid shape and a characteristic size of about  $2\text{-}3\mu\text{m}$ . They are the key players in both physiological haemostasis and pathological thrombosis. The first phenomenon occurs e.g. in case of an injured vessel. A blood clot forms and seals a wound to stop blood loss. Clotting needs three main steps. First, platelets adhere to thrombogenic surfaces. Second, they get activated and release procoagulant agonists. Third, the latter induce further activation, thus causing a positive feedback (coagulation cascade). The growing clot seals the wound.

Mechanical conditions affect these steps, such as atherosclerosis, medical devices, the differences between arteries and veins, or between artery centre and wall. Depending on the shear rate, platelets show different behaviour. At low shear rates ( $\dot{\gamma} < 1000\text{s}^{-1}$ ), platelets are slow compared to their environment (surfaces, dissolved proteins, other platelets). Thus, their receptors have enough time to interact and bind to surfaces. In turn, adjacent activated platelets are bridged by binding.

At high shear rates ( $1000\text{s}^{-1} < \dot{\gamma} < 10000\text{s}^{-1}$ ), platelet adhesion is supported by the von Willebrand factor (vWf) [174]. Thrombogenic surfaces have vWf immobilised on it, which, in turn, binds to the platelet via a transmembrane protein [122].

Alternating shear stress significantly enhances platelet aggregation [117, 153]. Probably, the period of high stress promotes initial interaction between vWf and a transmembrane protein, and the period of low stress decelerates this interaction to allow more binding time.

## 1.2 Physical Aspects of Blood Cells and Blood Flow

A physiological, mature RBC has a biconcave shape of  $6\text{-}8\mu\text{m}$  in diameter and  $2\mu\text{m}$  thickness. The RBC's non-sphericity permits shape changes at constant volume and surface area. Shape changes are induced by external forces. RBC deformation is reversible: after removing the force, the RBC recovers its original biconcave shape within 100-200ms [9, 74, 108, 170]. In vivo, the cell's dynamic viscoelastic rigidity and recovery time are important for the distribution and flow through microvessels [35]. Recovery time can be used as a measure for membrane properties, as it is linked to membrane viscosity  $\eta$  and shear elastic modulus  $\mu$  as  $t_c = \frac{\eta}{\mu}$  [74, 35], in case the shear modulus dominates.

The RBC membrane consists of a lipid bilayer and spectrin network (cytoskeleton; inner layer). They are connected by transmembrane proteins that can detach and reattach and thus, allow the bilayer and the cytoskeleton to slide with respect to each other [30]. The membrane encloses the cytosol, which for a RBC is a solution of haemoglobin. The membrane exhibits various mechanical features: the bilayer is incompressible and elastic to bending, the cytoskeleton is compressible and elastic to shearing. Thereby, a RBC is often modelled either as a vesicle or a capsule. It is eligible to combine the mechanical properties of

both models [46]. Elasticity and deformability are vital in microcirculation since RBCs have to squeeze through  $0.5\ \mu\text{m}$ -thick endothelial slits in spleen and they experience elastic reversible deformation during their 120 day life span [177]. Less deformability may lead to impaired perfusion, higher blood viscosity, ischemia, and occlusion in microvessels. Possible causes are changes in membrane mechanics, cytoplasm viscoelasticity and surface area or volume [177].

The lipid composition on the RBC membrane is different on inner and outer leaflet [70]. Thereby, the physical properties on both sides differ and thermodynamic forces act across the membrane (electrostatic field gradients, chemical potentials, etc.) [70].

In certain pathologies, the mechanical properties of a RBC are altered, leading to different flow behaviour and corresponding problems in transport functions. E.g. in case of sickle cell anaemia, due to their shape change, the cells tend to entangle or form clots, particularly close to vessel bifurcations. In case of malaria, a parasite invades the cells and makes it more spherical and rigid [44]. Thus, the cell cannot enter more narrow vessels anymore and supply them with oxygen.

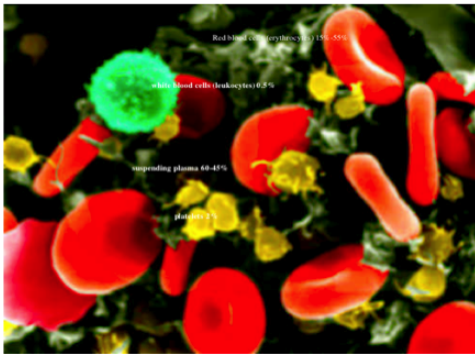


Figure 1.2: Whole blood with white (depicted in green) and red cell and platelets (depicted in yellow). Taken from reference [141]. Reprinted with permission.

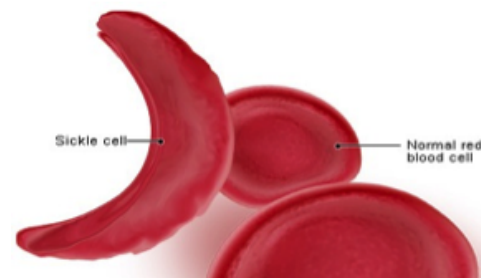


Figure 1.3: Sickle cell anaemia RBCs. Taken from medicinenet.com. Reprinted with permission.

### 1.3 Physical Aspects of the Cardiovascular System

The heart pumps oxygenated blood coming from the lungs to the tissue, where it is deoxygenated. This blood is pumped into the lungs again for (re-)oxygenation. The cardiac cycle comprises the alternating contraction and relaxation of the heart muscle [139]. During diastole, the chambers of the heart relax and fill with blood. During early diastole, both the atria and ventricles fill with blood. Towards the end of ventricular diastole, the atria contract to force blood into the ventricles. During systole, the chambers contract to eject blood. The so-called stroke work, performed by the heart during each beat, is the product of the rise in ventricular pressure (occurring during systole) and the stroke volume.

A physical description of the circulation consists of a pump (the heart) and a series of interconnected pipes (the blood vessels) [139]. The overall arrangement has two circulations in series: pulmonary and systemic circulation. Via the first, blood is pumped from the right side of the heart through the lungs, via the second, blood is pumped from the left side of the

heart to the rest of the body.

Heart pumping raises the pressure in the aorta above that of the large veins, where the pressure is close to that of the atmosphere [139]. This pressure difference makes blood flow around the systemic circulation. The pressure in the major arteries is the (systemic arterial) blood pressure. Analogously, the pressure difference of pulmonary arteries and -veins makes blood flow through the lungs. The structure of systemic blood vessels can be compared to a tree: arteries branch and get smaller (arterioles) until they reach the tissue as capillaries. There, oxygen is exchanged. The deoxygenated blood flows back in the opposite order: leaving the capillaries, it enters the small venules and eventually the larger veins. All vessels have their characteristic length scales and for studying them, a proper resolution has to be chosen.

During embryonic development, remodelling of the cardiovascular system makes the network more efficient [1]. It achieves its function (transport of nutrients and waste) with minimal effort (work performed by the heart, homeostasis) [1]. The system's hierarchy in most of both embryo and adult animals is a prime example: large vessels transport blood efficiently while small vessels exchange nutrients efficiently [1].

An idealised model for blood flow is the Poiseuille description. The vessel is considered as a rigid cylinder of radius  $r$  and the solvent as a Newtonian fluid of viscosity  $\eta$ . The flow profile is then parabolic:  $v(r) = -\frac{1}{4\eta} (r_0^2 - r^2) \frac{dp}{dz}$ . Pulsatile flow, caused by the beating heart, modulates the pressure gradient periodically:  $\frac{dp}{dz} = c_0 + c_1 e^{i\omega t}$  [1].

Experiments with chicken eggs show that the early embryo is small enough to accomplish mass transport via diffusion. However, later, the grown embryo needs flow (i.e. advection) for efficient transport. Thus, the embryonic heart has to start beating [1].

## 1.4 Models for Blood-Related Phenomena

This section gives an overview of various phenomena linked to the fluid dynamics of blood. It suggests how such phenomena can be modelled, partially differing conceptually from the cell-based model used here.

### 1.4.1 Haemorheology

In small blood vessels, the particulate nature of blood dominates [140, 109, 1]. The fact that blood is a suspension of RBCs becomes apparent when blood is forced through geometries with a diameter  $D$  that is of the same order or smaller than the dimensions of a RBC: for  $D < 6\mu m$ , the effective viscosity increases dramatically [1, 143].

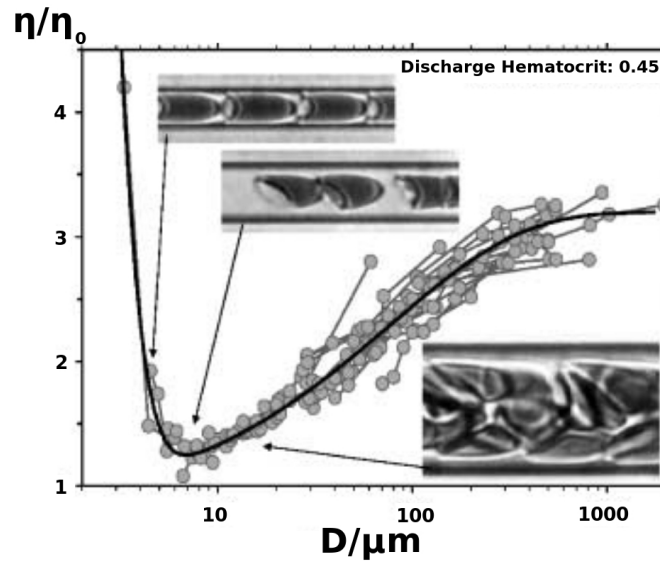


Figure 1.4: Relative effective viscosity as a function of blood vessel diameter. This viscosity is the apparent viscosity in a tube with a certain diameter, normalised by the plasma viscosity [1]. For tube diameters of 4.4, 7, and 17  $\mu\text{m}$ , micrographs of human blood flowing through glass tubes (flow is from left to right) are shown. Taken from reference [143]. Reprinted with permission.

Figure 1.4 shows the effective viscosity as a function of diameter  $D$ . For low  $D$ , RBCs strongly deform and align in a single file.

The radial distribution of RBCs shows that cells tend to migrate away from the wall, leaving a cell-free layer (CFL) near the wall. Its viscosity is lower than that of bulk blood, thereby, the CFL acts as an effective lubrication layer [42, 25, 140]. The CFL thickness is on the order of a RBC diameter [88]. The CFL occupies a larger relative volume in smaller blood vessels [85, 42]. Hence, the effective viscosity, obtained via Poiseuille's law, will be lower (Fåhræus-Lindqvist effect) [143, 1, 38]. For  $D$  larger than  $500\mu\text{m} = 0.5\text{mm}$ , the CFL is relatively thin. The Fåhræus-Lindqvist effect thus becomes negligible and blood can safely be considered continuous (one-phase) [1].

Another important phenomenon in haemodynamics is shear-thinning. The viscosity is not constant, as it would be in a Newtonian fluid, but decreases under shear stress. Figure 1.5 shows that both haematocrit and species affect haemorheology [31, 67].

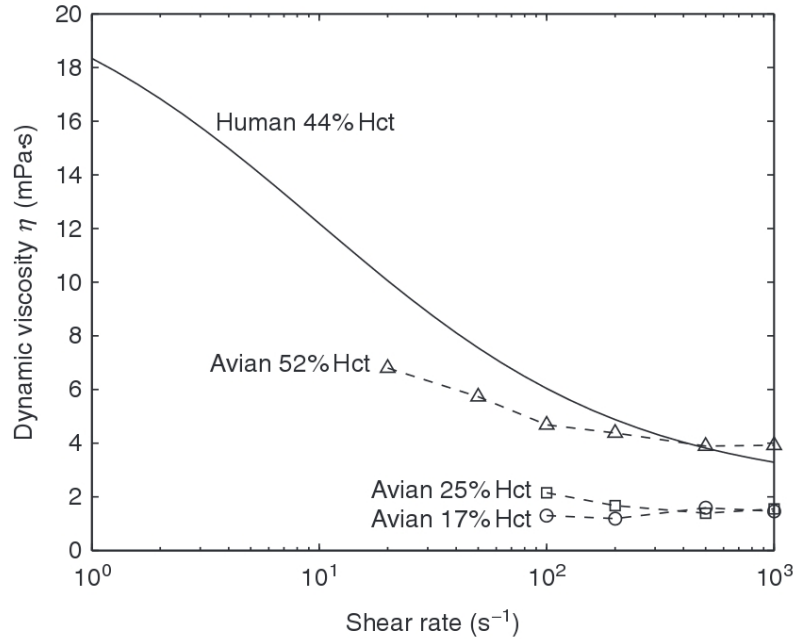


Figure 1.5: Dynamic viscosity as a function of shear rate. Both the viscosity values and the shear-thinning behaviour depend on species and haematocrit. Taken from references [62, 1, 5, 166]. Reprinted with permission.

In contrast to human RBCs, avian RBCs are nucleated. The latter deform less when forced through capillaries [55]. Since human RBCs are biconcave disks, they have a large surface-to-volume ratio, facilitating rouleaux formation, an alignment of RBCs in stacks [1]. Since nucleated avian RBCs are more spherical, they are less prone to rouleaux formation [5, 115]. However, different plasma proteins may also change the aggregation. Figure 1.5 shows that avian blood viscosity is lower and relatively constant [5]. The former is due to the lower haematocrit, while the latter is linked to the lower deformability and inability to form rouleaux [5, 55].

### 1.4.2 Haemolysis

Haemolysis is defined as the release of haemoglobin into the plasma due to a mechanical damage of the RBC membrane [1].

A RBC deforms in shear flow, while preserving volume and surface area. Above a critical shear stress, the membrane is forced to stretch. Haemoglobin may be released via complete rupture of the cell [144] or through pores appearing at high stress in the viscoelastic membrane [195]. Shear stress-exposure time is a key factor in haemolysis [103]. Below a critical shear stress threshold, surface-effects dominate, whereas above, shear-stress effects dominate. Haemolysis occurs as a power-law function of the shear stress  $\tau$  acting on the cells and the time  $t$  of exposure to that stress [103, 189, 188, 61, 194]. Thus, the damage index  $H$  is described as a power law:

$$H = C\tau^a t^b \quad (1.1)$$



with constants  $\mathcal{O}(C) = 10^{-5}$ ,  $a \approx 2$ ,  $b \approx 0.7$ .

Older RBCs have more viscous, stiffer membranes and a smaller surface area [161]. Presumably, damage by shear stress depends on the current level of damage. On top of that, damage accumulates over the lifetime of the cells. As soon as RBC have been damaged sufficiently, they are removed from the circulation by the spleen.

To consider this accumulation, infinitesimal damage is based on the idea of mechanical dose and shear stress-exposure *history* via a time integral [65, 64]:

$$dH = Cb \left( \int_{t_0}^t \tau(\epsilon)^{a/b} d\epsilon + H(t_0) \right)^{b-1} \tau(t)^{a/b} dt \quad (1.2)$$

### 1.4.3 Haemodynamic Quantities

Flow-input waveforms and vessel geometry, such as expansions, bends, bifurcations, or stents, alter and possibly disturb blood flow patterns [1]. This enables flow separation, reattachment, recirculation, stagnation, atherosclerosis and spreading of vascular cells towards the vessel interior [89]. To quantify changes in blood flow, the following quantities have been defined.

Wall shear stress (WSS) is crucial to study atherosclerosis [22]. WSS describes the viscous stress acting on the surface.

$$\vec{\tau}_w = \vec{n} \cdot \boldsymbol{\tau}_{ij} \quad (1.3)$$

with vector  $\vec{n}$  normal to the arterial wall surface and fluid viscous stress tensor  $\boldsymbol{\tau}_{ij}$ .

For the case of time-dependent flows, the time-averaged WSS is defined as

$$\text{TAWSS} = \frac{1}{T} \int_0^T |\vec{\tau}_w| dt \quad (1.4)$$

with duration  $T$  of the cardiac cycle.

WSS alters endothelial cell morphology and orientation. For  $\text{WSS} > 1$  Pa, endothelial cells elongate and align in flow direction [113]. At the sites of low WSS in a stented coronary artery, tissue regrows [99].

Pulsatile flow makes the shear stress oscillate, which influences in-stent restenosis [22]. Thus, an oscillatory shear index (OSI) is defined [94]:

$$\text{OSI} = \frac{1}{2} \left( 1 - \frac{\left| \int_0^T \vec{\tau}_w dt \right|}{\int_0^T |\vec{\tau}_w| dt} \right) \quad (1.5)$$

High oscillatory shear stress enhances arterial narrowing [193, 187, 1].

The relative residence time (RRT)

$$\text{RRT} = \frac{1}{(1 - 2 \text{OSI}) \text{TAWSS}} = \frac{T}{\left| \int_0^T \vec{\tau}_w dt \right|} \quad (1.6)$$

is critical for atherogenesis and in-stent restenosis and associated with the residence time of particles near the wall [73, 76].

## 1.5 Thermodynamics of Lipid Membranes

The membrane of erythrocytes consists of a cytoskeleton and a lipid membrane. The latter shall be considered more closely in this section; following the notion of and citing reference [70].

### 1.5.1 General Considerations

Biological membranes display a wealth of physical phenomena including phase transitions, propagating voltage pulses, variable permeability, structural transitions (as in exo- and endocytosis), and domain formation.

Thermodynamics is always valid as it is based on only two basic and intuitive laws: the conservation of energy and the maximum entropy principle. It thereby serves as a basis for physics on all length scales, e.g. on the level of biomembranes.

Cells and their compartments have a large variety of membranes. Membranes surround both the cell as a whole and each organelle as the nucleus, mitochondria, or the endoplasmic reticulum. The major building blocks of membranes are thousands of different lipid molecules. One example, DPPE, is shown in figure 1.6. The combination of a lipophilic (= hydrophobic) and a hydrophilic part is called 'amphiphilic' (Greek for 'loving both'). These basic building units self-assemble into larger structures, depending on the surrounding medium. In water, the hydrophobic tails avoid contact to the environment by forming e.g. circular shapes (micelles), with the hydrophobic heads outside, exposed to the water. Another possible shape is a bilayer as shown in figure 1.7.

At oil-water interfaces, lipids arrange such that the heads touch the water and the tails touch the oil. This interfacial layer reduces the surface tension.

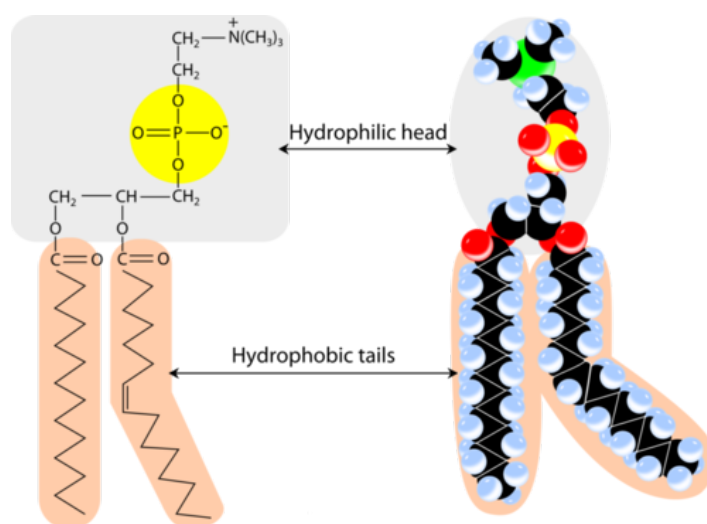


Figure 1.6: Head group and tail structure of phosphatidylethanolamine (DPPE) as well as the coarse-grained model of hydrophilic head and hydrophobic tails. Taken from <http://www.ck12.org/user:bGVldEBoYXJncmF2ZS5lZHU./book/General-Chemistry-FlexBook-by-Mrs.Tomi-Lee/section/15.3/>.

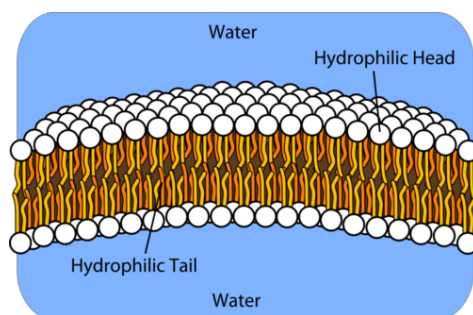


Figure 1.7: In an aqueous solution, phospholipids form a bilayer where the hydrophobic tails point towards each other, and only the hydrophilic heads are exposed to the water. Taken from <http://www.ck12.org/user:bGVldEBoYXJncmF2ZS5lZHU./book/General-Chemistry-FlexBook-by-Mrs.Tomi-Lee/section/15.3/>.

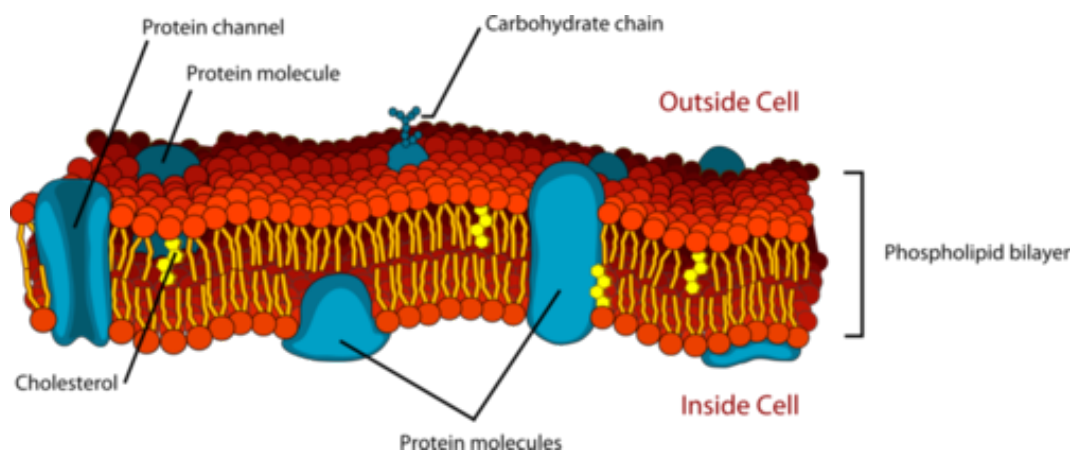


Figure 1.8: The phospholipid bilayer of a cell membrane contains embedded protein molecules which allow for selective passage of ions and molecules through the membrane. Taken from <http://www.ck12.org/user:bGVldEBoYXJncmF2ZS5lZHU./book/General-Chemistry-FlexBook-by-Mrs.Tomi-Lee/section/15.3/>.

The notion of thermodynamics and statistical mechanics comes into play since the plasma membrane of one eukaryotic cell contains  $\mathcal{O}(10^{10})$  lipid molecules. Thus, lipid membranes are thermodynamically large ensembles.

Biological molecules interact with specific binding partners, abundant lipid surfaces, protons, ions, and water. Additionally, different orientations and conformations complicate these interactions. In many cases, it is not feasible to investigate all possible interactions. Biological processes and cooperative phenomena such as membrane melting can be treated on a scale coarser than binary molecular interactions. In the case of biological systems, the variety of proteins, lipids, and ions is represented by their chemical potentials. These are functions of intensive thermodynamic variables as the concentrations of other molecules, temperature or pressure. In thermal equilibrium, a multimolecular ensemble such as a membrane fluctuates around the state of maximum entropy. Out of equilibrium, the first derivative of entropy constitutes the thermodynamic forces, driving the system to equilibrium. The second derivatives constitute the susceptibilities, such as heat capacity or elastic constants.

These are related through the Maxwell relations, such as:

$$\left(\frac{dS}{dp}\right)_{T,n_i} = -\left(\frac{dV}{dT}\right)_{p,n_i}. \quad (1.7)$$

They provide both deeper insights into membrane behaviour and access to quantities that are difficult to measure. In equation (1.7), the derivative of the entropy with respect to pressure is difficult to measure, yet it is equivalent to the isobaric volume expansion, which can be measured easily. Thereby, thermodynamics provides considerable insight into all the couplings between seemingly different (membrane) processes.

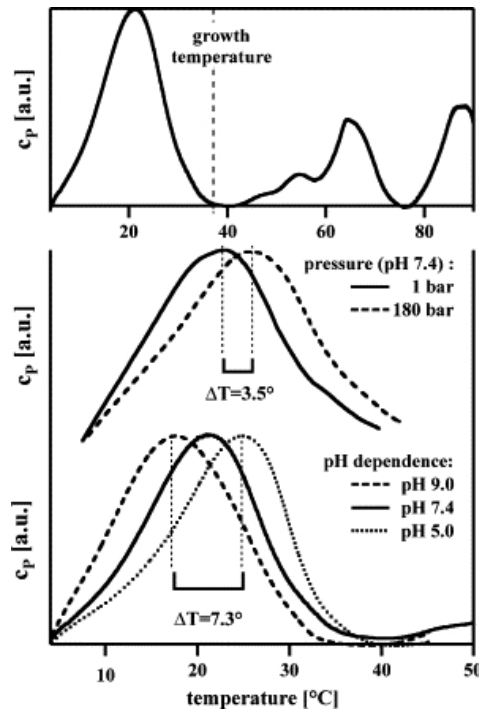


Figure 1.9: A calorimetric experiment on a native *E. coli* membrane. Below growth temperature, lipid melting takes place. Above growth temperature, protein unfolding takes place. Taken from reference [71]. Reprinted with permission.

## 1.5.2 Elasticity and Curvature

Lipid membranes can be described analogously to liquid crystals, as they are composed of axial molecules that influence each other in their orientation. In liquid crystalline phases, an equilibrium order of molecules exists, which can be altered by performing work (distortion). Let us consider an infinitely thin membrane without chirality in its molecules. The free energy density is described by Helfrich's form [72]:

$$g = \frac{1}{2}K_B (s_1 + s_2 - s_0)^2 + K_G s_1 s_2 \quad (1.8)$$

where  $s_1$  and  $s_2$  are the splays in the two directions of the membrane plane and  $s_0$  is the spontaneous splay.  $K_B$  is called bending modulus, even though it is technically rather a

splay modulus.  $K_G$  is the Gaussian modulus.

A vesicle, which can be used as a model for a RBC, has a closed structure. Due to this topological boundary condition, the elastic free energy is not necessarily minimal. Let us consider first the special case of a spherical vesicle ( $|R_x| = |R_y| = |R|$ ). Additionally, its membrane shall be made of the same lipids on both sides. Due to this symmetry, the spontaneous curvature vanishes. Integrating equation (1.8) yields the total elastic free energy:

$$G_{\text{vesicle}} = \frac{K_B}{2} \oint_A \left( \frac{4}{R^2} \right) dA + K_G \oint \frac{1}{R^2} dA = 8\pi K_B + 4\pi K_G \quad (1.9)$$

Thus, the total energy is independent of the radius. Both moduli typically have values on the order of  $10^{-19} J$ , which corresponds to about  $20k_B T$  in case of room or body temperature.

The free energy of equation (1.9) depends on shape and thus deformation. However, it can be shown that the integrated Gaussian term is independent of shape of the vesicle, as long as it is closed and topologically intact. Thus, for deformations one can ignore the Gaussian term.

It shall be emphasised that one assumption is not met in case of a RBC: its membrane is made of different lipids on both sides, see figure 1.10. Thus, there should be a non-zero spontaneous curvature.

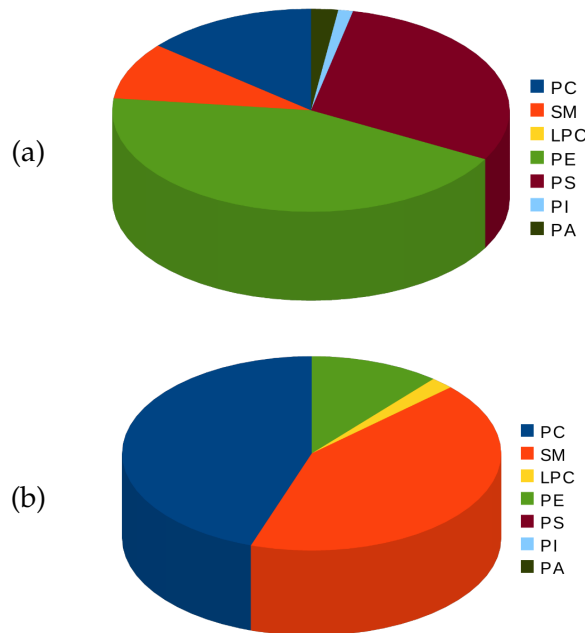


Figure 1.10: Composition of the (a) inner (b) outer leaflet of the RBC membrane. PC: phosphatidylcholine, SM: sphingomyelin, PE: phosphatidylethanolamine, PS: phosphatidylserine, PA: phosphatidic acid, LPC: Lysophosphatidylcholine. Data taken from references [148, 176, 190, 178, 198, 173].

### 1.5.3 Response Functions of a Membrane

Lipid melting is quantified via calorimetry as shown in figure 1.9. **Heat capacity** is defined as

$$c_p = \left( \frac{\delta Q}{dT} \right)_p \quad (1.10)$$

with  $\delta Q$  being the differential process-quantity heat and  $T$  being the temperature; under isobaric conditions. Considering  $dH = \delta Q + V dp$ , one can exchange  $\delta Q$  by  $dH$  in equation (1.10). In a canonical ensemble with Boltzmann probability distribution  $p(x) = \exp\left(-\frac{H(x)-H_0}{k_B T}\right)$ , where  $H(x)$  depicts the enthalpy of a certain state and index 0 the ground state, the heat capacity is linked to the fluctuations:

$$c_p = \frac{\langle H^2 \rangle - \langle H \rangle^2}{RT^2}. \quad (1.11)$$

Equation (1.11) is called fluctuation theorem [95].

Lipid membranes are compressible to a certain degree. Volume compression can be measured via ultrasonic velocity. Sound velocity depends on the **compressibility** of a medium:  $c_0 = \sqrt{\frac{1}{\kappa_s \rho}}$  for a 3D liquid or gas, with  $\rho$  being mass density and  $\kappa_s$  being the adiabatic compressibility.

Let us consider now an isothermal compression, in which the released heat is absorbed by a heat reservoir (aqueous environment). For lipid vesicles, this is fulfilled if the compression is much slower than the membrane relaxation. Hydrostatic pressure causes relative volume changes, with  $K_V$  being the modulus of compression:

$$\Delta p = -K_V \left( \frac{\Delta V}{V_0} \right) \quad (1.12)$$

The infinitesimal change in Gibb's free energy is  $dG = -SdT + Vdp$ . Here,  $dT = 0$ . Then, we consider the change in Gibb's free energy density:

$$g_V = \int \frac{\Delta V}{V_0} dp = -K_V \int \frac{\Delta V}{V_0} d \left( \frac{\Delta V}{V_0} \right) = \frac{1}{2} K_V \left( \frac{\Delta V}{V_0} \right)^2 \quad (1.13)$$

This corresponds to Hooke's law. For the change in area, the relations are analogous. This is also reflected in the potentials for the present RBC model. It should be noted that the membrane in this model comprises both lipid bilayer and cytoskeleton, but the contribution of both parts is assumed to be in the form of equation (1.13).

### 1.5.4 Shapes and Deformations of Vesicles

For closed vesicles, the integrated Gaussian term is constant and thus irrelevant. For spherical vesicles and symmetric membranes, the 'bending' term gets minimal, as the curvature terms enter the equation quadratically. For a sphere, the volume-to-area ratio is  $\frac{V}{A} = \frac{R}{3}$ . Membranes possess a water permeability depending on their excess heat capacity. Outside of the transition regime and for short periods of time, the membrane permeability for ions and water is low. Thereby, the volume can be assumed constant. Thus, a spherical vesicle cannot be deformed, because  $\frac{V}{A}$  has to remain constant.

However, if  $\frac{V}{A} < \frac{R}{3}$ , as for a RBC, the vesicle cannot get completely spherical, because no fluid can enter and increase the volume. Then, the minimal elastic free energy has to be found by assuming a fixed reduced volume  $\frac{V}{A^{\frac{3}{2}}}$ . Examples for shapes at different volume-to-area ratios are shown in figure 1.11.

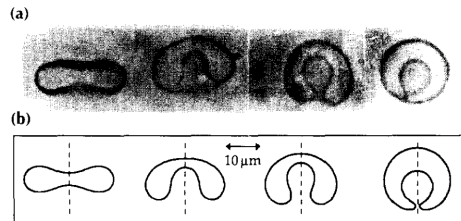


Figure 1.11: Temperature-induced 'endocytosis': unilamellar vesicles during a temperature increase of only 1K. Lower panel: theoretical shapes of minimal bending energy with constraints on volume, area, and total mean curvature. The shape at the very right represents a small spherical bud that is contained in the larger sphere; both spheres are connected by a small neck or 'worm-hole'. Taken from references [110, 16]. Reprinted with permission.

## 1.6 Blood Flow: Previous Numerical Approaches and Results

Blood has been studied numerically for several years. Particulate considerations, thus studies that model blood as a suspension of cells, are briefly summarised here.

The deformation of RBCs by micropipette aspiration, thus a purely static system, has been studied because it characterises the elasticity and plasticity of the cytoskeleton [29]. The cytoskeleton of RBCs has been modelled by coarse-grained Monte Carlo simulations. Two- and three-body effective potentials represent the nonlinear chain elasticity and sterics of more microscopic models. The cytoskeleton is represented by a triangulated network and used in three different versions. Two of them are stress free (with/out internal attraction) and one of them is prestressed. These models are used in simulations regarding a finite ambient temperature. The prestressed model agrees best with experiments, thus, the anisotropic strain of the triangulated mesh is focused to understand how a cytoskeleton is deformed in experiments. Segmented polymer chains (spectrin level model) can be replaced by effective potentials, reducing the degrees of freedom.

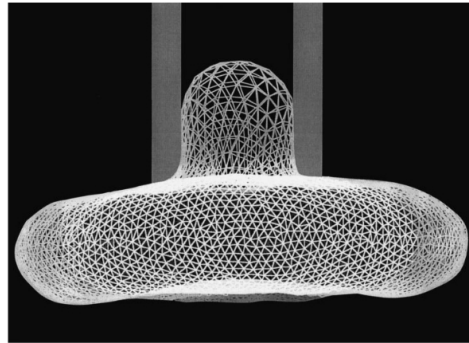


Figure 1.12: RBC aspirated in a micropipette. The reduced volume of the cell is 0.6 and the cell shape is initially stress-free. Taken from reference [43].

To study the impact of depletion-mediated RBC aggregation on blood rheology with a fully cellular approach, a 3D model coupling Navier-Stokes equation with cell interactions has been introduced [111]. An immersion continuum model tracks the RBC deformation. This model captures effects such as shear thinning, the impact of cell rigidity on blood viscosity, and the Fåhræus-Lindqvist effect, which is linked to axial migration of deformable cells. Concerning aggregation, the change in viscosity due to break-up of rouleaux structures was shown. Lower RBC deformability and shear rates  $> 0.5s^{-1}$  facilitate disaggregation and affect the effective viscosity.

To simulate 3D RBCs subject to simple shear flow, cells have been approximated by Newtonian liquid drops enclosed by Skalak membranes, accounting for membrane shear elasticity and membrane area incompressibility [158]. RBCs have an initially biconcave resting shape, and the internal fluid is assumed to be equivalent to the ambient fluid. At large shear rates, the cells perform a swinging motion, in which inclination angle periodically oscillates and the shape deforms during membrane tank-treading. With decreasing shear rate, the swinging amplitude of the cell increases, and eventually, triggers a transition to tumbling motion. During this transition, the apparent viscosity of the suspension increases monotonically. The effect of haematocrit and vessel diameter on the velocity profile, flow resistance and cell-free layer has also been studied [43]. The cell membrane is modelled as a viscoelastic network and a suspension of cells models whole blood. The distribution of cells shows a migration and the formation of a cell-free layer, reproducing the Fåhræus-Lindqvist effect. The CFL effectively lubricates the flow of the cells concentrated in the centre. The CFL formation agrees with *in vitro* and *in vivo* experiments.



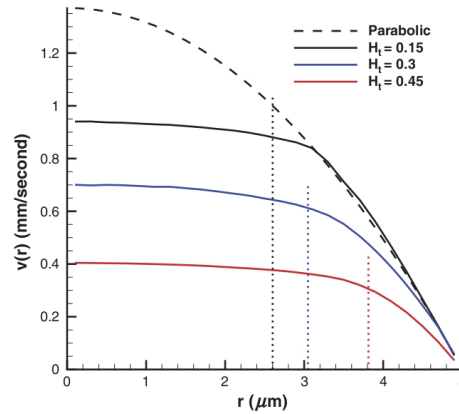


Figure 1.13: Velocity profiles  $v(r)$  for blood flow in a cylindrical vessel of diameter  $2r = 40\mu\text{m}$  for different haematocrit  $H_t$ . The dashed line represents the analytical velocity profile for a purely Newtonian fluid (continuous). Dotted lines mark the CFL thickness. Taken from reference [43]. Reprinted with permission.

Higher haematocrit leads to both blunter velocity profiles and larger blood flow resistance.

The dynamic phase behaviour of single RBCs in linear shear flow has been studied because it characterises the coupling of all shape, deformation, and dynamics [191]. The model includes not only resistance against shear deformation, area dilatation, and bending, but also considers the viscosity difference between inner and suspending fluids. Thus, a larger variety of shapes has been observed. At moderate bending rigidity, the newly introduced breathing motion shows flow alignment and deformations or swinging motion with dimples periodically emerging and disappearing. The shapes-/dynamics transition depends on the viscosity difference.

The dynamics of RBCs in low shear-rate flows has also been studied by a multiscale fluid-structure interaction model incorporating several coarse-graining levels, down to the spectrin polymer level [134]. The stress-free state of the cytoskeleton is spheroidal, thereby, it is predictable that the cell maintains its biconcave shape during tank-treading motions. As the stress-free state approaches a sphere, the threshold shear rate for tank-treading decreases. At low shear rates, the RBC response is a measure for distribution of shear stress in the cytoskeleton in the natural state.



## Chapter 2

# Numerical Methods

### 2.1 Simulation Framework

Blood is a liquid that shows shear-thinning and its viscosity depends on the flow conditions. Thereby, blood cannot be considered as a Newtonian fluid. We intend to link the behaviour of blood cells to the flow properties of the blood suspension. Thus, it is essential to separate properly different length scales. The RBC is on the micrometre ( $\mu m$ ) scale and its characteristic shape recovery time is about 100-200ms [9, 74, 108, 170]. In contrast, the solvent molecules move much faster at a time scale of  $10^{-14}s$ . Thereby, at the scale of a cell, the motion of solvent molecules can be neglected and their impact on the cell can be modelled as stochastic collisions. Here, we consider small fluid volumes as constituents of the plasma surrounding the RBC. Assuming a density of  $n = 12$  (simulation units, see below), these volumes are on the  $\mu m$  scale and represent clusters of many water molecules ( $\mathcal{O} = 10^9$ ). The explicit consideration of water volumes allows the simulation of hydrodynamic interactions, which are mediated by the solvent, e.g. in case of flow.

The Navier-Stokes equation (NSE) describes the flow of a viscous fluid. It is derived from Newton's second law and assumes that the fluid stress is the sum of a diffusing viscous and a pressure term. To model blood plasma via the NSE, one can assume incompressibility as blood plasma mainly consists of water. Thus, the NSE becomes:

$$\begin{aligned} \nabla \cdot \vec{v} &= 0 \\ \rho \left( \frac{\partial \vec{v}}{\partial t} + (\vec{v} \cdot \nabla) \vec{v} \right) &= -\nabla p + \eta \nabla^2 \vec{v} + \vec{f}_{\text{ext}} \end{aligned} \quad (2.1)$$

We consider a regime in which dissipation dominates inertia (low Reynolds number  $Re = \frac{nvL}{\eta}$ ). Thus, the inertia term on the left side of equation (2.1) can be neglected and we obtain the Stokes equation. In our mesoscale computer simulations, we use the package *LAMMPS* [138] modified by our group. The fluid particles represent microscale fluid volumes; this resolution is appropriate on the scale of a RBC.

#### 2.1.1 Smoothed Particle Hydrodynamics

Smoothed Particle Hydrodynamics (SPH) is a numerical method discretising partial differential equations into particles  $i$  of a certain mass  $m_i$  (and other physical quantities like density  $\rho_i$  and pressure  $p_i$ ), moving along with the flow [90, 57]. SPH was first applied in astrophysics, but now in various fields.

Essential in this method is the fact that the particles themselves are employed as mobile integration nodes, at whose places the quantities are calculated (in contrast to methods based on fixed lattices). This simplifies the simulation of complex geometries, free boundaries or vacuum regions, yet reduces spatial resolution.

The hydrodynamic equations are approximated by first averaging of a spatial field quantity  $f(\vec{r})$  with a kernel-convolution and then discretising the equations. The set of field variables {density  $\rho$ , velocity  $\vec{v}$ , energy  $e$ , pressure  $P$ , heat flux  $Q$ } is interpolated by means of kernel interpolation.

$$f(\vec{r}) \approx \int_V f(\vec{r}') W(|\vec{r} - \vec{r}'|; h) dV' \quad (2.2)$$

with  $r = |\vec{r} - \vec{r}'|$  being the distance. The normalised kernel  $W$  approximates the  $\delta$ -distribution. It has to be at least once continuously differentiable and has to vanish for distances larger  $r$  than the so-called smoothing length  $h$ . Thereby, interactions occur only between adjacent particles, allowing the use of cell lists.

A kernel for three dimensional systems is given by

$$W(r) = \frac{8}{\pi h^3} \begin{cases} 6 \left(\frac{r}{h}\right)^3 - 6 \left(\frac{r}{h}\right)^2 + 1 & \text{for } 0 \leq \frac{r}{h} < \frac{1}{2} \\ 2 \left(1 - \frac{r}{h}\right)^3 & \text{for } \frac{1}{2} \leq \frac{r}{h} \leq 1 \\ 0 & \text{for } \frac{r}{h} > 1 \end{cases} \quad (2.3)$$

Equation (2.2) is further approximated by a sum. The function is evaluated at the current position  $\vec{r}_i$  of particle  $i$ :

$$f(\vec{r}_i) = \sum_{j=1}^N \frac{m_j}{\rho(\vec{r}_j)} f(\vec{r}_j) W(|\vec{r}_i - \vec{r}_j|; h) \quad . \quad (2.4)$$

Thus, spatial derivatives are easily obtained:

$$\vec{\nabla} f(\vec{r}) \approx \int_V f(\vec{r}') \vec{\nabla}' W(|\vec{r} - \vec{r}'|; h) dV' \quad . \quad (2.5)$$

It is therefore possible to describe the basic hydrodynamic equations in a system of discretised particle quantities  $f$ , where only  $f$  and its temporal derivatives are unknown.

A drawback of this method is its lack of uniqueness. One should choose those versions that provide symmetries (like conservation of momentum) on the scale of particles.

The Euler equation can be discretised as follows:

$$\frac{d\vec{v}_i}{dt} = - \sum_{j=1}^N m_j \frac{p_j + p_i}{\rho_i \rho_j} \vec{\nabla} W_{ij}(h) \quad (2.6)$$

The expression for the density of particle  $i$ ,  $\rho_i$ , is simply obtained from the particle distribution:

$$\rho_i = \sum_{j=1}^N m_j W_{ij}(h) \quad . \quad (2.7)$$

The particles move with the velocity of the fluid

$$\frac{d\vec{r}_i}{dt} = \vec{v}_i \quad (2.8)$$

and their state is described by

$$p_i = \rho_0 \rho_i^\gamma, \quad (2.9)$$

which, along with equations (2.6) and (2.7), describe the system completely.

Special attention has to be paid to the *initial distribution* of particles, as it defines the physical problem to a large extent. This distribution has to approximate the given initial density and fluid field. The differences in the density can be achieved by the particles' positions or their masses (or combination of these). A modified version of the Leap-Frog-Integrator is used, with a characteristic time step of  $\Delta t = \frac{\eta h}{\max_{i=1 \dots N}(\bar{v}_i)}$ . The analysis of the resulting particle distribution comprises the evaluation of the physical quantities at the particles' positions. On account of the discretisation, numerical artefacts such as pressure (shock) waves can occur. To reduce such effects, the acceleration in equation (2.6) is modified by a pressure-like term, the so-called *artificial viscosity*:

$$\left. \frac{d\vec{v}_i}{dt} \right|_{\text{art. visc}} = - \sum_{j=1}^N m_j \Pi_{ij} \nabla_i W_{ij}(h) \quad . \quad (2.10)$$

Advantages of SPH is e.g. the fact that no lattice is needed and thus, also more complex geometries are feasible. On top of that, both viscosity and equation of state are set as input parameters. Drawbacks are e.g. the low spatial resolution. Further details are outlined in reference [90].

### 2.1.2 Dissipative Particle Dynamics

DPD is a simulation method capable of describing systems on mesoscopic length scales, bridging the atomistic and the macroscopic scales [66]. Thereby, it allows to study the structure formation and supramolecular aggregation of macromolecules. This mesoscopic length-scale is relevant for many soft and condensed matter systems.

The DPD-interactions are governed by three different forces between particles:

$$\vec{F}_{\text{tot}} = (F_C + F_D + F_R) \hat{r}_{ij} \quad (2.11)$$

describing conservative, dissipative and random (thermal) contributions, which all act along the connective line of two particles.

A weighting function, depending on particle distance, is used for every force:

$$w(r) = \left(1 - \frac{r}{r_c}\right)^\kappa \quad (2.12)$$

where  $r_c$  is the cutoff radius beyond which  $w$  vanishes:  $w(r > r_c) = 0$ .  $\kappa$  determines the steepness of  $w$  and thereby, the influence of distant neighbours. We employ  $\kappa = 0.15$ .

In the following, two interacting particles  $i$  and  $j$  are considered. A conservative force models the mutual repulsion of soft spheres, a dissipative force models friction (viscosity) and a random force models the coupling to a thermal bath:

$$\begin{aligned} \vec{F}_{ij}^C &= a_{ij} w^R(r_{ij}) \hat{r}_{ij} \\ \vec{F}_{ij}^D &= -\gamma_{ij} w^D(r_{ij}) (\hat{r}_{ij} \cdot \vec{v}_{ij}) \hat{r}_{ij} \\ \vec{F}_{ij}^R &= \sigma_{ij} w^R(r_{ij}) \zeta_{ij} (\Delta t)^{-\frac{1}{2}} \hat{r}_{ij} \end{aligned} \quad (2.13)$$

$\zeta_{ij}$  is a Gaussian random number with zero mean and unit variance and  $\Delta t$  is the timestep. In order to obtain a Gibbs-Boltzmann equilibrium distribution, the weight functions have to be related to each other and the friction and random parameters have to obey the fluctuation-dissipation theorem [34]:

$$w^D(r) = [w^R(r)]^2 \quad \text{and} \quad \sigma^2 = 2\gamma k_B T. \quad (2.14)$$

DPD is an NVT method that respects the third Newtonian law of actio & reactio, thus yielding momentum conservation and thereby preserving hydrodynamics.

With the *soft* conservative interaction, the particles represent molecules or liquid elements rather than atoms, permitting a larger timestep in comparison to Molecular Dynamics (MD). The liquid elements are considered portions of the fluid, representing moving thermodynamic subsystems [33]. On top of that, the soft interaction does not diverge at  $r = 0$ , as it is the case of a Lennard-Jones-interaction in MD.

To conclude, the advantages of DPD are:

- thermodynamic consistency
- appropriate representation of thermal fluctuations
- modelling of a viscous fluid

An essential drawback is that both viscosity and equation of state have to be obtained from a (preparatory) simulation.

### 2.1.3 Smoothed Dissipative Particle Dynamics

SDPD is a simulation method which combines the advantages of both SPH and DPD, and avoids their drawbacks [33]. SPH offers a discrete version of the Navier-Stokes-equations and a sound physical interpretation, but suffers from thermodynamic inconsistencies; it does not explicitly consider the 2<sup>nd</sup> law. In contrast, DPD is thermodynamically consistent and can describe thermal fluctuations and dissipation, but the physical interpretation is rather vague. With DPD's conservative forces, one cannot generate an arbitrary equation of state, the transport coefficients are not immediately related to the model parameters and the physical scale is undefined [33]. SDPD is suitable for a length scale at which the fluid flow recognises the underlying molecular nature of the fluid, describing fluctuations of the hydrodynamic variables [100]. In SDPD, the fluid is divided into subsystems, characterised by position  $\vec{r}_i$ , velocity  $\vec{v}_i$ , mass  $m_i$ , entropy  $S_i$ , volume  $\mathcal{V}_i$  and energy  $E_i$ .

The equations of state are:

$$\begin{aligned} T_i &= \frac{\partial E^{\text{eq}}}{\partial S_i} \\ P_i &= -\frac{\partial E^{\text{eq}}}{\partial \mathcal{V}_i} \end{aligned} \quad (2.15)$$

Similar to SPH, an interpolant function as in equation (2.3) is employed. A set of equations describes the independent variables  $\vec{r}_i$ ,  $\vec{v}_i$ , and  $S_i$  [33] with both reversible and irreversible dynamics:

$$\begin{aligned}
m\dot{\vec{v}}_i &= \sum_j \left[ \frac{P_i}{d_i^2} + \frac{P_j}{d_j^2} \right] F_{ij} \vec{r}_{ij} - \left( \frac{5\eta}{3} - \zeta \right) \sum_j \frac{F_{ij}}{d_i d_j} \vec{v}_{ij} - 5 \left( \zeta + \frac{\eta}{3} \right) \sum_j \frac{F_{ij}}{d_i d_j} \hat{e}_{ij} \hat{e}_{ij} \cdot \vec{v}_{ij} \\
T_i \dot{S}_i &= (\phi)_i - 2\kappa \sum_j \frac{F_{ij}}{d_i d_j} T_{ij} \\
(\phi)_i &= \left( \frac{5\eta}{6} - \frac{\zeta}{2} \right) \sum_j \frac{F_{ij}}{d_i d_j} \vec{v}_{ij}^2 + \frac{5}{2} \left( \zeta + \frac{\eta}{3} \right) \sum_j \frac{F_{ij}}{d_i d_j} (\hat{e}_{ij} \cdot \vec{v}_{ij})^2
\end{aligned} \tag{2.16}$$

$\phi$  is the viscous heating. Friction forces increase internal energy to conserve total energy. The particles interact with each other within the range  $h$  of the interpolant function. Repulsion depends on pressure and density. Friction depends on the relative velocities. The  $\vec{v}_{ij}$  - term breaks the conservation of total angular momentum.

The entropy equation describes heat conduction, minimising temperature differences between particles by corresponding energy exchange and conserving total energy on account of its symmetries.

### 2.1.4 Integration of Equations of Motion

To update the position  $\vec{r}$ , velocity  $\vec{v}$  and angular velocity  $\vec{\omega}$  of particle  $i$  from time  $t$  to  $t + dt$ , Newton's second law is followed:

$$\dot{\vec{r}}_i = \vec{v}_i, \quad \dot{\vec{v}}_i = \sum_{j=1}^N \frac{\vec{F}_{ij}}{m_j}, \quad \dot{\vec{\omega}}_i = \sum_{j=1}^N \frac{\vec{N}_{ij}}{I_j}. \tag{2.17}$$

$\vec{F}_{ij}$  and  $\vec{N}_{ij}$  are the force and torque, respectively, for a particle  $j$  acting on particle  $i$ .  $m_i$  and  $I_i$  are the mass and the moment of inertia, respectively, of particle  $i$ .  $\vec{\omega}$  is required particularly for SDPD with angular momentum conservation [121].

In analogy to the procedure in reference [6], a velocity-Verlet algorithm approximates the temporal integration:

$$\begin{aligned}
\vec{r}_i(t + dt) &= \vec{r}_i(t) + dt \vec{v}_i(t) + \frac{1}{2} dt^2 \vec{f}_i(t) \\
\tilde{\vec{v}}_i(t + dt) &= \vec{v}_i(t) + \frac{1}{2} dt \vec{f}_i(t) \\
\vec{f}_i(t + dt) &= \vec{f}_i(\vec{r}_i(t + dt), \tilde{\vec{v}}_i(t + dt)) \\
\vec{v}_i(t + dt) &= \vec{v}_i(t) + \frac{1}{2} dt (\vec{f}_i(t) + \vec{f}_i(t + dt))
\end{aligned} \tag{2.18}$$

with  $\vec{f}$  being the force per unit mass.

## 2.2 Present RBC Models

Early modelling of blood flow can be found e.g. in reference [155]; later numerical studies comprise e.g. references [125, 44, 163, 26]. Reference [50] reviews numerical simulation

techniques describing blood on the cell-scale.

Until today, there are several different RBC models. They may differ conceptually, in their scope of validity and scope of application. Some models are described in the following sections.

### 2.2.1 Vesicle Model

A 2D vesicle is considered, representing an impermeable membrane made of a bilayer of phospholipids, as a simplistic representation of a RBC [83, 84]. Their bending rigidity is  $\kappa = 3 \cdot 10^{-19} J$  and the typical RBC diameter (the diameter of a sphere having the same area) is about  $6\mu m$ . The vesicle's reduced area is defined as its actual area over that of a circle having the same perimeter. For human RBCs, the reduced area is 0.6.

Area and volume constraints originate from the following: at room- and at physiological temperature, the membrane is fluidic (compare to figure 1.9) [83]. The membrane can be viewed as a 2D incompressible fluid. This incompressibility property implies the inextensibility of the membrane, and therefore, the conservation of local area. Furthermore, since the vesicle encloses an incompressible fluid and the membrane permeability is very small, the vesicle volume must be conserved. Due to membrane impermeability, the membrane velocity is equal to the fluid velocity of the adjacent layer. Thereby, and because of the incompressibility condition  $\nabla \cdot \vec{v} = 0$  for fluids, the enclosed volume is automatically conserved. The area of the membrane is not conserved automatically. In order to conserve membrane local area (or perimeter in 2D), a surface (local) Lagrange multiplier  $\zeta(s, t)$  is introduced. It depends on the curvilinear coordinate  $s$  along the vesicle contour and on time  $t$ .  $\zeta(s, t)$  is the surface analogue of the pressure field  $p(\vec{r}, t)$  which enforces local volume conservation of a 3D fluid.

Mechanically, the membrane can be viewed as a thin shell, where the soft (or easy) mode is the bending one. The corresponding energy is given by the Helfrich curvature energy [72]:

$$E = \frac{\kappa}{2} \int_{\text{vesicle}} H^2 ds + \int_{\text{vesicle}} \zeta(s, t) ds \quad (2.19)$$

where  $\kappa$  is the membrane rigidity and  $H$  is the local membrane curvature.  $ds$  is the elementary arc length along the vesicle contour. A spontaneous curvature  $H_0$  is not considered. The second integral constraints the area in 3D (perimeter in 2D).

Deriving the vesicle energy  $E$  with respect to the membrane displacement, one obtains the membrane forces. The vesicle membrane possesses bending forces, local area conservation and tension forces  $\zeta$  against membrane extension or compression.

$$\vec{f} = \left[ \kappa \left( \frac{\partial^2 H}{\partial s^2} + \frac{H^3}{2} \right) - \frac{H}{\zeta} \right] \vec{n} + \frac{\partial \zeta}{\partial s} \vec{t} \quad (2.20)$$

including normal ( $\vec{n}$ ) and tangent ( $\vec{t}$ ) terms. The perimeter conservation is alternatively achieved by describing the cohesive forces among boundary elements by quasi-rigid springs. The fluids inside and outside the vesicle ('inner and outer fluids') are same in reference [83]. No-slip boundary conditions at the membrane are used (see also section 2.6.2). Due to a small Reynolds number ( $Re \approx 10^{-2}$ ), the fluid flow is approximated by Stoke's equation



[83]:

$$\begin{aligned} -\vec{\nabla}p + \eta\nabla^2\vec{v} &= \vec{f} \\ \vec{\nabla} \cdot \vec{v} &= 0 \end{aligned} \quad (2.21)$$

with pressure  $p$ , velocity  $\vec{v}$  and  $\vec{f}$  is the force imposed by the deformable vesicle membrane on the two fluids.

Blood vessels are elastic and thus, react to stresses from the fluid. In the microvasculature (especially in the capillaries), the inertia is small and the Stokes regime is a good approximation. A boundary integral formulation is used. Both vesicle membrane and vessel wall forces modify the imposed Poiseuille flow so that the velocity of each point of the membrane is

$$\vec{v}(\vec{x}_0) = \frac{1}{\eta} \oint_{\text{vesicle}} \vec{G}(\vec{x} - \vec{x}_0) \cdot \vec{f}(\vec{x}) ds + \frac{1}{\eta} \int_{\text{walls}} \vec{G}(\vec{x} - \vec{x}_0) \cdot \vec{f}_w(\vec{x}) ds \quad (2.22)$$

with viscosity  $\eta$  and free space Green's function

$$G_{ij}(\vec{x} - \vec{x}_0) = -\delta_{ij} \ln |\vec{x} - \vec{x}_0| + \frac{(\vec{x} - \vec{x}_0)_i (\vec{x} - \vec{x}_0)_j}{(\vec{x} - \vec{x}_0)^2} \quad (2.23)$$

The membrane contour is discretised ([83, 20]). The contribution of the undisturbed Poiseuille flow can simply be added due to linearity of the Stokes equations.

The force of the flexible walls  $\vec{f}_w$  is assumed Hookean. The vessel wall elasticity is affected by the glycocalyx [184]. This is a soft, brush-like biopolymer covering the endothelium, on which cells "surf". The wall rigidity is estimated to be  $K \propto E/W$  [11] where  $E \approx 10Pa$  [184] is the effective Young modulus and  $W \approx 0.2\mu m$  [184] is the glycocalyx thickness. When compared to the membrane, the wall is stiff, so its response to fluid stresses is quasi-instantaneous. This is confirmed by numerical studies [84, 175]. After calculating the forces, equation (2.22) is used to determine the velocities, which, in turn, are used to calculate the positions via an Euler scheme.

### 2.2.2 Hyperelastic Model

A hyperelastic model accounts for the shear resistance of the cytoskeleton and the area dilation resistance of the lipid bilayer, while Helfrich's bending model accounts for the bending resistance of the lipid bilayer [60].

The transport of deformable particles within a carrying fluid is modelled. The particles, in turn, may carry an internal fluid differing from the external fluid. Both fluids are assumed incompressible and Newtonian. Thus, the flows are subject to continuity and Navier-Stokes equation:

$$\begin{aligned} \nabla \cdot \vec{v} &= 0 \\ \rho \left( \frac{\partial \vec{v}}{\partial t} + (\vec{v} \cdot \nabla) \vec{v} \right) &= -\nabla p + \nabla \cdot \left[ \eta \left( (\nabla \vec{v}) + (\nabla \vec{v})^T \right) \right] \end{aligned} \quad (2.24)$$

with fluid velocity  $\vec{v}$ , time  $t$ , pressure  $p$  and viscosity  $\eta$ . Density variations are neglected and thus,  $\rho = \text{const}$ . The flexible membrane is modelled as an infinitely thin, massless and completely closed structure  $S$ .

The hyperelastic model is defined by Keller and Skalak's strain energy function  $W_{SK}$  [156], with the in-plane principal values of strain  $\lambda_1$  and  $\lambda_2$ , membrane shear modulus  $E_s$  and area dilation modulus  $E_a$  (measured in  $\frac{N}{m}$ ).

$$W_{SK} = \frac{E_s}{4} \left[ (\lambda_1^2 + \lambda_2^2 - 2)^2 + 2(\lambda_1^2 + \lambda_2^2 - \lambda_1^2 \lambda_2^2 - 1) \right] + \frac{E_a}{4} (\lambda_1^2 \lambda_2^2 - 1)^2. \quad (2.25)$$

The non-linear nature of this model allows for strain hardening effects [156]. Helfrich's bending model [72] has the following bending energy function:

$$W_b = \frac{E_b}{2} \int_S (2\kappa - c_0)^2 dS \quad (2.26)$$

Fluid-structure coupling is achieved by the immersed boundary and front-tracking methods. Adherence of the fluid over the membrane (no-slip) makes fluid velocity continuous at the membrane location and equal to the membrane velocity. The membrane is transported by the fluid. The membrane coordinates  $\vec{X}(t)$  are related to the fluid velocity  $\vec{u}(t)$  as follows:

$$\frac{d\vec{X}(t)}{dt} = \vec{U}(\vec{X}(t), t) = \int_{\Omega} \vec{u}(\vec{x}, t) \delta(\vec{X}(t) - \vec{x}) d\vec{x} \quad (2.27)$$

The fluid domain  $\Omega$  comprises both inner and outer fluids. Particle deformation enables fluid inhomogeneity (different viscosities inside and outside) and exerts a reaction force  $\vec{f}$  on the fluid.

$$\vec{f}(\vec{x}, t) = \int_S \vec{F}(\vec{X}(t), t) \delta(\vec{X}(t) - \vec{x}) dS \quad (2.28)$$

For the right stress discontinuity across the membrane,  $\vec{f}$  is added on the right side of equation (2.24).

The fluid equations are discretised using unstructured grids. This introduces discrete Dirac functions  $w_m$  into the transport equations  $\vec{U}$  and  $\vec{f}$  of the membrane vertices. The hyperelastic membrane forces are calculated by a first-order finite element method [21]. Let us consider a membrane deformation with the displacements  $u$  and  $v$  in x- and y-direction, respectively. The membrane is modelled with a 2-dimensional hyperelastic law  $W$ . Reducing it to first order gives:

$$\delta W = \{\delta u\}^T \left[ \frac{\partial W}{\partial \lambda_1} \frac{\partial \lambda_1}{\partial u} + \frac{\partial W}{\partial \lambda_2} \frac{\partial \lambda_2}{\partial u} \right] + \{\delta v\}^T \left[ \frac{\partial W}{\partial \lambda_1} \frac{\partial \lambda_1}{\partial v} + \frac{\partial W}{\partial \lambda_2} \frac{\partial \lambda_2}{\partial v} \right] \quad (2.29)$$

With the principle of virtual work, one identifies the forces  $F_x$  and  $F_y$ :

$$\delta W = \frac{1}{V_e} \left( \{\delta u\}^T \{F_x\} + \{\delta v\}^T \{F_y\} \right) \quad (2.30)$$

### 2.2.3 Combined Immersed Boundary Lattice Boltzmann & Finite Element Method

In references [93, 92], a combined 3D model is used: lattice Boltzmann (LB) [157, 159] for the fluid solver, a constitutive model for the membrane dynamics, and a finite element method (FEM) for the strains in the capsule. An immersed boundary method (IBM) captures the

interaction of the fluid and the membrane.

The lattice-Boltzmann-equation (2.31) discretises the Boltzmann-equation. It introduces a number of  $q$  populations  $f_i$  ( $i = 0, \dots, q - 1$ ) streaming along a regular lattice with constant  $\Delta x$  in discrete time steps  $\Delta t$ . Those populations can be regarded as mesoscopic particle packets which propagate and collide.  $f_i$  evolve as

$$f_i(\vec{x} + \vec{c}_i \Delta t, t + \Delta t) - f_i(\vec{x}, t) = -\frac{1}{\tau} (f_i(\vec{x}, t) - f_i^{\text{eq}}(\vec{x}, t)) + F_i \Delta t \quad (2.31)$$

where  $\tau$  is the fluid relaxation parameter, linked to viscosity and the speed of sound as  $\nu = c_s^2 (\tau - \frac{1}{2}) \Delta t$  and  $c_s = \sqrt{\frac{1}{3} \frac{\Delta x}{\Delta t}}$ .

At each time step  $t$ , the populations propagate along the  $q$  discretised velocity vectors  $\vec{c}_i$  to the next neighbours. At those points, they collide according to the right-hand side of equation (2.31). Equilibrium populations are

$$f_i^{\text{eq}} = w_i \rho \left( 1 + 3\vec{c}_i \cdot \vec{u} + \frac{9}{2} (\vec{c}_i \cdot \vec{u})^2 - \frac{3}{2} \vec{u} \cdot \vec{u} \right) \quad (2.32)$$

with  $w_i$  being lattice weights. Appropriately chosen, the fluid is isotropic and the Navier-Stokes-equations are approximated. Equation (2.32) resembles a truncated Maxwell distribution, approximating small Mach numbers.  $F_i$  in equation (2.31) incorporates body force densities  $\vec{f}$  which represents fluid-membrane coupling or external forces:

$$F_i = \left( 1 - \frac{1}{2\tau} \right) w_i \left( \frac{\vec{c}_i - \vec{u}}{c_s^2} + \frac{\vec{c}_i \cdot \vec{u}}{c_s^4} \vec{c}_i \right) \cdot \vec{f} \quad (2.33)$$

The macroscopic fluid properties are obtained from the populations  $f_i$ . At each fluid lattice node, density and velocity are extracted from the zeroth and first moments, respectively:

$$\begin{aligned} \rho &= \sum_i f_i \\ \rho \vec{u} &= \sum_i f_i \vec{c}_i + \frac{\Delta t}{2} \vec{f}. \end{aligned} \quad (2.34)$$

Simple shear flow is implemented via a bounce-back method of moving walls [98], with the velocity  $v_w$ . For a valid LB method, the Mach number, and thus  $v_w$ , has to be small. For the flow to be Stokesian, the Reynolds number has to be small, further reducing  $v_w$ .

The constitutive model for the membrane is described by the total energy  $W = W_s + W_b + W_A + W_V$ , made up of contributions such as areal strain, bending, surface and volume conservation. A hyperelastic model (neither viscosity nor plasticity) describes the areal strain energy density  $W_s = \int w_s dA$  which depends only on the invariants  $I_1 = \lambda_1^2 + \lambda_2^2 - 2$  and  $I_2 = \lambda_1^2 \lambda_2^2 - 1$ , which are the local principal in-plane stretch ratios. This applies for a thin membrane with isotropic and homogeneous elastic properties.

Deformations of biological cells can have non-linear stress-strain relations and this has to be considered by the energy model [156]:

$$w_s = \frac{k_s}{12} (I_1^2 + 2I_1 - 2I_2) + \frac{k_\alpha}{12} I_2^2 \quad (2.35)$$

with elastic shear modulus  $k_s$  and area dilation modulus  $k_\alpha$ .

The capsule membrane is triangulated and the membrane forces are determined at the nodes.

The strains  $\lambda$  are obtained from the node displacements, described by the linear displacement field  $\vec{v}(x, y)$ . The displacement gradient tensor  $\mathbf{D}$  leads to the strain:

$$\begin{aligned}\lambda_1^2 + \lambda_2^2 &= \text{tr} \mathbf{D}^T \mathbf{D} \\ \lambda_1^2 \lambda_2^2 &= \det \mathbf{D}^T \mathbf{D}\end{aligned}\quad (2.36)$$

With the principle of virtual work, the forces by node  $i$  on the fluid are calculated:

$$F_i = -\frac{\partial W(\vec{x}_i)}{\partial x_i} \quad (2.37)$$

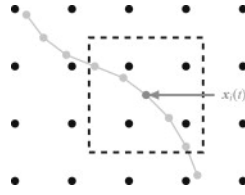


Figure 2.1: Immersed boundary method in 2D. The forces of the membrane mesh (light grey) affect the fixed fluid grid (black) via the interpolation stencil (dashed square). Taken from reference [93].

In IBM, an arbitrary membrane coordinate system (coordinates  $\vec{x}_i(t)$ ) is coupled to the fixed regular fluid lattice (coordinates  $\vec{X}$ ) [135, 136]. As the membrane is deformed, it exerts a force  $\vec{F}_i(t)$  on the fluid, which experiences a body force density:

$$\vec{f}(\vec{X}, t) = \sum_{\text{node } i} \vec{F}_i(t) \delta(\vec{X} - \vec{x}_i(t)) \quad (2.38)$$

with kernel  $\delta$  being a discretised Dirac delta distribution with finite support. Its choice defines momentum and angular momentum conservation.

The new velocities of membrane node  $i$  are calculated through the new lattice velocities and the old node positions:

$$\vec{u}_i(t + \Delta t) = \sum_{\vec{X}} \vec{u}(\vec{X}, t + \Delta t) \delta(\vec{X} - \vec{x}_i(t)) \quad (2.39)$$

At the membrane, a no-slip boundary condition is assumed. Thus, the membrane moves with the ambient fluid. The membrane nodes are advected via the Euler rule:

$$\vec{x}_i(t + \Delta t) = \vec{x}_i(t) + \vec{u}_i(t + \Delta t) \Delta t \quad (2.40)$$

## 2.2.4 Multiscale Model

The multiscale model considers the viscoelasticity of lipid bilayer and cytoskeleton, the flexible connectivity between them, and the interactions with inner and outer fluids [134]. Characteristic is the multiscale structural description of the membrane (see figure 2.2), predicting physical mechanisms of the dynamic response at molecular level.

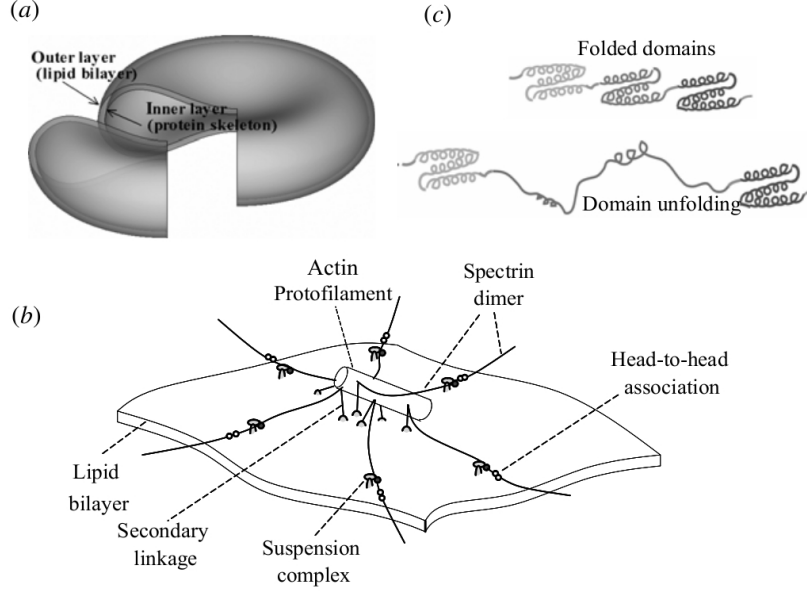


Figure 2.2: Multiscale model: (a) complete cell level (b) protein skeleton molecular detailed level (c) spectrin level. Taken from reference [134].

The **complete cell level** models the membrane as two continuous layers using FEM. The skeleton and bilayer interact via a normal contact force and via a lateral slide due to the mobility of the skeleton-bilayer pinning points. The normal direction follows a linear spring-softened potential, while the tangential direction follows viscous friction. The type of friction is determined by the diffusion of transmembrane proteins. Although the overall surface area is conserved, bilayer and skeleton can differ locally in their deformations. The constitutive properties of the bilayer are taken from measurements, while the constitutive properties of the skeleton are calculated by the intermediate level. The generalised Voigt-Kelvin stress-strain relation [36] describes viscoelasticity:

$$\Theta_1 h_i = \bar{T} + \frac{\mu_i}{2\lambda_1^2 \lambda_2^2} (\lambda_1^2 - \lambda_2^2) + 2\mu_i \frac{1}{\lambda_1} \frac{D\lambda_1}{Dt} \quad (2.41)$$

where  $\Theta_{1/2}$  are the principal stresses,  $\bar{T}$  is the isotropic tension,  $\lambda_{1/2}$  are the principal stretches and  $\mu_i$  is the surface shear stiffness.  $D/Dt$  is the material derivative and  $\nu_i$  is the surface viscosity.  $h_i$  is the layer thickness ( $i$  for bilayer or cytoskeleton).  $\Theta_2$  can be calculated exchanging the indices 1 and 2 in equation (2.41).

The **protein skeleton molecular detailed level** yields the constitutive law for the inner layer. It models the junctional complex and considers the dynamic response of the fully coupled skeleton-bilayer structure. The junction between spectrin and actin protofilament, and thermal effects are considered, based on the molecular architecture.  $\mu_s$  and  $\bar{T}$  depend on deformation and are fed into the complete cell model to represent the cytoskeleton:

$$\begin{aligned} \mu_s &= \frac{1}{A_0} \frac{\partial \Phi}{\partial \beta} \Big|_{\alpha} \\ \bar{T} &= \frac{1}{A_0} \frac{\partial \Phi}{\partial \alpha} \Big|_{\beta} - \frac{C}{A^2} \end{aligned} \quad (2.42)$$

with junction complex strain energy  $\Phi$ , initial and current junction areas  $A_0$  and  $A$ , steric coefficient  $C$ ,  $\alpha = \lambda_1\lambda_2 - 1$  and  $\beta = \frac{\lambda_1^2 + \lambda_2^2}{2\lambda_1\lambda_2} - 1$ . For the bilayer,  $\bar{T} = K_b(\lambda_1\lambda_2 - 1)$  with area stiffness  $K_b$ .

The **spectrin level** uses a stress-strain model based on the Arrhenius equation to model the mechanical properties of spectrin, including (un)folding reactions. Spectrin is a multidomain protein able to overstretch due to unfolding of domain or multiple repeats. Thus, its transient force-extension curve has a sawtooth shape, and each peak represents an unfolding event [146, 101]. This curve also depends on the *rate* of extension.

An information-passing algorithm couples the levels: predictions of more detailed levels are summarised as constitutive laws and input into the coarser levels. Conversely, 3D configurations and deformations, predicted by the complete cell level, are used by the skeleton level to determine mesoscale mechanics and mechanical loads at the protein links ('mechanically induced structural remodelling').

The fluid-structure interaction is modelled by a boundary element method (BEM) and a distribution of stokeslets on the membrane surface. To discretise the boundary integral equation, isoparametric bilinear quadrilateral boundary elements are used, avoiding the shear-locking problem [13, 179]. The principle of virtual work relates surface traction and nodal forces [179]. The boundary integral equation of interface dynamics [142] is the basis for the BEM:

$$\begin{aligned} \vec{v}^f(\vec{x}_0) = & \frac{2}{1 + \Lambda} \vec{v}_0^f(\vec{x}_0) \\ & - \frac{1}{4\pi\eta_1(\Lambda + 1)} \int \int_{\Gamma_{fb}} \mathbf{G}(\vec{x}, \vec{x}_0) \cdot \Delta \vec{t}^f(\vec{x}) d\Gamma(\vec{x}) \\ & + \frac{1 - \Lambda}{4\pi(\Lambda + 1)} \int_{p.v.} \int_{\Gamma_{fb}} \vec{v}^f(\vec{x}) \cdot \mathbf{T}(\vec{x}, \vec{x}_0) \cdot \vec{n}(\vec{x}) d\Gamma(\vec{x}) \end{aligned} \quad (2.43)$$

with the undisturbed velocity field  $\vec{v}_0^f(\vec{x}_0)$ , fluid-solid boundary  $\Gamma_{fb}$  and the ratio of internal and external fluid viscosity  $\Lambda$ .  $\Delta \vec{t}^f$  is the discontinuity in the interfacial surface traction.  $\int_{p.v.}$  means principal value integration.  $\mathbf{G}$  and  $\mathbf{T}$  are the Green's functions for velocity and stress, respectively.

## 2.3 Red Blood Cell Model of this Thesis

RBCs of humans and other mammals have neither a nucleus nor intracellular organelles [91]. Their cytoskeleton is only two-dimensional. The effective volume  $V_{\text{eff}}$  is the ratio of the volume of an arbitrary object to the volume of a sphere with the same surface area  $A_{\text{tot}}$ . For RBCs,  $V_{\text{eff}} \approx 0.63$ . Thus, RBCs are deformable, i.e., the cell shape can vary under constant  $A_{\text{tot}}$  and  $V$ , which is necessary for its physiological functioning. The cell volume is stabilised homeostatically by ion pumps [75, 91]. Physically-mechanically, a mammalian RBC is a thin viscoelastic shell filled with a viscous fluid and suspended into another viscous fluid.

The RBC is modelled as an impenetrable membrane enclosing an inner fluid. When required, we use bounce-back reflections to reflect fluid particles on the membrane, both from inside

and outside [40]. The membrane is modelled as a triangulated network of springs, featuring stretching, bending and compression resistance. The membrane is made up of  $N_v = 500 - 3000$  vertices, see figure 2.3. Governing potentials, numerical implementation and parameter values are identical to those in reference [46], except when noted in the text.

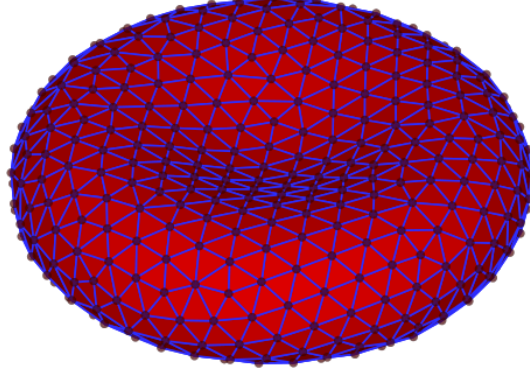


Figure 2.3: The RBC membrane is composed of  $N = 500 - 3000$  vertices, which are interconnected by springs, triangles and dihedrals. Taken from reference [130].

### 2.3.1 Membrane Triangulation

To build the RBC membrane,  $N_v$  vertices are distributed randomly on a spherical surface. The vertices are displaced by assigning electrostatic-like interactions to them [39]. The resulting mutual repulsion shall distribute them more evenly. The positions of the vertices are projected onto an axisymmetric shape that models the RBC [39, 37]:

$$z(r) = \pm D_0 \sqrt{1 - r} (c_0 + c_1 r + c_2 r^2) \quad (2.44)$$

with  $r = \frac{x^2 + y^2}{D_0^2}$ , cell diameter  $D_0$ ,  $c_0 = 0.1035805$ ,  $c_1 = 1.001279$ , and  $c_2 = -0.561381$ .

The spring and bending energies are further relaxed by flipping adjacent triangles appropriate for energy minimisation [41].

### 2.3.2 Membrane Potentials

The RBC membrane is composed of  $N_v$  vertices. Depending on the phenomena under consideration, the inner fluid might be separated from the outside (see section 2.6.1) [39]. Otherwise, the membrane is permeable and the inner fluid is equivalent to the outer fluid.

The vertices are grouped as bonds, triangles and dihedrals. A preferably homogeneous distribution of sizes and triangulation degree is pursued [39]. The membrane potentials govern the interactions among the DPD particles constituting the cell [39]. The following potential models the **area and volume conservation constraints**, analogously to a Hookean spring:

$$V_{angle} = \frac{k_a (A - A_0^{tot})^2}{2A_0^{tot}} + \sum_{k \in 1 \dots N_t} \frac{k_d (A_j - A_0^k)^2}{2A_0^k} + \frac{k_v (V - V_0^{tot})^2}{2V_0^{tot}} \quad (2.45)$$

with  $A$  being the membrane area,  $A_0^{tot}$  the global equilibrium area,  $A_k$  the area of the  $k$ th triangle,  $A_0^k$  the equilibrium area of the  $k$ th triangle,  $V$  the volume and  $V_0^{tot}$  the equilibrium volume. Furthermore,  $k_a$ ,  $k_d$  and  $k_v$  are the global area, local area and volume constraint constants, respectively. The related forces  $\vec{F} = -\nabla V$  for the area constraint are:

$$\begin{aligned}(f_{x1}, f_{y1}, f_{z1}) &= \alpha(\vec{\xi} \times \vec{a}_{32}) \\ (f_{x2}, f_{y2}, f_{z2}) &= \alpha(\vec{\xi} \times \vec{a}_{13}) \\ (f_{x3}, f_{y3}, f_{z3}) &= \alpha(\vec{\xi} \times \vec{a}_{21})\end{aligned}\tag{2.46}$$

with  $\vec{a}_{ij}$ ,  $(i, j) \in \{1, 2, 3\}$  the three edge vectors of one triangle, the normal  $\vec{\xi} = \vec{a}_{21} \times \vec{a}_{31}$  and  $A_k = |\vec{\xi}|/2$ . For the global area conservation,  $\alpha = \beta_\alpha/(4A_k)$  with  $\beta_\alpha = k_a(A - A_0^{tot})/A_0^{tot}$  for the  $k$ th triangle. For the local area constraint,  $\alpha = -k_d(A_k - A_0)/(4A_0A_k)$ . The volume constraint force is

$$\begin{aligned}(f_{x1}, f_{y1}, f_{z1}) &= \frac{\beta_v}{6}(\vec{\xi}/3 + \vec{t}_c \times \vec{a}_{32}) \\ (f_{x2}, f_{y2}, f_{z2}) &= \frac{\beta_v}{6}(\vec{\xi}/3 + \vec{t}_c \times \vec{a}_{13}) \\ (f_{x3}, f_{y3}, f_{z3}) &= \frac{\beta_v}{6}(\vec{\xi}/3 + \vec{t}_c \times \vec{a}_{21})\end{aligned}\tag{2.47}$$

with  $\vec{t}_c$  being the centre of mass of the  $k$ th triangle and  $\beta_v = \frac{k_v(V - V_0^{tot})}{V_0^{tot}}$ .

To model shear elasticity, a **bond potential** connects two vertices. An attractive worm-like-chain model, combined with a repulsive power function, models a spring-behaviour between vertices:

$$\begin{aligned}U_{\text{bond}} &= U_{\text{wlc}} + U_{\text{pow}} \\ U_{\text{wlc}} &= k_B T \frac{l_m}{4p} \frac{3x^2 - 2x^3}{1 - x} \\ U_{\text{pow}}(l_i) &= \begin{cases} \frac{k_p}{(m-1)l_i^{m-1}} & \text{for } m > 0, m \neq 1 \\ -k_p \log(l_i) & \text{for } m = 1 \end{cases}\end{aligned}\tag{2.48}$$

with  $x = l/l_m \in (0, 1)$ ,  $l$  the spring length,  $l_m$  the maximum spring extension,  $p$  the persistence length and  $k_B T$  the energy per unit mass,  $k_p$  the force coefficient and  $m$  an exponent. The forces are

$$\begin{aligned}\vec{f}_{\text{wlc}}(l) &= -\frac{k_B T}{p} \left( \frac{1}{4(1-x^2)} - \frac{1}{4} + x \right) \hat{I}_{ij} \\ \vec{f}_{\text{pow}}(l) &= \frac{k_p}{l^m} \hat{I}_{ij}\end{aligned}\tag{2.49}$$

with  $\hat{I}_{ij} = \vec{l}_{ij}/l$  being the vector of unit length between the spring ends  $i$  and  $j$ ,  $l = |\vec{l}_{ij}|$ ,  $x = l/l_m$ . In the simulation  $p$  and  $k_p$  are not known, but the macroscopic shear modulus is



given by

$$\mu_0 = \frac{\sqrt{3}}{4} \left( \frac{k_B T}{p l_m x_0} \left( \frac{x_0}{2(1-x_0)^3} - \frac{1}{4(1-x_0)^2} + \frac{1}{4} \right) + \frac{k_p(m+1)}{l_0^{m+1}} \right) \quad (2.50)$$

with  $l_0$  being the equilibrium spring length. If the spring length equals the equilibrium spring length, the superposition of the two forces (equations (2.49)) should be zero and we obtain for  $k_p$ :

$$k_p = \frac{l_0^m}{p} k_B T \left( \frac{1}{4(1-x_0)^2} - \frac{1}{4} + x_0 \right) \quad (2.51)$$

A **bending potential** between two adjacent triangles with a common edge determines the angle between the normals of these two triangles:

$$V_{\text{bend}} = \sum_{j \in 1..N_s} k_b [1 - \cos(\theta_j - \theta_j^0)] \quad (2.52)$$

with  $\theta_j$  being the instantaneous and  $\theta_j^0$  the spontaneous angle between the triangles. The force is given by

$$\begin{aligned} (f_{x1}, f_{y1}, f_{z1}) &= & b_{11}(\vec{\xi} \times \vec{a}_{32}) + b_{12}(\vec{\zeta} \times \vec{a}_{32}) \\ (f_{x2}, f_{y2}, f_{z2}) &= & b_{11}(\vec{\xi} \times \vec{a}_{13}) + b_{12}(\vec{\xi} \times \vec{a}_{34} + \vec{\zeta} \times \vec{a}_{13}) + b_{22}(\vec{\zeta} \times \vec{a}_{34}) \\ (f_{x3}, f_{y3}, f_{z3}) &= & b_{11}(\vec{\xi} \times \vec{a}_{21}) + b_{12}(\vec{\xi} \times \vec{a}_{42} + \vec{\zeta} \times \vec{a}_{21}) + b_{22}(\vec{\zeta} \times \vec{a}_{42}) \\ (f_{x4}, f_{y4}, f_{z4}) &= & b_{12}(\vec{\xi} \times \vec{a}_{23}) + b_{22}(\vec{\zeta} \times \vec{a}_{23}) \end{aligned} \quad (2.53)$$

with the triangle normals  $\vec{\xi}$  (see above) and  $\vec{\zeta} = \vec{a}_{34} \times \vec{a}_{24}$  and the corresponding areas  $A_1 = \xi/2$  and  $A_2 = \zeta/2$  and  $b_{11} = -\beta_b \cos \theta / \xi^2$ ,  $b_{12} = \beta_b / (\xi \zeta)$  and  $b_{22} = \beta_b \cos \theta / \zeta^2$  with  $\beta_b = k_b (\sin \theta \cos \theta_0 - \cos \theta \sin \theta_0) / \sqrt{1 - \cos^2 \theta}$ . Note that  $k_b = \frac{2}{\sqrt{3}} k_c$  with bending rigidity  $k_c$  (see also equation 1.8 and section 1.5.2, there, the bending rigidity is called  $K_B$ ).

In this work, mostly  $K_B = 70 k_B T$  is used.

## 2.4 Choices about the Rheological Properties of RBCs

### Stress-Free State

An important question concerns the stress-free shape of a RBC. This shape is defined as the state of zero shear stress [134, 87, 162]. Under physiological conditions, a stressed, biconcave shape with a constant surface area prevails. This so-called resting shape is characterised by minimal elastic energy, which comprises the shear energy of the cytoskeleton and bending energy of the bilayer [134].

An indicator for a spherical stress-free shape is a low critical shear rate for the resting shape, to transit from tumbling to tank-treading dynamics in shear flow [134, 171]. On the other hand, a RBC has a shape memory of the resting shape, corroborating that membrane elements are distinguishable and do not originate from a spherically symmetric state [47]. In those studies, a RBC membrane was marked with tracer particles. Applying a shear force, the membrane elements change their positions. After stopping the force and relaxing the

cell, the tracers return to their former position. Thus, each surface element has its particular place, i.e. memory effect. This has been discussed recently [26, 134].

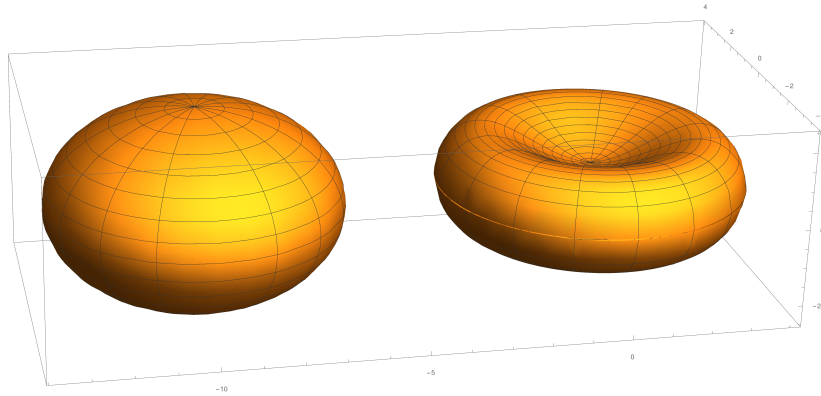


Figure 2.4: Two candidates for the RBC stress-free shape.

In this thesis, a spheroidal stress-free shape of  $\frac{V}{V_0} = 96\%$  is chosen [86, 105].  $V_0$  is the volume of a sphere of equal surface area. The spheroid can be identified as the nucleated erythroblast originating from the bone marrow. During maturation, the erythroblast (see graphics 2.5,1.1) expels its core to become the anucleate erythrocyte [118, 23]. We use volume deflation at constant surface area to obtain a biconcave resting shape of  $\frac{V}{V_0} = 64\%$ . This is in contrast to reference [46], where a biconcave stress-free shape was used. This has consequences on the cell's flow behaviour, see section 5.5.

A spheroid is described mathematically by

$$\left(\frac{x^2 + y^2}{a^2}\right)^2 + \left(\frac{z}{b}\right)^2 = 1 \quad (2.54)$$

with  $a, b$  being radii [185]. Its area is  $S = 2\pi a^2 + \pi \frac{b^2}{e} \ln\left(\frac{1+e}{1-e}\right)$  with the ellipticity  $e = \sqrt{1 - \left(\frac{b}{a}\right)^2}$ . Its volume is  $V = \frac{4}{3}\pi a^2 b$ .

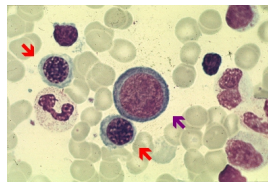


Figure 2.5: Erythroblasts still have a cell nucleus, which is expelled during maturation to become an erythrocyte. Taken from Imperial College London, Department of Medicine.

### Cytosol Viscosity

A further important factor for determining RBC dynamics is the viscosity ratio  $\lambda$  of cytosol (inner fluid) and blood plasma (outer, surrounding fluid) [191]. *In vivo*, for physiological conditions,  $\lambda \approx 5$ . Experiments were often performed with  $\lambda < 1$  [3, 49, 183]. Numerical studies often use equal viscosities ( $\lambda = 1$ ) for simplicity [158, 46]. Changes with  $\lambda$  in the phase diagram for cell shapes were verified, in agreement with experiments [163].

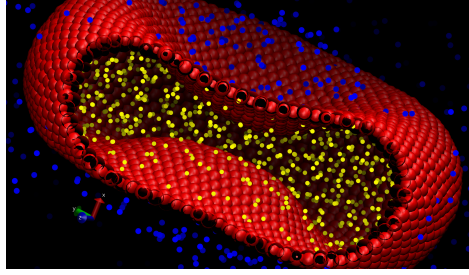


Figure 2.6: Simulation snapshot of a RBC with separate inner and outer fluid.

## 2.5 Simulation Units of Measurement

In order to relate the parameter values employed in the simulations (superscript  $M$ ) with their corresponding physical values (superscript  $P$ ) and to be able to compare simulations with experiments, the parameters have to obey certain dimensionless ratios. We construct dimensionless ratios which have to be equal in simulation and reality [132]. Considering e.g. the viscosity  $\eta$ , which has a unit of  $Pa \cdot s = \left[ \frac{\text{force}}{\text{area}} \cdot \text{time} \right]$ , the dimensionless ratio can be:

$$\frac{\eta^P \cdot D^P}{\tau^P \cdot Y^P} = \frac{\eta^M \cdot D^M}{\tau^M \cdot Y^M} \quad . \quad (2.55)$$

It is practical to select measures accessible in experiments. With the help of their dimensionless ratios, the remaining simulation parameters can be obtained. If, for example, the effective radius of a RBC has  $D^P = 3.3335 \mu m$  in reality and  $D^M = 3.3335$  chosen in silico, other lengths in the simulation can also be found using this relation. With  $\mu_0^M = 180$ ,  $\mu_0^P = 7.7 \cdot 10^{-7} \frac{N}{m}$ ,  $\eta^P = 10^{-3} Pa \cdot s$ ,  $\eta^M = 32.85$  and  $\tau^M = 1$ , a corresponding physical time scale of  $\tau^P = 0.0071 s$  can be found.

The unit of the shear modulus can also be formed in terms of energy and RBC radius [133]. The expression  $\mu D^2$  has units of energy. It corresponds to the energy cost of a given pre-defined stretch applied to a membrane patch of area  $R^2$ . On the other hand,  $k_B T$  gives the typical energy stored in fluctuations. This way,  $\frac{\mu D^2}{k_B T}$  is simply the ratio of these two energy scales, as  $\frac{L}{R}$  is a ratio of two length scales.

## 2.6 Boundary Conditions in Flow

These concepts have been developed in reference [39].

### 2.6.1 Impermeability of Membranes and Walls

In order to mimic boundary effects correctly, different microscopic behaviours are conceivable. To start with the classical behaviour, specular reflection refers to the law of reflection (the angle of incidence equals the angle of reflection). However, on the length scales considered here, this is not necessarily valid. The reason is that the real surface might exhibit a rough structure at the microscale.

In order to correctly model no-slip and the distribution of temperature and density close to a boundary, several procedures have to be implemented. Particle trajectories close to a boundary (solid or dynamic) are checked for boundary crossing. If yes, the exact time of contact  $t' = (p - x^{BC}) / (v^{BC} - v^p)$  and position of contact  $\vec{p}'$  are calculated.  $p$  and  $v^p$  are the position and velocity of the particle; BC refers to the boundary. The particle moves to the boundary until  $t'$ , then it is reflected and moves away from the boundary. New velocities and positions are assigned, conserving linear momentum for the system of particle and boundary. This is illustrated for the case of a triangulated boundary. The plane of one triangle is described as:

$$(\vec{n} \cdot \vec{s} + n_d) = 0 \quad (2.56)$$

where  $\vec{n}$  is the surface normal and  $n_d$  can be obtained by setting  $\vec{s}$  equal to one of the corner vertices. To see if the particle is on the positive or negative side of the surface normal, the following scalar product is defined:

$$b(t) = \vec{n}(t) \cdot (\vec{p}(t) - \vec{s}_1(t)) \quad (2.57)$$

If  $b(0)b(\Delta t) \leq 0$ , crossing has happened and reflection is needed. Instead of specular reflection, here, mostly the *bounce back* method is used. It essentially reverses the particle's motion:

$$\vec{v}_{new}^p = 2\vec{v}^{BC} - \vec{v}_{old}^p \quad (2.58)$$

$$\vec{p}_{new} = \vec{p}' + (\Delta t - t') \vec{v}_{new}^p \quad (2.59)$$

### 2.6.2 No-Slip Boundary Conditions and Adaptive Shear Force

The adaptive shear force corrects the velocities of particles close to non-periodic boundaries. The tangential components of these velocities shall match the shear rate (velocity gradient) determined by the boundary's velocity  $v_t^{BC}$ . Every particle interacts with its neighbours within a distance of  $r_c$  (sphere of interaction centred around a particle, see figure 2.8). Close to a solid boundary, this sphere contains wall particles. As they have equal velocities, the wall lacks a velocity gradient, see figure 2.7.

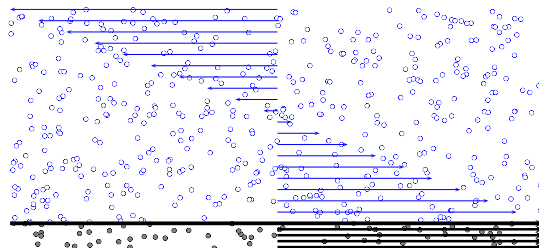


Figure 2.7: Velocities of solvent (blue) and wall particles (grey) shown as arrows.

In order to correct this, all particles close to the boundary, i.e.  $h < r_{shear}$ , experience a tangential force:

$$F_t^k(h) = C_k (\Delta v_t) w(h) \quad (2.60)$$

with  $k$  being the iteration number and the weight function

$$w(h) = \left(1 - \frac{r}{r_{shear}}\right)^{power} \quad (2.61)$$

and the iterative *adaptive force strength*

$$C_{k+1} = C_k + \alpha \Delta v_t \quad (2.62)$$

where  $\alpha$  is a relaxation parameter.  $\Delta v_t = v_t^{BC} - v_t^{est}$ . The estimated velocity is extrapolated from the near-boundary velocity profile, which is obtained through local cell averaging. After a number of iterations, the particles' velocities approach the boundary's velocity ( $\rightarrow \Delta v_t \approx 0$ ) so that  $F_t^k(h)$  and  $C_k$  converge to constant values.

Additional pressure forces minimise disturbances in density profile. Particles close to a boundary experience an imbalance of forces, as each of them interacts with a not-fully spherical region of fluid particles, see figure 2.8.

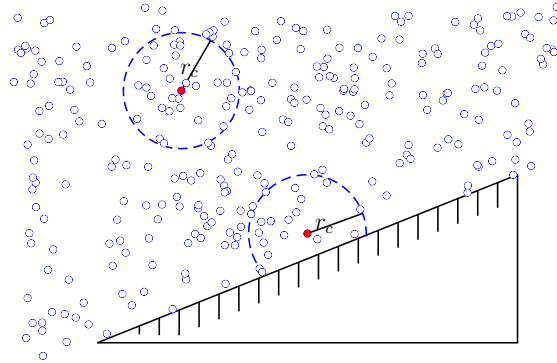


Figure 2.8: Interactions of a solvent particle in bulk and of a solvent particle close to wall.



## Chapter 3

# Light Scattering by a RBC

### 3.1 Introduction

Light scattering (LS) is used frequently in condensed and soft matter to investigate the structure and dynamics of the constituting particles [28], [18], particularly for polymer and colloidal suspensions [128]. Dynamic Light Scattering (DLS) can be employed for the monitoring of certain medical conditions without the need of contrast agents or radiation doses [124]. In this work, the theoretical framework corresponds to the Rayleigh Gans Debye - approximation (RDG), which is appropriate for small ratios of the refractive indices of scatterer and surrounding medium. This approximation assumes elastic scattering, such that the wavelength is not altered by the scattering process [28]. Multiple scattering and light absorption are neglected; the dielectric permittivity is set to unity.

The scattered electric field strength is proportional to a Fourier component<sup>1</sup> of the instantaneous microscopic density of scatterers [28]. The reason is that an assembly of particles acting like a set of scattering centres at the different positions  $\vec{r}_i$  induces a different phase shift  $\Delta\phi$  of the scattered light. The scattered field strength  $\vec{E}_s$  of an incident monochromatic plane wave is influenced by the particles' instantaneous positions  $\vec{r}_i(t)$  which determine the density  $\rho(t)$ . This structural information can only be obtained if the mutual distances between particles are on the order of the incident wavelength. Then, the scattered waves from different particles interfere destructively or constructively and allow conclusions on the structure, shape and motion of suspended components.

In light scattering experiments [124, 150, 96, 104, 12], a laser beam is directed to a sample and the scattered light is measured at a scattering angle. The part of the sample that is illuminated by the (laser) light is called scattering volume [114, 27]. The distance between detector and source has to satisfy the far-field-approximation, which describes the incident and scattered light as plane waves. The finite size of the detector is considered theoretically by integrating over the detector area [114, 81]. This finite area corresponds to a certain range of scattered wave vectors  $\vec{k}_s$ , thus momentum transfer vectors  $\vec{q}$ , resulting in an average over temporally fluctuating speckles. The correlation decreases with increasing coherence area occupied by the detector, due to the averaging out of less correlated fluctuations. Here, the time correlations of the scattering amplitudes are averaged over the orientations of the momentum transfer  $\hat{q}$ , which is equivalent to averaging over the orientations of the scatterer. Experimental LS suffers from several difficulties: impurities or air bubbles in the samples,

---

<sup>1</sup>This component is determined by the direction in which the scattered light is measured.

strong light absorption, particle sedimentation, multimodal distributions, high polydispersity and particle interactions. Such problems are absent in simulations, making numerical LS approaches appropriate for complementary comparisons and validations, despite a number of modelling assumptions.

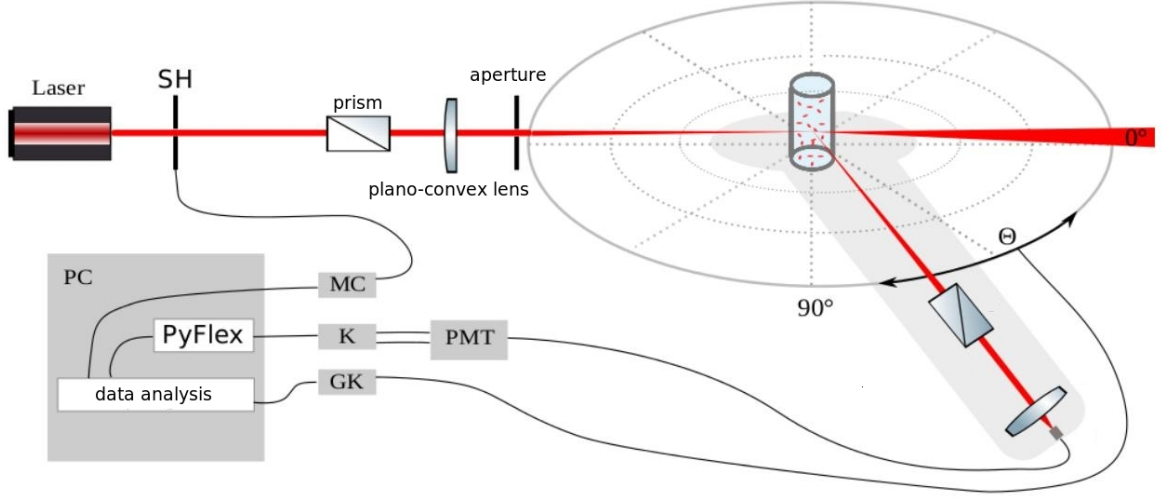


Figure 3.1: Experimental setup for light scattering. A laser beam traverses optical devices until it hits the (blood) sample. A detector receives the light that is scattered at an angle  $\Theta$  to the transmitted beam. Then, the signal is processed by a correlator and analysed in a PC. Taken from reference [150].

## 3.2 Characteristic Quantities

The total scattered electric field strength of the incident light (characterised by the strength  $\vec{E}_0$  and wave vector  $\vec{q}_0$ ) can be described by the contributions of all scattering centres, each with an individual scattering strength  $f(\vec{r})$ :

$$\vec{E}_s = \sum_{j=1}^N \int_{V_j} f(\vec{r}) e^{i(\vec{q}_0 - \vec{q}_s) \cdot \vec{r}} \vec{E}_0 d\vec{r} \quad (3.1)$$

with  $\vec{q}_s$  being the scattered wave length.  $f(\vec{r})$  is only non-zero within the  $N$  particles, thereby, the integration does not need to be performed over the whole macroscopic region of interest, but only over the corresponding regions  $V_j$ .

While in experiments absolute field strengths are considered, in simulations, the relative phase change due to the positions of scattering centres suffices. The interference of scattered waves can be described by the superposition of all scattering phases, which is called the scattering amplitude:

$$A_b(\vec{q}) = \int_V \underbrace{e^{i\vec{q} \cdot \vec{r}}}_{\stackrel{\text{def}}{=} \vec{\nabla} \cdot \vec{\psi}(\vec{r}, \vec{q})} d^3r \stackrel{\text{Gauss}}{=} \oint_A \vec{\psi}(\vec{r}, \vec{q}) \cdot \hat{n} d^2r \quad . \quad (3.2)$$



Here, the divergence (Gauss) theorem can be employed to relate the bulk scattering amplitude (corresponding to the volume) with the surface amplitude [132]. The surface integral is later useful in connection with the triangulated surface of a cell.  $\vec{\psi}(\vec{r}, \vec{q})$  is chosen such that its divergence is the exponential function in the volume integral.

The ergodicity of a system of cells is also employed in the field of scattering [28]; time averages are equivalent to ensemble averages. Light scattering quantities are measured as a function of the scattering angle  $\Theta_s$ , which, at some fixed wavelength  $\lambda$ , sets the magnitude of the wave vector  $q$ :

$$q = |\vec{q}_0 - \vec{q}_s| = \frac{4\pi}{\lambda} \sin\left(\frac{\Theta_s}{2}\right) . \quad (3.3)$$

Equation (3.3) includes the difference of incoming and scattered wave vector, and describes the momentum transfer of incident light wave to an object.

The interpretation of  $A_b(\vec{q})$  in experiments requires ensemble averaging over the orientations and positions of the suspended particles. In experiments or simulations, this ensemble average is obtained by time averaging. Thus, the amplitude should be collected over a time interval that is much larger than the time required for the suspended particles to attain all accessible configurations.

### 3.2.1 Form Factor

The form factor describes the interference of the scattered electric fields from different volume elements of the same particle [28]. First, the scattering amplitude  $\mathbf{B}_j$  of the  $j^{\text{th}}$  colloidal particle of volume  $V_j^0$  is introduced.

$$\mathbf{B}_j(\vec{q}) \equiv \int_{V_j^0} \frac{\epsilon(\vec{r}') - \epsilon_f}{\epsilon_f} e^{i\vec{q}\cdot\vec{r}'} d\vec{r}' \quad (3.4)$$

$\epsilon(\vec{r})$  is the isotropic dielectric constant at point  $\vec{r}$ , which is generally inhomogeneous.  $\epsilon_f$  is the dielectric constant of the suspending fluid, which is assumed homogeneous.

The form factor is defined as the squared absolute value of the scattering amplitude normalised by its value without momentum transfer:

$$P(q) \equiv \left| \frac{B(q)}{B(0)} \right|^2 \quad (3.5)$$

Considering the special case of spherical (radius  $a$ ) and optically homogeneous particles ( $\epsilon(r) = \epsilon_0$ ), the form factor can be simplified to

$$P(q) = \left| \frac{3}{a^3} \int_0^a r^2 \frac{\sin(qr)}{qr} dr \right|^2 = \left[ 3 \frac{qa \cos(qa) - \sin(qa)}{(qa)^3} \right]^2 \quad (3.6)$$

### 3.2.2 Structure Factor

The structure factor accounts for the interference of fields scattered from different (Brownian) particles. The structure factor is interesting because it is the Fourier transform of the pair-correlation function  $g(r)$ , which can predict many thermodynamic properties of a colloidal

system [28].

$$S\mathcal{F}(q) \equiv \frac{1}{N} \sum_{i,j=1}^N \mathbf{B}_i(\vec{q}) \mathbf{B}_j(\vec{q}) \langle e^{i\vec{q} \cdot (\vec{r}_i - \vec{r}_j)} \rangle = 1 + 4\pi\bar{\rho} \int_0^\infty r^2 (g(r) - 1) \frac{\sin(qr)}{qr} dr \quad (3.7)$$

### 3.2.3 Dynamic Scattering Function

In dynamic light scattering (DLS), the dynamic scattering function is employed [137, 132, 169]. It is a time-averaged correlation function with time lag  $t$  and reference time  $t_0$ . For a single scatterer, it is given by:

$$\begin{aligned} S(\vec{q}, t) &= \langle A(\vec{q}, t_0) A^*(\vec{q}, t_0 + t) \rangle_{t_0} \\ &= \langle e^{i\vec{q} \cdot (\vec{r}_{CM}(t_0) - \vec{r}_{CM}(t_0+t))} \int e^{i\vec{q} \cdot \vec{r}'(t_0)} dV' \int e^{-i\vec{q} \cdot \vec{r}'(t_0+t)} dV' \rangle_{t_0} \end{aligned} \quad (3.8)$$

The global position  $\vec{r}$  of each scattering element is the sum of the centre of mass (CM) and a local vector:

$$\vec{r} = \vec{r}_{CM} + \vec{r}' \quad (3.9)$$

The  $\vec{r}_{CM}(t_0) - \vec{r}_{CM}(t_0 + t)$  in the prefactor is the distance the CM has passed within  $t$ , which yields information about the dynamics of the scattered object(s). Global translations do not affect the scattering intensity or the form factor (3.5), but they influence the correlation function.

In order to sample over the scatterer orientation,  $S(\vec{q}, t)$  is averaged over the orientations of the momentum transfer  $\hat{q}$ . In the RDG theory,  $\vec{q}$  occurs only at the scalar product  $\vec{q} \cdot \vec{r}$ , thereby, this method of sampling is possible.

$$\begin{aligned} S(q, t) &= \langle S(\vec{q}, t) \rangle_{\hat{q}} \\ &\propto \exp(-q^2 D_{\text{eff}}(q)t) \end{aligned} \quad (3.10)$$

Thus, the simulation has to be long enough for the correlations to decay.

The decay is approximated as a monoexponential function, characterised by the effective diffusion constant  $D_{\text{eff}}(q)$ . To obtain  $D_{\text{eff}}(q)$ , the initial slope of  $-\ln\left(\frac{S(q,t)}{S(q,0)}\right)$  vs.  $t$  is fitted and divided by  $q^2$ .

Equation (3.10) is exact for a rigid sphere, with  $D_{\text{eff}}(q) = D_T$ . Rotational diffusion is not relevant in this case.

In general,  $D_{\text{eff}}(q)$  has a limiting behaviour as:

$$\begin{aligned} \lim_{q \rightarrow 0} D_{\text{eff}}(q) &= D_T \\ \lim_{q \rightarrow \infty} D_{\text{eff}}(q) &= D_{\text{rot}} \end{aligned} \quad (3.11)$$

where  $q$  (equation (3.3)) is a quantity of reciprocal space. Small  $q$  correspond to large length scales and vice versa. Thus, the limit of small  $q$  describes translational motion while the limit of large  $q$  describes rotational motion.

Equation (3.10) can be motivated as follows: let us consider a suspension of diffusing, scattering particles. Instead of the amplitude  $A(\vec{q}, t)$ , we can consider the concentration  $c(\vec{r}, t)$ . This is justified, since an amplitude can arise only at the locations of scattering particles (see also equation (3.7) with the pair correlation function).

Fick's law of diffusion is given by:

$$\frac{\partial c(\vec{r}, t)}{\partial t} = D \nabla^2 c(\vec{r}, t) \quad (3.12)$$

In this partial differential equation, diffusion coefficient  $D$  is assumed to be independent of position and concentration. Solving equation (3.12) by Fourier transform yields:

$$\tilde{c}(\vec{q}, t) = \tilde{c}_0 \exp(-Dq^2 t) \quad (3.13)$$

### 3.3 Light Scattering by Simple Objects

In order to validate numerical calculation of scattering quantities, the model is applied to simple shapes with analytically obtained scattering amplitude.

#### 3.3.1 Light Scattering by Spheres

The form factor of a sphere has been described in equation (3.6) and the effective diffusion coefficient of a sphere in references [96, 17, 151].

Here, a spherical shell is modelled as an ensemble of vertices connected by springs and arranged as triangles. The form factor of this triangulated model sphere is obtained from the surface integral in equation (3.2). It is calculated as the sum of the scattering contributions of all triangles. It reproduces accurately the theoretical prediction, which can be seen in figure 3.2. Deviations occur only at the zeroes of equation (3.6) where destructive interferences extinguish the scattered signal. These zeroes show up as singularities in the logarithmic plot.

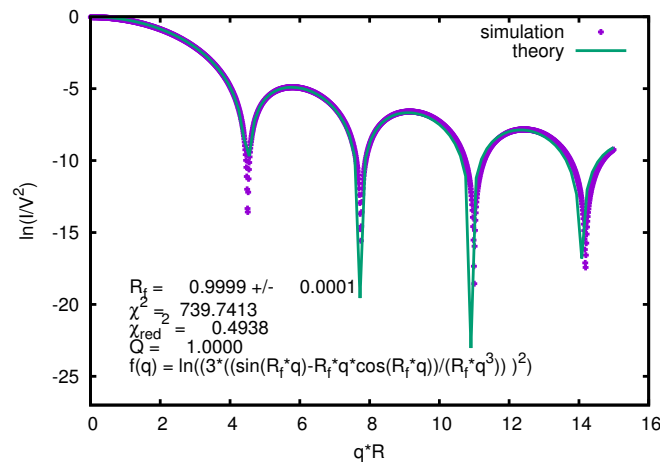


Figure 3.2: Form factor of a sphere; comparison of a numerical calculation and the analytical result from equation (3.6). The momentum transfer  $\vec{q}$  is in x-direction. Due to symmetry, all directions of  $\vec{q}$  yield equivalent form factors.

To calculate the correlation functions and the effective diffusion coefficient, the simulated sphere was subjected to Langevin dynamics. The advantage of a Langevin simulation, compared to DPD, lies with a lower computational cost as no explicit solvent needs to be simulated. In addition, rotational dynamics or (an)isotropic friction are not important in the case of a spherically symmetric object. The parameters are listed in table 3.1. The simulation

Symbol	Meaning	in units of	value
$R$	sphere radius	$l = 1\mu m$	1
$\sigma$	diameter of the vertices	$l$	0.25
$m$	vertex mass	$m$	1
$T$	temperature of the system	$\frac{\epsilon}{k_B}$	1
damp	damping time of Langevin model	$\sqrt{\frac{ml^2}{\epsilon}}$	0.5
$\epsilon$	Lennard-Jones interaction	$\epsilon$	1
$n_{sim}$	number of simulation steps	1	$3 \cdot 10^6$
$\Delta t$	width of DPD time step	$\sqrt{\frac{ml^2}{\epsilon}}$	$10^{-4}$

Table 3.1: System parameters used for DLS on a sphere.

results, depicted in figure 3.3 fit well to the theoretical expectation that  $D_{\text{eff}} = D_T$  [96], [17], [151]. The deviations appear only at the  $q$ -values for which the logarithmised form factor shows those singularities mentioned above. It should be noted here that the scaling of figures 3.2 and 3.3 is different; the  $q$ -axis of the form factor is normalised by the sphere's radius  $R = 1\mu m$  and the  $q$ -axis of the effective diffusion coefficient  $D_{\text{eff}}(q)$  is normalised by  $l_{\text{min}}$  (in analogy to reference [132]). The latter is the smallest length scale ( $\cong$  resolution) of the DLS-calculation and given by the average of triangle edge length  $l_{\text{min}} = \sqrt{\frac{4A}{\sqrt{3}n_{\text{tri}}}} \approx 0.15\mu m$ , where  $A$  is the object's total surface area and  $n_{\text{tri}}$  the number of triangles composing the surface.

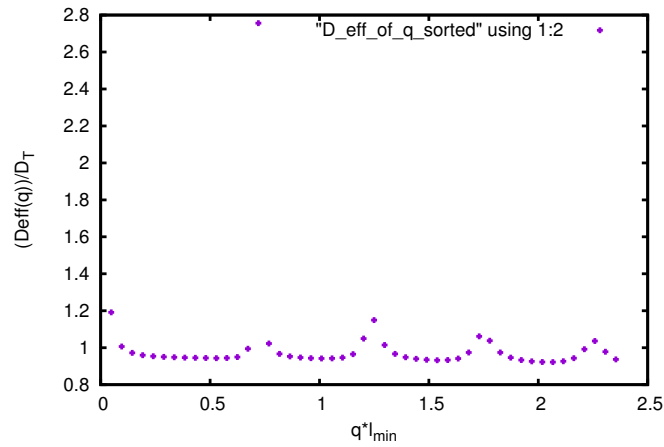


Figure 3.3: Effective diffusion coefficient of a sphere.

### 3.3.2 Light Scattering by Cylinders

Due to the cylinder's geometry, its amplitude differs for  $\vec{q}$  parallel or perpendicular to the cylinder axis.

Here, these two directions are considered as they have analytically calculable amplitudes. The modelling and calculation is analogous to that of the sphere in section 3.3.1. For a cylinder with radius  $R = 5\mu\text{m}$  and length  $L = 20\mu\text{m}$ , the corresponding amplitudes are:

$$\begin{aligned} A(\vec{q}_{\parallel}) &= \frac{2\pi R^2}{q} \sin(qL/2) \\ A(\vec{q}_{\perp}) &= \frac{2\pi LR}{q} J_1(qR) \end{aligned} \quad (3.14)$$

where  $J_1$  is the Bessel function of the first kind of order 1. Normalising the amplitude by the scatterer's volume (here,  $V = \pi R^2 L$ ), taking the absolute square and taking its logarithm, one obtains the form factor. It is compared to theory in figures 3.4 and 3.5. The fit function, gained from equation (3.14), accurately reproduces the size parameters.

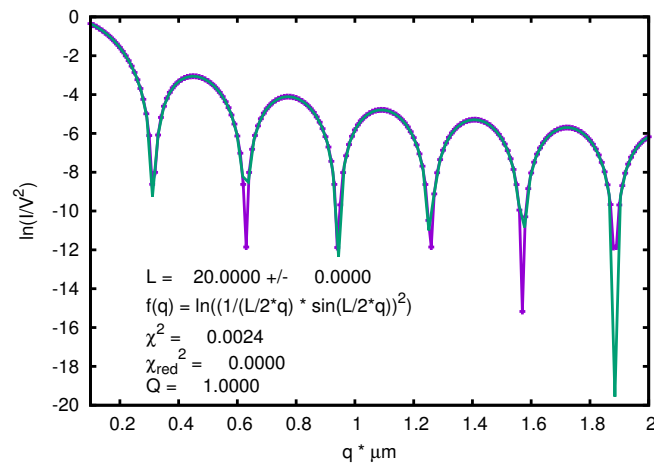


Figure 3.4: Form factor of a cylinder; comparison of a numerical calculation and the analytical result from equation (3.14).  $\vec{q}$  is in axial direction.

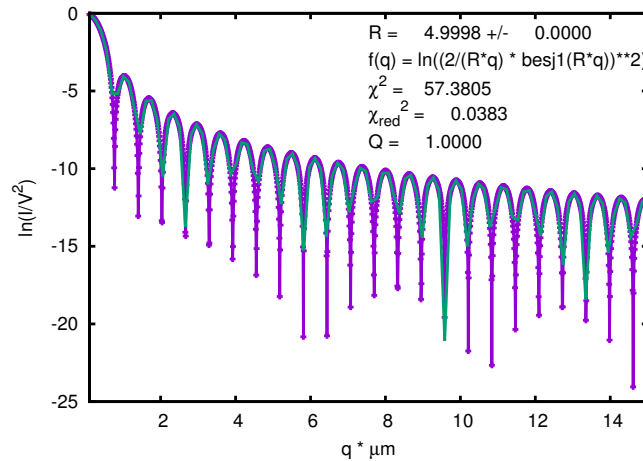


Figure 3.5: Form factor of a cylinder; comparison of a numerical calculation and the analytical result from equation (3.14).  $\vec{q}$  is in lateral direction.

## 3.4 Light Scattering by Red Blood Cells

### 3.4.1 Introduction

Both static and dynamic scattering properties of red blood cells (RBCs) are investigated. Scattering techniques allow experimentalists to measure various blood flow properties [106]. However, it is not always clear how different signals (e.g., static and dynamic structure factor) can be interpreted. Thus, simulated trajectories of a single moving RBC are analysed *a posteriori* with a parallel C-code written for light scattering calculations. Scattering properties of a diffusing or flowing cell are examined to distinguish (superimposing) effects, such as translation, rotation or deformation in a physiologically realistic environment.

These results can be employed both for validation of the theoretical approach and the interpretation of experimental data [145], such as scattering in Couette or Poiseuille flow. The insights from these studies could deepen the understanding of specific types of blood flow and lead to a development of improved means of detection [7].

Measuring time-dependent velocity fields is important when studying the cardiovascular system. Doppler ultrasound velocimetry provides one velocity component along a profile. Velocities are determined from the Doppler shift in the sound scattered by moving RBCs [1]. Ultrasound frequencies between 20 and 55 MHz yield a resolution of the order of tens of microns [129, 77]. While Doppler ultrasound is viable to explore the velocity fields in *large* vessels, the resolution is limited by the sound frequency. Using monochromatic, coherent laser light instead improves the resolution drastically [1]. As the velocities of RBCs and light differ by orders of magnitude, the Doppler shift will be difficult to detect. Thereby, a second signal is mixed with the first. This heterodyned signal is order of magnitude lower in frequency. It yields the Doppler shift and thus, local blood velocity [1] (laser-Doppler velocimetry).

The haemoglobin suspended in cytosol causes RBCs - and thereby whole blood - to both scatter and absorb light in the UV, blue and green spectral range [116].

The diffraction pattern from illumination of a dilute suspension of RBCs has been investigated experimentally [123, 150]. This allows to draw conclusions about the inhomogeneity

in cell shape and deformability and about a cell's characteristic motion. As these properties may differ for normal and pathological situations, light scattering can be used to measure the state of health of erythrocytes. The properties of the intensity of scattered light, such as the speckle pattern on a screen, quantify the variance in cell shape-parameter. Optical force on diseased blood cells and the haemoglobin refractive index were studied [63]. Earlier studies span from theoretical approaches using ellipsoidal disks to experimental approaches using rat erythrocytes [52, 154].

The absorption spectrum of blood is used for blood analysis, e.g. in a pulseoxymeter to measure the oxygen saturation. In our simulations, the phenomenon of absorption is neglected. In light scattering it is essential to consider the dielectric constant of a sample, in terms of its homogeneity and isotropy. The ability of RBCs to scatter light originates from iron-containing haemoglobin, which is presumably homogeneously distributed within a cell. The dielectric constant parallel and perpendicular to the main axis are different in the case of birefringence. This can have two causes: form birefringence by multiple scattering or from intrinsic birefringence by a specific molecular structure. For simplicity, both causes are neglected in simulations.

RBCs are more comparable to thick disks than to spheres. Light scattering by a rod of length  $L$  and thickness  $D$  has been treated theoretically [28], see also section 3.3.2. The auto-correlation function is found to be multi-exponential, even for a dilute case. The number of non-negligible exponentials depends on the value of the momentum transfer. For larger values of the momentum transfer, rotational motion gains impact and more exponentials are required to represent the decay of the correlation function properly. For smaller scattering angles such that  $|\vec{q}| \cdot L < 1$  and  $|\vec{q}| \cdot D < 1.2$ , rotational motion does not significantly influence the decay and translational motion dominates. Unlike for spherical scatterers, changes in orientation also change the interference of scattering signals from different parts of the object, thereby changing the form factor.

In this chapter, the membrane is assumed to be permeable and the inner fluid has the same viscosity as the outer fluid.

### 3.4.2 Index of Refraction of Blood and Choice of Wavelength

The open-source software *ADDA* [192] can be employed to calculate scattering by considering the object as a discretisation of cubic dipoles interacting with the incident light according to classical electrodynamics. This approach makes it possible (and necessary) to regard quantities like incident and scattered beam *separately*, unlike only their difference in the RDG-approach. Furthermore, the index of refraction  $n$  can be set individually for different parts of the scatterer.

$n$  is generally a complex quantity; its imaginary part describes the absorption of light. The value of  $n$  for haemoglobin [196], single RBC [131] and whole blood solution [116] has been researched in the last decades with varying outcomes.

Here, the  $n$ -value obtained in reference [131] is employed as it fits best our dilute approach where a single cell is considered (several cells and multiple scattering is not feasible with *ADDA* due to the high computational cost). Their value of  $n$  is obtained by tomographic phase microscopy [24], where a wavelength of 633nm was used. Wavelength-dependency of haemoglobin was investigated [196] and it is assumed that this result is close to the value needed here for a wavelength of 802nm. This value of  $\lambda$  was chosen for comparison with the results from the experimental group at University Konstanz, led by Professor G.Maret.

$\lambda = 802nm$  is the isosbestic wave length at which light absorption is equal for oxygenated and deoxygenated blood [150, 116]. Thus, oxygen saturation should have no impact on light scattering in these experiments.

ADDA is built for static scattering functions. A framework parallel code was developed to process each snapshot of a RBC trajectory and input the static information (position, orientation) into ADDA. The static data was processed by ADDA while the correlation was computed using the developed framework code.

Due to computational expense and inconsistencies with the RDG results, the ADDA approach was not pursued further. Only the  $q^2$  dependence in equation (3.10) was obtained, yet the function  $D_{\text{eff}}(q)$  was so different from that of the RDG approach that conclusions were not eligible.

### 3.4.3 Static Light Scattering by a Single Red Blood Cell

The dynamics of RBCs in shear flow and their aggregation at low shear rates has been studied by laser diffractometry [68]. Figure 3.6 nicely combines shear and aggregation ordering in one plot of the scattered light (ordinate). The abscissa shows the time course before and after the shear motion has been stopped. When still in shear motion, RBCs are elongated and aligned. The light signal is thus small. After the flow has been stopped, the cells disorder and give rise to more light scattering. Due to the lack of shear forces, they can aggregate with time and thereby reorder. Thus, scattering decreases again. The conclusion is that disordering makes the RBC suspension turbid and increases its scattering. Light is scattered multiple times from cells in proximity with different orientations. This is more probable in a suspension of random distribution and orientations than in an ordered phase, such as separate stacks of rouleaux. Ordering, due to shearing or aggregation, decreases scattering.

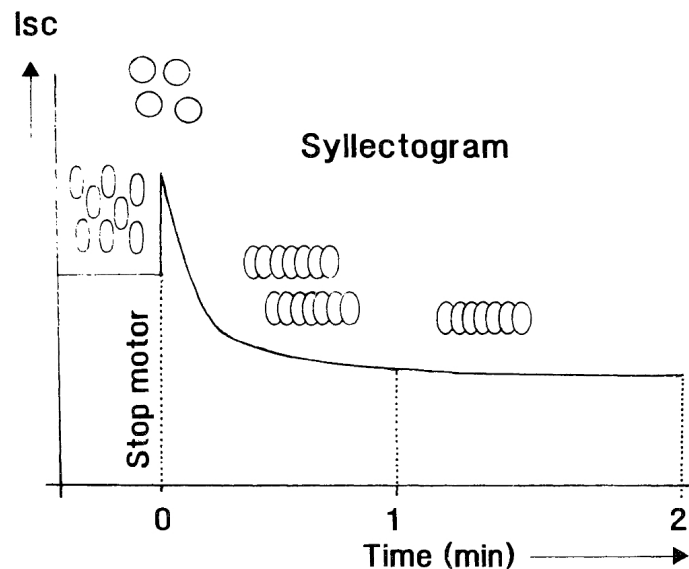


Figure 3.6: Light scattering depends on the ordering of RBCs. Cells are first sheared, then flow is stopped. Subsequently, cells start to aggregate. Taken from reference [68]. Reprinted with permission.



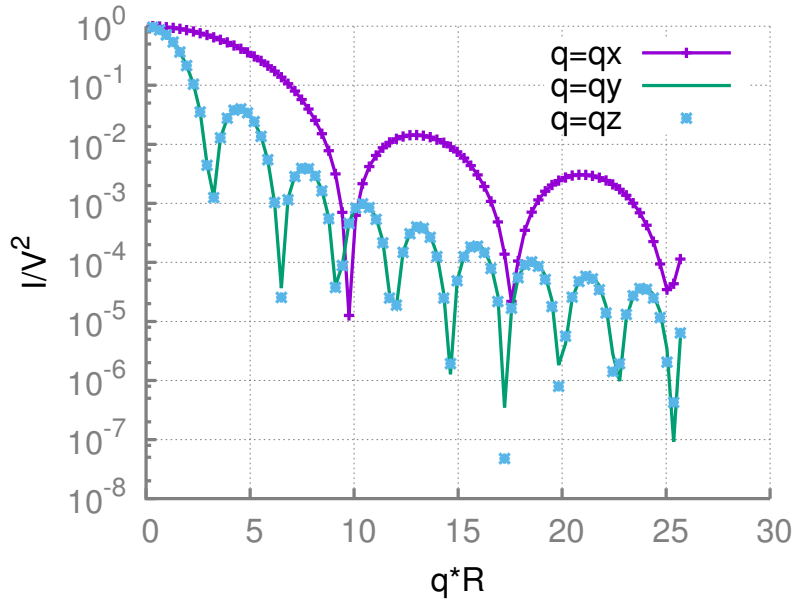


Figure 3.7: Form Factor of a RBC for different directions of momentum transfer  $\vec{q}$ .  $R$  is the effective radius, which is the radius of a sphere of the same surface area.

Here, a single RBC is considered. The calculation of quantities such as the form factor is analogous to section 3.3.1.

Figure 3.7 shows the form factor of a RBC oriented in  $\hat{x}$ . The orientation of a RBC is given by its axis of symmetry. The cell's symmetry is clearly reflected in the form factors for different directions of momentum transfer  $\vec{q}$ . It is either parallel ( $\vec{q} = q\hat{e}_x$ ) or perpendicular ( $\vec{q} = q\hat{e}_y/z$ ) to the cell's axis of symmetry. Due to the cell's cylindrical symmetry, the form factors for  $\vec{q} = q\hat{e}_y$  and for  $\vec{q} = q\hat{e}_z$  overlap.

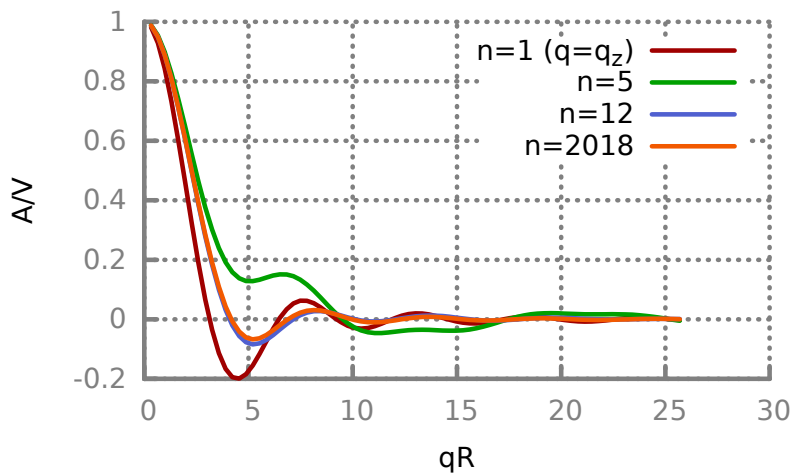


Figure 3.8: Scattering Amplitude of a RBC obtained by orientational averaging.  $n$  is the sample size.  $n = 12$  is sufficient to obtain a representative average.

Figure 3.8 shows the scattering amplitude vs. dimensionless parameter  $qR$  for a RBC. Different curves show the averages of the amplitude, sampling over different orientations of  $\vec{q}$ . Due to the RBC anisotropy, the direction of momentum transfer matters. For the static case, however, about 10 different orientations are sufficient for a converged average.

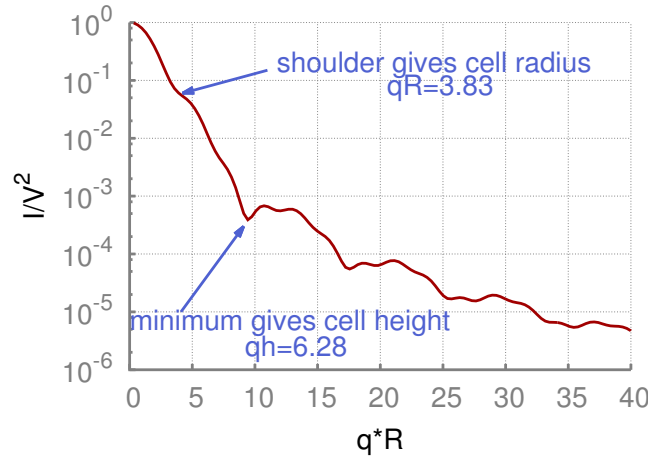


Figure 3.9: Intensity of a RBC obtained by temporal averaging (see section 3.2).

Figure 3.9 shows the scattering intensity of a RBC, temporally averaged. Thus, these data come from a simulated trajectory, involving translational, rotational and vibrational motion. The time average means that the cell is arbitrarily oriented towards  $\vec{q}$  (and vice versa). Comparing the RBC to a cylinder, with equation (3.14), the first zeros of these amplitudes are at  $q = \frac{2\pi}{L}$  and  $q \approx \frac{3.83}{R}$ . For the RBC values of  $R = 3.25\mu\text{m}$  and  $L = 2.6\mu\text{m}$ , one can identify approximately a minimum and a shoulder indicating the effect of shape parameters on the scattering.

### 3.4.4 Dynamic Light Scattering by a Single Diffusing Red Blood Cell

Equation (3.10), applied to RBCs diffusing in a viscous solvent, yields information about both cell structure and diffusive motion. Here, emphasis is put on the effect of membrane fluctuations on DLS signals. Thus, cells of different bending rigidities are examined. The values are given in relation to an energy unit:  $\frac{\kappa}{k_B T} = 10; 20; 40$ .

RBC flickering has been described as a random process of stochastic bending oscillations of the whole RBC surface having a broad wavelength distribution on the cell scale [91]. The flickering of an erythrocyte membrane is of both active (metabolic energy conversion) and passive (thermal fluctuations) nature [91, 172]. Potentially, DLS can shed light on RBC membrane motion and distinguish these contributions. In the present simulations, the fluctuations are purely thermal. Comparing these numerical data with experimental data, differences caused by a metabolic activity could be identified.

In a fourth parameter set we employ  $\frac{\kappa}{k_B T} = 20$  but a Young's modulus  $Y$  is reduced by a factor of 6.2 (correspondingly, the shear modulus is reduced by a factor of 7.4). This was done to compare the results to those of an MPC simulation by Matti Peltomaeki (unpublished work). Cell area and volume constraint parameters and simulation box size have also been adjusted to this former study (see table 3.2).

Symbol	Meaning	value
$A$	total cell area	132.899
$V$	cell volume	92.2088
$D_r$	effective radius	$\sqrt{\frac{A}{\pi}} = 2R = 6.5$
$k_B T$	temperature	1.0
$L$	system size	$\frac{80}{5.7} D_r$
$k_d$	local area constraint	$\frac{4.2 \cdot 10^6 k_B T}{D_r^4} A_t$
$k_a$	global area constraint	0.0
$k_V$	volume constraint	$\frac{3.4 \cdot 10^4 k_B T}{D_r^6} V$
$Y_M$	Young's modulus	$\frac{k_B T^M}{k_B T^P} \left(\frac{D^P}{D^M}\right)^2 Y_P$
$c_0$	spontaneous curvature	$C_0 R = 3$

Table 3.2: System parameters used in section 3.4.4. Basic length is  $1\mu m$ . Upper index  $M$  denotes *model*, while upper index  $P$  denotes *physical* units.  $Y$  differs in the fourth setup.

A non-zero spontaneous curvature is applied in order to compensate for the effect of a nearly spherical stress-free shape [134]. Without spontaneous curvature, such a cell is prone to develop a cup-shape. Still, only the fourth setup with reduced Young's modulus shows a persistent biconcave shape; all other setups eventually exhibit cup-shapes. This has to be considered when interpreting the scattering data. For each of the cells, a trajectory was calculated and analysed a posteriori by a DLS-code written in C.

An estimate for the decay time of the amplitude correlation function in equation (3.10) is  $\tau_{\text{decay}} = \frac{1}{Dq^2} = \frac{6\pi\eta R}{k_B T q^2}$ . To capture this dynamics for the analysis, the time interval for saving cell configurations is set finer than  $\tau_{\text{decay}}$ .

The total simulation length is also crucial, because the cell has to perform enough rotations to significantly decorrelate the scattering amplitude from that for the initial orientation. Rotational diffusion time is approximated by the value for a sphere:  $\tau_{\text{rot}} = \frac{1}{2D_r} = \frac{4\pi\eta R^3}{k_B T}$ . The total simulation time for the four setups is about 20 times longer than  $\tau_{\text{rot}}$  to ensure sufficient rotation of a cell.

Using equation (3.10) for fitting the correlation function with a monoexponential decay function (see figures 3.10 and 3.11), the effective diffusion coefficient  $D_{\text{eff}}$  is obtained. In contrast to a constant  $D_{\text{eff}}$  for a diffusing sphere (figure 3.3), for a RBC, it shows characteristic peaks (figure 3.12). The error bars in figure 3.12 have been generated by a more expensive analysis that considers the standard deviations arising from orientational averaging. For some  $|q|$ -values, the fits yield different values of  $D_{\text{eff}}$  if these standard deviations are considered as error bars, particularly for the low  $Y$  simulation.

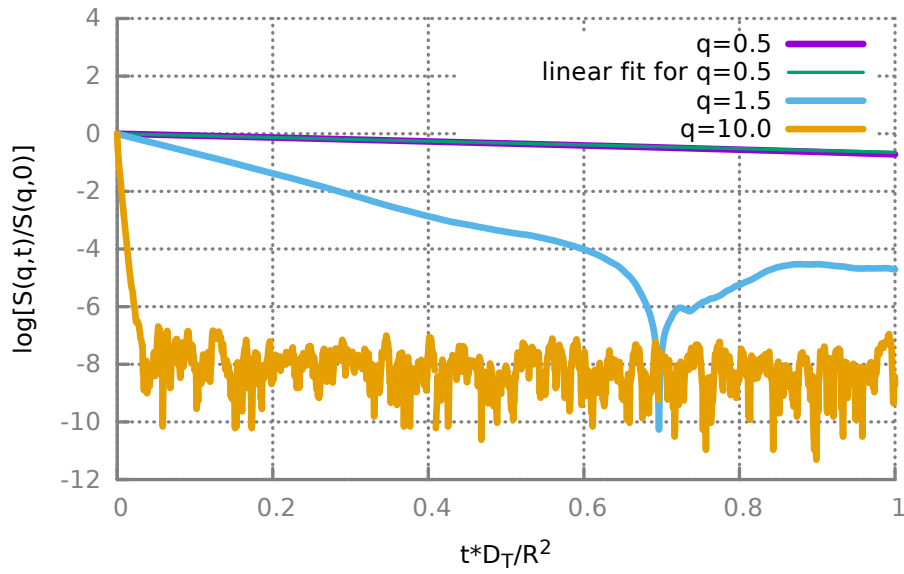


Figure 3.10: Decay of intermediate scattering function  $S(q, t)$  for  $\kappa_B = 10k_B T$  and different  $q$ . The decay is much faster for higher  $q$ , because relaxation times become smaller at smaller length scales.

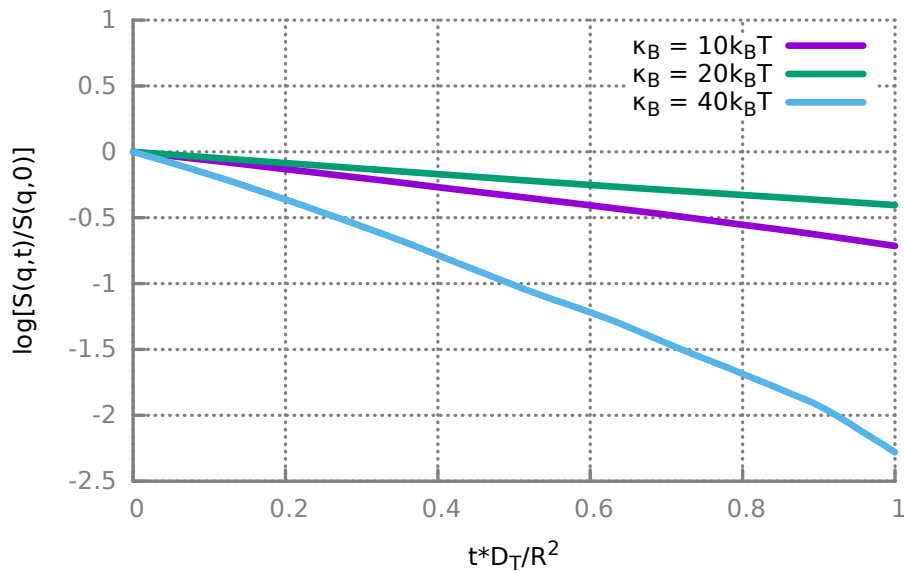


Figure 3.11: Decay of intermediate scattering function  $S(q, t)$  for  $q = 0.5/\mu m$  and different bending rigidities  $\kappa_B$ .  $\kappa_B$  has clearly an influence on the decay of the correlation. The curves for  $\kappa_B = 10k_B T$  and  $\kappa_B = 20k_B T$  are almost the same; yet  $\kappa_B = 40k_B T$  is clearly faster. This non-linear dependence is reflected in the effective diffusion coefficient in figure 3.12.

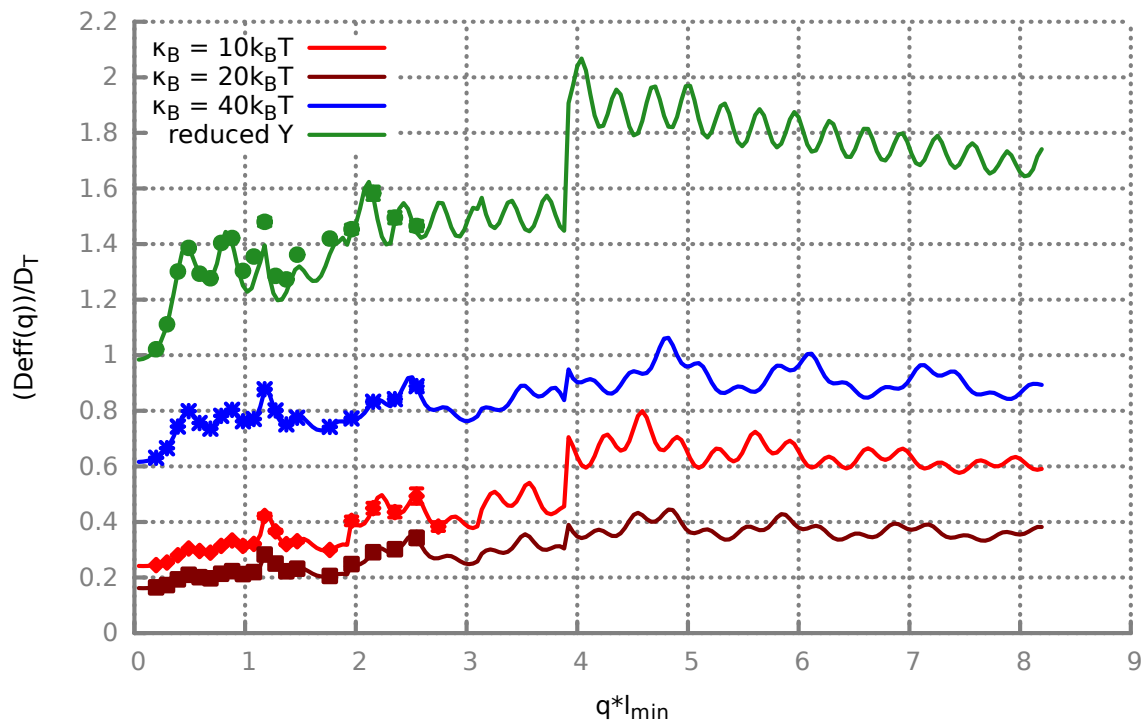


Figure 3.12: Effective diffusion coefficient of a RBC. Different values of the bending rigidity  $\kappa_B$  show the impact of membrane fluctuations. The setup with reduced Young's modulus, which is the only one exhibiting a biconcave shape, shows stronger diffusion and different curve characteristics. All curves have been normalised with individual translational diffusion coefficients  $D_T$ . The symbols on the curves show the error bars obtained from the orientational averaging.

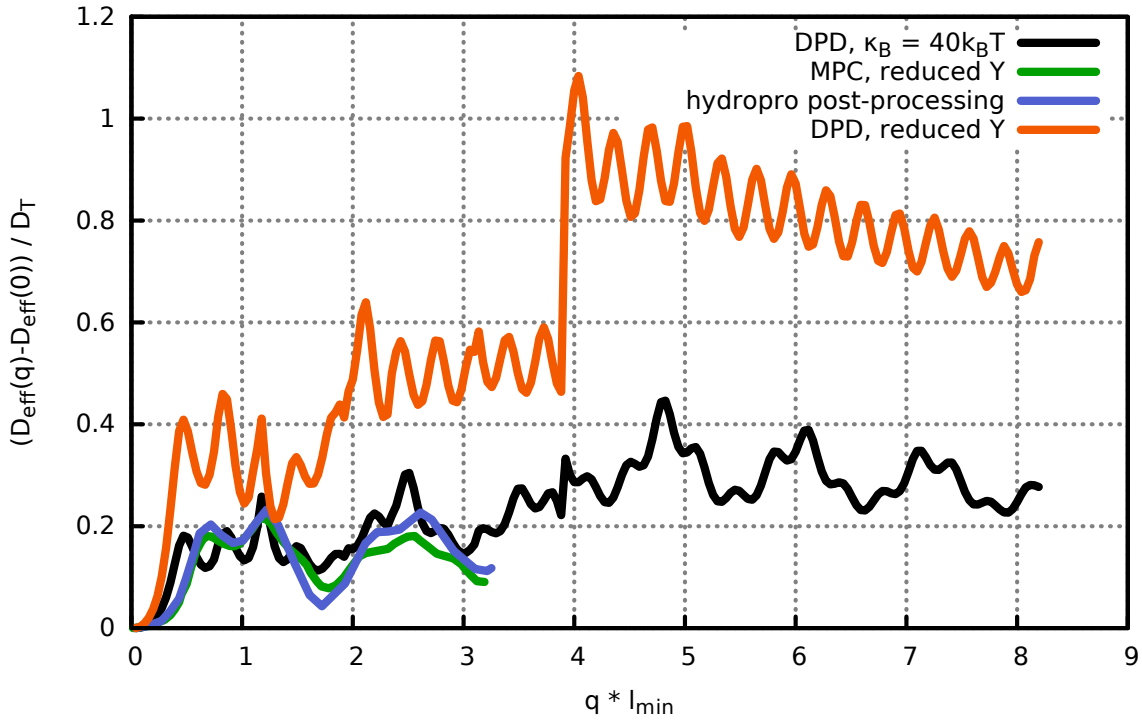


Figure 3.13: Effective diffusion coefficient of a RBC, compared to results of a MPC simulation by Matti Peltomaeki and Simón Poblete (unpublished work). All curves have been normalised with individual translational diffusion coefficients  $D_T$  and minimum length scale  $l_{\min}$ . The plots differ significantly in magnitude and shape.

Figure 3.13 shows a comparison of DPD results to DLS-analysis of an MPC simulation by Matti Peltomaeki and Simón Poblete (unpublished work). MPC was used to produce the cell trajectory and a post-processing tool has been used to calculate the scattering functions. The hydropro result is also based on the MPC trajectory. Hydropro is described in section 3.4.5.

The curves in figure 3.13 differ significantly. In the cases of reduced Young's modulus, all cell force parameters should match. That is why, the differences have to arise either from the simulation method or the degree of discretisation. The latter means the number of vertices constituting the RBC. In case of MPC,  $N_v = 500$ , whereas in DPD,  $N_v = 1000$ . To distinguish the possible reasons for the discrepancy, the MPC result is compared with another DPD simulation with  $N_v = 500$  in figure 3.14.

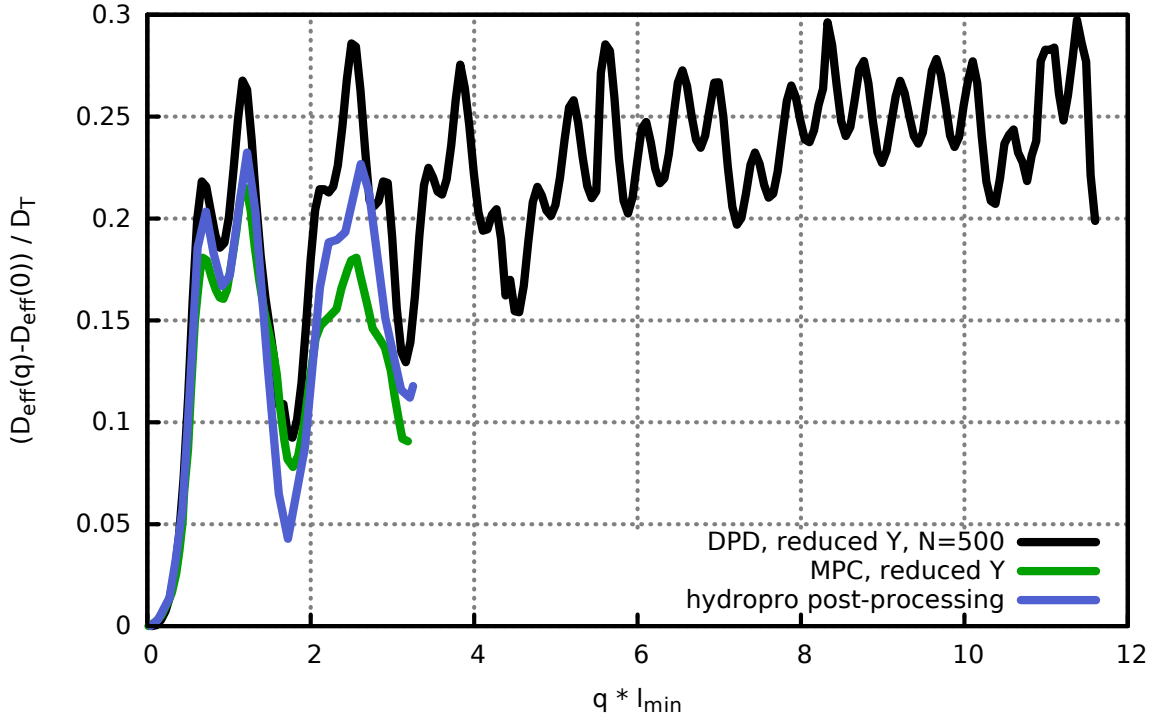


Figure 3.14: Effective diffusion coefficient of a RBC, compared to results of a MPC simulation by Matti Peltomaeki and Simón Poblete (unpublished work). All setups use cells modelled by 500 membrane vertices.

Figure 3.14 shows a better agreement between DPD and MPC results, particularly in the small  $qR$ -regime.

We conclude from these comparisons, that for light scattering, the following conditions are important:

- cell properties, described by Young's modulus  $Y$  or bending rigidity  $\kappa$
- different cell resolutions (number of vertices) lead to different characteristics of the effective diffusion coefficient  $D_{\text{eff}}$
- different simulation techniques agree for momentum transfer (scattering angle)  $q l_{\text{min}} < 2$ , but deviate for  $q l_{\text{min}} > 2$ .

### 3.4.5 Diffusion Coefficient from Hydropro

The effective diffusion coefficient  $D_{\text{eff}}$  of a rigid scatterer defined by a set of vertices  $\mathbf{r}_i$  can be obtained from the expression [19]

$$D_{\text{eff}}(q) = \frac{1}{q^2 S(q)} \sum_{j,k} \left\langle b_j b_k e^{-i\mathbf{q}\cdot\mathbf{r}_j} \left( \begin{array}{c} \mathbf{q} \\ \mathbf{q} \times \mathbf{r}_j \end{array} \right) \mathbf{D} \left( \begin{array}{c} \mathbf{q} \\ \mathbf{q} \times \mathbf{r}_k \end{array} \right) e^{i\mathbf{q}\cdot\mathbf{r}_k} \right\rangle \quad (3.15)$$

with  $\mathbf{D}$  being the diffusion matrix,  $S(q)$  being the static form factor and  $b_j$  being the scattering length of particle  $j$ . A bead model of a discocyte is constructed by taking a volume occupied by a hcp-lattice of particles of radius  $r_b$  each and removing all particles outside the discocyte volume. The diffusion matrix is calculated on the remaining set of particles using the software HYDRO++ [58, 59]. The calculation introduces hydrodynamic interactions between the beads of the model using the Kirkwood-Riseman approximation with volume correction for the calculation of rotational properties [58]. The hydrodynamic radius of the particles assumes the values  $5a$ ,  $3a$ ,  $2a$  and  $1.5a$ . The  $D_{\text{eff}}$  converges below  $r = 2a$ , and it changes by less than 0.5% when  $r \approx 1.5a$ . Both translational and rotational diffusion coefficients agree well with those of the MPC simulations. The orientational average is performed over 2500  $q$ -vectors.

### 3.4.6 Multiple Scattering

Before considering the scattering by several cells, the concept of multiple scattering is briefly outlined. The light scattered by one object can act as an incident beam on adjacent objects, leading to secondary scattering. This can hardly be calculated due to high computational cost. Ray tracing [107, 164, 14, 15] is not possible in the framework of Rayleigh-Debye-Gans approximation for the case of multiple scattering. So far, there has been only static considerations for simplified scattering geometries [102].

For RBCs, multiple scattering is non-negligible under certain geometrical conditions, such as if the cells are aligned in direction of the incident light, as it might be the case for Rouleaux structures or flow through narrow vessels [69]. However, if the cells are aligned laterally to the incident light, simple concepts like superposition of the scattered fields of the individual cells can be employed. For example, for the scattered light of aggregates of blood platelets and polystyrene beads, adding single components is a valid approximation [119]. However, in this reference, RDG is not favoured as it does not regard multiple scattering within a single scatterer. On the other hand, this effect is expected to be small for RBCs as the biconcave shape does not provoke strong multiple scattering from one part of the cell to another. Azimuthal averaging (corresponding in a certain way to the orientational diffusion in a dynamic study such as ours) eliminates the interference of partial waves in the far field, except for near-forward or backward scattering or orientations coinciding with the incident direction [69, 119].

For the cases of free diffusion, where multiple cells are aligned randomly, or shear, where the orientation of the cells is constantly changed, superposition approaches are justified. The superposition of the light scattering amplitudes of different RBCs can be implemented straight-forwardly into the Rayleigh-Debye-Gans code used in our work.

### 3.4.7 Red Blood Cells in Shear Flow

#### Theory

Cells in shear flow show different structure and dynamics than in equilibrium. They deform and align according to the flow. These affect optical properties of the blood cell solution, such as absorption, scattering and anisotropy [116, 97, 51].

Scattering by RBCs in shear flow is used for medical analysis in ektacytometry [68]. Cells are sheared in a Couette double-cylinder setup and a laser illuminates the sample. The diffrac-



tion pattern produced by the cells allows conclusions on cell deformability. Deformation by shear flow is linked to light reflectance and transmission [10]. RBCs are randomly oriented in equilibrium (no flow) and have a maximum absorption and scattering cross-section per cell [116]. Cell morphologies associated with higher degrees of organisation, such as aligned RBCs in flow, scatter less. With increasing shear rate, the random cell orientation is decreased and thus, the cross sections decrease asymptotically. The aligning of cells levels off at a shear rate of about  $200s^{-1}$ .

DLS measurements become complex when shear flow is present [27, 4, 53, 114, 181]. Indeed, shear flow induces decorrelation at small time scales compared to diffusing motion, reducing DLS to a shear-rate measurement. For instance, the signal produced by oscillating blood flow can be disturbed by contributions of extravascular tissue shearing, which arises from blood pressure [124]. To distinguish these contributions, the contribution of shear flow to the DLS signals is investigated. In general, if light is scattered from a particle moving in a fluid with a velocity  $\vec{v}$ , the frequency is Doppler-shifted by the projection of the velocity difference between two particles  $i$  and  $j$  in the direction of the momentum-transfer vector  $\vec{q} \cdot \vec{v}_{ij}$  [114], with  $\vec{q} = \vec{k}_s - \vec{k}_0$  as defined above.

In contrast to diffusion [81], for shear experiments [114] the geometry of source and detector changes the correlation function. When the scattered light is produced by particles that are spatially correlated, as in fluid flow (seeded by small, light-scattering particles), this spatial averaging alters the form of the intensity correlation function  $g(t)$ . This is because particles separated by large distances  $r$ , (considered as incoherent) contribute less to  $g(t)$ .

The effect of shear rate on the orientation of scatterers and its influence on the intensity correlation function, as well as the establishment of a shear plateau above a critical shear rate  $\dot{\gamma}_c$ , leading to partitioning of the fluid into regions of low shear rate/low turbidity/high birefringence and high shear rate/high turbidity/low birefringence have been investigated [145]. The different bands are characterised by different  $\dot{\gamma}$ , turbidity and birefringence<sup>2</sup>. The treatment in reference [145] of turbidity through shear-induced structures (SIS) can be employed in future when examining multiple RBCs in shear flow. SIS can give rise to new scattering centres.

DLS by small, rigid particles under shear conditions is described theoretically [27, 17, 150, 4, 53, 114, 145]. Next, it shall be outlined for which conditions light scattering is applicable to measure the shear rate.

Figure 3.15 shows the experimental setup to measure DLS in shear. The typical DLS quantities are defined as above;  $D_a$ ,  $D_f$ ,  $L$  and the Photomultiplier Tube (PMT) are means of detection of the speckle pattern. The rhombic shape of the scattering volume  $V$  (grey) arises from the intersection of the incident beam with the detected image and shall not be confused with the shear motion, whose gradient is in  $y$ -direction.

---

<sup>2</sup>Birefringence describes the anisotropic scattering of light; a dependence of the index of refraction on polarisation and direction of incident light:  $n(\vec{P}, \hat{k})$

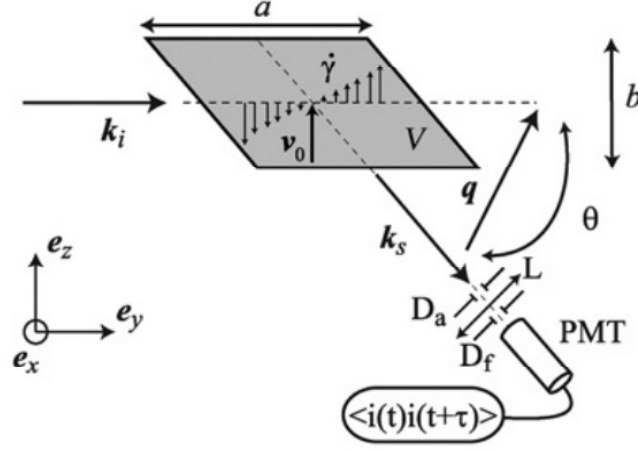


Figure 3.15: Experimental setup to measure DLS in shear flow (taken from reference [27]).

The auto-correlation function in equation (3.10) can be separated as follows:

$$S(q, t) = 1 + C_S |g'(q, t)|^2 \quad (3.16)$$

with  $C_S$  being the device contrast. In case of both identical and independent scatterers, the heterodyne correlation function  $g'(t)$  becomes:

$$g'(t) = \int_V \langle e^{-i\vec{q} \cdot (\vec{r}(t) - \vec{r}_0)} \rangle d\vec{r}_0 = \int_V \hat{p}(\vec{q}, t, \vec{r}_0) d\vec{r}_0 \quad (3.17)$$

where  $\hat{p}(\vec{q}, t, \vec{r}_0)$  is the Fourier transform of  $p(\vec{r}, t, \vec{r}_0)$ , which is the probability to find a particle at  $\vec{r}(t)$  when initially ( $t = 0$ ) at  $\vec{r}_0$ .

For the shear flow applied in this work, the velocity field is described as

$$\vec{v}(\vec{r}) = \vec{v}_0 + \dot{\gamma}(z_0 - z)\hat{e}_x \quad (3.18)$$

with  $\vec{v}_0$  being the mean velocity in the scattering volume,  $\dot{\gamma}$  the shear rate,  $z_0$  the profile's centre and  $\hat{e}_x$  the flow direction. Our flow, vorticity and gradient directions differ from those of figure 3.15. Here,  $\vec{v}_0 = \vec{0}$ .

The transformed probability is given by [27]:

$$\hat{p}(\vec{q}, t, \vec{r}_0) = \exp \left( \underbrace{-Dq^2 t}_{\text{diffusion}} - i \underbrace{\vec{q} \cdot \vec{v}(\vec{r}_0)}_{\text{Doppler shift}} t - \underbrace{D \frac{(\dot{\gamma} q_x)^2}{3} t^3 - D \dot{\gamma} q_x q_z t^2}_{\text{coupling diffusion \& shear}} \right) \quad (3.19)$$

where  $\vec{r}_0$  is the position at time  $t = 0$ .

Several time scales derived from this expression have to be considered:

- diffusion decorrelation time  $\tau_D = \frac{1}{Dq^2}$
- transit time  $\tau_t = \frac{L}{v_0}$  through the scattering volume  $V$ ;  $L$  is the characteristic size of  $V$

- shear decorrelation time  $\tau_{\dot{\gamma}} = \frac{1}{q_x L \dot{\gamma}}$  (see equation (3.20))

The term with shortest time scale dominates and allows to measure the corresponding motion (diffusion, transit or shear).

In case  $\tau_t$  is large compared to the other time scales, equation (3.17) can be simplified to

$$g'(t) \approx \exp(-Dq^2 t - i\vec{q} \cdot \vec{v}(\vec{r}_0)t) \times \underbrace{\int_V \exp(-i\dot{\gamma} q_x z t) dz}_{\text{shear-modified spatial coherence of the scattered light}} \quad (3.20)$$

Here,  $v_0 = 0$ , leading to  $\tau_t = \infty$ . Both walls move in opposite directions and the cell, on average, remains in the box centre.

In reference [145], a Couette geometry is investigated with parameters such that  $\frac{\tau_t}{\tau_{\dot{\gamma}}} \approx 10$ , meaning that the fluid is profiled at the moving wall and that the transit term in equation (3.19) can be neglected. Thus, to determine  $\dot{\gamma}$ , the only condition that has to be met concerns the Péclet number:  $\text{Pe} = \frac{\tau_D}{\tau_{\dot{\gamma}}} \gtrsim 1$ . For certain ratios of time scales, it is possible to obtain the diffusion coefficient ( $\tau_D \ll \tau_{\dot{\gamma}} \rightarrow q_x L \dot{\gamma} \ll Dq^2$ ). However, this is not pursued in this thesis. DLS will be employed to access the local shear rate [53]. The shear contribution to the scattering functions is the quantity of interest. Now only basic directions of  $\vec{q}$  are considered:  $\hat{q} = \hat{e}_i$  with  $i$  being  $x$  or  $y$  or  $z$ .

For the present parameter values, the conditions to measure  $\dot{\gamma}$  are:

$$\tau_D \gg \tau_{\dot{\gamma}} \rightarrow Dq^2 \ll q_x L \dot{\gamma} \quad (3.21)$$

Let us consider light scattering with  $\hat{q} = \hat{e}_x$ , thus  $Dq_x \ll L\dot{\gamma}$ .

With  $L = 30$  for the simulation box in both flow and gradient direction,  $\mathcal{O}(D) = 10^{-3} - 10^{-4}$  and  $\mathcal{O}(\dot{\gamma}_{\min}) = 10^{-1}$ , the resulting condition is  $q_x \ll 500/\mu\text{m}$ , which is fulfilled here.

$$\tau_t \gg \tau_{\dot{\gamma}} \rightarrow \frac{L}{v_0} \gg \frac{1}{q_x L \dot{\gamma}} = \frac{L_z}{q_x L \Delta v_x} \quad (3.22)$$

with  $\Delta v_x$  being the wall velocity. If both walls move in opposite directions,  $v_0 = 0$  and the condition is already fulfilled. In case of one stationary wall,  $v_0 = \frac{1}{2}v_x$  and:

$$q_x \gg \frac{1}{2L} \quad (3.23)$$

which is fulfilled for all  $|q|$  considered.

Now let us consider light scattering with  $\mathbf{q}_x = \mathbf{0}$ , namely the vorticity ( $\vec{q} = |q|\hat{e}_y$ ) and the gradient ( $\vec{q} = |q|\hat{e}_z$ ) directions. Both  $\tau_D \ll \tau_{\dot{\gamma}}$  and  $\tau_t \ll \tau_{\dot{\gamma}}$  apply, so that the shear rate will not be measurable via the correlation decay. Yet it is interesting for which conditions diffusion or transit (convection) will dominate the decay. Therefore, the order of magnitude of the time scale ratio  $\mathcal{O}\left(\frac{\tau_t}{\tau_D}\right) = \mathcal{O}\left(\frac{Dq^2}{\frac{v_0}{L}}\right)$  has to be calculated.

For different wall velocities  $v_x$ , different effects will dominate. If  $v_0 = 0$ , the diffusion will, on average, dominate as there is no preferred direction for transit motion. For one stationary wall,  $v_0 = \frac{1}{2}v_x$ . For small  $v_x$ , a high enough  $q$  can make  $\tau_t$  an order of magnitude larger than  $\tau_D$  and thus, diffusion will dominate. For large wall velocities, transit motion can dominate the scattering signal.

Reference [53] describes the homodyne correlation function for a general linear flow for the case of short  $\tau_{\dot{\gamma}}$  compared to the other time scales:

$$g_{ho}(\vec{q}, t) = \left| \int \int \int I(\vec{x}) \exp(-i\vec{q}\dot{\Gamma}\vec{x}t) d^3\vec{x} \right|^2 \quad (3.24)$$

In this work, the shear flow is directed in positive  $x$  and the gradient in  $z$ -direction. This implies the following shear matrix

$$\dot{\Gamma} = \begin{pmatrix} 0 & 0 & \dot{\gamma} \\ 0 & 0 & 0 \\ 0 & 0 & 0 \end{pmatrix} \quad (3.25)$$

which leads to  $\vec{q}\dot{\Gamma}\vec{x} = q_x\dot{\gamma}z$  and

$$\begin{aligned} g_{ho}(\vec{q}, t) &= \left| -\frac{L_x L_y}{i q_x \dot{\gamma} t} [\exp(-i q_x \dot{\gamma} L_z t) - 1] \right|^2 \\ &= \left( \frac{2 L_x L_y}{q_x \dot{\gamma} t} \sin\left(\frac{1}{2} q_x \dot{\gamma} L_z t\right) \right)^2 \\ &= \left( \frac{V}{\alpha} \sin(\alpha) \right)^2 \end{aligned} \quad (3.26)$$

with  $\alpha \stackrel{\text{def}}{=} \frac{1}{2} q_x \dot{\gamma} L_z t$  and  $V = L_x L_y L_z$ .

$$\lim_{t \rightarrow 0} g_{ho}(\vec{q}, t) = |V|^2 \quad (3.27)$$

## Simulation Results

The influence of Couette flow on light scattering signals is examined. The purpose is to show that the shear motion is reflected in the scattering signals. Additionally, different shapes due to shearing cause different behaviour of the scattering functions.

Two planar, rigid walls are located at  $z = -\frac{L_z}{2}$  and  $z = \frac{L_z}{2}$ . The space between the walls is filled with solvent and a RBC. The walls move with constant, but opposing velocities in  $x$ -direction. Via friction and hydrodynamics, the wall motion induces a shear flow. Different wall velocities  $v_x$  are tested corresponding to different shear rates given by  $\dot{\gamma} = \frac{\Delta v_x}{L_z}$ .

For DLS by RBCs in shear flow, we deal with the scattering amplitude (and its temporal auto-correlation function), depending on *two* variables  $q$ -magnitude and shear rate.

It is important to note that the theory in section 3.4.7 assumes small, rigid particles. Thereby, rotations and deformations, typical for RBCs in shear flow, are not represented in that formalism. Thus, relations cannot be transferred directly, such as the conditions under which the shear rate is measurable by light scattering.

Simple shear flow simulations of shear rates in the range of  $57 - 2005 s^{-1}$  have been analysed with a post-processing C-code. These simulations are described in section 4.3.1. The difference to the analysis in section 3.4.4 is that here, no orientational averaging is performed. The different directions (flow, gradient and vorticity) shall remain separate to identify their effects on light scattering. Thus, all functions are shown for these three different directions.

Examples of the correlation decay are shown in figures 3.16, 3.17, 3.18. The temporal correlations for different shear rates show oscillations. For certain directions and magnitudes of  $\vec{q}$ , these oscillations roughly match in scale. Considering however that the lag time is scaled by the individual shear rates, it is clear that the oscillation rate is coupled to the shear rate.

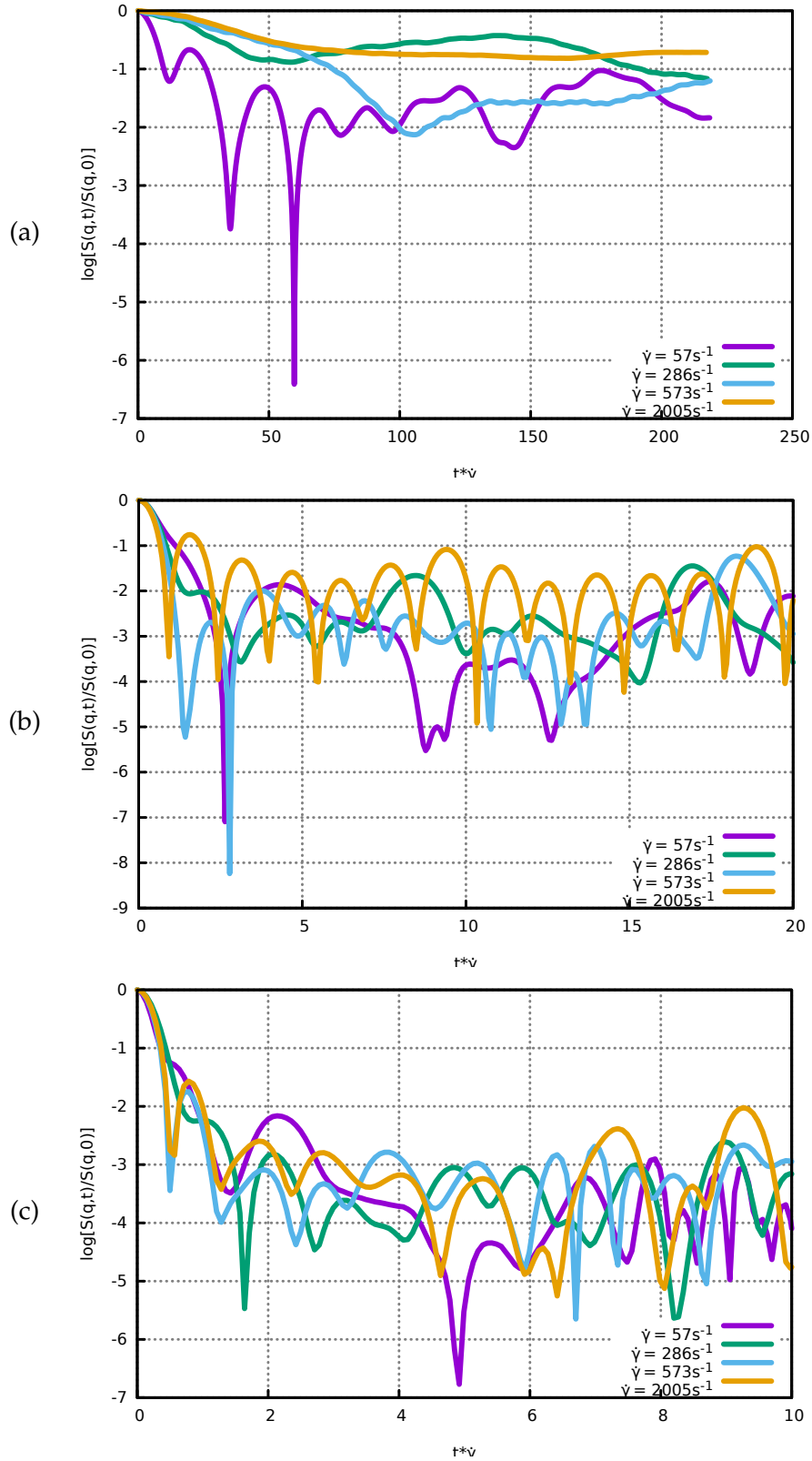


Figure 3.16: Decay of correlation function  $S(q,t)$  for different shear rates and  $q$  values. Here,  $\vec{q}$  is in the flow direction. (a)  $q = 0.5/\mu m$ : the normalised oscillation rates differ among different shear rates. (b)  $q = 2.5/\mu m$ : apart from the smallest shear rate, the normalised oscillation rates are in the same order of magnitude among different shear rates. (c)  $q = 5.0/\mu m$ : the normalised oscillation rates are in the same order of magnitude among different shear rates.

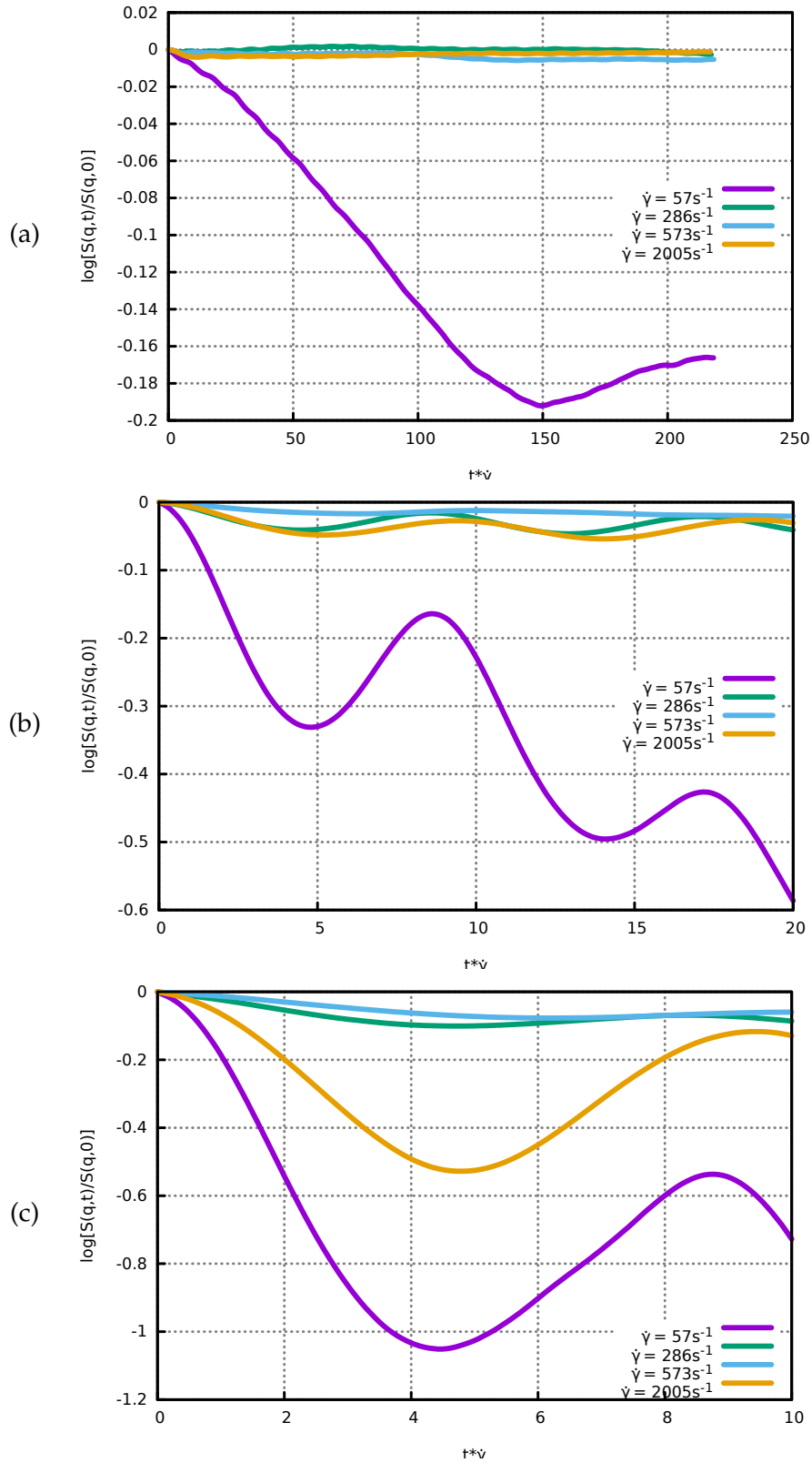


Figure 3.17: Decay of correlation function  $S(q, t)$  for different shear rates and  $q$  values. Here,  $\vec{q}$  is in the vorticity direction. (a)  $q = 0.5/\mu\text{m}$ : the decays are too slow to recognise the oscillation rates. (b)  $q = 2.5/\mu\text{m}$ : the normalised oscillation rates are in the same order of magnitude among different shear rates. (c)  $q = 5.0/\mu\text{m}$ : the normalised oscillation rates are in the same order of magnitude among different shear rates.

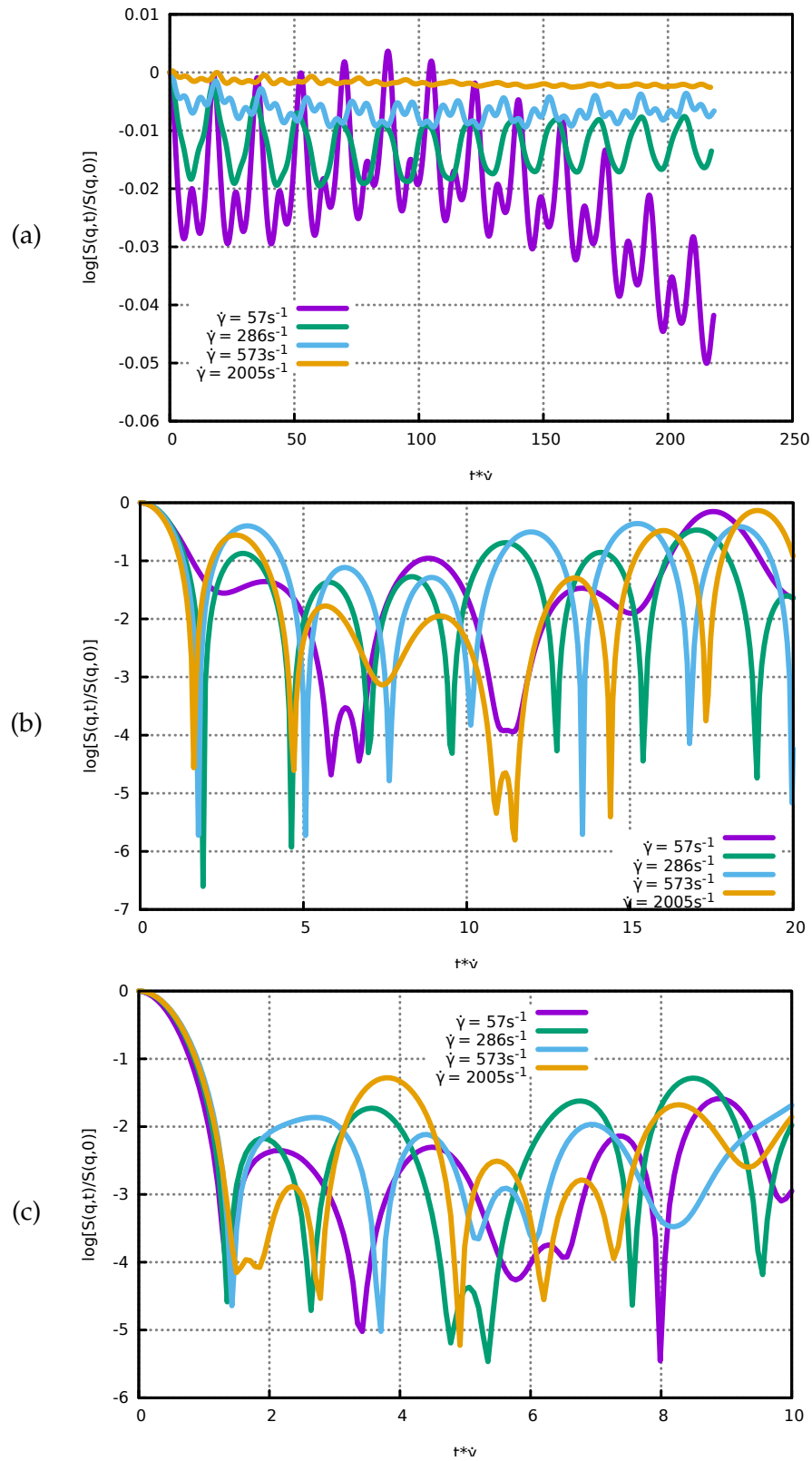


Figure 3.18: Decay of correlation function  $S(q, t)$  for different shear rates and  $q$  values. Here,  $\vec{q}$  is in the gradient direction. (a)  $q = 0.5/\mu\text{m}$ : the normalised oscillation rates are in the same order of magnitude among different shear rates. (b)  $q = 2.5/\mu\text{m}$ : the normalised oscillation rates are in the same order of magnitude among different shear rates. (c)  $q = 5.0/\mu\text{m}$ : the normalised oscillation rates are in the same order of magnitude among different shear rates..



Equation (3.10) assumes diffusion. Thereby, it is not suitable for scattering under shear motion. Thus, our analysis focuses on the correlation decay and defines quantities which describe the connection of shear motion and scattering signals. First, the average intensity is shown in figures 3.19, 3.20, 3.21. It is equivalent to the correlation function for zero time lag:  $\langle I(q, t) \rangle_t = S(q, t = 0)$ . The average intensity has been normalised by the RBC volume to make it dimensionless.

Second, the half-life of correlation functions is shown in figures 3.22, 3.23, 3.24. It is defined as the time after which the correlation has decreased to half of its value at time lag zero:  $S(q, \tau_{1/2}) = \frac{1}{2}S(q, 0)$ . Additionally, it has been normalised by the shear rate:  $\tau'_{1/2} = \tau_{1/2} \bar{\dot{\gamma}}$  to make it dimensionless.

Third, the dominant frequency of the decay of the correlation function is shown in figures 3.25, 3.26, 3.27. It is obtained from a Fourier analysis of  $S(q, t)$  in time. Additionally, it has been normalised by the shear rate:  $f' = f/\bar{\dot{\gamma}}$  to make it dimensionless. It is important to point out that the normalisation by  $\bar{\dot{\gamma}}$  values differs among the four curves in each figure.

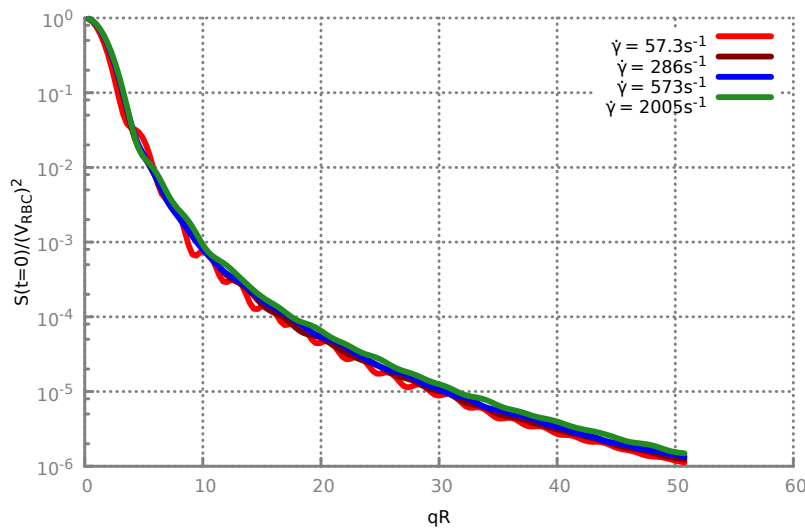


Figure 3.19: The average intensity  $\langle I(q, t) \rangle_t = S(q, t = 0)$  in the flow direction. The typical oscillatory pattern, as seen in figure 3.7, disappears at higher shear rates. The less biconcave the cell gets (see the trilobe shape in section 4.3.1), the more the average intensity deviates from that of the original RBC.

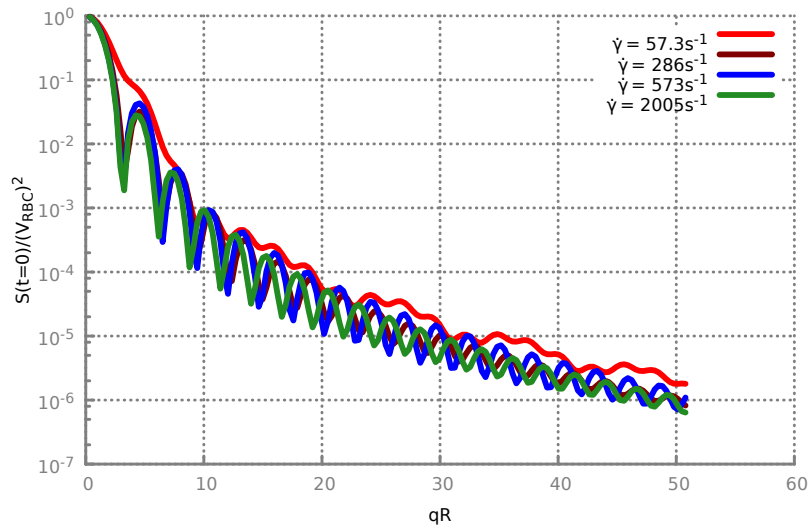


Figure 3.20: The average intensity  $\langle I(q, t) \rangle_t = S(q, t = 0)$  in the vorticity direction. The typical oscillatory pattern, as seen in figure 3.7, is not very apparent at the lowest shear rate. The curve for the lowest shear rate seems to be the envelope for the other curves.

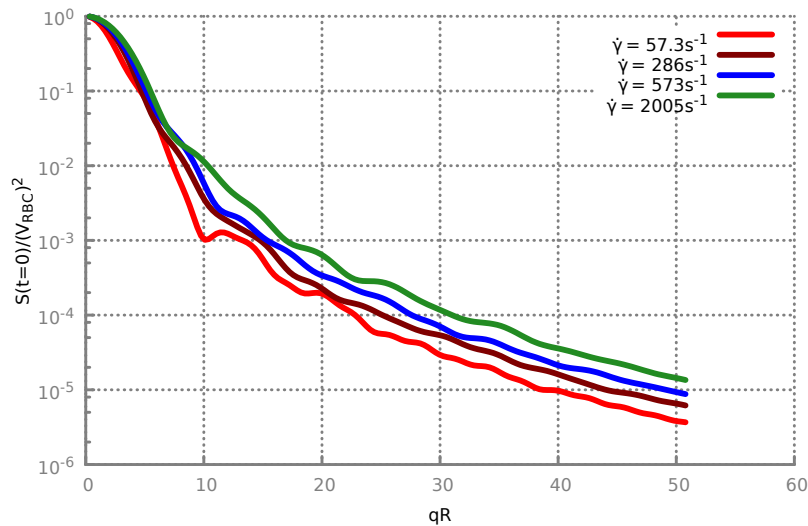


Figure 3.21: The average intensity  $\langle I(q, t) \rangle_t = S(q, t = 0)$  in the gradient direction. Higher shear rates lead to larger intensity values.

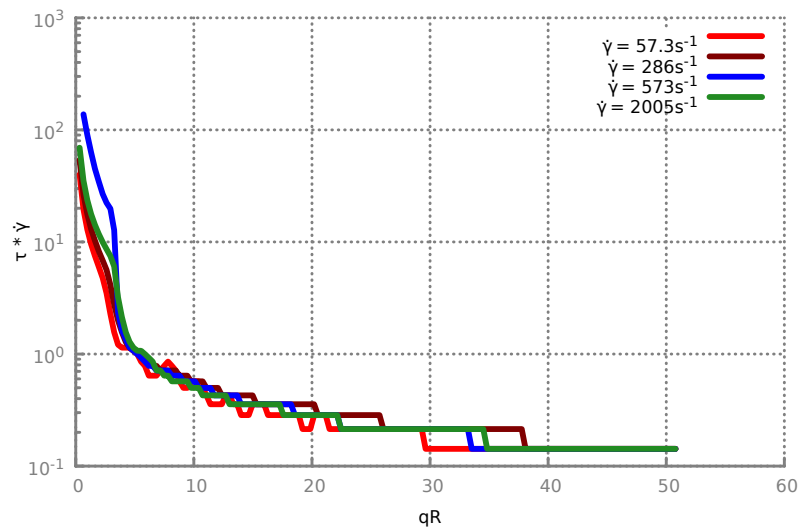


Figure 3.22: Half-life time  $\tau_{1/2}$  of the correlation function in the flow direction. Here, a logarithmic scale is used. As already seen for the case of diffusion (section 3.4.4), higher magnitude of the momentum transfer  $|q|$  leads to faster correlation decay ( $\tau_{1/2}$  decreases with  $|q|$ ). The normalised half-life time is nearly independent of shear rate.

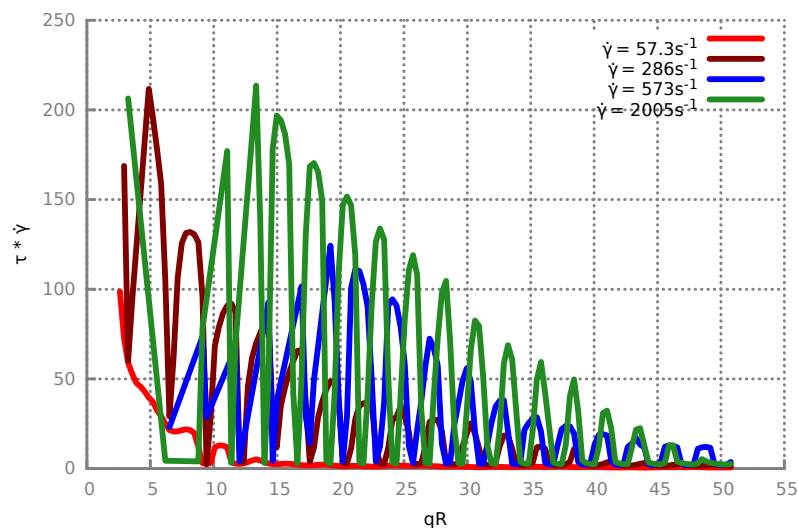


Figure 3.23: Half-life time  $\tau_{1/2}$  of the correlation function in the vorticity direction. Here, a linear scale is used. Apparent are the oscillations with  $|q|$  which get stronger with shear rate.

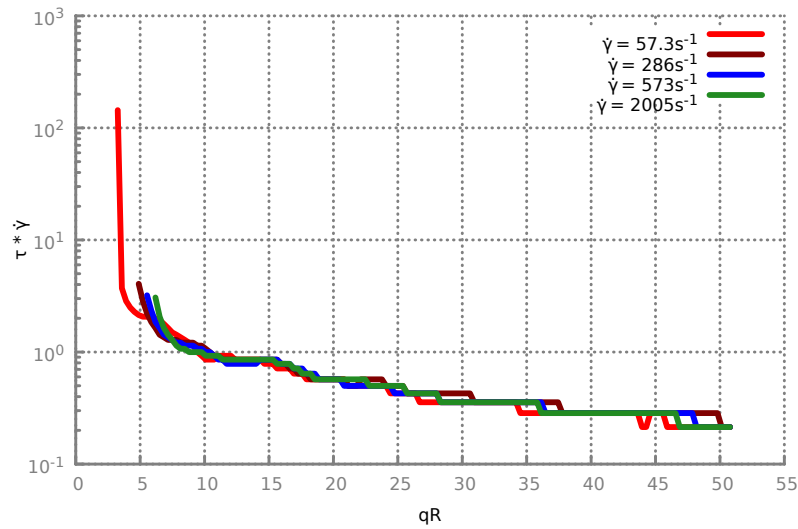


Figure 3.24: Half-life time  $\tau_{1/2}$  of the correlation function in the gradient direction. Here, a logarithmic scale is used. As already seen for the case of diffusion (section 3.4.4), higher magnitude of the momentum transfer  $|q|$  leads to faster correlation decay. The normalised half-life time is nearly independent of shear rate.

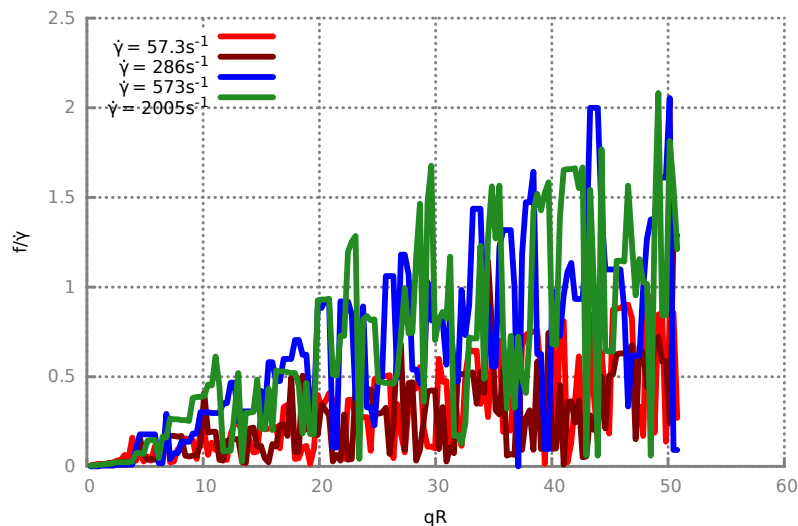


Figure 3.25: Dominant frequency of decay of the correlation function in the flow direction. Higher magnitude of the momentum transfer  $|q|$  or higher shear rates cause a faster correlation decay.

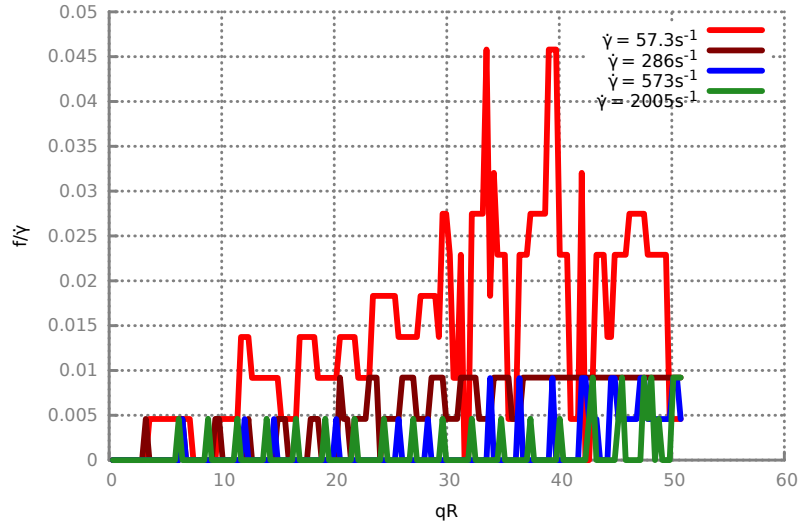


Figure 3.26: Dominant frequency of decay of the correlation function in the vorticity direction. The dependencies are different here in comparison to the cases of flow and gradient direction, and the different orders of magnitude of  $\frac{f}{\bar{\gamma}}$  have to be considered.

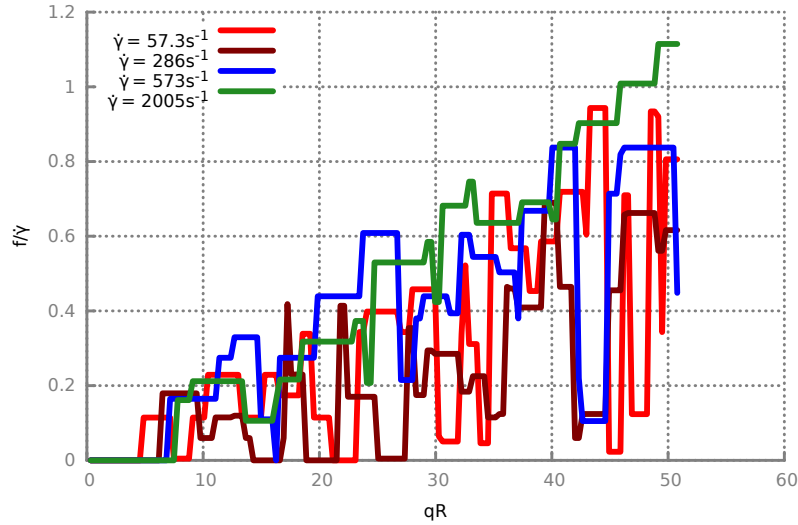


Figure 3.27: Dominant frequency of decay of the correlation function in the gradient direction. Higher magnitude of the momentum transfer  $|q|$  causes faster correlation decay. In all cases, the decay frequency  $f$  is in the range of the shear rate  $\bar{\gamma}$ .

For the decay in flow direction, as already seen for the case of diffusion (section 3.4.4), a higher magnitude of the momentum transfer  $|q|$  (corresponding to larger scattering angles in experiments) leads to a faster correlation decay ( $f$  increases with  $|q|$ ). Higher shear rates cause higher decay frequencies, even if the frequencies are normalised by  $\bar{\gamma}$ . Both values are on the same order of magnitude:  $f/\bar{\gamma} = \mathcal{O}(1)$ . Thus, it is possible to infer the underlying shear rate from scattering in the flow direction. The decay in vorticity direction behaves

differently: lower shear rates result in higher decay frequencies. Additionally,  $f/\bar{\dot{\gamma}} \ll 1$ . Thus, it would be difficult to infer the underlying shear rate from scattering in the vorticity direction. The decay frequency in gradient direction shows the same  $|q|$ -dependence as that in the flow direction. However, the dependence on shear rate is not that clear. Nevertheless, the decay frequency is strongly related to the shear rate:  $f/\bar{\dot{\gamma}} = \mathcal{O}(1)$ . Thus, also by scattering in the gradient direction, it is possible to infer the underlying shear rate.

### 3.5 Comparison with Polymers in Shear Flow

Here, the scattering signal of a RBC in shear flow has been linked to the shear rate. Analogously, the tumbling motion of polymers in shear flow has been linked to the shear rate [78, 79].

Polymers in shear flow exhibit a non-periodic, cyclic tumbling motion, characterised by rotations and shape changes. The polymer (re)coils and stretches during rotation. This can be compared to the motion of a trilobe or a quadrulobe, which are RBC shapes occurring in simple shear flow, see section 4.3.1. Dilute and semidilute concentrations are considered [78, 79]. Instead of the scattering amplitude, the radius of gyration tensor is used to construct a time correlation. It allows conclusion from the tumbling frequency to the shear rate. The tumbling frequencies depend on the so-called Weissenberg number, which is the shear rate scaled by the relaxation time  $\bar{\dot{\gamma}} \tau$ . The tumbling frequency depends on the shear rate as  $f \propto \bar{\dot{\gamma}}^{2/3}$ . In the athermal case, a linear dependence is found.

As here, different directions are considered: flow, gradient and vorticity. In the dilute case, however, for polymers, all directions have similar frequencies. These frequencies differ only in the semidilute case.

The consideration of different concentrations hints at dynamics light scattering of RBCs at different haematocrit, a possible future scenario for simulations. It is interesting to check if also for RBCs, the frequencies in different directions will diverge for higher concentrations.

### 3.6 Conclusion

Light scattering signals depend sensitively on many cell properties, such as the bending rigidity or the Young's modulus. We have compared the DLS signals obtained from different simulation techniques, namely dissipative particle dynamics and multi-particle collision dynamics. Equality is found only for matching resolution, bending rigidity, and Young's modulus. The course of  $D_{\text{eff}}(q)$  characterises the shape of a diffusing object. The  $D_{\text{eff}}(q)$  of cup-shaped RBCs differs from that of biconcave RBCs. Thus, light scattering signals can distinguish cells of different shape properties. This provides a basis to non-invasively distinguish cells of different (pathological) states, such as malaria or sickle cell anaemia. Diffusing RBCs of different bending rigidities were simulated. Cells of higher bending rigidity are less prone to thermally induced membrane fluctuations. Dynamic light scattering (DLS) provides a basis to draw conclusions on membrane fluctuations. The nature of membrane fluctuations, passive (thermal) or active (metabolic) or a combination, has been discussed recently [172]. The present RBC model does not include active membrane fluctuations. By comparing via DLS the simulational purely thermal membrane fluctuations with experimental membrane fluctuations, one might identify differences corresponding to active contribu-

tions.

In case of RBCs in shear flow, under certain conditions, light scattering signals, such as the decay of the scattering amplitude correlation function, allow conclusions on the shear rate. The dominant frequency of this decay is on the order of the shear rate, if the momentum transfer  $\vec{q}$  is either in the flow or gradient direction.

This relation could measure shear rates in vivo non-invasively, which is interesting in case of altered flow conditions, e.g. vessel occlusions [1].





## Chapter 4

# Dynamics of a RBC in Simple Shear Flow

### 4.1 Introduction

In this chapter, the impact of shear stress on the dynamics of RBCs is studied. Shear stress occurs in the cardiovascular system in various situations. For example, shear stress occurs in cylindrical vessels, close to stents, in the heart and at bifurcations. In the case of stents, an insufficient shear stress can lead to thrombogenesis, thus to in-stent restenosis and vessel occlusion [1].

Simple shear flow is the simplest setup to model shear stress. Two planar walls are placed at a distance  $L$ , with a fluid of viscosity  $\eta_0$  between them. The walls move in opposite directions, parallel to their planes. The interjacent (Newtonian) fluid develops planes of different velocities; these planes follow the wall motion parallel. Across the fluid, a linear velocity gradient establishes. Simple shear flow comprises extensional and rotational forces [28].

Here, in the first setup, a single RBC is placed between the walls to study its behaviour when subject to an environment in simple shear flow. In the second approach, realistic haematocrits are probed. Multiple RBCs are added to the fluid. They increase the effective viscosity of the interjacent fluid and affect each other by hydrodynamic and direct (volume exclusion) interactions.

Simple shear flow is often called Couette flow after the French physicist who performed experiments with the flow between two counter-rotating cylinders. Taylor-Couette flow refers to the work of the British physicist who studied the stability of Couette Flow [165].

Here, simulations are performed in narrow slits with a characteristic size similar to that of microvessels. This study is motivated by previous simulations [45], where a biconcave stress-free shape was used, and by experiments of the group of M. Abkarian (University of Montpellier, unpublished work, [112]). Here, a spheroidal stress-free shape will be used. Additionally, a realistic viscosity ratio of five is employed and its effect on the dynamics, shapes, and transition between various types of motion is investigated. Simulations for different shear rates show different shapes and dynamics. Also, the initial orientation of a RBC seems to matter. In agreement with unpublished experiments, the RBC adopts different shapes for different shear rates. Increasing the shear rate, the cell rolls, becomes a trilobe, and finally, becomes a quadrulobe. Moreover, the tank-treading behaviour is suppressed in favour of a trilobe dynamics. We will discuss the importance of the viscosity contrast on

the flow resistance, and the effect of different stress-free shapes of the RBC [134, 26] on its dynamics in flow.

## 4.2 Models & Methods

### 4.2.1 Numerical Method

We employ a combination of dissipative particle dynamics (DPD, see section 2.1.2 and references [66, 40]) with smoothed DPD (SDPD, see section 2.1.3) conserving angular momentum [33, 121]. SDPD is used for the bulk interactions as we can specify the pressure equation of state and viscosity directly. DPD is used for the coupling of RBC membrane and surrounding fluids as we can specify the friction interaction directly. The friction force is adjusted to properly transfer the shear stresses by the fluids, thus allowing no-slip at the membrane. SDPD is used analogously to reference [46].

For the viscosity contrast to have an effect, the inner solvent must not mix with the outer solvent, see graphics 2.6. This requires an impenetrable membrane, which is implemented numerically by bounce-back reflections, see section 2.6.1.

### 4.2.2 Measured Quantities

An important quantity of measure is the orientation of a cell relative to the flow direction. It is found through the gyration tensor

$$G_{ij} = \frac{1}{N} \sum_n^N (x_{n,i} - x_{c,i}) \cdot (x_{n,j} - x_{c,j}) \quad (4.1)$$

where  $i$  and  $j$  are  $x$ ,  $y$ , or  $z$ ;  $\vec{x}_n$  is the position of membrane vertex  $n$  and  $\vec{x}_c$  is the centre of mass of the cell. Diagonalisation of the gyration tensor  $G_{ij}$  yields its eigenvalues  $\lambda_i$ . Then, the eigenvector that corresponds to the smallest eigenvalue is determined. This vector is defined as the cell's orientation. Its projection onto the flow direction can show rotations of the cell in the slit.

The eigenvalues are also used to construct another important measure, the asphericity  $\mathcal{O}$ , which characterises the deviation from a sphere:

$$\mathcal{O} = \left[ (\lambda_1 - \lambda_2)^2 + (\lambda_2 - \lambda_3)^2 + (\lambda_3 - \lambda_1)^2 \right] / (2R_g^4) \quad (4.2)$$

with  $R_g^2 = \lambda_1 + \lambda_2 + \lambda_3$ .

Furthermore, the eigenvalues are used to construct the acylindricity  $\mathcal{C}$ , which characterises the deviation from a cylinder:

$$\mathcal{C}_1 = \frac{\lambda_3^2 - \lambda_2^2}{\lambda_3^2 + \lambda_2^2} \quad (4.3)$$

with analogous definitions for  $\mathcal{C}_2$  and  $\mathcal{C}_3$  [149]. These quantities have been used in experiments as well [167].

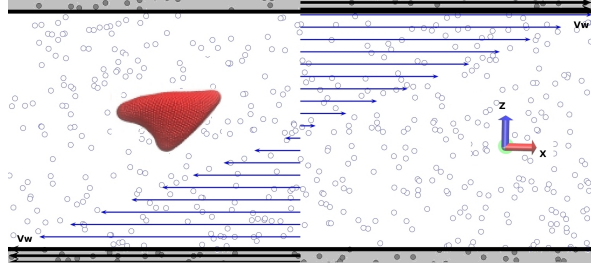


Figure 4.1: Simple Shear Flow,  $\dot{\gamma} = \frac{2v_w}{D}$ ,  $\vec{v} = \dot{\gamma}z\hat{e}_x$ .

### 4.2.3 Single Cell in a Couette-Flow Setup with Walls

Simulations of a single RBC in shear flow (Couette flow) have been performed, see figure 4.1. This setup will be called ‘dilute’ further on. Two planar walls, with a separation in  $z$ -axis, move in opposite directions ( $\pm\hat{x}$ ) and create a linear flow field. We model the walls by immobile particles that have the same density, temperature and radial distribution function as the fluid. The shear rate is homogeneous, and so is the shear stress, when proper no-slip boundary conditions are enforced. These conditions are ensured by using an adaptive shear force [45]. It adjusts the wall friction to compensate for the slip, which arises due to a lack of velocity gradient in the wall.

The fact that the shear rate is independent of the position implies the following shear matrix (velocity gradient matrix)

$$\dot{\Gamma} = \begin{pmatrix} 0 & 0 & \dot{\gamma} \\ 0 & 0 & 0 \\ 0 & 0 & 0 \end{pmatrix} \quad (4.4)$$

with  $\dot{\Gamma}_{ij} = \nabla_j v_i$ .

The box size is kept fixed, only the shear rate is varied. The shear rate is given by the ratio of the walls’ velocity difference and their distance:  $\dot{\gamma} = \frac{2v_w}{D}$ . The viscosity is chosen to satisfy a low Reynolds number of  $Re = 0.3$  for a fixed dimensionless shear rate  $\dot{\gamma}^*$ . Thereby, the viscosity is calculated as:

$$\eta = \sqrt{\frac{n \kappa_r \dot{\gamma}^*}{Re D_r}}. \quad (4.5)$$

Thus, the wall velocity is determined to be

$$\vec{v}_w = \frac{D}{2} \sqrt{\frac{Re \kappa_r \dot{\gamma}^*}{n D_r^5}} \hat{e}_x. \quad (4.6)$$

The real (physical) shear rate is obtained by dividing the dimensionless shear rate by the physical relaxation time (at 20° Celsius and in water):  $\dot{\gamma}_{\text{real}} = \dot{\gamma}^*/1.1\text{s}$ . Four different shear rates  $57\text{s}^{-1}$ ,  $286\text{s}^{-1}$ ,  $573\text{s}^{-1}$  and  $2005\text{s}^{-1}$  were simulated.

The initial orientation of the cell affects its dynamics [32]. It is studied in section 4.3.1.

### 4.2.4 Multiple Cells in Shear Flow using Lees-Edwards Boundary Conditions

A further set of simulations has been performed using multiple cells that make up 45% of the simulation box volume. This corresponds to the physiological systemic haematocrit.

This setup will be called ‘dense’ further on. 128 cells are put into a box of  $32 \times 32 \times 28.4 \mu\text{m}^3$ . Here, Lees-Edwards boundary conditions are used. This means that the simulation box is fully periodic and particles leaving the box in shear-gradient direction are assigned the opposite velocity. No walls and no adaptive shear forces are required. In these simulations, flow is in  $y$ -direction, while the gradient direction is  $x$ , implying the shear matrix (velocity gradient matrix) to be

$$\dot{\Gamma} = \begin{pmatrix} 0 & 0 & 0 \\ \dot{\gamma} & 0 & 0 \\ 0 & 0 & 0 \end{pmatrix} . \quad (4.7)$$

## 4.3 Results

### 4.3.1 Single Cell in Couette-Flow Setup with walls

The simulations have been performed for four different shear rates and two different initial orientations. All eight simulations are at least 12 million time steps long; this corresponds to 7.6s, 1.5s, 0.76s and 0.22s for shear rates  $57\text{s}^{-1}$ ,  $286\text{s}^{-1}$ ,  $573\text{s}^{-1}$  and  $2005\text{s}^{-1}$ , respectively.

#### Shapes and Dynamics Observed in Couette Flow

In table 4.1, we show characteristic motions that appear for different shear rates and initial orientations. The motions are listed in their order of appearance. Visual analysis of the trajectories is the first step to identify these motions, and the quantitative analysis (see below) confirms essential differences among them. It is apparent that the cell’s motion not only depends on the shear rate, but also on the initial orientation. Two interpretations are possible: first, the trajectories should be longer to decorrelate the motion from the initial orientation, as it seems to be the case for  $\dot{\gamma} = 57\text{s}^{-1}$ , where rolling eventually dominates. Second, for each shear rate, there could be multiple metastable states that are accessed depending on conditions such as the initial orientation. For cells that are initially tilted, the rolling/wheeling motion is preserved up to medium shear rates. At shear rates  $\dot{\gamma} = 57\text{s}^{-1}$  and  $\dot{\gamma} = 2005\text{s}^{-1}$ , the simulations for upright and tilted initial orientation finally agree. For the low shear rate, both configurations show rolling, while for the high shear rate, both configurations show a quadrulobe transforming into a trilobe.

#### Distinct Shapes and their Geometry

We identify different shapes and describe them by their extensions in the directions of flow, gradient and vorticity. The extension is the maximum length of the cell in a particular direction.

For a cell that tumbles initially and then rolls like a wheel, the cell extensions develop as shown in figure 4.2. A typical trilobe cell is shown in figure 4.3. Characteristics are the different sizes and their amplitudes, e.g. the size in vorticity direction is the largest and fluctuates least. Figure 4.4 shows the initially upright quadrulobe transforming into a trilobe.

$\dot{\gamma}$	<b>upright orientation</b>
$57s^{-1}$	rotations in shear plane, rotating cup, flipping around vorticity, rotating cup, precessing around vorticity, wheeling
$286s^{-1}$	rotations in shear plane, axis gets unstable, trilobe
$573s^{-1}$	early trilobe, rotations, two dimples + one notch, rotations and squeezings, stable rotations
$2005s^{-1}$	quadrulobe rotations, stable phase, squeezing, deformation, elongation, trilobe
$\dot{\gamma}$	<b>tilted orientation</b>
$57s^{-1}$	rotations, wobbling, precession around vorticity, wheeling cup with oval shape
$286s^{-1}$	precession, rolling, cup, squeezed in gradient direction, tank-treading
$573s^{-1}$	wheeling, tumbling, wobbling, quadrulobe cap, wheeling, rotation of squeezed cup or parachute-like, shape changes, parachute-like
$2005s^{-1}$	shrivelled quadrulobe rotating, stable phase, quadrulobe with shape changes, trilobe

Table 4.1: For four shear rates and two initial orientations, different shapes and dynamics appear which change with time. The description of shapes for each shear rate is in temporal order.

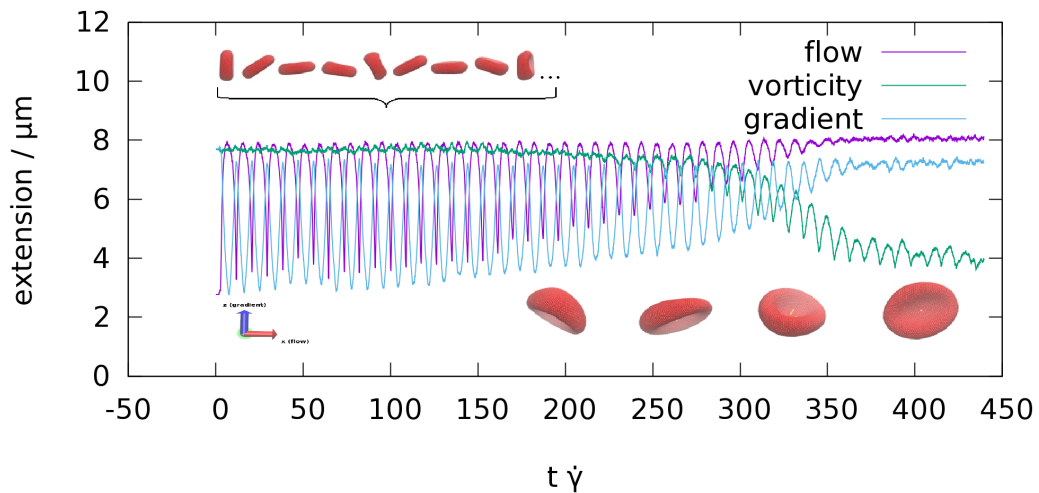


Figure 4.2: Extensions of a single cell in different directions at shear rate of  $57s^{-1}$ . The transition from tumbling to rolling is visible when the cell gets smaller in vorticity direction and the sizes in flow and gradient direction tend towards constant values.

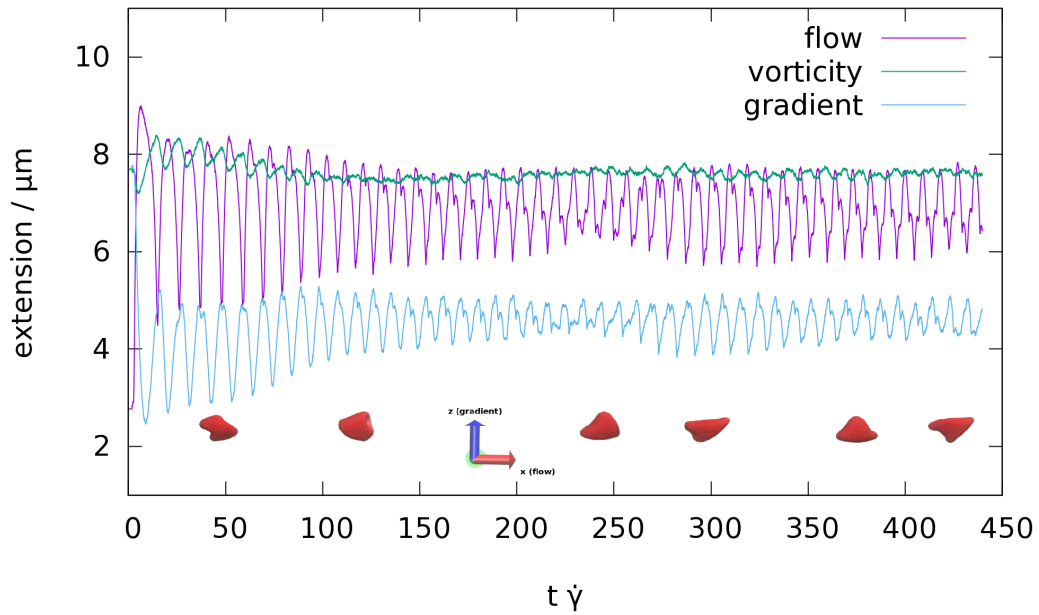


Figure 4.3: Extensions of a single cell in different directions at shear rate of  $573s^{-1}$ . Offsets and amplitudes differ among the directions.

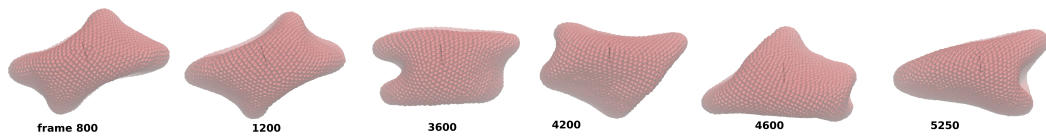


Figure 4.4: At high shear rates ( $2005s^{-1}$ ), a quadrulobe is found. With time, it may transform into a trilobe.

### Quantifying the Different Types of Motion

All simulations show a strong dependency of RBC shape and dynamics on shear rate. For example, the angle to flow direction shows these differences in figure 4.5. On top of that, the cells require a long time to acquire their final shapes/dynamics; for example the rolling motion at shear rate  $57s^{-1}$ , which does not set in until  $t\bar{\gamma} \approx 350$ . Then, the cells are oriented to both the flow and gradient direction with  $90^\circ$  and to the vorticity direction with  $180^\circ$ , which corresponds to  $0^\circ$  due to shape symmetry. Still, the cell oscillates about this orientation, which seems to be stable.

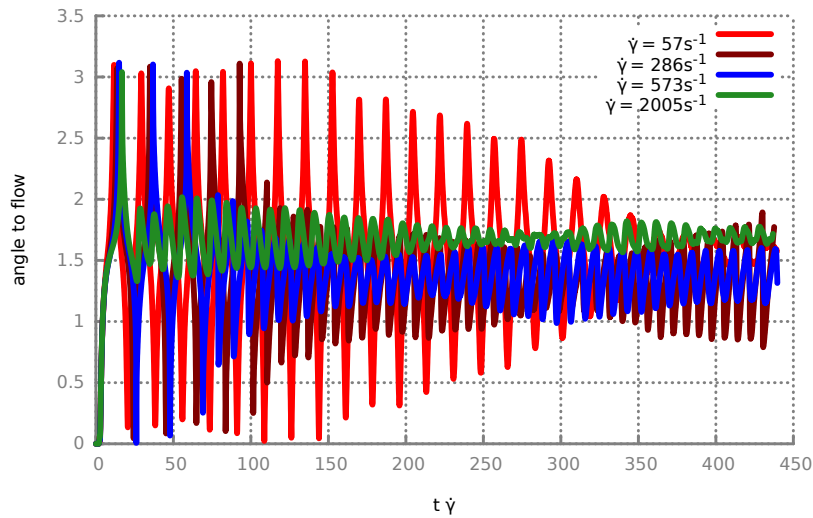


Figure 4.5: Orientation angle of initially upright cells.

In order to distinguish shape changes and membrane motion, we consider two different measures. Both describe the angle to the flow direction, but one comes from the gyration tensor and the other one comes from the connective vector of a tracer vertex and the centre of the cell. Often, both angles are synchronised in the beginning but tend to deviate later on. This can be considered a transition from tumbling to tank-treading-motion, such that the membrane motion gets decoupled from the shape motion.

Figure 4.6 contrasts both measures for a typical rolling cell. As soon as rolling in the shear plane is established, the shape hardly changes whereas the membrane performs  $2\pi$ -rotations. In figure 4.7, one can see that the shape change is first coupled to the membrane motion. After five full rotations of the cell, the deformations alter the shape (vertex distribution) such that the gyration tensor yields different orientations. Due to these deformations, the cell faces a smaller range of orientations and oscillates in a half rotation cycle. Thus, it attains the double frequency compared to the membrane motion.

For the quadrulobe at high shear rates  $\dot{\gamma} = 2005 s^{-1}$ , the curves (not shown) look similar to the trilobe case. Therefore, these measures are not very useful to distinguish trilobe and quadrulobe. Yet this method is suitable to identify rolling and to separate it from multilobe-shapes.

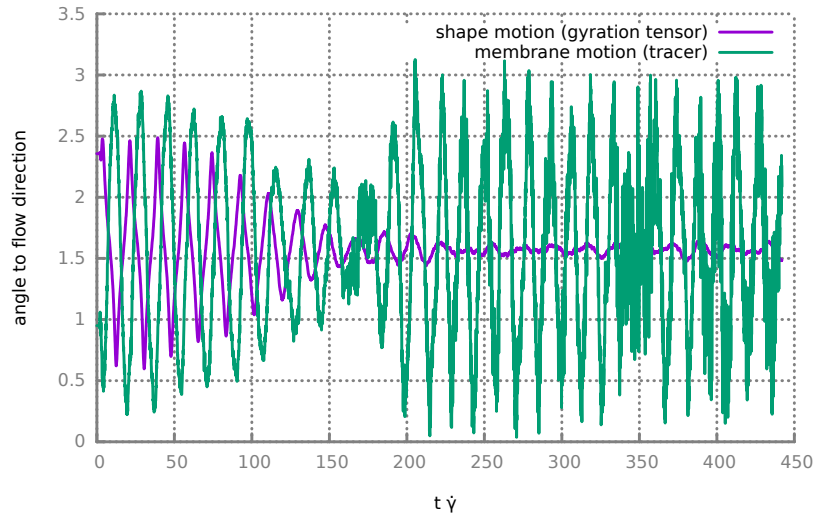


Figure 4.6: Membrane and shape motion of a typical rolling cell at shear rate of  $57s^{-1}$ . Dilute system, initially tilted cell.

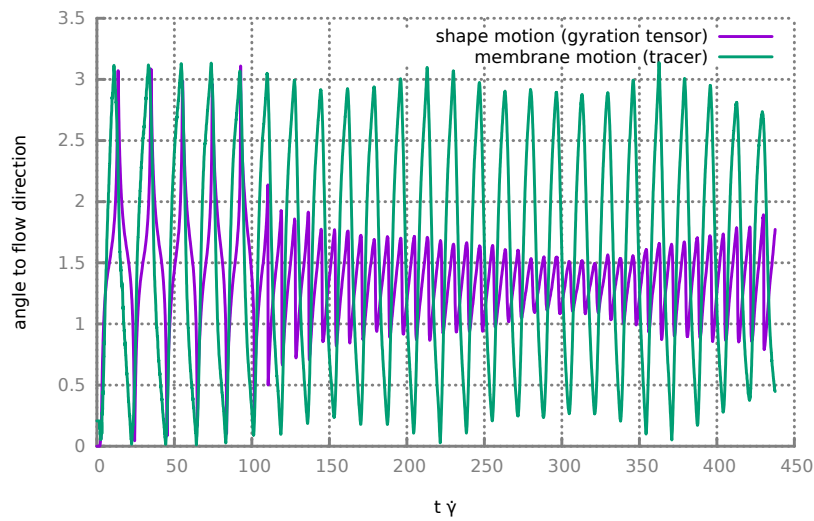


Figure 4.7: Membrane and shape motion of a typical trilobe at shear rate of  $286s^{-1}$ . Dilute system, initially upright cell.

### Dependence on Initial Orientation

As suggested in reference [32], here, the effect of the cell's axis of revolution initially being off-shear-plane is studied. For low ( $57s^{-1}$ ) and high ( $2005s^{-1}$ ) shear rates, two different initial angles do not cause essential differences. However, it is important to note that the cells need a long time to decorrelate from the initial orientation, see figure 4.8, where behaviour is dissimilar until  $t\bar{\gamma} \approx 350$ . Then, the angles of upright and tilted cell also agree separately in gradient and vorticity direction (not shown). This agreement is also reflected in the as-



phericity, shown in figure 4.9. In contrast, for intermediate shear rates as  $286s^{-1}$  and  $573s^{-1}$ , different initial orientations lead to different shapes and dynamics, see figure 4.10.

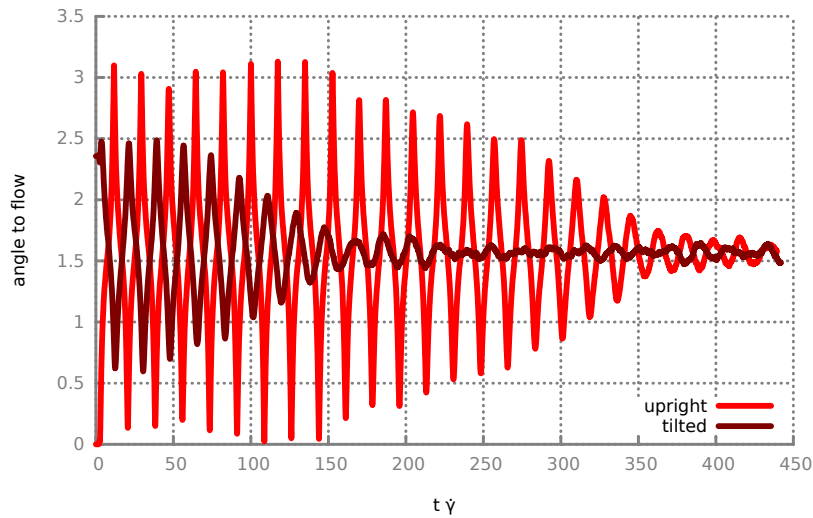


Figure 4.8: Orientation angle of cells at shear rate  $57s^{-1}$ ; different initial orientations.

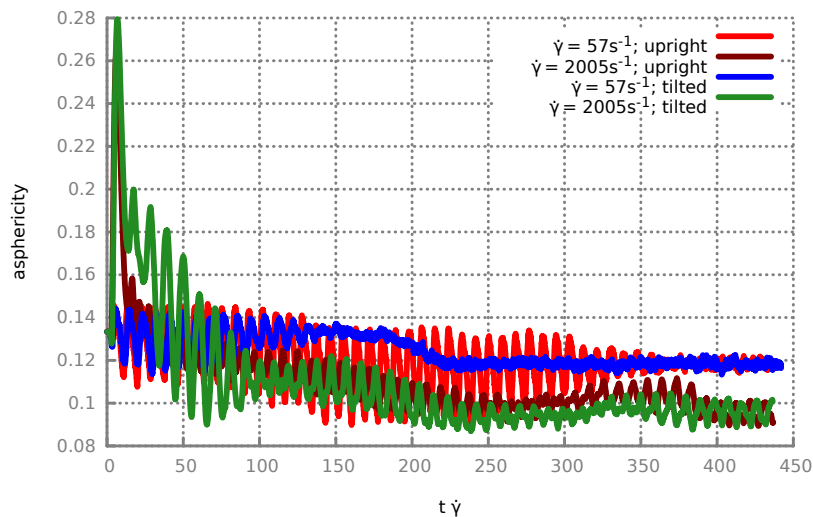


Figure 4.9: Asphericity of cells at shear rates  $57s^{-1}$  and  $2005s^{-1}$  for different initial orientations. The high shear rates agree and both exhibit quadrulobes transforming to trilobes. The low shear rates agree only at large times, when both have established the rolling motion. Still, these different shapes can be distinguished by the asphericity.

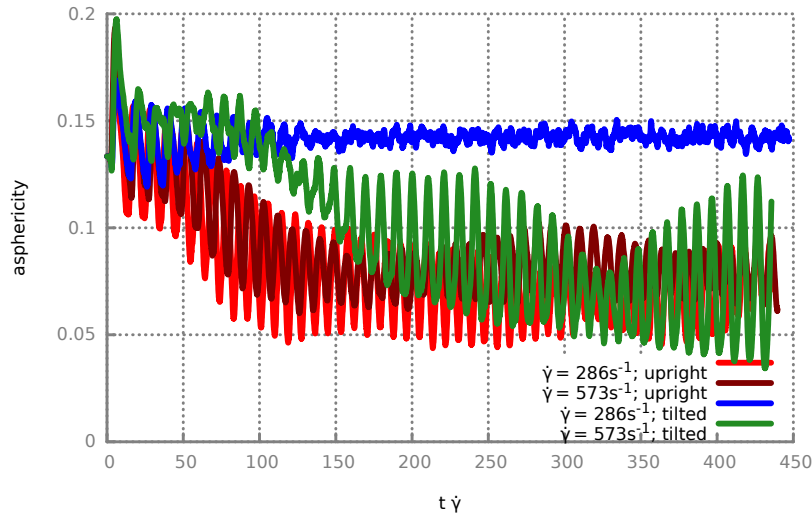


Figure 4.10: Asphericity of cells at shear rates  $286s^{-1}$  and  $573s^{-1}$  for different initial orientations. The tilted cell at  $\dot{\gamma} = 286s^{-1}$  is clearly distinguished from the upright cell at the same shear rate. Its value is higher (closer to the RBC's equilibrium) and shows less fluctuations. Thus, its rolling motion can be identified by the asphericity.

This orientation dependency agrees with the results in reference [182]. Wang et. al. find trajectories that change with initial orientation for  $G = \frac{\mu k a \hat{c} \eta_{out} \bar{\gamma} D_R / 2}{E \mu_0} = 0.004$  and  $G = 0.001$ , whereas for  $G = 0.01$ , their trajectories are rather similar (here, the shear modulus is  $\mu_0$ ). Our shear rates range is between  $G = 0.043$  and  $G = 1.5$ . Furthermore, the comparison is precarious due to a different viscosity contrast (unity) and the fact that Wang et. al. use a capsule and not a RBC.

In fact, we had expected that the thermal fluctuations present in our (S)DPD simulations would average out the effects of initial orientations. Yet, this does not seem to be the case for all shear rates, at least not within the simulation time scale considered here. Thus, this system may possess multiple quasistable states.

### Effect of Membrane Viscosity

In our RBC model, membrane viscosity is not incorporated. Thus, differences to experiments can arise. The group of M. Abkarian indicated a slightly different aspect ratio under shear flow in experiments. *In vitro*, the cell is extended less in flow direction, in favour of the extension in the vorticity direction.

To check possible impacts of the membrane viscosity, we used a cell with higher internal viscosity (contrast 10) as an effective membrane viscosity. Bending displacements of a membrane always induce the motion of adjacent layers of fluids, namely, intracellular haemoglobin solution and suspension medium [91]. Thus, the energy dissipation in the course of bending deformations of erythrocytes is affected by the viscosities of its cytoplasm and the medium.

From the trajectories, it is clear that the cell with higher viscosity contrast (VC) needs a higher shear rate to become a trilobe. For a shear rate of  $\dot{\gamma} = 2005s^{-1}$ , both cells have similar

shapes. The results in figures 4.11 and 4.12 show that the cell with higher internal viscosity gets more elongated in vorticity, but less elongated in flow direction, compared to the VC5-case. This agrees with the experiments. Thus, higher internal viscosity makes certain cell behaviour more realistic and is a good candidate to model the effects of membrane viscosity.

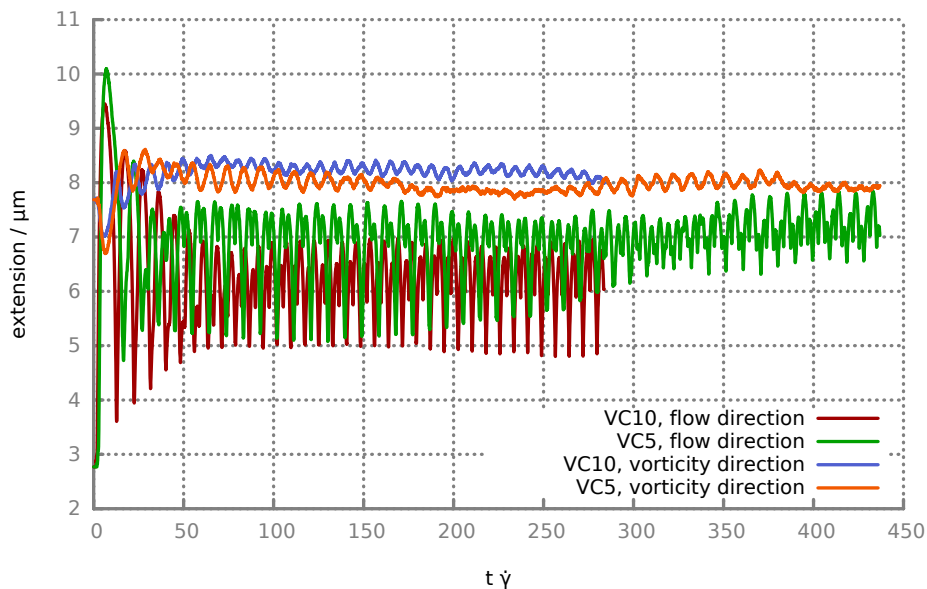


Figure 4.11: Extensions of cells with different internal viscosity. VC is the viscosity contrast of inner and outer fluids.  $\dot{\gamma} = 2005\text{s}^{-1}$ .

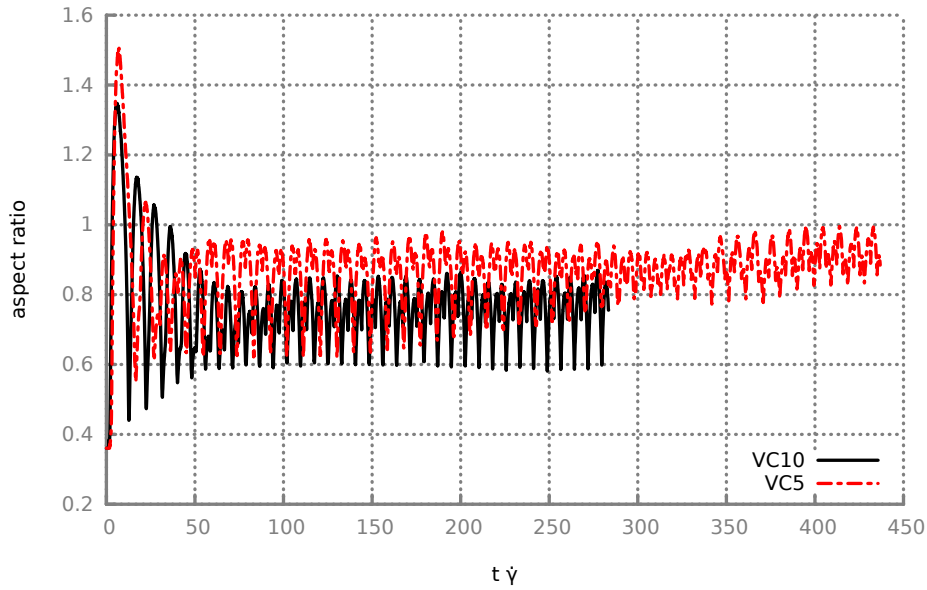


Figure 4.12: Aspect ratios of cells with different internal viscosity. The aspect ratio is the ratio of the extension in flow and the extension in vorticity direction. VC is the viscosity contrast of inner and outer fluids.  $\dot{\gamma} = 2005s^{-1}$ .

### 4.3.2 Multiple Cells in Shear Flow using Lees-Edwards Boundary Conditions

#### Distribution of Shape Parameters

We consider the cells' extension in gradient, flow and vorticity directions, the eigenvalues of the gyration tensor and corresponding acylindricities. Their distribution is obtained by both temporal and ensemble averaging. In figure 4.13, one can identify different ranges for the eigenvalues. Furthermore, smaller eigenvalues show sharper distributions, which is advantageous here, as we mostly need the smallest eigenvalue to quantify the cell's orientation. Figure 4.14 shows that the smallest eigenvalue is larger and its distribution is broader for shear rates  $30s^{-1}$  and  $100s^{-1}$  and gets smaller and sharper for shear rates from  $500s^{-1}$  to  $2000s^{-1}$ .

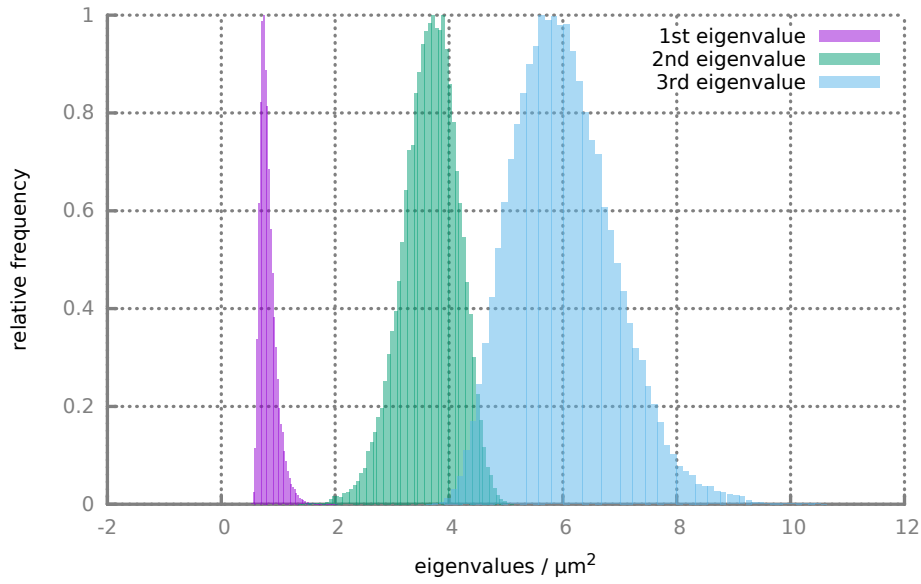


Figure 4.13: Histogram of the gyration tensor's eigenvalues.  $\dot{\gamma} = 1000s^{-1}$ .

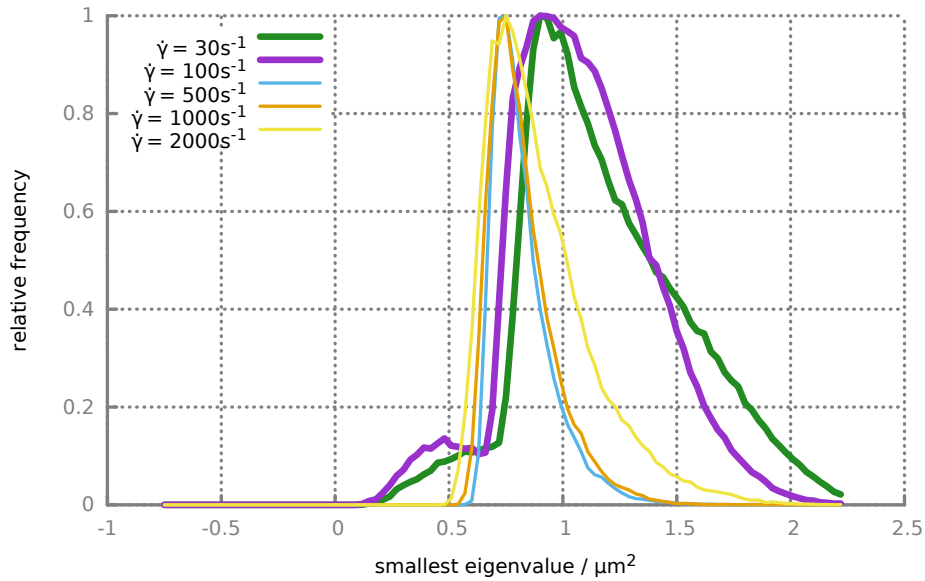


Figure 4.14: Histogram of the gyration tensor's smallest eigenvalue at different shear rates.

For a shear rate of  $1000s^{-1}$ , figure 4.15 shows that the cell is rather flat (or lying) in gradient direction, where different layers of cells are driven over each other; the cells are compressed in vorticity direction and elongated in flow direction (the equilibrium value of  $8\mu m$  lying between the two peaks). This corroborates the visual assessment.

Figure 4.16 shows, for low shear rates  $30s^{-1}$  and  $100s^{-1}$ , a size of about  $8\mu m$ , which is close to the equilibrium value, and a rather narrow distribution. For high shear rates from  $500s^{-1}$

to  $2000s^{-1}$ , the cells are extended to about on average  $9\mu m$  and their distribution gets larger. This means that beyond a critical shear energy, the cells deform more strongly both through compression and extension.

Figure 4.17 shows the acylindricity calculated using equation (4.3). The acylindricity  $C_1$  corresponds to the plane that is orthogonal to the first (thus smallest) eigenvalue's eigenvector. It has both the lowest value and broadest distribution. This confirms that the smallest eigenvalue corresponds to the orientation of the flat side of a RBC, which is most cylindrical, thus has lowest acylindricity. The other two acylindricities resemble each other in value and width and thus, reflect the cell's symmetry in the directions orthogonal to the direction with smallest eigenvalue.

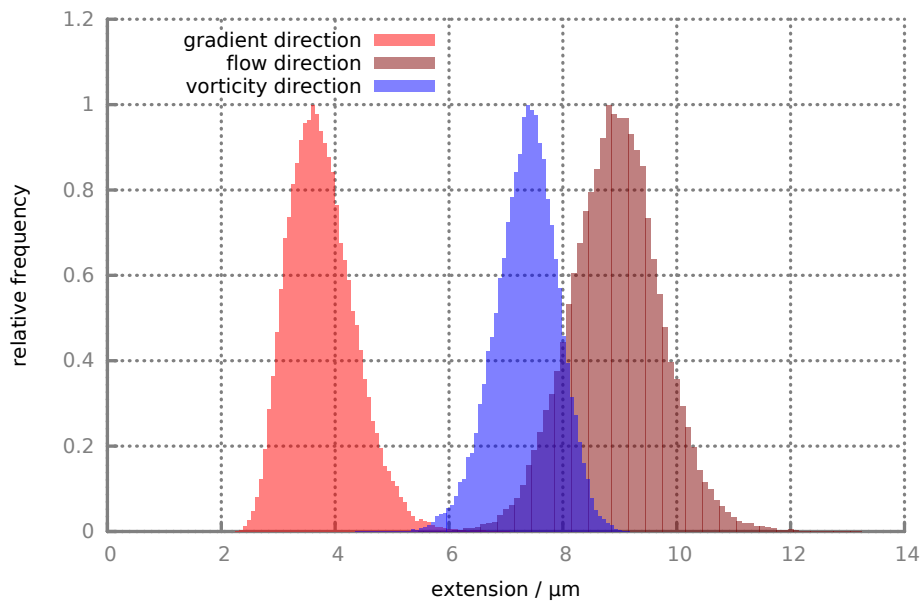


Figure 4.15: Histogram of the cell extensions in different directions.  $\dot{\gamma} = 1000s^{-1}$ .

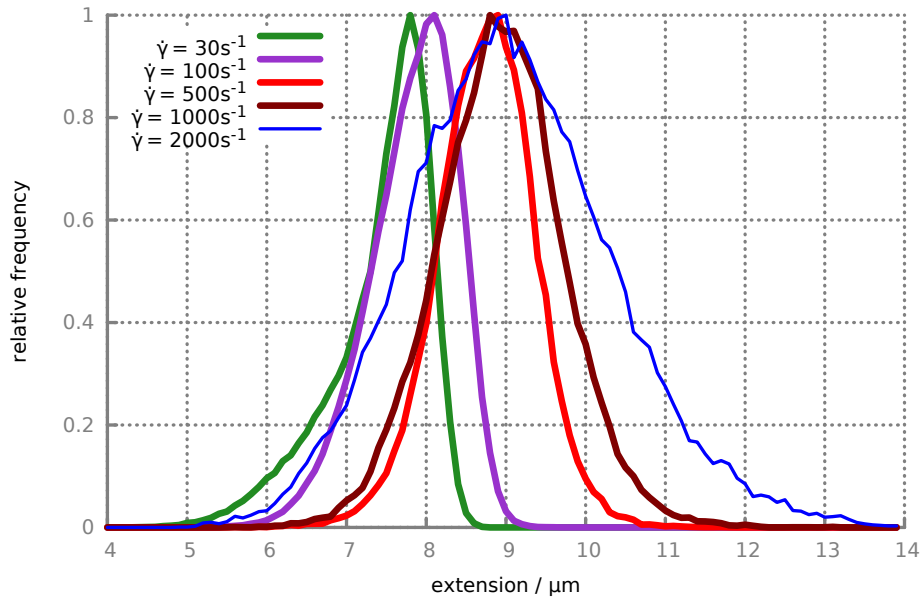


Figure 4.16: Histogram of the cell extension in flow direction for different shear rates.

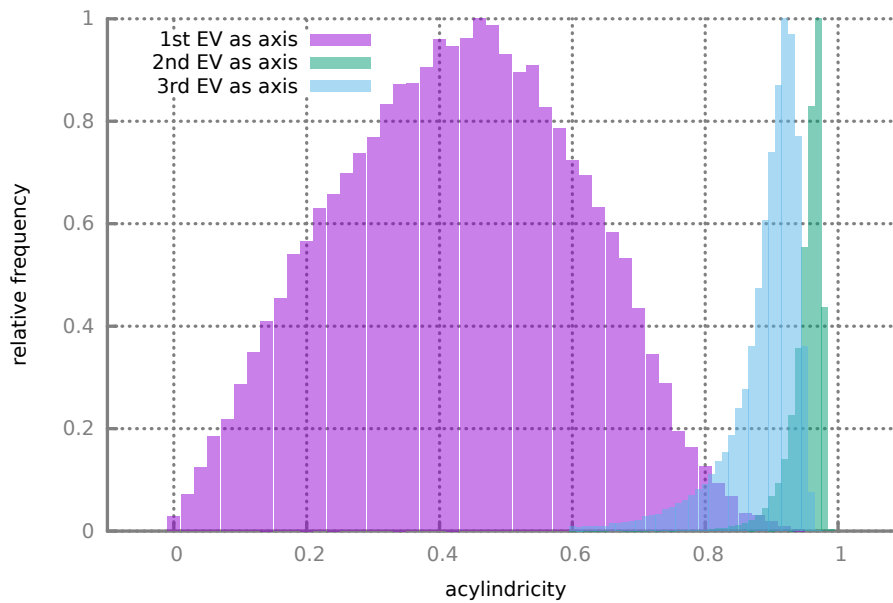


Figure 4.17: Histogram of the cell acylindricity corresponding to different cell axes.  $\dot{\gamma} = 1000s^{-1}$ .

### Comparison in Terms of Shear Rate and Haematocrit

The performed analysis is two-fold: first, as an ensemble average of cells, second, considering a few representative cells (randomly picked). In each time step, only bulk cells are analysed. Bulk cells are those cells that are not divided by periodic boundary conditions,

which act in the gradient direction. Thus, the ensemble average comprises about 60-70 (and not all 128) cells in each time step.

The cells' orientation is obvious from visualisation and confirmed by the angle statistics, see figures 4.18, 4.19, 4.20 and 4.21. The separation (two peaks) in figures 4.20, 4.21 arises from the calculation method: after a slight deformation, the cell can be interpreted as facing the opposite direction. Thus, values differing by  $\approx 180^\circ$  actually mean a similar orientation. Figure 4.21 shows a less pronounced orientation for shear rate  $57s^{-1}$ , reflecting the different stages of motion before, eventually, rolling takes place. For the simulations with physiological systemic haematocrit, throughout the five different shear rates, the average cell is predominantly aligned with its flat side parallel to the layers of constant flow velocity.

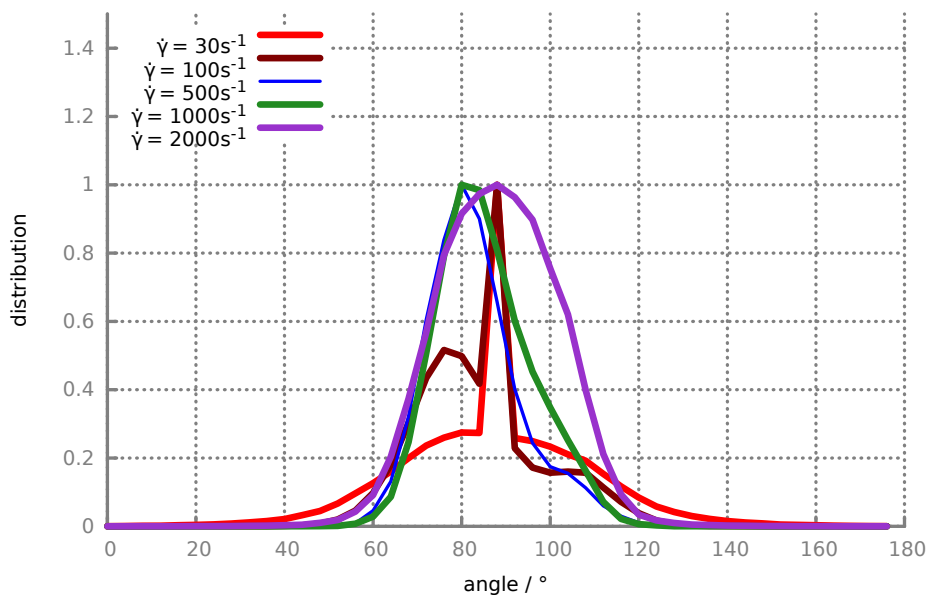


Figure 4.18: Histogram of the average cell's angle to the flow direction (ensemble average of Lees-Edwards simulation,  $H=45\%$ ).



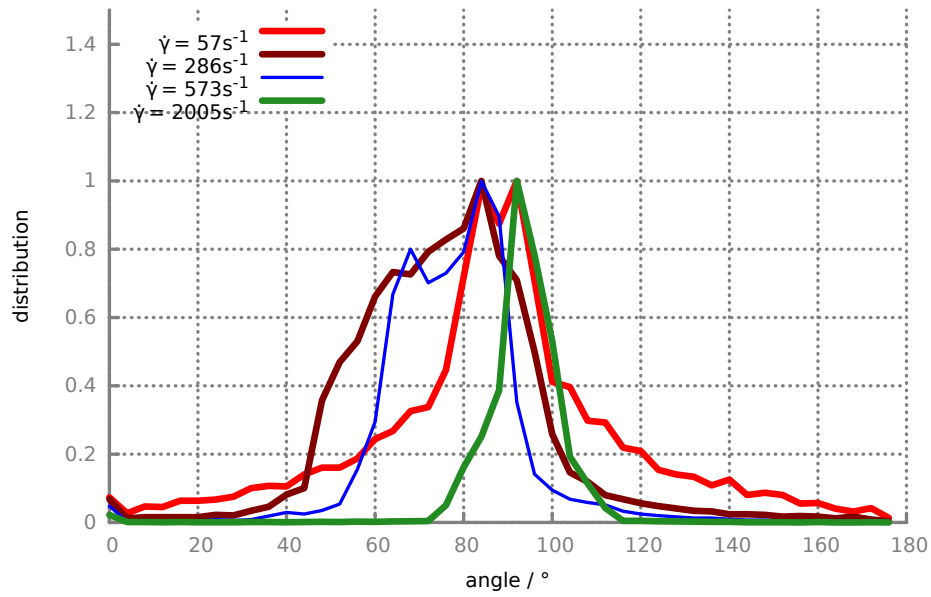


Figure 4.19: Histogram of the single cell's angle to the flow direction (Couette flow with walls).

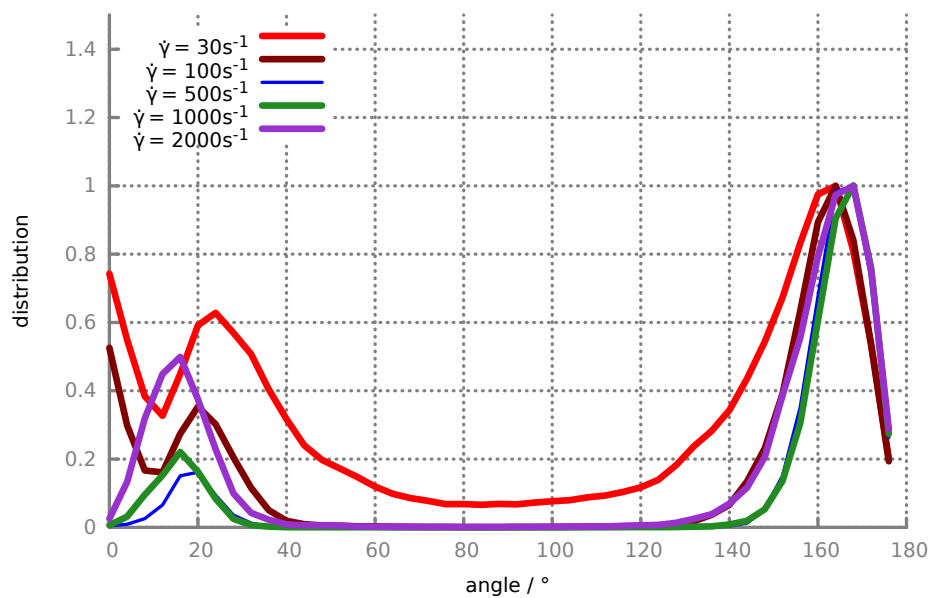


Figure 4.20: Histogram of the average cell's angle to the gradient direction (ensemble average of Lees-Edwards simulation,  $H=45\%$ ).

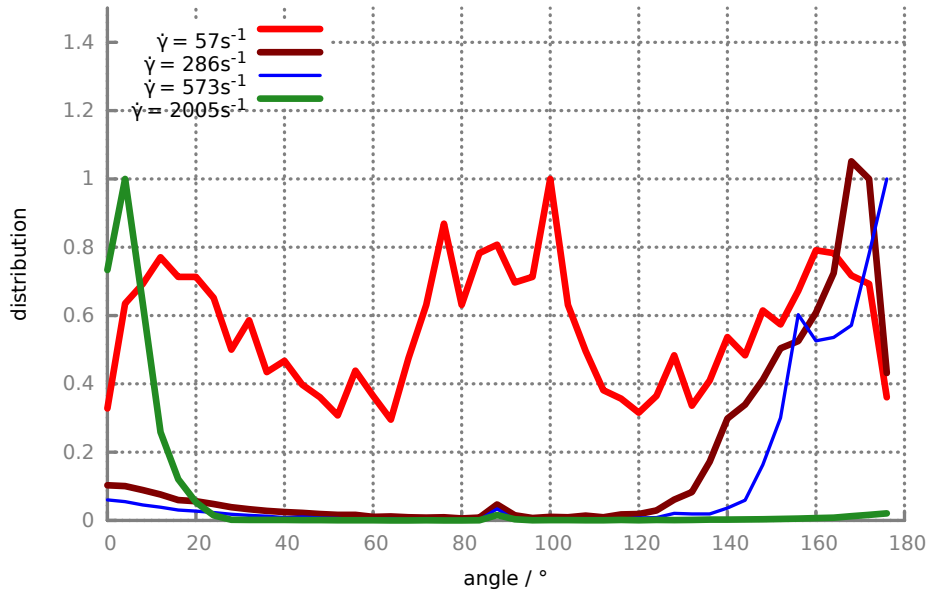


Figure 4.21: Histogram of the single cell's angle to the gradient direction (Couette flow with walls). All cells are initially in upright position.

In figure 4.22, we compare the shape changes of cells at different shear rates. We choose the shear rates  $286s^{-1}$  and  $573s^{-1}$  with upright initial orientation (taken from the dilute setup) for comparison as they show trilobes. Thus, we have a reference to identify possible trilobe properties in the dense simulation. Both setups deviate from the equilibrium value, which is 0.133 here. The crowded cells get more aspherical, while the single cell gets more spherical. After increasing the shear rate, the cells get more elongated, thus less spherical. The crowded system shows higher asphericity and shape changes that are more irregular compared to the dilute case.

In figure 4.23, the shape of a single cell is compared to the shape of crowded cells. Therefore, we consider the asphericity of a single cell, of some exemplary cells from the dense system, and its ensemble average value. It is apparent that the cells of the dense system are more aspherical and show more severe and more irregular shape changes in comparison to the single cell.

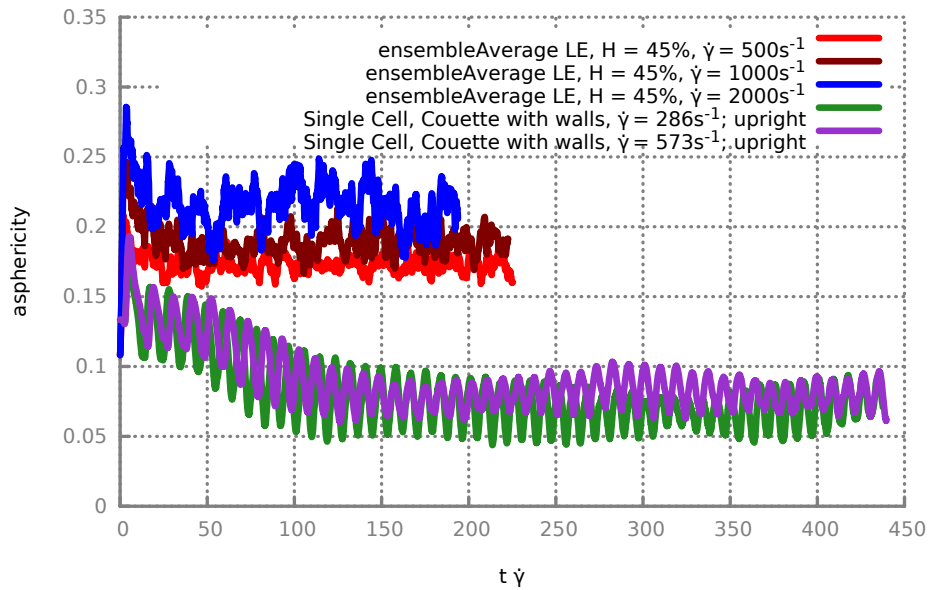


Figure 4.22: Asphericity of cells at different shear rates for crowded and single cell cases.

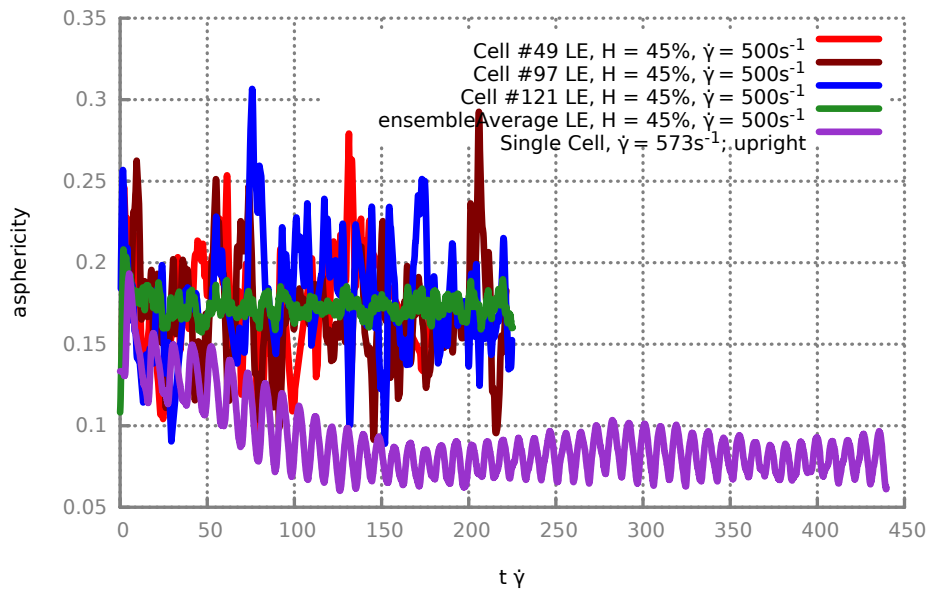


Figure 4.23: Asphericity of cells at comparable shear rates  $\approx 500s^{-1}$  for different haematocrit.

### Shear Stress and Whole Blood Viscosity

In each simulation, virial functions are used to calculate the stress. For each potential, such as DPD interaction between membrane and fluid or bond potential of the vertices, the virial provides a contribution to total stress. The stress is calculated as a symmetric  $3 \times 3$  matrix  $\tau$ . The most interesting entry is  $\tau_{xy}$  as it corresponds to the shear stress.

Dividing  $\tau_{xy}$  by the dimensional shear rate  $\frac{\Delta v_y}{\Delta L_x}$ , we obtain the viscosity of whole blood. Normalised to the solvent's viscosity, it has the values shown in table 4.2.  $\frac{\eta}{\eta_0}$  shows shear-thinning. The viscosity values agree with experiments by the group of M. Abkarian (University of Montpellier, unpublished work). From the percental contributions of the different potentials, one can see that with increasing shear rate, the bulk solvent (SDPD) and the solvent/membrane coupling (DPD) gain importance. Meanwhile, membrane potentials contribute less and less with increasing shear rate.

### Medium Haematocrit

In microcirculation, the haematocrit is lower than in arteries or veins. Thereby, we have performed simulations at  $H = 20\%$  and  $H = 30\%$ . The results for stress contributions and overall viscosity are shown in table 4.2.

	$\dot{\gamma} (s^{-1})$	$\frac{\eta}{\eta_0}$	kinetic	SDPD	DPD	LJ/cut	bonds	angles	dih
(a)	30	5.71	-0.05	41.71	0	0	58.89	-2.11	1.57
	100	4.16	-0.05	56.37	0	0	39.89	1.94	1.85
	500	2.85	-0.01	62.36	13.81	0.01	18.55	4.77	0.52
	1000	2.6	0.01	65.99	15.78	0.01	13.71	4.16	0.36
	2000	2.4	0.04	66.49	17.30	0.01	12.32	3.62	0.22
(b)	$\dot{\gamma} (s^{-1})$	$\frac{\eta}{\eta_0}$	kinetic	SDPD	DPD	LJ/cut	bonds	angles	dih
	500	1.7	-0.03	84.90	0.0	0.0	12.86	1.66	0.59
	1000	1.57	-0.01	89.28	0.0	0.0	8.77	1.64	0.32
	2000	1.47	0.02	92.75	0.00	0.00	5.74	1.31	0.17
(c)	$\dot{\gamma} (s^{-1})$	$\frac{\eta}{\eta_0}$	kinetic	SDPD	DPD	LJ/cut	bonds	angles	dih
	500	2.20	-0.01	80.70	0.00	0.00	15.76	2.85	0.70
	1000	2.00	0.01	85.97	0.00	0.00	10.88	2.75	0.39
	2000	1.86	0.05	88.98	0.00	0.00	8.32	2.42	0.22

Table 4.2: For different shear rates, the relative viscosity of whole blood and percental contributions of different potentials to the total stress in the shear plane are shown. LJ means Lennard-Jones-interaction (among membrane vertices). Bond-, angle-, and dihedral-stress contributions are also shown. (a) Haematocrit  $H = 45\%$ . (b) Haematocrit  $H = 20\%$ . (c) Haematocrit  $H = 30\%$ .

Relative viscosity and stress distribution are similar to the case of  $H = 45\%$  described in section 4.3.2. Figure 4.24 gathers these results. The data confirm the expectations: there is shear thinning, and higher haematocrit leads to a higher viscosity.

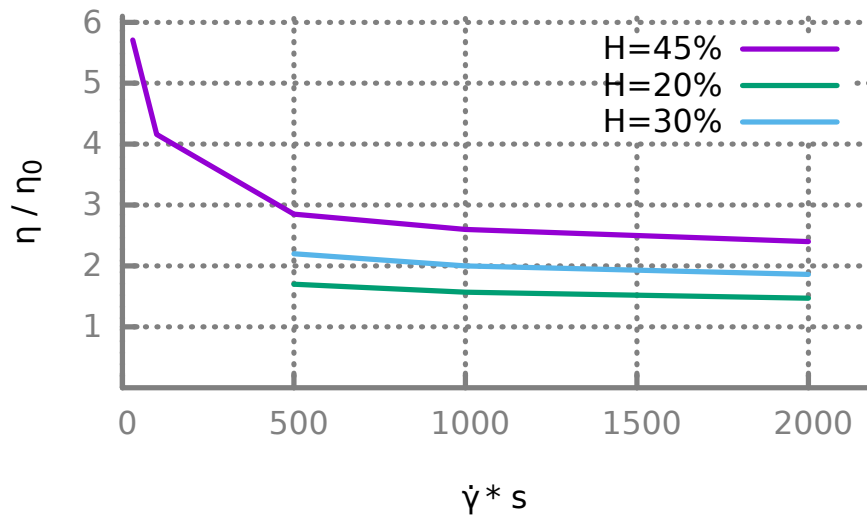


Figure 4.24: Shear thinning of RBC suspension at different haematocrits.

Figure 4.25 shows the cell's extension in flow direction for different values of  $H$  and  $\dot{\gamma} = 2000s^{-1}$ . The cell size increases with  $H$ .  $\dot{\gamma}$  does not seem to have a significant effect on the cell size, when considering the same graphs for  $\dot{\gamma} = 500s^{-1}$  and  $\dot{\gamma} = 1000s^{-1}$  (not shown). For the extension in gradient direction (figure 4.26) however, the dependencies on  $H$  and  $\dot{\gamma}$  are not clear. For the sake of completeness, we also add the extension in the vorticity direction in figure 4.27. Again, the dependencies on  $H$  and  $\dot{\gamma}$  are not clear.

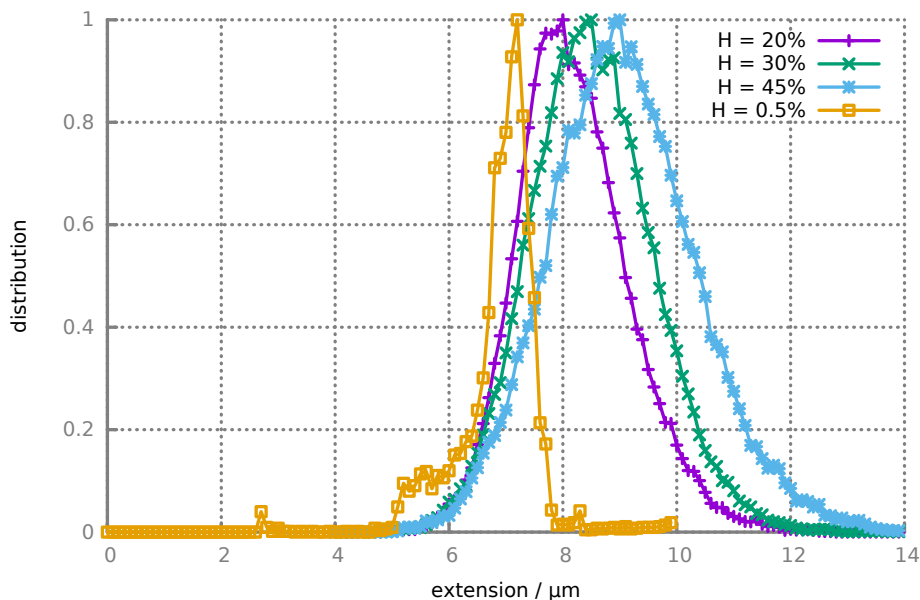


Figure 4.25: Extension of the cell in flow direction at a shear rate  $\dot{\gamma} = 2000s^{-1}$ . Histograms for different haematocrits.

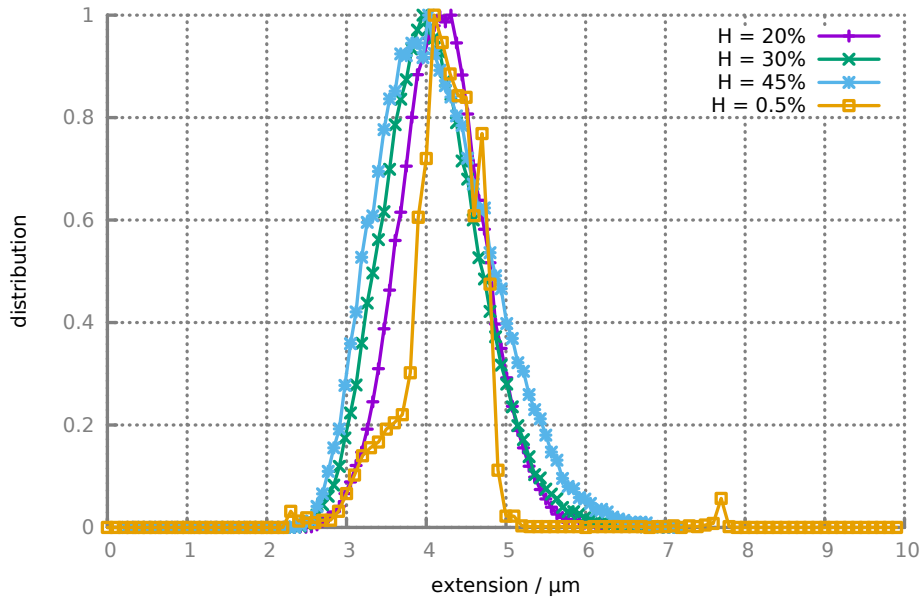


Figure 4.26: Extension of the cell in gradient direction at a shear rate  $\dot{\gamma} = 2000\text{s}^{-1}$ . Histograms for different haematocrits.

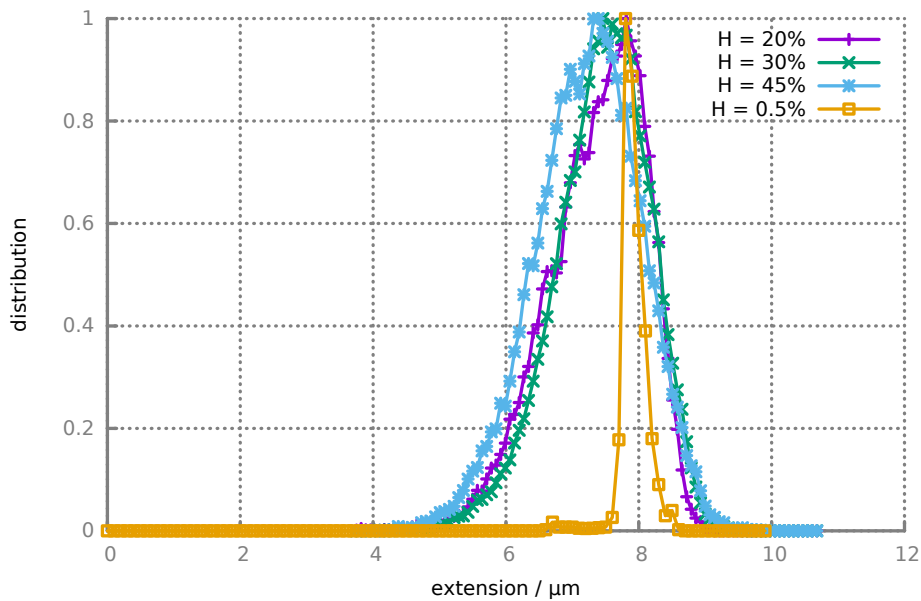


Figure 4.27: Extension of the cell in vorticity direction at a shear rate  $\dot{\gamma} = 2000\text{s}^{-1}$ . Histograms for different haematocrits.

In order to have a better overview when looking at both different shear rates *and* haematocrits, we plot only the mean values obtained from the histograms in figures 4.28, 4.29, and 4.30. We also include the values for the single cell ( $H \approx 0.5\%$ ).

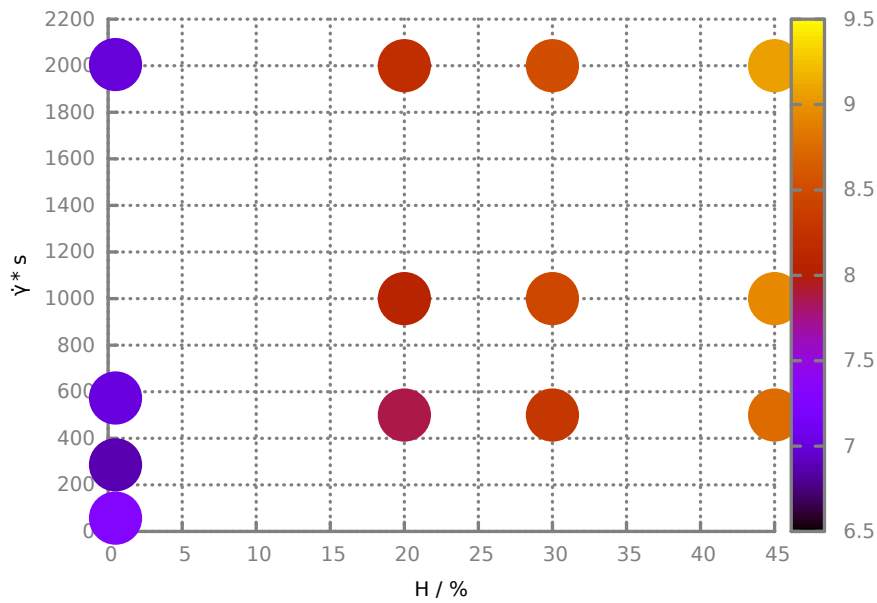


Figure 4.28: Extension of the cell in flow direction at different haematocrits and shear rates. For higher haematocrit, the cells get more stretched. Shear rate is less influential.

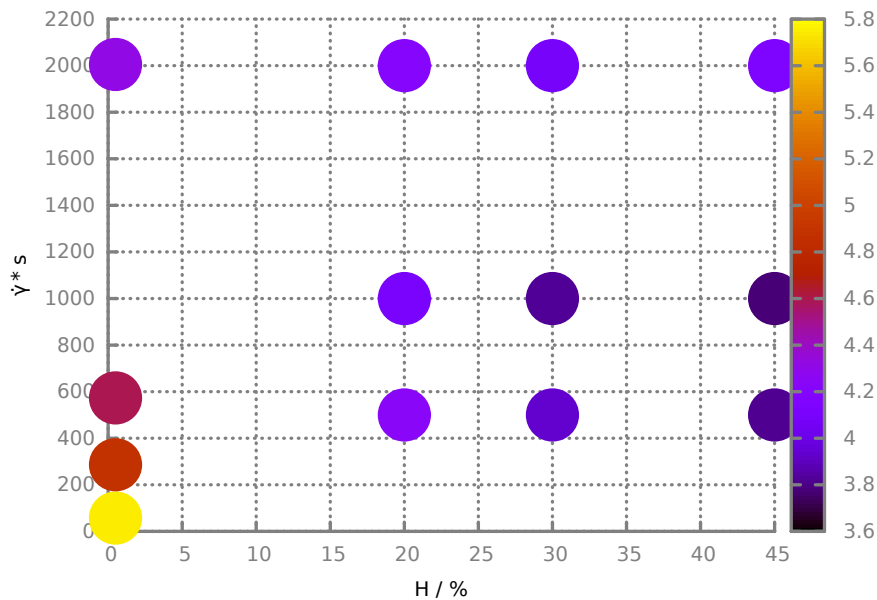


Figure 4.29: Extension of the cell in gradient direction at different haematocrits and shear rates. High stretching is only possible for dilute systems and low shear rates.

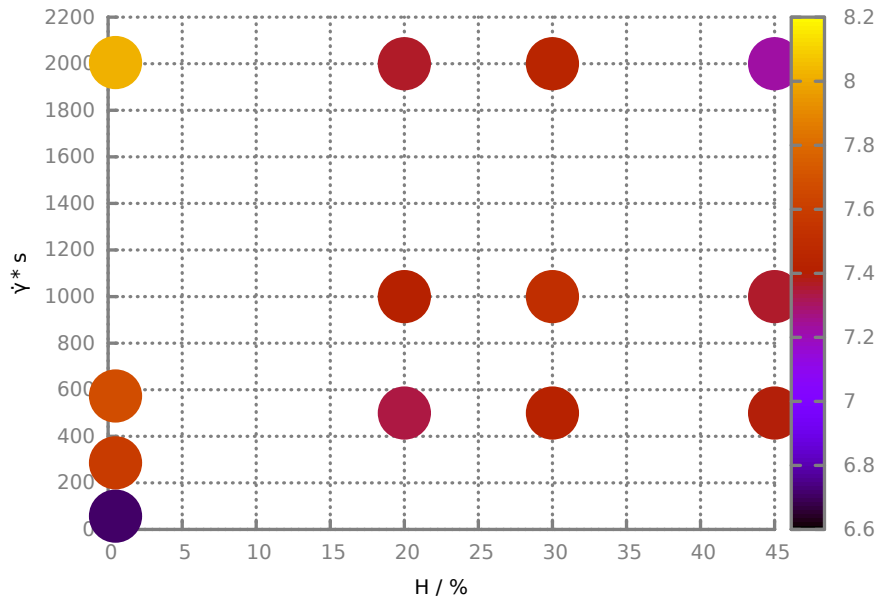


Figure 4.30: Extension of the cell in vorticity direction at different haematocrits and shear rates. High stretching is only possible for dilute systems and high shear rates.

## 4.4 Conclusion

The simulations of a RBC in simple shear flow agree well with the experiments when the sequence of shapes and dynamics is compared. For increasing shear rate, cup shapes, trilobes and quadrulobes are found.

The initial orientation might affect the cell behaviour. However, it is possible that after a sufficient simulation time, this influence will disappear. We could not definitely answer this question due to computational limitations. We have found that two cells with different initial orientation show the same rolling motion after almost the whole simulation time. This indicates that other shapes and motions can be also transient as well.

We have found essential differences for the shapes of RBCs at different haematocrits. First, single cells are more spherical than cells in a more concentrated solution. Second, the higher the haematocrit, the more the cells are stretched in flow direction. For both low haematocrit and low shear rates, cells experience only small forces between the walls and thus, can extend in gradient direction. For both low haematocrit and high shear rates, cells are stretched in vorticity direction.

The suspension's viscosity depends on both haematocrit and shear rate. With a higher cell concentration, the fraction of more viscous fluid is higher. However, the effective viscosity of the suspension is not simply the superposition of the viscosity of its components. Deformation and mutual interaction also affect the effective viscosity. In the past, tank-treading was identified as a cause for the shear-thinning of blood. Tank-treading has been studied for a range of shear rates ( $0-1000 \text{ s}^{-1}$ ) [48]. Noteworthy, their surrounding medium had a viscosity about 10 to 60 times larger than that of water, a condition that promotes tank-treading of RBCs. If the viscosity contrast  $\lambda$  is larger than one (see section 2.4), tank-treading is suppressed. Here, we set  $\lambda = 5$  and find trilobes. We associate the formation of trilobes with the



lower suspension viscosity.

In addition to the viscosity contrast, also membrane viscosity is essential. Certain effects of membrane viscosity, such as elongation in flow, can be modelled by a higher internal fluid viscosity. We have tested different measures, such as the asphericity or the distribution of orientation angles, for suitability to describe and distinguish these effects.



## Chapter 5

# Dynamics of a RBC in Tube Flow

### 5.1 Introduction

The dynamics of RBCs subject to external flow and geometrical confinement is relevant for fundamental research and biomedical applications (e.g drug delivery [120]). To study the fluid-mechanical behaviour of RBCs, we consider the flow of a single RBC in a microtube with a size similar to microvessels.

The ambient solvent is driven by a pressure gradient creating a Poiseuille flow, which serves as a minimalistic model for the passage of blood through microvessels. The present study differs from the *in vivo* situation in the following aspects: idealised flow and vessel geometry; dilute suspension (single cell) and no membrane viscosity. Despite these limitations, we can investigate the basic dynamics of a cell and its reaction to external flow conditions and confinement.

This study is motivated by our previous simulations [46], where the viscosity ratio between the RBC cytosol and suspending media was equal to one. Now, a realistic viscosity ratio of five is employed and its effect on the dynamics, shapes, and transition between various types of motion is investigated.

A RBC shows different shapes and dynamic states, depending on conditions such as flow, confinement, physiological/pathological state and cell age [105]. Classical motions from simple shear flow are tumbling and tank-treading (TT) [48, 54]. More recent discoveries illustrate e.g. swinging or vacillating-breathing dynamics [191]. This sensitivity towards physiological conditions offers diagnostic prospects. One could potentially infer the health status from cell shapes or draw conclusions from the whole-blood viscosity, which depends on the shapes and dynamics of its constituents.

Here, we emphasise the effects of shear rate and confinement. We provide phase diagrams with the different cell shapes. Simulations for different shear rates and confinements lead to phase diagrams of shapes and dynamics differing from the previously predicted diagrams [46]. We can identify two dominant shapes: parachutes (symmetric to flow profile) and slippers (asymmetric to flow profile). In agreement with the previous studies, the parachute shape of RBCs occurs at strong confinements and high shear rates, whereas at weak confinements, an unstable slipper shape occurs. The slipper may experience strong deformations depending on the shear rate. The slippers all rotate and deform continuously, and can be subdivided into two types: one with rather tumbling motion and the other one with rather tank-treading motion. Additionally, there are snaking cells at low shear rates.

The question of the stability of slippers has been raised in many works [125, 84, 2, 82, 168, 46]. Here, all slippers are unstable and their motion could be called as stationary rotation-deformation. We will discuss the importance of the viscosity contrast on the flow resistance, and the effect of different stress-free shapes of the RBC [134, 26] on its dynamics in flow.

## 5.2 Models & Methods

### 5.2.1 Numerical interaction model

Here, we employ the same methods as described in section 4.2.1.

### 5.2.2 Simulated Scenario

We simulate the flow of a single cell suspended in a viscous liquid inside a cylindrical, hollow tube of length  $50 \mu\text{m}$ , see figure 5.1. Its axis is aligned with the x-direction. The tube diameter  $D = 2R$  determines the confinement  $\chi = \frac{D_c}{D}$ . The external fluid mimics the blood plasma, the internal fluid mimics the cytosol. The basic length scale is one micrometre, in contrast to reference [46]. A pressure drop  $\Delta P$  is achieved in the tube by applying a force  $f$  on each fluid particle. The pressure gradient equals the force per volume:  $\frac{\Delta P}{L} = f n$ ,  $n$  being the density. The constant pressure drop in the cylindrical tube causes a Poiseuille flow, characterised by the velocity profile:

$$\vec{v}(\vec{r}) = \frac{1}{4\eta} \frac{\Delta P}{L} (R^2 - r^2) \hat{e}_x \quad (5.1)$$

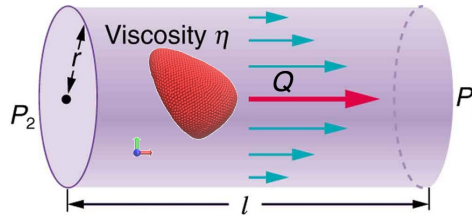


Figure 5.1: Tube flow with Poiseuille velocity profile  $\vec{v}(\vec{r}) = \frac{1}{4\eta} \frac{\Delta P}{L} (R^2 - r^2) \hat{e}_x$ . <http://cnx.org/contents/031da8d3-b525-429c-80cf-6c8ed997733a@8.8:89>

The mean velocity is half of the centre (maximum) velocity:  $U = \frac{u_c}{2}$ . The pressure drop is linked to the flow rate  $Q$  as:  $\Delta P = \frac{128\eta L Q}{\pi D^4}$ , while the flow rate  $Q$  is linked to the mean velocity as:  $Q = \frac{\pi}{4} D^2 U$  [1].

In general, vessel bifurcations or upstream curvature disturb the parabolic profile [1]. The distance required to return to the fully developed parabola is the entrance or inlet length  $L$  [186]:

$$\frac{L}{D} \approx 0.08 Re + 0.7. \quad (5.2)$$

In the simulations performed here, periodic boundary conditions are employed. Thereby, the flow is everywhere parabolic, if the impact of the RBC is neglected.

### 5.2.3 Simulation Parameters and Scaling Equations

The density is set to  $n = 12$  to provide a resolution sufficient to model large flow rates, which cause strong membrane deformations. The temperature is set to  $k_B T^M = 0.2$ . The masses for external fluid and wall particles are  $m = 1$ , for internal fluid particles  $m = 2$  and for membrane vertices  $m = 3$ . To compare with other studies, we set these dimensionless quantities:

1. The Reynolds number  $Re = \frac{n\bar{\gamma}D_r^2}{\eta}$  defines the ratio of inertial to friction forces.  $n$  is the density,  $\bar{\gamma}$  is the dimensional shear rate and  $\eta$  is the external fluid's viscosity.  $Re \leq 0.3$  throughout this work.
2.  $\lambda = \frac{\eta_i}{\eta_o}$  denotes the viscosity contrast between cytosol and external plasma.  $\lambda = 5$  in the reference system.
3.  $\dot{\gamma}^* = \bar{\gamma} \cdot \tau$  is the dimensionless shear rate.  $\tau$  is the RBC's relaxation time given by  $\tau = \frac{\eta D_r^3}{\kappa_r}$ .  $\dot{\gamma}^*$  is also the ratio of shear and bending energies. It is varied to study its effect on shapes and dynamics of RBCs.

Via the Hagen-Poiseuille solution, these three quantities determine the following quantities:

- $\eta_o = \sqrt{\frac{\dot{\gamma}^* n \kappa_r}{D_r Re}}$  is the external viscosity
- $\eta_i = \lambda \eta_o$  is the internal viscosity
- $f = \frac{32 \kappa_r \dot{\gamma}^*}{D_r^3 D n}$  is the pressure force, representing the pressure gradient within the tube. This force is applied to each fluid particle.
- $\bar{\gamma} = \sqrt{\frac{\dot{\gamma}^* Re \kappa_r}{D_r^3 n}}$  is the dimensional shear rate, used here to normalise time. Counterintuitively, it does not depend linearly on the dimensionless shear rate  $\dot{\gamma}^*$ . The reason is the scaling of  $\eta$  to comply with a certain  $\dot{\gamma}^*$  and  $Re$ .

Noteworthy, varying  $\dot{\gamma}^*$  to study different phases affects all these quantities. However, the viscosity only sets the timescale and the important physical quantity is the shear *stress*, which is given by

$$\eta \bar{\gamma} = \frac{\dot{\gamma}^* \kappa_r}{D_r^3} \quad (5.3)$$

### 5.2.4 Red Blood Cell Model

The RBC is modelled as an impenetrable membrane enclosing an inner fluid. We use bounce-back reflections to reflect fluid particles on the membrane, both from inside and outside [40]. The membrane is modelled as a triangulated network of springs, featuring stretching, bending and compression resistance. The membrane is made up of  $N = 3000$  vertices. Governing potentials, numerical implementation and parameter values are identical to those in reference [46], except where noted.

### 5.2.5 Vessel Model

Blood vessels consist of vascular smooth muscle cells, elastin and collagen fibers. Thus, they exhibit a variety of mechanical and rheological properties, such as anisotropy, incompressibility, residual stresses and non-linearity [197, 8, 127]. For the length scales considered here, a vessel appears rigid in comparison to a RBC. Thus, we neglect these properties and a vessel is treated as a rigid, impermeable, hollow cylindrical tube. We model it by immobile particles that have the same density, temperature and radial distribution function as the fluid.

## 5.3 Distinguishing Different Shapes and Dynamics

We choose the set-up with a viscosity contrast of five as our reference set-up (denoted VC5). This means that the cell's internal fluid has a viscosity that is five times the viscosity of the external fluid. This represents the physiological viscosity ratio. Different set-ups are studied in section 5.5.

In analogy to reference [46], we consider quantities such as the distance to the centre line, asphericity (see equation (4.2)) and angle to flow direction (see equation (4.1)) (figures 5.2, 5.4, 5.5). Additionally, in figure 5.6, we consider the bending energy, calculated by the potential energies of all adjacent triangles. For theory, see also section 1.5.2. This data are shown depending on two important variables  $\chi$  and  $\dot{\gamma}^*$ . The confinement

$$\chi = \frac{D_r}{D} \quad (5.4)$$

is the ratio of cell and tube diameters, and the dimensionless shear rate

$$\dot{\gamma}^* = \frac{\bar{\gamma}\eta D_r^3}{\kappa_r} \quad (5.5)$$

is the ratio of shear and bending energies. Larger membrane rigidity, as in some infected cells, yields smaller values for  $\dot{\gamma}^*$  [160, 84]. Thus, a wide interval of relevant  $\dot{\gamma}^*$ -values for healthy and diseased cells is covered.

Strong confinements lead to a stronger alignment: closer proximity to the tube's centreline, less rotations and a more spherical shape. Oscillations in orientation decline (see figure 5.3) and there is a trend towards constant alignment. Low shear rates can withstand this trend up to a certain confinement. Below certain shear rates, cells can remain in their relatively free motion (a rotating, rather aspherical cell motion around the centreline) even for strongest confinements. Vice versa, for weak confinements of  $\chi \leq 0.44$ , the oscillatory, free motion is kept even for high shear rates.

For high enough  $\dot{\gamma}^*$ , the shear energy provided by the flow is sufficient to deform the cell to a slipper shape or a parachute (see figure 5.6). Small vessels reduce the entropy of cells and cause stronger alignment. Furthermore, the flow profile in small vessels has a higher curvature. Cells moving through different layers of shear planes experience different forces and can exhibit asymmetric shapes and tank-treading motion. At strong confinements, the cell is preferably located at the centre and shows less shape changes, as seen for the parachute cases.

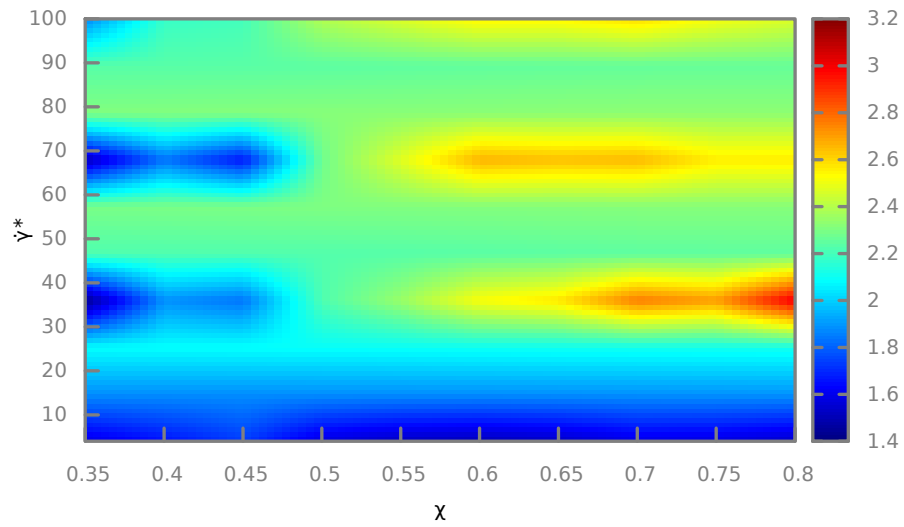


Figure 5.2: Angle to the flow direction for varying  $\dot{\gamma}^*$  and  $\chi$  in the case of VC5. Both higher shear rate and confinement promote a more symmetrical alignment of the cells (parachutes).

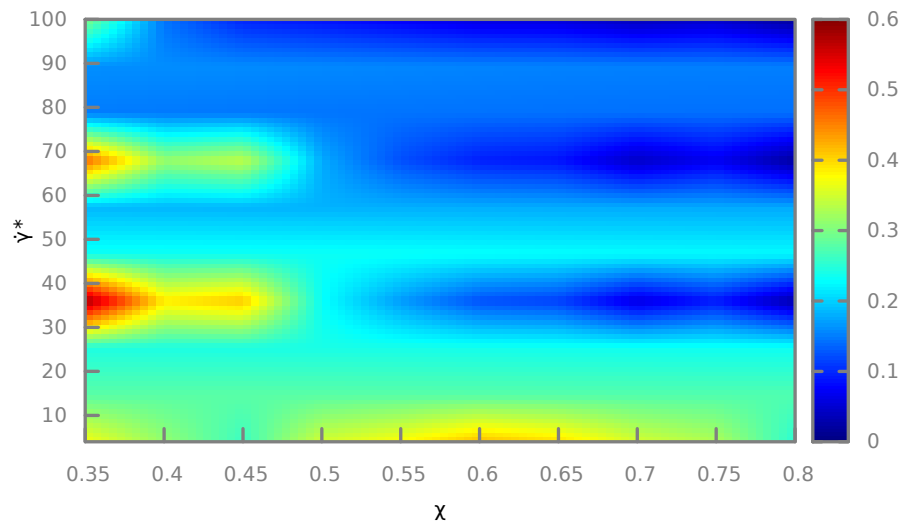


Figure 5.3: Variation in the angle to the flow direction for varying  $\dot{\gamma}^*$  and  $\chi$  in the case of VC5. Both higher shear rate and confinement promote a steadier alignment of the cells. Here, the variation is the standard deviation.

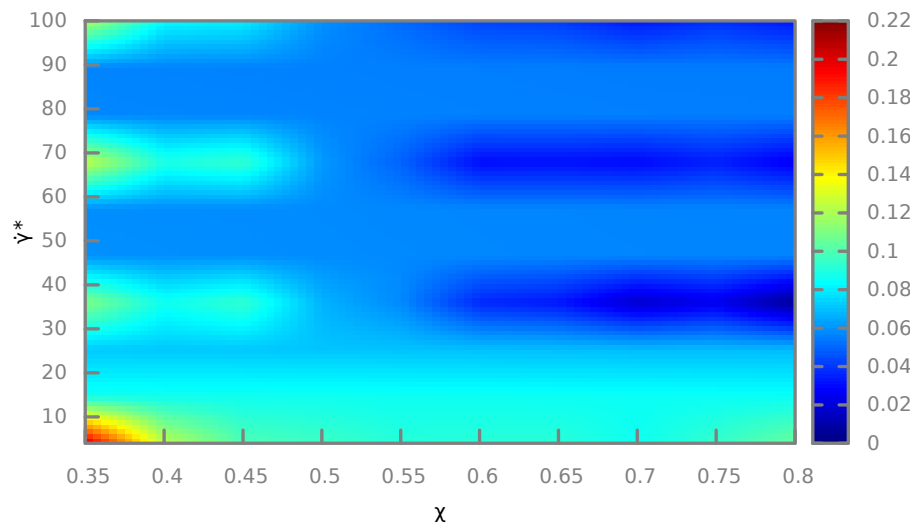


Figure 5.4: Distance to the centre line for varying  $\dot{\gamma}^*$  and  $\chi$  in the case of VC5. Both higher shear rates and confinements bring the cell closer to the centre line.

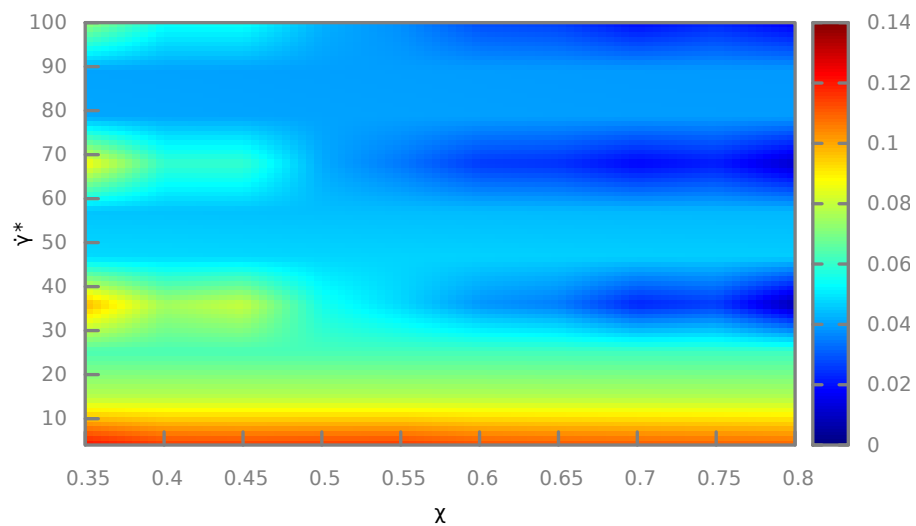


Figure 5.5: Asphericity for varying  $\dot{\gamma}^*$  and  $\chi$  in the case of VC5. Both higher shear rates and confinements promote a more spherical cell, whereas low shear rates promote a less spherical cell.



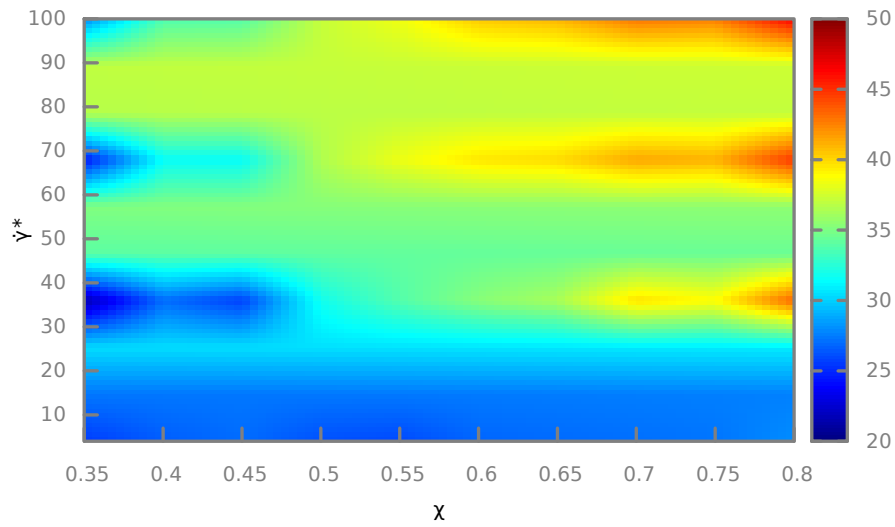


Figure 5.6: Bending energy for varying  $\dot{\gamma}^*$  and  $\chi$  in the case of VC5. Cells are bent more strongly for both higher shear rates and confinements.

## 5.4 Domains of Shapes and Dynamics

We identify four different shapes/dynamics. Their appearance depends on the values of  $\dot{\gamma}^*$  and  $\chi$ . Figure 5.7 illustrates them.

### 5.4.1 Phase Diagram

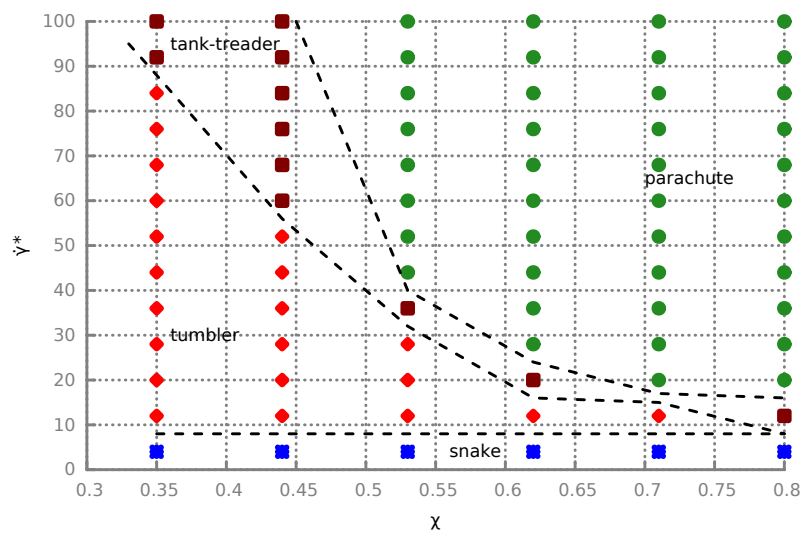


Figure 5.8: Phase Diagram for VC5.

The phase diagram for a viscosity contrast of five (*VC5*) is designed analogously to that in reference [46], where equal viscosities and a biconcave stress-free shape were used. The shapes/dynamic regions occupy similar domains; yet the slippers show essential differences. For *VC5*, the stable slipper is suppressed, but an asymmetric cell, rotating and deforming in the flow, prevails. In the deformation, a cell loses its dimple facing upstream and develops an additional dimple facing downstream.

Some slippers tend to tumble while others tend to tank-tread. The tumblers rotate as a whole and their angle to the flow direction oscillates through the whole range from 0 to  $2\pi$  (see figure 5.13). The tank-treaders show a constant inclination angle while minor shape changes also occur. The membrane, along with dimples and protrusions, rotates around the inner fluid. In contrast to tumblers, the angle to the flow direction attains only limited values (see figure 5.9).

In comparison to the phase diagram in reference [46], the tank-treaders here require a higher shear rate. A possible reason is that a tank-treader needs energy to deform and bend the membrane and rotate it relative to the inner volume. If this inner volume is more viscous, there is more friction and more energy is needed. The shearing has to provide this additional energy. The snaking regime is restricted to low shear rates, similar to reference [46].

Here, the parachute region ends at  $\chi \approx 0.5$ , in contrast to reference [46], where it extends to  $\chi \approx 0.4$ . Presumably, a cell with higher inner friction more strongly hinders shape deformations, so to transform the cell into a parachute, a higher pressure force or entropic force is required. The tank-treading slippers accumulate at weaker confinements and high shear rates. The relatively large tubes offer enough space for cell rotations; the cell can be located asymmetrically to the different cylindrical shear layers. High shear forces provide enough energy for deformations and membrane rotations. Tank-treaders also show up in a narrow belt ranging from weak confinements and high shear rates to strong confinements and low shear rates. In general, strong confinements promote parachutes. As the cell cannot move as much off-centre as for larger tubes, it is enforced symmetrically into the shear layers and experiences radially symmetrical shear forces. The result is a symmetric shape like the parachute. If the dimensionless shear rate is low, the effect of symmetrical forces gets less important. Thereby, asymmetric shapes can occur. Unconfined slippers have been studied [82, 163].

The parachutes for  $\dot{\gamma}^* \geq 52$  and  $\chi = 0.53$  are not symmetric and thus called slippers. They make up the boundary between symmetric parachutes and tank-treaders. Unlike the other slippers typically found here, they do not show the rotation-deformation-scheme; only occasional reorientations and transient, partial membrane motion.

## 5.4.2 Representative Examples

To compare different shapes/dynamics, we select four representative cases.

We choose ( $\dot{\gamma}^* = 4; \chi = 0.71$ ) for the snaking, (36; 0.35) for the tumbling slipper, (76; 0.44) for the tank-treading slipper and (68; 0.71) for the parachute. The angle  $\alpha$  oscillates, thus, the cell rotates in all cases but the parachute (figure 5.9). In the snaking regime, the oscillations have a smaller amplitude; there is no complete rotation, only back-and-forth motions. The parachute shows a stationary alignment with the tube axis.

The distance to the centre line in figure 5.10 is normalised by the cell's diameter, and not by the tube's diameter as in reference [46], so the different confinements should be taken into account when comparing. Thereby, the tank-treading cell departs about three times as much

from the centre as the parachute, the tumbling cell about twice and the snaking cell about five times. In absolute terms, the parachute barely moves away from the centre whereas the others have similar distances.

For the asphericity in figure 5.11, the different types are clearly distinguishable. After initial rearrangements in the developing flow, the parachute gets rather spherical. The slippers oscillate, but among them, the tank-treader shows smaller frequency and smaller average than the tumbling slipper. The tank-treader's biconcave shape is lost to a larger extent than the tumbler's, leading to the lower average value. The snaking is closest to the equilibrium RBC value of 0.15 and fluctuates only slightly.

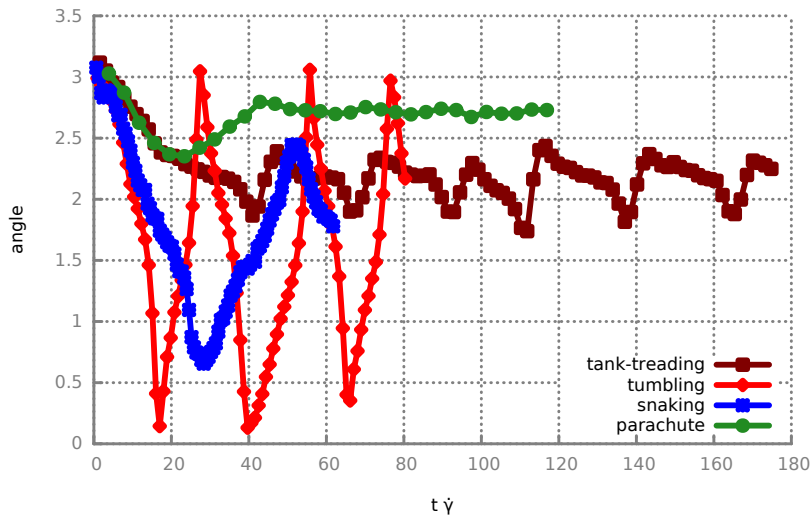


Figure 5.9: Orientation angle to the flow direction of different cell shapes.

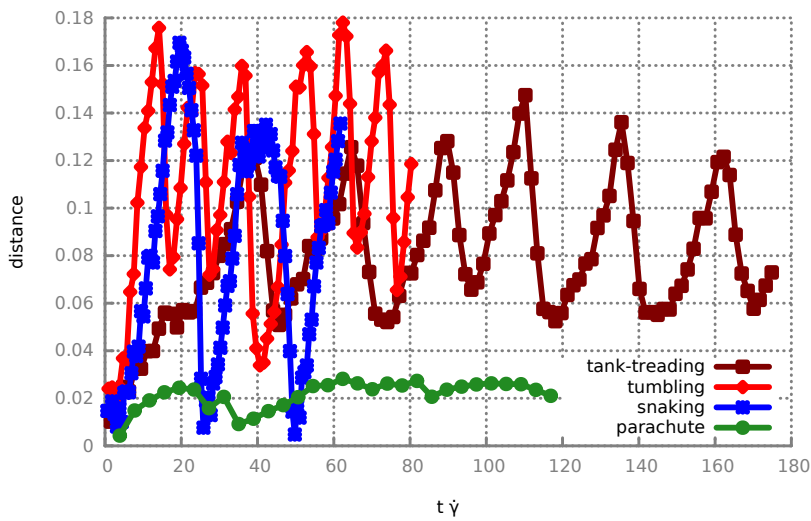


Figure 5.10: Distance to the centre line of different cell shapes.

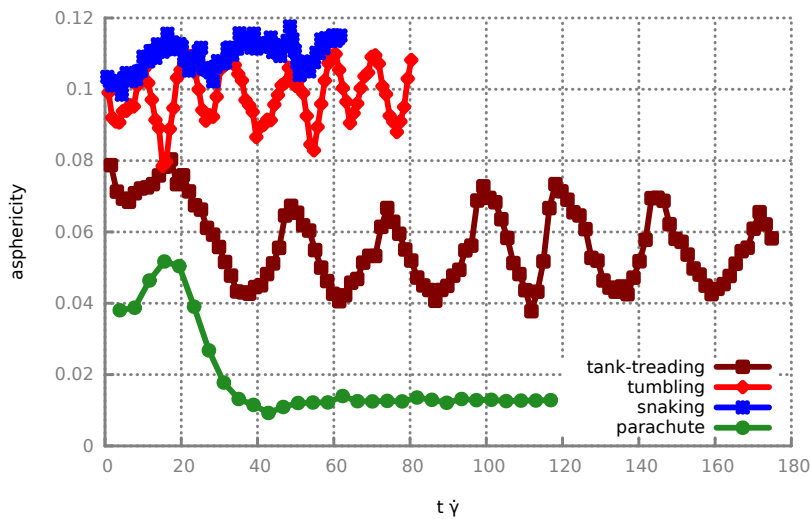


Figure 5.11: Asphericity of different cell shapes.

The angular distribution in figure 5.12 distinguishes the parachute shape with its sharp maximum around  $150^\circ$ . A perfect parachute would peak at  $180^\circ$ . One possible reason is that the simulation time is still not long enough to probe all accessible configurations. Furthermore, asymmetric shapes in symmetric flow can increase flow efficiency [82]. The tank-treader also has a peak, around  $125^\circ$ , so it also prefers a certain orientation. This corresponds to the rather steady inclination angle of the cell interior. This is in contrast to the tumbling cell, which can face all directions, visible by the rather flat distribution of angles in figure 5.12.

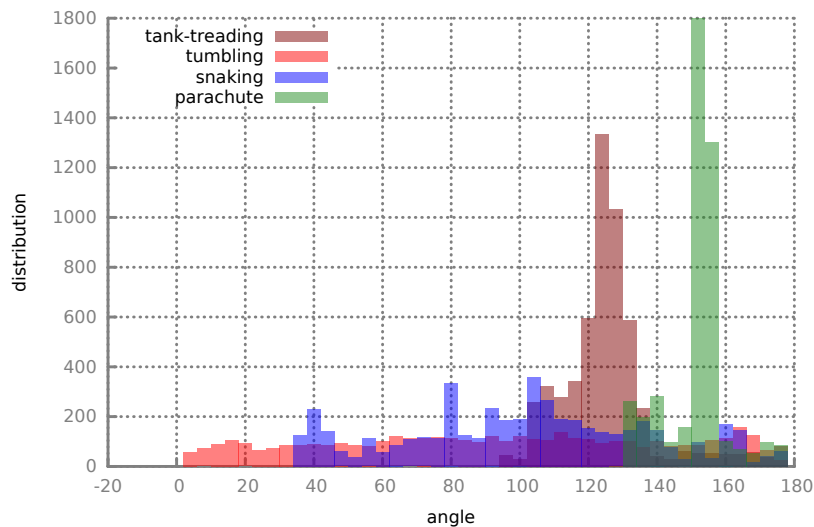


Figure 5.12: The histogram for orientation angles in flow direction clearly distinguishes tank-treaders and parachutes.

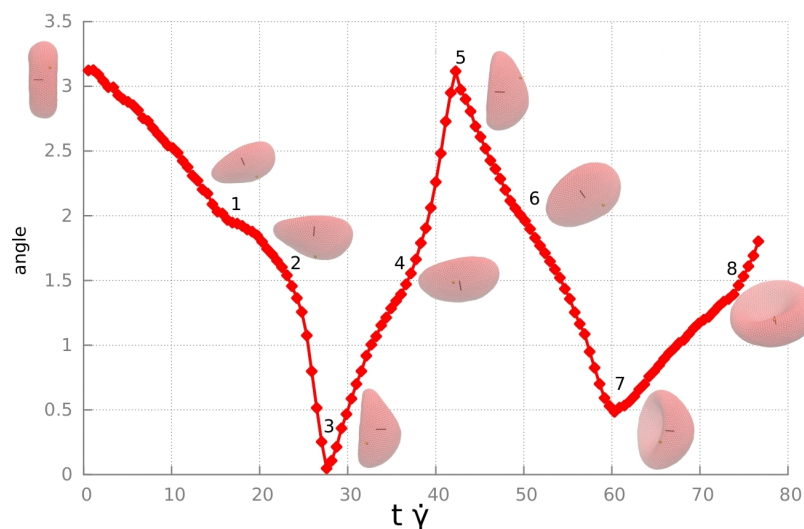


Figure 5.13: Orientation dynamics of a tumbling slipper.

In order to further elucidate the dynamics of a cell, the angle of a tumbling slipper

(20; 0.44) is chosen, see figure 5.13. Different phases of the rotation and deformation can be distinguished.

1. The cell is 'lying', i.e. the normal facing out of its flat side is perpendicular to the tube axis (flow direction). The flow can grasp under the lower side of the cell.
2. Rotation and deformation starts.
3. The cell is 'standing'; its front dimple has almost vanished.
4. The cell is a lying cup; rotation/deformation starts again.
5. The cell is 'standing'; its front dimple (facing the flow direction) has almost vanished.
6. The cell is a lying cup; rotation/deformation starts again.
7. The cell is 'standing'; its front dimple has almost vanished.
8. The cell has a cup-shape, there is no front dimple.

From  $t \bar{\gamma} = 60$  on, the dynamics is superimposed by a rotation around the y-axis. At point 7, the angle does not go back to 0 because the tumbling rotation is not perfect and neither is the orientation of its axis. The apparent decrease at  $\alpha = \pi$  is due to the implementation of the angle by the arc cosine of a directional vector, so the actual rotation proceeds beyond this point up to  $\alpha \approx 2\pi$ .

From the steepness of the curve, it is visible that the angular velocity changes during this motion. A possible reason for this de-/acceleration might be that in certain phases, the symmetry axis of the cell is oriented perpendicular to the flow; thereby, the cell touches only a few adjacent shear planes. When the flow starts turning the cell, it experiences the influences of more shear planes and the velocity gradient from one cell rim to another increases.

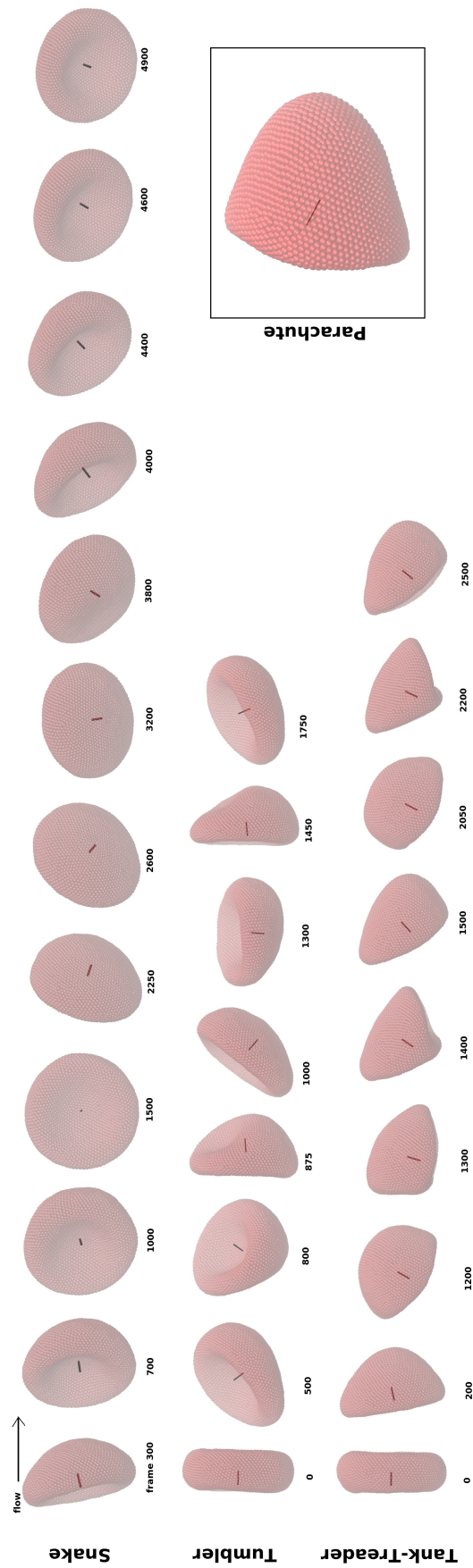


Figure 5.7: Four different shapes/dynamics of RBCs found in tube flow.

## 5.5 Comparative Parameter Set-Ups

To study the influence of membrane and fluid properties on the shapes and dynamics, we investigate modified set-ups. Each time, we changed one specific parameter (in comparison to the reference system *VC5* described above):

- Viscosity contrast of one (denoted *VC1*)
- Viscosity contrast of three (denoted *VC3*)
- less deformable cell: the RBC's Young's modulus is increased by a factor of five (denoted *lessDef*)
- spontaneous curvature: the RBC's membrane is altered by imposing a spontaneous curvature (denoted *spont*)

### 5.5.1 Viscosity Contrast of One

In this set-up, the inner and outer fluids have the same viscosity. The only difference to the set-up in reference [46] is the stress-free shape of the RBC: instead of a biconcave shape, here, it is a spheroid with 96% of the volume of a sphere of equal surface area (the model is described in section 2.4). Further volume deflation to 64% transforms it into the biconcave, stressed shape that is used here.

First, the phase diagram for *VC1* in figure 5.14 shall be compared to the phase diagram in reference [46] to identify the effect of the stress-free shape. Please keep in mind that here, the confinement range is extended in comparison to the diagram in reference [46]. For weak confinements such as  $\chi = 0.35$  and  $\chi = 0.44$ , the boundary between tumblers and tank-treaders is similar in both cases. Yet here, the domain of parachutes is extended towards low shear rates such that for  $\chi \geq 0.45$ , the slippers are hardly present. The spheroidal stress-free shape is prone to be deformed into a parachute, which is closer to a sphere (see also figure 5.11). Thus, by approaching their original configuration, the membrane elements are in a favourable bending state. This happens although the bending energy is higher for parachutes (see figure 5.6). Probably, the shear elastic energy plays an important role in this context.

Second, the present phase diagram for *VC1* in figure 5.14 shall be compared to the phase diagram for *VC5* in figure 5.8 to identify the effect of the viscosity contrast. An apparent difference is the shift in the boundary between slippers and parachutes. In both set-ups, for higher shear rates ( $\dot{\gamma}^* \geq 60$ ), the boundary is at a certain confinement  $\chi$ , independent of the shear rate  $\dot{\gamma}^*$ . However, for *VC1*, it lies at low  $\chi \approx 0.3$ , whereas for *VC5*, it lies at a medium  $\chi \approx 0.5$ . Potentially, for a high viscosity contrast, the cell gets effectively more rigid and a stronger confinement is needed to force the cell into a stable parachute with its stationary shape and constant inclination angle. This question is addressed further in section 5.6. It looks as if the *VC5* diagram as a whole is shifted to the left (weaker confinements). This also indicates that the tank-treaders form a rather slim, diagonal belt broadening towards weak confinements and high shear rates.



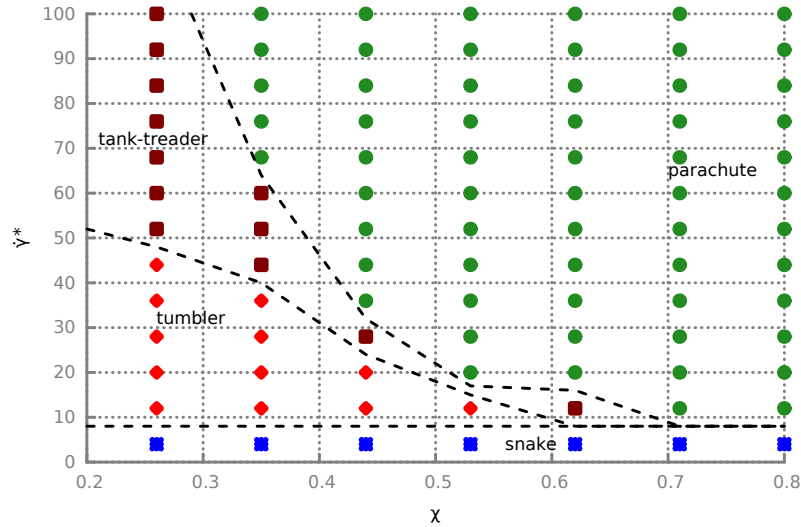


Figure 5.14: Phase Diagram for  $VC1$  with extended confinement range to find the boundary. Compared to the phase diagram in reference [46], the effect of a different stress-free shape can be identified. Compared to figure 5.8, the effect of the viscosity contrast can be identified.

### 5.5.2 Viscosity Contrast of Three

In this set-up, the inner and outer fluids have a medium viscosity contrast of three. We expect this set-up to be an intermediate stage between  $VC1$  and  $VC5$ . Comparing the phase diagrams in figures 5.14, 5.15 and 5.8, we can see a clear trend: as the inner viscosity increases, the parachute domain is shifted to stronger confinements. The cell becomes effectively more rigid and a stronger confinement ( $\rightarrow$  a velocity profile of stronger curvature) is needed to deform the cell to a parachute (see figure 5.6). Between parachutes and tumblers, there is usually a layer of tank-treaders. With their steady inclination angle and periodic deformations/rotations, this layer can be a transition from the strict alignment of a parachute to the rotations of a tumbler.

We have to emphasise that the differences between  $VC1$  and  $VC3$  are larger than those between  $VC3$  and  $VC5$ . For example, the parachute-TT-boundary is only slightly shifted between  $VC3$  and  $VC5$ . Some shapes for  $VC5$  at  $\chi = 0.53$  and high shear rates are unclear and correspond most likely to asymmetric parachutes. Thus, the cell's viscosity contrast is an important parameter to consider.

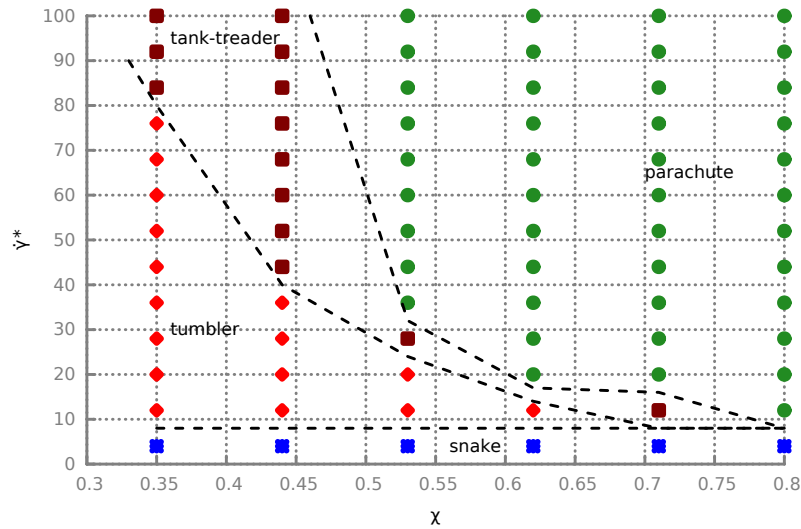


Figure 5.15: Phase Diagram for VC3. This intermediate viscosity contrast confirms the trend that the parachute domain is shifted to stronger confinements with increasing inner viscosity.

### 5.5.3 Less Deformable

This set-up is identical to the reference set-up VC5 except for an increased Young's modulus. Here, the straining resistance is five times higher than the physiological value and corresponds to  $9.45 \cdot 10^{-5} \frac{N}{m}$ . The phase diagram in figure 5.16 clearly shows the dominance of tumblers and disappearance of parachutes, in comparison to figure 5.8. There is a slim domain at  $\chi = 0.71$ , which shows features of the tank-treading slippers; but here, the rotation/deformation cannot be completed and the cells remain in some squeezed state.

Again, tank-treading makes up a transition layer between tumblers and parachutes. The diagram could be thought of as figure 5.8 shifted to stronger confinements; thereby, a less deformable cell could correspond to a physiological cell in a weaker confinement. Thus, a less deformable cell needs a stronger confinement ( $\rightarrow$  a velocity profile of stronger curvature) to become a parachute. Taking into account the effect of viscosity contrast, the Young's modulus has an effect comparable to a higher inner viscosity; making the cell less deformable and more prone to tumbling.

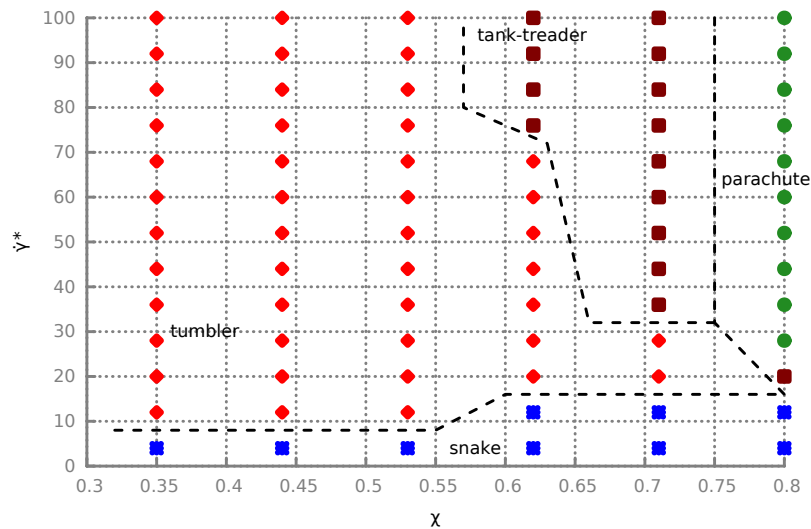


Figure 5.16: Phase Diagram for *lessDef*. A less deformable cell is more prone to tumbling. It requires a stronger confinement to become a parachute.

#### 5.5.4 Spontaneous Curvature

This set-up is identical to the reference set-up *VC5* except for an additional spontaneous curvature, inspired by figure 4 in reference [134]. The boundary between tank-treaders and parachutes is hard to identify. The tank-treaders at high shear rates with  $\chi = 0.53$  could also be considered as asymmetric parachutes with membrane motion. Thus, the difference to figure 5.8 is not so apparent. The tendency, however, is clear: cells with a spontaneous curvature are harder to deform into a symmetric parachute. Thus, the regions are shifted towards higher confinements, which is needed to deform the cells into tank-treaders or parachutes.

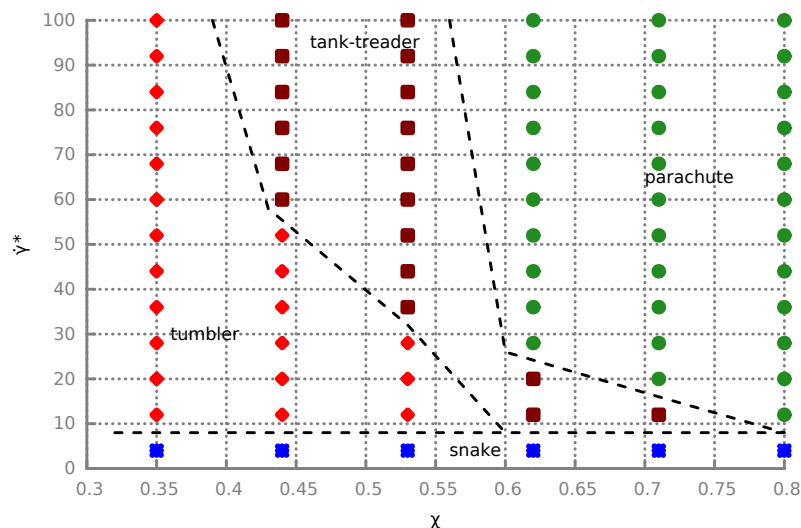


Figure 5.17: Phase Diagram for *spont*. A stronger confinement is required to deform cells with a spontaneous curvature into parachutes or tank-treaders.

## 5.6 A Closer Look at the Transition near the Border

Why does the cell with higher inner viscosity favour tank-treaders over parachutes? Comparing figures 5.8 and 5.14, we see that the borders are shifted in favour of tank-treaders when increasing the cytosol viscosity. However, this is counterintuitive: a parachute has an almost stable shape and thus, its inner fluid does not have to be moved so much. This is in contrast to the tank-treader, where the inner fluid is constantly in motion. Considering that we use no-slip boundary conditions at the membrane, for both outer and inner fluid, it is clear that rotations and deformations of the membrane require rearranging of the inner fluid as well. Thus, the *parachute* should be more appropriate if the inner viscosity is *high*.

A possible explanation is the initial equilibration phase, when the biconcave shape is transformed into snaking cell, tumbler, tank-treader or parachute. The start-up phase of RBCs in Poiseuille flow has been studied [167]. In this phase, more deformation energy is required for a parachute than for a tank-treader. Thus, a tank-treader would be more easy to obtain in a high-viscosity-contrast simulation in comparison to a parachute.

In order to verify this, two boundary cases were examined closer. We set up simulations for confinement  $\chi = 0.44$  and shear rates  $\dot{\gamma}^* = 76$  and  $\dot{\gamma}^* = 84$ . For these values, different shapes are found depending on the viscosity contrast. For both setups, there are two scenarios: one with increasing (VC1  $\rightarrow$  VC5) and one with decreasing (VC5  $\rightarrow$  VC1) viscosity contrast. This means that after the first half of the simulation (6 million time steps), when the equilibration phase is completed and a steady characteristic motion has been established, the viscosity of the inner solvent particles is altered. Although this consideration might not have a physiological counterpart, it is interesting to clarify the influence or importance of the equilibration phase on the flow behaviour.

1.  $\dot{\gamma}^* = 76$ , increasing viscosity:  
The RBC starts as a parachute in the first half. After increasing the inner viscosity, it becomes a tank-treader that changes its rotation handedness. One clockwise, then one counter-clockwise; then, this pattern repeats a further time.
2.  $\dot{\gamma}^* = 84$ , increasing viscosity:  
The RBC starts as a parachute in the first half. After increasing the inner viscosity, it becomes a tank-treader with steady rotation handedness.
3.  $\dot{\gamma}^* = 76$ , decreasing viscosity:  
The RBC starts as a tank-treader and after decreasing the inner viscosity, it becomes a parachute.
4.  $\dot{\gamma}^* = 84$ , decreasing viscosity:  
The RBC starts as a tank-treader and after decreasing the inner viscosity, it becomes a classical tank-treader: rotations and deformations vanish; the cell obtains a steady inclination angle while the membrane rotates around the inner liquid. This is intuitive: when the inner viscosity is not higher than the outer, it is easier to rotate the membrane even at a constant shape. This membrane motion at constant shape drags the inner fluid along.

As the change of inner viscosity causes shape changes, it is shown that the equilibration phase does not determine the future behaviour for the cases studied here. It is the *viscosity contrast* that matters. A parachute is more likely maintained in low viscosity-contrast

simulations, whereas the tank-treader is more likely maintained in high viscosity-contrast simulations. This issue needs further studies regarding flow field and flow efficiency close to the membrane, both inside and outside the cell.

## 5.7 Conclusion

The flow of RBCs through a rigid cylinder is a basic model for blood flow in a vessel. It exhibits a variety of shapes and dynamics depending on both flow and cell properties; such as the shear rate, confinement, Young's modulus, viscosity contrast and the stress-free shape of the cell. Different measures, such as the asphericity, the orientation angles or their distributions, were tested for suitability to distinguish different shapes and dynamics. Criteria for identification have been introduced for each shape/dynamics.

For each shape/dynamics, a domain of shear rate and confinement was found. This gives rise to phase diagrams, analogously to previous studies [84, 46, 163]. Different phase diagrams point out how different domains and their boundaries change with flow conditions. Some details require further analysis, e.g. the shift of the boundary between tank-treading and parachutes when changing the viscosity contrast.



## Chapter 6

# Conclusion and Outlook

In this work, numerical simulations of RBCs under various flow conditions were performed. Computer simulations are a third pillar besides theories and experiments. Numerical studies of haemodynamics and haemorheology can test theories of blood flow, confirm experimental results, motivate experimental studies, and tackle scenarios that are difficult to access *in vivo* or *in vitro*.

A particle-based simulation method allows for the study of cell dynamics, hydrodynamics, membrane deformations, and thereby, rheology. The cell is built up of an elastic membrane enclosing a viscous cytosol. The cell is embedded in a fluid with generally different viscosity. Smoothed dissipative particle dynamics (SDPD) was used to model bulk fluid, such as the ambient solvent and the cytosol. For SDPD, density and viscosity of a fluid are input directly. This is an advantage of SDPD compared to dissipative particle dynamics (DPD) in the case of modelling bulk fluids. In DPD, the friction parameter is input and the viscosity has to be determined by performing a simulation in advance. This makes DPD more suitable for modelling the interaction of a fluid and a structure such as a membrane or a wall. The friction can be adjusted such that the shear force at the membrane is compensated, giving rise to no-slip boundary conditions.

Focus of the study has been on the motion and deformation of a RBC in different kinds of shear flow and the suitability of certain quantities to describe the cell behaviour. Such quantities of measure are e.g. light scattering signals or shape characteristics like asphericity and acylindricity.

In comparative setups of diffusing RBCs, it was shown that the light scattering signal sensitively depends on many cell properties, such as the bending rigidity or the Young's modulus (stretching resistance). We have also compared the dynamic scattering functions obtained from different simulation techniques, namely dissipative particle dynamics and multi-particle collision dynamics. Equality was found only for matching resolution, bending rigidity, and Young's modulus. Central to light scattering is the scattering amplitude, which is a spatial Fourier transform of the scatterer's geometry. It describes the light scattered by an object that is large compared to the wavelength of the incoming light. Thereby, the light scattered from different parts of the object differ in phase. Under each scattering angle, which is the angle at which the scattered light is detected, the superposition of light of different phases causes interferences that are characteristic for the scatterer's geometry. Birefringence and multiple scattering were neglected; the dielectricity was set to unity. The dynamic scattering quantity considered here has been the effective diffusion coefficient  $D_{\text{eff}}$ , which was obtained from

the decay of the scattering amplitude self-correlation in time.  $D_{\text{eff}}$  depends on the scattering angle, which is related to the momentum transfer  $\vec{q}$ , the difference between incoming and scattered wave vector. The course of  $D_{\text{eff}}(q)$  is characteristic for the shape of a diffusing object. For a diffusing sphere, this quantity is  $q$ -independent and equal to the diffusion coefficient  $D_T$  from Einstein's fluctuation-dissipation theorem. The deviation from  $D_T$  characterises aspherical shapes. The  $D_{\text{eff}}(q)$  of cup-shaped RBCs differs from that of biconcave RBCs. Thus, light scattering signals can distinguish cells of different shape. This provides a basis to non-invasively distinguish cells of different (pathological) states, such as malaria or sickle cell anaemia. Diffusing RBCs of different bending rigidities were simulated. The bending energy parameter was set in relation to the thermal energy of the system. Cells of higher bending rigidity are less prone to thermally induced membrane fluctuations. Dynamic light scattering (DLS) provides a basis to draw conclusions on membrane fluctuations. The nature of membrane fluctuations, passive (thermal) or active (metabolic) or a combination, has been discussed recently [172]. The present RBC model does not include active membrane fluctuations. If DLS is used to compare the simulational purely thermal membrane fluctuations with experimental membrane fluctuations, one might identify differences corresponding to active contributions.

In case of RBCs in shear flow, under certain conditions, light scattering signals allow conclusions on the shear rate. For the case of flow, the scattering signal considered has been the decay of the scattering amplitude correlation function in time. The dominant frequency of this decay is on the order of the shear rate, if the momentum transfer  $\vec{q}$  is either in the flow or gradient direction. This relation could enable non-invasive measuring of shear rates *in vivo*, which is an important quantity in case of altered flow conditions, e.g. in case of vessel occlusions [1].

Through the motion of a RBC in simple shear flow, general and basic behaviours could be identified. A single RBC was placed between two planar walls moving in opposite directions. For this set-up, the possibility of periodic boundary conditions in simulations is advantageous. If the cell is transported out of the simulation domain by the flow, it will re-enter on the opposite side. This enables linear flow patterns, which are harder to establish in experiments. For different shear rates, we have found a sequence of shapes and dynamics, in agreement with experiments of the group of M. Abkarian (University of Montpellier, unpublished work). For shear rates up to  $100\text{s}^{-1}$ , the cell is biconcave to cup-shaped and rolls like a wheel. For shear rates up to  $1000\text{s}^{-1}$ , the cell is a trilobe with dimples, notches and protrusions. For shear rates on the order of  $2000\text{s}^{-1}$ , the cell has a quadrulobe shape, but can also return to the trilobe. Besides visual analysis of the trajectories, measures such as the angle to the flow direction, the asphericity and the motion of a membrane tracer have been used to distinguish different shapes. The asphericity is a measure for the deviation from a sphere, and it is derived from the distribution of membrane elements. The membrane tracer is analogous to e.g. a dextran bead attached to the membrane in experiments. Yet the *in silico* tracer is advantageous: both the procedure of attachment and the additional mass are avoided, and with them, a possible alteration of flow behaviour. Furthermore, histograms for the angle to the flow or gradient direction or histograms for the size of the cell have been presented. These measures are particularly suitable to identify the rolling cell.

Besides the single cell set-up, three set-ups of realistic haematocrit  $H$  were simulated and analysed.  $H = 20\%$  and  $H = 30\%$  correspond to the microcirculation, while  $H = 45\%$  corresponds to larger venes and arteries. These set-ups show collective effects such as alignment and mutual volume exclusion. Single cells are more spherical than cells at higher haemat-



ocrit. The higher the haematocrit, the more the cells are stretched in flow direction. For both low haematocrit and low shear rates, cells experience only small forces between the walls and thus, can extend in gradient direction. For both low haematocrit and high shear rates, cells are stretched in vorticity direction. The histograms were obtained from both time and ensemble averaging. In comparison to the dilute set-up with only one RBC, ensemble effects could be identified.

The sum of virial stresses in the shear plane yields the overall shear stress. By dividing through the shear rate, the suspension viscosity was obtained, which is between the solvent and the cytosol viscosity, as expected. Furthermore, shear thinning effects also found in experiments could be examined. The deformations, partial tank-treading motions and alignment effects of the cells influence the suspension viscosity. Traditionally, tank-treading with steady shape and constant inclination angle has been identified for the shear-thinning of blood. Together with recent experiments by the group of M. Abkarian, the present simulations suggest that shape changes and rotations, as seen in the case of a trilobe, are crucial. Furthermore, the initial orientation changes the cell motion. However, it is possible that the deviations of cells of different initial orientation vanish with time. Cells with different initial orientation both show rolling motion after sufficient time. This indicates that other shapes and motions could be also transient as well.

In a further setup, a larger viscosity contrast was employed to substitute membrane viscosity. Membrane motion induces cytosol motion, particularly in case of no-slip boundary conditions, thus, dissipation in the membrane can be addressed to the cytosol [91]. The results agree better with experiments, thus showing the validity of this approach.

A RBC in tube flow is subject to a Poiseuille velocity profile. The cell exhibits different shapes and dynamics, depending on various cell properties and flow conditions. The behaviour of flowing cells was studied for different shear rates and confinements, i.e. vessel diameters. Comparative setups point out the importance of both the viscosity contrast and the nature of the stress-free shape. We have found two major groups of shapes and dynamics. First, for high shear rates and strong confinements, there are parachute-like cells. Second, for low shear rates or weak confinements, there are slippers. The parachutes are not perfectly symmetric, in contrast to previous studies [80]. The reason for the asymmetry may arise from anisotropic membrane stresses; it has also been discussed in terms of flow efficiency [82]. The parachutes require both a strong confinement and high shear rate, in order to decrease entropy and have enough energy to deform the cell, respectively. The slippers split up into three subgroups: tumblers, tank-treaders and snaking cells. The tumblers rotate and deform. Their deformation is small such that the cell shape can still be identified during a  $360^\circ$ -rotation. The tank-treaders, however, deform so severely that their cell shape is rebuilt during rotation and the inclination angle remains in a limited range. This motion requires more shear energy than the tumblers. The snaking cells exhibit small deformations and slightly oscillate around an orientation angle. Summing up, a rich variety of shapes and dynamics was found, depending on the flow conditions. Several measures were introduced to identify and distinguish these shapes and dynamics. Among them is the inclination angle, which was obtained by diagonalising the gyration matrix, representing the distribution of membrane elements. This angle distinguishes tumblers and tank-treaders. Another measure is the asphericity, obtained by the eigenvalues of the gyration matrix. This measure distinguishes slippers and parachutes. This distinguishment has also been achieved by the distribution of inclination angles, as parachutes are mostly oriented  $150^\circ$  towards the flow direction. Besides, visual assessment through the trajectory videos has complemented the

identification process.

Having identified the different shapes and dynamics, phase diagrams were provided, showing the regimes of a certain shape in terms of shear rate and confinement, and the boundaries between different shapes [84, 46, 163]. The regime of parachutes is located in the upper right corner of strong confinements and high shear rates. A layer of tank-treaders surrounds the parachutes and separates them from the tumblers. The snaking cells are located on the bottom at low shear rates. Having introduced a phase diagram, certain cell properties were altered and the simulations at the boundaries of shapes and dynamics were repeated. This has given rise to new phase diagrams with shifted boundaries. The changes in phase diagrams are consistent and could be explained by the altered cell properties. In case of increasing cytosol viscosity, the boundary of parachutes and slippers is shifted to stronger confinements. The cell becomes effectively more rigid and a stronger confinement, thus, a velocity profile of stronger curvature, is needed to form a parachute. Increasing the Young's modulus has a comparable effect; making the cell less deformable and more prone to tumbling. It is remarkable that the cell with higher inner viscosity favours tank-treaders over parachutes. Considering the strong, oscillating deformations of a tank-treader, it should be energetically more costly than the steady parachute. This was first thought to be due to the start-up phase, in which the biconcave cell transforms into one of the types [167]. To clarify its effect, simulations were set up in which, long after the start-up phase, the inner viscosity changes. It turned out that the viscosity contrast decides over the shapes. This still needs further investigation.

In the future, the following research directions are conceivable and promising.

First, the light scattering signals of an ensemble of cells can be calculated. Using a physiological haematocrit will yield more realistic scattering signals. It could also provide insights into the collective alignment of cells [68]. However, under certain conditions, multiple scattering has to be accounted for and implemented [69].

Second, the rheology of a blood suspension including physiological fractions of RBCs, WBCs, platelets and von Willebrand factor could be studied via simple shear flow setups to gain insight into their interactions in flow.

Third, the impact of viscosity contrast on the boundary between parachutes and tank-treading cells should be clarified, regarding flow field and its efficiency.

The confinements of this study are geometrically simple and rigid. In fact, real blood vessels show bifurcations, occlusions, constrictions due to deposits, and a finite elasticity. This could be incorporated into future flow simulations. Furthermore, the question of modelling membrane viscosity will have to be addressed. Present implementations either lack a realistic effect or stability.

Simulations of the dynamics of blood cells have potential for further optimisations and future successful applications of complementing theories and experiments.

## Chapter 7

# Thanks & Acknowledgements

I thank the institutes ICS-2 and IAS-2 for a friendly working atmosphere & a multicultural environment. I have enjoyed doing my PhD here among people of so many different nationalities. Thus, I have expanded both my professional and my cultural knowledge. I have also appreciated the mutual helpfulness and support.

I thank my supervisors Dmitry Fedosov and Gerhard Gompper for their support and discussions with them. I had the chance to visit several interesting conferences and present my work by giving a talk or showing a poster. I also appreciated the discussions and cooperation with experimental researchers which helped me to gain insight into the experimental approach.

I acknowledge the Jülich Supercomputing Centre and the local IFF cluster for providing hardware resources and computational time.

I thank the BioSoft research school for interesting seminars, courses and personal encounters among PhD students. It was a good opportunity to broaden my knowledge about biophysical research and to increase my soft skills.

I thank the institute KOMET 331 of the Johannes Gutenberg-Universität Mainz, where I had written my diploma thesis, for providing the environment to learn many numerical techniques that I have applied during my PhD. I have appreciated the good working atmosphere and the supervision by Friederike Schmid and Hans Behringer.

I thank my Jülich flat-mates and my improvisational theatre group 'lauter' from Cologne for friendships and welcome diversions.

I thank my family for the material and mental support throughout my whole studies and PhD time. Thank you very much for keeping the faith in me.



# Bibliography

- [1] *Heat Transfer and Fluid Flow in Biological Processes*. Academic Press, 2015.
- [2] ABKARIAN, M., FAIVRE, M., HORTON, R., SMISTRUP, K., BEST-POPESCU, C. A., AND STONE, H. A. Cellular-scale hydrodynamics. *Biomedical Materials* 3, 3 (Sep 2008).
- [3] ABKARIAN, M., FAIVRE, M., AND VIALLAT, A. Swinging of red blood cells under Shear Flow. *PRL* 98, 18 (May 4 2007).
- [4] ACKERSON, B.J., AND CLARK, N.A. Dynamic light scattering at low rates of shear. *J. Phys. France* 42, 7 (1981), 929–936.
- [5] AL-ROUBAIE, S., JAHNSEN, E. D., MOHAMMED, M., HENDERSON-TOTH, C., AND JONES, E. A. V. Rheology of embryonic avian blood. *American J. of Physiology-Heart and Circulatory Physiology* 301, 6 (Dec 2011), H2473–H2481.
- [6] ALLEN, M., AND TILDESLEY, D. *Computer Simulation of Liquids*. Oxford Science Publ. Clarendon Press, 1989.
- [7] ARIFLER, D., MACAULAY, C., FOLLEN, M., AND GUILLAUD, M. Numerical investigation of two-dimensional light scattering patterns of cervical cell nuclei to map dysplastic changes at different epithelial depths. *Biomedical Optics Express* 5, 2 (Feb 1 2014), 485–498.
- [8] BADEL, P., GENOVESE, K., AND AVRIL, S. 3D Residual Stress Field in Arteries: Novel Inverse Method Based on Optical Full-field Measurements. *ArXiv e-prints* (Mar. 2013).
- [9] BASKURT, O., AND MEISELMAN, H. Determination of red blood cell shape recovery Time constant in a Couette system by the analysis of light reflectance and ektacytometry. *Biorheology* 33, 6 (Nov-Dec 1996), 489–503.
- [10] BAUERSACHS, R., WENBY, R., PFAFFEROTT, C., WHITTINGSTALL, P., AND MEISELMANN, H. Determination of Red-Cell Deformation via Measurement of Light Transmission through RBC Suspensions under Shear. *Clinical Hemorheology* 12, 6 (Nov-Dec 1992), 841–856.
- [11] BEAUCOURT, J., BIBEN, T., AND MISBAH, C. Optimal lift force on vesicles near a compressible substrate. *EPL (Europhysics Letters)* 67, 4 (2004), 676.
- [12] BELAU, M., NINCK, M., HERING, G., SPINELLI, L., CONTINI, D., TORRICELLI, A., AND GISLER, T. Noninvasive observation of skeletal muscle contraction using near-infrared Time-Resolved reflectance and diffusing-wave spectroscopy. *J. of Biomedical Optics* 15, 5 (Sep-Oct 2010).

- [13] BELYTSCHKO, T., LIU, W., MORAN, B., AND ELKHODARY, K. *Nonlinear Finite Elements for Continua and Structures*. Wiley, 2014.
- [14] BERGSTROM, D., POWELL, J., AND KAPLAN, A. F. H. A ray-tracing analysis of the absorption of light by smooth and rough metal surfaces. *J. of Applied Physics* 101, 11 (Jun 1 2007).
- [15] BERGSTROM, D., POWELL, J., AND KAPLAN, A. F. H. The absorption of light by rough metal surfaces - a three-dimensional ray-tracing analysis. *J. of Applied Physics* 103, 10 (May 15 2008).
- [16] BERNDL, K., KAS, J., LIPOWSKY, R., SACKMANN, E., AND SEIFERT, U. Shape Transformations of Giant Vesicles - Extreme Sensitivity to Bilayer Asymmetry. *Europhysics Letters* 13, 7 (Dec 1 1990), 659–664.
- [17] BERNE, B., AND PECORA, R. *Dynamic light scattering: with applications to chemistry, biology, and physics*. Wiley, 1976.
- [18] BLÜGEL, S. AND ANGST, M. AND BRÜCKEL, T. AND RICHTER, D. AND ZORN, R. Scattering Theory: Born Series. vol. 33, Forschungszentrum Jülich GmbH, JCNS, PGI, ICS, IAS.
- [19] BU, Z., BIEHL, R., MONKENBUSCH, M., RICHTER, D., AND CALLAWAY, D. Coupled protein domain Motion in Taq polymerase revealed by neutron spin-echo spectroscopy. *Proceedings of the National Academy of Sciences of the United States of America* 102, 49 (Dec 6 2005), 17646–17651.
- [20] CANTAT, I., KASSNER, K., AND MISBAH, C. Vesicles in haptotaxis with hydrodynamical dissipation. *Eur. Phys. J. E* 10, 2 (2003), 175–189.
- [21] CHARRIER, J., SHRIVASTAVA, S., AND WU, R. Free and Constrained Inflation of Elastic Membranes in Relation to Thermoforming - Non-Axisymmetric Problems. *J. of Strain Analysis for Engineering Design* 24, 2 (Apr 1989), 55–74.
- [22] CHATZIZISIS, Y. S., COSKUN, A. U., JONAS, M., EDELMAN, E. R., FELDMAN, C. L., AND STONE, P. H. Role of endothelial Shear stress in the natural history of coronary atherosclerosis and vascular remodeling - Molecular, cellular, and vascular behavior. *J. of the American College of Cardiology* 49, 25 (Jun 26 2007), 2379–2393.
- [23] CHEN, K., LIU, J., HECK, S., CHASIS, J. A., AN, X., AND MOHANDAS, N. Resolving the distinct stages in erythroid differentiation based on dynamic changes in Membrane protein expression during erythropoiesis. *Proceedings of the National Academy of Sciences of the United States of America* 106, 41 (Oct 13 2009), 17413–17418.
- [24] CHOI, W., FANG-YEN, C., BADIZADEGAN, K., OH, S., LUE, N., DASARI, R. R., AND FELD, M. S. Tomographic phase microscopy. *Nature Methods* 4, 9 (Sep 2007), 717–719.
- [25] COKELET, G., AND GOLDSMITH, H. Decreased Hydrodynamic Resistance in the 2-Phase Flow of Blood through Small Vertical Tubes at Low Flow-Rates. *Circulation Research* 68, 1 (JAN 1991), 1–17.

- [26] CORDASCO, D., YAZDANI, A., AND BAGCHI, P. Comparison of Erythrocyte dynamics in Shear Flow under different stress-free configurations. *Physics of Fluids* 26, 4 (Apr 2014).
- [27] DESTREMAUT, F., SALMON, J.-B., QI, L., AND CHAPEL, J.-P. Microfluidics with on-line Dynamic Light Scattering for Size Measurements. *Lab on a Chip* 9, 22 (2009), 3289–3296.
- [28] DHONT, J. *An Introduction to Dynamics of Colloids*. Elsevier, Amsterdam, 1996.
- [29] DISCHER, D., BOAL, D., AND BOEY, S. Simulations of the erythrocyte cytoskeleton at large deformation. II. Micropipette aspiration. *Biophysical Journal* 75, 3 (SEP 1998), 1584–1597.
- [30] DISCHER, D., MOHANDAS, N., AND EVANS, E. Molecular Maps of Red-Cell Deformation - Hidden Elasticity and in-situ Connectivity. *Science* 266, 5187 (Nov 11 1994), 1032–1035.
- [31] DUNCAN, AND PRASSE. *Veterinary Laboratory Medicine: Clinical Pathology*. Wiley-Blackwell, 2011.
- [32] DUPIRE, J., SOCOL, M., AND VIALLAT, A. Full dynamics of a red blood cell in Shear Flow. *Proceedings of the National Academy of Sciences of the United States of America* 109, 51 (Dec 18 2012), 20808–20813.
- [33] ESPAÑOL, P., AND REVENGA, M. Smoothed dissipative particle dynamics. *Phys. Rev. E* 67 (Feb 2003), 026705.
- [34] ESPANOL, P., AND WARREN, P. Statistical mechanics of dissipative particle dynamics. *EPL (Europhysics Letters)* 30, 4 (1995), 191.
- [35] EVANS, E. Structure and Deformation Properties of Red Blood-Cells - Concepts and Quantitative Methods. *Methods in Enzymology* 173 (1989), 3–35.
- [36] EVANS, E., AND HOCHMUTH, R. Membrane Viscoelasticity. *Biophys. J.* 16, 1 (1976), 1–11.
- [37] EVANS, E., AND SKALAK, R. *Mechanics and Thermodynamics of Biomembranes*. CRC Press, 1980.
- [38] FAHRAEUS, R., AND LINDQVIST, T. The viscosity of the blood in narrow capillary tubes. *American J. of Physiology* 96, 3 (Mar 1931), 562–568.
- [39] FEDOSOV, D. A. Multiscale modeling of blood flow and soft matter, 2010. Copyright - Copyright ProQuest, UMI Dissertations Publishing 2010; Last updated - 2010-11-26; DOI - 2184243261; 55411541; 66569; 9781124304205; 3430093; First page - n/a; M1: 3430093; M3: Ph.D.
- [40] FEDOSOV, D. A., CASWELL, B., AND KARNIADAKIS, G. E. A Multiscale Red Blood Cell Model with Accurate Mechanics, Rheology, and Dynamics. *Biophys. J.* 98, 10 (May 19 2010), 2215–2225.

- [41] FEDOSOV, D. A., CASWELL, B., AND KARNIADAKIS, G. E. Systematic coarse-graining of spectrin-level red blood cell models. *Computer Methods in applied Mechanics and Engineering* 199, 29-32 (2010), 1937–1948.
- [42] FEDOSOV, D. A., CASWELL, B., POPEL, A. S., AND KARNIADAKIS, G. E. Blood Flow and Cell-Free Layer in Microvessels. *Microcirculation* 17, 8 (2010), 615–628.
- [43] FEDOSOV, D. A., CASWELL, B., POPEL, A. S., AND KARNIADAKIS, G. E. Blood flow and cell-free layer in microvessels. *Microcirculation* 17, 8 (2010), 615–628.
- [44] FEDOSOV, D. A., LEI, H., CASWELL, B., SURESH, S., AND KARNIADAKIS, G. E. Multiscale Modeling of Red Blood Cell Mechanics and Blood Flow in Malaria. *Plos comp. Biology* 7, 12 (Dec 2011).
- [45] FEDOSOV, D. A., PAN, W., CASWELL, B., GOMPPER, G., AND KARNIADAKIS, G. E. Predicting Human blood viscosity in silico. *Proceedings of the National Academy of Sciences of the United States of America* 108, 29 (Jul 19 2011), 11772–11777.
- [46] FEDOSOV, D. A., PELTOMAEKI, M., AND GOMPPER, G. Deformation and dynamics of red blood cells in Flow through cylindrical microchannels. *Soft Matter* 10, 24 (2014), 4258–4267.
- [47] FISCHER, T. Shape memory of Human red blood cells. *Biophys. J.* 86, 5 (May 2004), 3304–3313.
- [48] FISCHER, T., STOHLRIESEN, M., AND SCHMID-SCHÖNBEIN, H. Red-Cell as a Fluid Droplet - Tank Tread-like Motion of Human Erythrocyte-Membrane in Shear-Flow. *Science* 202, 4370 (1978), 894–896.
- [49] FISCHER, T. M. Tank-Tread frequency of the red cell Membrane: Dependence on the viscosity of the suspending medium. *Biophys. J.* 93, 7 (Oct 2007), 2553–2561.
- [50] FREUND, J. B. Numerical Simulation of Flowing Blood Cells. In *Annual Review of Fluid Mechanics*, Vol. 46, Davis, S.H. and Moin, P., Ed., vol. 46 of *Annual Review of Fluid Mechanics*. 2014, pp. 67+.
- [51] FROJMOVIC, M., AND PANJWANI, R. Blood cell structure-function studies: light transmission and attenuation coefficients of suspensions of blood cells and model particles at rest and with stirring. *The J. of Laboratory and Clinical Medicine* 86, 2 (1975), 326–43.
- [52] FUJIME, S., AND KUBOTA, K. Dynamic Light-Scattering from Dilute Suspensions of Thin Disks and Thin Rods as Limiting Forms of Cylinder, Ellipsoid and Ellipsoidal Shell of Revolution. *Biophys. Chemistry* 23, 1-2 (Nov 1985), 1–13.
- [53] FULLER, G., RALLISON, J., SCHMIDT, R., AND LEAL, L. The Measurement of Velocity-Gradients in Laminar-Flow by Homodyne Light-Scattering Spectroscopy. *J. of Fluid Mechanics* 100, Oct (1980), 555–&.
- [54] FUNG, Y. *Biomechanics Mechanical Properties of Living Tissues*. Springer New York, New York, NY, 1993.



- [55] GAEHTGENS, P., WILL, G., AND SCHMIDT, F. Comparative Rheology of Nucleated and Non-Nucleated Red-Blood-Cells .2. Rheological Properties of Avian Red-Cell Suspensions in Narrow Capillaries. *Pflugers Archiv-European J. of Physiology* 390, 3 (1981), 283–287.
- [56] GANONG, W. *Review of Medical Physiology (stm09)*. Appleton & Lange, 2003.
- [57] GANZENMÜLLER, G. C., AND STEINHAUSER, M. O. The implementation of smooth particle hydrodynamics in lammeps. A guide to the sph-user package, Fraunhofer Ernst-Mach Institut für Hochgeschwindigkeitsdynamik Freiburg, Germany, 2011.
- [58] GARCIA DE LA TORRE, J., DEL RIO ECHENIQUE, G., AND ORTEGA, A. Improved calculation of rotational diffusion and intrinsic viscosity of bead models for macromolecules and nanoparticles. *J. of Physical Chemistry B* 111, 5 (Feb 8 2007), 955–961.
- [59] GARCIA DE LA TORRE, J., NAVARRO, S., LOPEZ MARTINEZ, M., DIAZ, F., AND LOPEZ CASCALES, J. HYDRO: a computer program for the prediction of hydrodynamic properties of macromolecules. *Biophysical J.* 67, 2 (1994), 530–531.
- [60] GIBAUD, E. Numerical simulation of red blood cells flowing in a blood analyzer. Phd thesis, Université de Montpellier, I2S IMAG, 2015.
- [61] GIERSIEN, M., WURZINGER, L., OPITZ, R., AND REUL, H. Estimation of Shear Stress-Related Blood Damage in Heart-Valve Prostheses - in vitro Comparison of 25 Aortic Valves. *International J. of Artificial Organs* 13, 5 (May 1990), 300–306.
- [62] GIJSEN, F., VAN DE VOSSE, F., AND JANSSEN, J. The influence of the non-Newtonian properties of blood on the Flow in large arteries: steady Flow in a carotid bifurcation model. *J. of Biomechanics* 32, 6 (Jun 1999), 601–608.
- [63] GONGORA, J., AND FRATALOCCHI, A. Optical force on diseased blood cells: Towards the optical sorting of biological matter. *Optics and Lasers in Engineering* 76 (2016), 40 – 44. Special Issue: Optical Methods in Nanobiotechnology.
- [64] GRIGIONI, M., DANIELE, C., MORBIDUCCI, U., D’AVENIO, G., DI BENEDETTO, G., AND BARBARO, V. The power-law mathematical model for blood damage prediction: Analytical developments and physical inconsistencies. *Artificial Organs* 28, 5 (May 2004), 467–475.
- [65] GRIGIONI, M., MORBIDUCCI, U., D’AVENIO, G., DI BENEDETTO, G., AND DEL GAUDIO, C. A novel formulation for blood trauma prediction by a modified power-law mathematical model. *Biomechanics and Modeling in Mechanobiology* 4, 4 (Dec 2005), 249–260.
- [66] GROOT, R., AND WARREN, P. Dissipative particle dynamics: Bridging the gap between atomistic and mesoscopic simulation. *J. chemical Physics* 107, 11 (Sep 15 1997), 4423–4435.
- [67] GULLIVER, G. Observations on the Sizes and Shapes of the Red Corpuscles of the Blood of Vertebrates, with Drawings of them to a uniform Scale, and extended and revised Tables of Measurements. *Proceedings of the Zoological Society* 1, 1 (1875), 474–495.

- [68] HARDEMAN, M., GOEDHART, P., DOBBE, J., AND LETTINGA, K. Laser-Assisted Optical Rotational Cell Analyser (LORCA) .1. a New Instrument for Measurement of Various Structural Hemorheological Parameters. *Clinical Hemorheology* 14, 4 (Jul-Aug 1994), 605–618.
- [69] HE, J., KARLSSON, A., SWARTLING, J., AND ANDERSSON-ENGELS, S. Light scattering by multiple red blood cells. *J. of the Optical Society of America A-Optics Image Science and Vision* 21, 10 (Oct 2004), 1953–1961.
- [70] HEIMBURG, T. *Thermal Biophysics of Membranes*. Wiley-VCH, 2007.
- [71] HEIMBURG, T., AND JACKSON, A. The thermodynamics of general anesthesia. *Biophysical J.* 92, 9 (2007), 3159 – 3165.
- [72] HELFRICH, W. Elastic Properties of Lipid Bilayers - Theory and Possible Experiments. *Zeitschrift fur Naturforschung C-A J. of Biosciences C* 28, 11-1 (1973), 693–703.
- [73] HIMBURG, H., GRZYBOWSKI, D., HAZEL, A., LAMACK, J., LI, X., AND FRIEDMAN, M. Spatial comparison between wall Shear stress measures and porcine arterial endothelial permeability. *American J. of Physiology-Heart and Circulatory Physiology* 286, 5 (May 2004), H1916–H1922.
- [74] HOCHMUTH, R., WORTHY, P., AND EVANS, E. Red-Cell Extensional Recovery and the Determination of Membrane Viscosity. *Biophys. J.* 26, 1 (1979), 101–114.
- [75] HOFFMANN, E., AND SIMONSEN, L. Membrane Mechanisms in Volume and pH Regulation in Vertebrate Cells. *Physiological Reviews* 69, 2 (Apr 1989), 315–382.
- [76] HOI, Y., ZHOU, Y.-Q., ZHANG, X., HENKELMAN, R. M., AND STEINMAN, D. A. Correlation Between Local Hemodynamics and Lesion Distribution in a Novel Aortic Regurgitation Murine Model of Atherosclerosis. *Annals of Biomedical Engineering* 39, 5 (May 2011), 1414–1422.
- [77] HU, N., AND CLARK, E. Hemodynamics of the Stage-12 to Stage-29 Chick-Embryo. *Circulation Research* 65, 6 (Dec 1989), 1665–1670.
- [78] HUANG, C., GOMPPER, G., AND WINKLER, R. Non-equilibrium relaxation and tumbling times of polymers in semidilute solution. *Journal of Physics: Condensed Matter* 24, 28 (2012), 284131.
- [79] HUANG, C., SUTMANN, G., GOMPPER, G., AND WINKLER, R. Tumbling of polymers in semidilute solution under shear flow. *EPL (Europhysics Letters)* 93, 5 (2011), 54004.
- [80] ICHI TSUBOTA, K., WADA, S., AND YAMAGUCHI, T. Particle method for computer simulation of red blood cell motion in blood flow. *Computer Methods and Programs in Biomedicine* 83, 2 (2006), 139 – 146.
- [81] JAKEMAN, E., OLIVER, C., AND PIKE, E. Effects of Spatial Coherence on Intensity Fluctuation Distributions of Gaussian Light. *J. of Physics Part a General* 3, 5 (1970), L45–&.

- [82] KAOUI, B., BIROS, G., AND MISBAH, C. Why do red blood cells have asymmetric shapes even in a symmetric flow? *Phys. Rev. Lett.* 103 (Oct 2009), 188101.
- [83] KAOUI, B., RISTOW, G. H., CANTAT, I., MISBAH, C., AND ZIMMERMANN, W. Lateral migration of a two-dimensional vesicle in unbounded poiseuille flow. *Phys. Rev. E* 77 (Feb 2008), 021903.
- [84] KAOUI, B., TAHIRI, N., BIBEN, T., EZ-ZAHRAOUI, H., BENYOUSSEF, A., BIROS, G., AND MISBAH, C. Complexity of vesicle Microcirculation. *Physical Review E* 84, 4, 1 (Oct 5 2011).
- [85] KATANOV, D., GOMPPER, G., AND FEDOSOV, D. A. Microvascular blood flow resistance: Role of red blood cell migration and dispersion. *Microvascular Research* 99 (MAY 2015), 57–66.
- [86] KHAIRY, K., FOO, J., AND HOWARD, J. Shapes of Red Blood Cells: Comparison of 3D Confocal Images with the Bilayer-Couple Model. *Cellular and Molecular Bioengineering* 1, 2-3 (Sep 2008), 173–181.
- [87] KHAIRY, K., AND HOWARD, J. Minimum-energy vesicle and cell shapes calculated using spherical harmonics parameterization. *Soft Matter* 7 (2011), 2138–2143.
- [88] KIM, S., ONG, P. K., YALCIN, O., INTAGLIETTA, M., AND JOHNSON, P. C. The cell-free layer in microvascular blood Flow. *Biorheology* 46, 3 (2009), 181–189. 13th International Congress of Biorheology/6th International Conference on Clinical Hemorheology, Penn State Univ, State Coll, PA, Jul 09-13, 2008.
- [89] KLEINSTREUER, C., HYUN, S., BUCHANAN, J., LONGEST, P., ARCHIE, J., AND TRUSKEY, G. Hemodynamic parameters and early intimal thickening in branching blood vessels. *Critical Reviews in Biomedical Engineering* 29, 1 (2001), 1–64.
- [90] KLEY, W., AND SPEITH, R. Numerische Hydrodynamik; Kapitel 7: Smoothed particle hydrodynamics. University lecture, Universität Tübingen, Institut für Astronomie und Astrophysik Abt. Computational Physics, 2006.
- [91] KONONENKO, V. L. Flicker in Erythrocytes. I. Theoretical Models and Registration Techniques. *Biologicheskie Membrany* 26, 5 (Sep–Oct 2009), 352–369.
- [92] KRÜGER, T., HOLMES, D., AND COVENEY, P. V. Deformability-based red blood cell separation in deterministic lateral displacement devices-A simulation study. *Biomecrofluidics* 8, 5 (Sep 2014).
- [93] KRÜGER, T., VARNIK, F., AND RAABE, D. Efficient and accurate simulations of deformable particles immersed in a fluid using a combined immersed boundary lattice boltzmann finite element method. *Computers and Mathematics with Applications* 61, 12 (2011), 3485 – 3505. Mesoscopic Methods for Engineering and Science Proceedings of ICMES-09 Mesoscopic Methods for Engineering and Science.
- [94] KU, D., GIDDENS, D., ZARINS, C., AND GLAGOV, S. Pulsatile Flow and Atherosclerosis in the Human Carotid Bifurcation - Positive Correlation between Plaque Location and Low and Oscillating Shear-Stress. *Arteriosclerosis* 5, 3 (1985), 293–302.

- [95] KUBO, R. Fluctuation-Dissipation Theorem. *Reports on Progress in Physics* 29, 1 (1966), 255–&.
- [96] KUNZ, D., THURN, A., AND BURCHARD, W. Dynamic light scattering from spherical particles. *Colloid and Polymer Science* 261, 8 (1983), 635–644.
- [97] KURODA, K., AND FUJINO, M. On the cause of the increase in light transparency of erythrocyte suspension in flow. *Biorheology* 1, 3 (1963), 167–182.
- [98] LADD, A., AND VERBERG, R. Lattice-Boltzmann simulations of particle-fluid suspensions. *J. of Statistical Physics* 104, 5-6 (Sep 2001), 1191–1251.
- [99] LADISA, J., OLSON, L., MOLTHEN, R., HETTRICK, D., PRATT, P., HARDEL, M., KERSTEN, J., WARLTIER, D., AND PAGEL, P. Alterations in wall Shear stress predict sites of neointimal hyperplasia after stent implantation in rabbit iliac arteries. *American J. of Physiology-Heart and Circulatory Physiology* 288, 5 (May 2005), H2465–H2475.
- [100] LANDAU, L., AND LIFSHITZ, E. *Fluid Mechanics, Second Edition: Volume 6 (Course of Theoretical Physics)*. Butterworth-Heinemann, 1987.
- [101] LAW, R., CARL, P., HARPER, S., DALHAIMER, P., SPEICHER, D., AND DISCHER, D. Cooperativity in forced unfolding of tandem spectrin repeats. *Biophys. J.* 84, 1 (Jan 2003), 533–544.
- [102] LEE, S.-C. Scattering by multiple perfectly conducting cylinders buried in a lossy half space. *J. of Quantitative Spectroscopy & Radiative Transfer* 146, SI (Oct 2014), 314–320.
- [103] LEVERETT, L., LYNCH, E., ALFREY, C., AND HELLUMS, J. Red Blood-Cell Damage by Shear-Stress. *Biophys. J.* 12, 3 (1972), 257–&.
- [104] LI, J., NINCK, M., KOBAN, L., ELBERT, T., KISSLER, J., AND GISLER, T. Transient functional blood Flow change in the Human brain measured noninvasively by diffusing-wave spectroscopy. *Optics Letters* 33, 19 (Oct 1 2008), 2233–2235.
- [105] LIM, H., WORTIS, M., AND MUKHOPADHYAY, R. Stomatocyte-discocyte-echinocyte sequence of the Human red blood cell: Evidence for the bilayer-couple hypothesis from Membrane mechanics. *Proceedings of the National Academy of Sciences of the United States of America* 99, 26 (Dec 24 2002), 16766–16769.
- [106] LIM, J., DING, H., MIR, M., ZHU, R., TANGELLA, K., AND POPESCU, G. Born approximation model for light scattering by red blood cells. *Biomedical Optics Express* 2, 10 (Oct 1 2011), 2784–2791.
- [107] LIN, J. Y. Y., SMITH, H. L., GRANROTH, G. E., ABERNATHY, D. L., LUMSDEN, M. D., WINN, B., ACZEL, A. A., AIVAZIS, M., AND FULTZ, B. MCViNE – An object oriented Monte Carlo neutron ray tracing simulation package.
- [108] LINDERKAMP, O., AND MEISELMANN, H. Geometric, Osmotic, and Membrane Mechanical-Properties of Density-Separated Human Red-Cells. *Blood* 59, 6 (1982), 1121–1127.

- [109] LIPOWSKY, H. Microvascular rheology and hemodynamics. *Microcirculation* 12, 1 (Jan-Feb 2005), 5–15. Spring Symposium on Half a Century of Discovery and Innovation, Natl Inst Hlth Campus, Tokyo, JAPAN, 2004.
- [110] LIPOWSKY, R. The morphology of lipid membranes. *Current Opinion in Structural Biology* 5, 4 (1995), 531 – 540.
- [111] LIU, Y., AND LIU, W. K. Rheology of red blood cell aggregation by computer simulation. *Journal of Computational Physics* 220, 1 (DEC 20 2006), 139–154.
- [112] LOISEAU, E., MASSIERA, G., MENDEZ, S., MARTINEZ, P. A., AND ABKARIAN, M. Microfluidic Study of Enhanced Deposition of Sickle Cells at Acute Corners. *Biophys. J.* 108, 11 (Jun 2 2015), 2623–2632.
- [113] MALEK, A., ALPER, S., AND IZUMO, S. Hemodynamic Shear stress and its role in atherosclerosis. *JAMA-J. of the American Medical Association* 282, 21 (Dec 1 1999), 2035–2042.
- [114] MALOY, K., GOLDBURG, W., AND PAK, H. Spatial Coherence of Homodyne Light-Scattering from Particles in A Convective Velocity-Field. *Physical Review A* 46, 6 (Sep 15 1992), 3288–3291.
- [115] MATHUR, U., AND ADAVAL, S. Laboratory studies on avian blood under simulated crash conditions. . *Indian J. of Aerospace Medicine* 37, 2 (Dec 1993), 1–5.
- [116] MEINKE, M. C., FRIEBEL, M., AND HELFMANN, J. *Optical Properties of Flowing Blood Cells*. Wiley-VCH Verlag GmbH & Co. KGaA, 2011, pp. 95–132.
- [117] MERTEN, M., CHOW, T., HELLUMS, J., AND THIAGARAJAN, P. A new role for P-selectin in Shear-induced platelet aggregation. *Circulation* 102, 17 (Oct 24 2000), 2045–2050.
- [118] MOHANDAS, N., AND GALLAGHER, P. G. Red cell Membrane: past, present, and future. *Blood* 112, 10 (Nov 15 2008), 3939–3948.
- [119] MOSKALENSKY, A. E., STROKOTOV, D. I., CHERNYSHEV, A. V., MALTSEV, V. P., AND YURKIN, M. A. Additivity of light-scattering patterns of aggregated biological particles. *J. of Biomedical Optics* 19, 8 (Aug 2014).
- [120] MÜLLER, K., FEDOSOV, D. A., AND GOMPPER, G. Margination of micro- and nanoparticles in blood Flow and its effect on drug delivery. *Scientific Reports* 4 (May 2 2014).
- [121] MÜLLER, K., FEDOSOV, D. A., AND GOMPPER, G. Smoothed dissipative particle dynamics with angular momentum conservation. *J. of comp. Physics* 281 (Jan 15 2015), 301–315.
- [122] NESBITT, W., KULKARNI, S., GIULIANO, S., GONCALVES, I., DOPHEIDE, S., YAP, C., HARPER, I., SALEM, H., AND JACKSON, S. Distinct glycoprotein Ib/V/IX and integrin alpha(IIb)beta(3)-dependent calcium signals cooperatively regulate platelet adhesion under Flow. *J. of Biological Chemistry* 277, 4 (Jan 25 2002), 2965–2972.

- [123] NIKITIN, S. Y., KORMACHEVA, M. A., PRIEZZHEV, A. V., AND LUGOVTSOV, A. E. Laser beam scattering on an inhomogeneous ensemble of elliptical discs modelling red blood cells in an ectacytometer. *Quantum Electronics* 43, 1 (2013), 90–93.
- [124] NINCK, M., UNTENBERGER, M., AND GISLER, T. Diffusing-wave spectroscopy with dynamic contrast variation: disentangling the effects of blood Flow and extravascular tissue Shearing on signals from deep tissue. *Biomedical Optics Express* 1, 5 (Dec 1 2010), 1502–1513.
- [125] NOGUCHI, H., AND GOMPPER, G. Shape transitions of Fluid vesicles and red blood cells in capillary Flows. *Proceedings of the National Academy of Sciences of the United States of America* 102, 40 (Oct 4 2005), 14159–14164.
- [126] OF MEDICINE, U. N. L. Medical encyclopedia: Rbc count. medline plus. <https://www.nlm.nih.gov/medlineplus/ency/article/003644.htm#Normal%20Values>, Feb 2016.
- [127] OIE, T., MURAYAMA, Y., FUKUDA, T., NAGAI, C., OMATA, S., KANDA, K., YAKU, H., AND NAKAYAMA, Y. Local elasticity imaging of vascular tissues using a tactile mapping system. *J. of Artificial Organs* 12, 1 (2009), 40–46.
- [128] OKUBO, T., KIRIYAMA, K., NEMOTO, N., AND HASHIMOTO, H. Static and dynamic light-scattering of colloidal gases, liquids and crystals. *Colloid and Polymer Science* 274, 2 (1996), 93–104.
- [129] OOSTERBAAN, A. M., URSEM, N. T. C., STRUIJK, P. C., BOSCH, J. G., VAN DER STEEN, A. F. W., AND STEEGERS, E. A. P. Doppler Flow velocity waveforms in the embryonic chicken heart at developmental stages corresponding to 5-8 weeks of Human gestation. *Ultrasound in Obstetrics & Gynecology* 33, 6 (Jun 2009), 638–644.
- [130] PAN, W., FEDOSOV, D. A., CASWELL, B., AND KARNIADAKIS, G. E. Predicting dynamics and rheology of blood Flow: a comparative study of multiscale and low-dimensional models of red blood cells. *Microvascular Research* 82, 2 (Sep 2011), 163–170.
- [131] PARK, Y., DIEZ-SILVA, M., POPESCU, G., LYKOTRAFITIS, G., CHOI, W., FELD, M. S., AND SURESH, S. Refractive index maps and Membrane dynamics of Human red blood cells parasitized by Plasmodium falciparum. *Proceedings of the National Academy of Sciences of the United States of America* 105, 37 (Sep 16 2008), 13730–13735.
- [132] PELTOMAEMI, M., GOMPPER, G., AND KROLL, D. M. Scattering intensity of bicontinuous microemulsions and sponge phases. *J. Chemical Physics* 136, 13 (Apr 7 2012).
- [133] PELTOMAKI, M., AND GOMPPER, G. Sedimentation of single red blood cells. *Soft Matter* 9 (2013), 8346–8358.
- [134] PENG, Z., MASHAYEKH, A., AND ZHU, Q. Erythrocyte responses in low-shear-rate flows: effects of non-biconcave stress-free state in the cytoskeleton. *J. of Fluid Mechanics* 742 (3 2014), 96–118.
- [135] PESKIN, C. Flow Patterns around Heart Valves - Numerical Method. *J. of comp. Physics* 10, 2 (1972), 252–&.

- [136] PESKIN, C. *The immersed boundary method*, vol. 11. Acta Numerica, 2002.
- [137] PIAZZA, R., AND DEGIORGIO, V. Rotational and Translational Self-Diffusion Coefficients of Interacting Brownian Spheres. *J. of Physics - Condensed Matter* 5, 34B (Aug 23 1993), B173–B182. International Symp. on Potentials and Correlations in the Physics of Condensed Matter, in Honor of Mario P. Tosi, Pavia, Italy, Sep 21–23, 1992.
- [138] PLIMPTON, S. Fast Parallel Algorithms for Short-range Molecular-Dynamics. *J. of comp. Physics* 117, 1 (Mar 1 1995), 1–19.
- [139] POCOCK, G., RICHARDS, C., AND RICHARDS, D. *Human Physiology (Oxford Core Texts)*. Oxford University Press, 2013.
- [140] POPEL, A., AND JOHNSON, P. Microcirculation and hemorheology. *Annual Review of Fluid Mechanics* 37 (2005), 43–69.
- [141] POSSINGER, K., AND REGIERER, A. E. *Facharzt Hämatologie Onkologie*. Urban & Fischer, Elsevier, 2006.
- [142] POZRIKIDIS, C. Axisymmetric Motion of a file of red blood cells through capillaries. *Physics of Fluids* 17, 3 (Mar 2005).
- [143] PRIES, A., AND SECOMB, T. Rheology of the Microcirculation. *Clinical Hemorheology and Microcirculation* 29, 3-4 (2003), 143–148. 5th Asian Congress for Microcirculation, MANILA, PHILIPPINES, Feb 20–22, 2003.
- [144] RAND, R. Mechanical Properties of Red Cell Membrane .2. Viscoelastic Breakdown of Membrane. *Biophys. J.* 4, 4 (1964), 303–&.
- [145] RAUDSEPP, A., AND CALLAGHAN, P. T. A rheo-Optical study of Shear rate and Optical Anisotropy in wormlike micelles solutions. *Soft Matter* 4, 4 (2008), 784–796.
- [146] RIEF, M., PASCUAL, J., SARASTE, M., AND GAUB, H. Single molecule force spectroscopy of spectrin repeats: Low unfolding forces in helix bundles. *J. of Molecular Biology* 286, 2 (Feb 19 1999), 553–561.
- [147] ROSENSON-SCHLOSS, R., VITOLO, J., AND MOGHE, P. Flow-mediated cell stress induction in adherent leukocytes is accompanied by modulation of morphology and phagocytic function. *Medical & Biological Engineering & Computing* 37, 2 (Mar 1999), 257–263.
- [148] ROTHMAN, J., AND LENARD, J. Membrane Asymmetry. *Science* 195, 4280 (1977), 743–753.
- [149] RUDNICK, J., BELDJENNA, A., AND GASPARI, G. The shapes of high-dimensional random walks. *J. of Physics A: Mathematical and General* 20, 4 (1987), 971.
- [150] SCHLÖTTER, M. Dynamische Lichtstreuung an natürlichen und künstlichen Erythrozyten in Suspension. diploma thesis, Universität Konstanz, Soft Matter Physics LS Maret, 2013.
- [151] SCHMIDT, M., BURCHARD, W., AND FORD, N. Quasi-Elastic Light-Scattering - an ExperimentAL-Study of Polydispersity. *Macromolecules* 11, 3 (1978), 452–454.

- [152] SETTEMBRE, C., FRALDI, A., MEDINA, D. L., AND BALLABIO, A. Signals from the lysosome: a control centre for cellular clearance and energy metabolism. *Nature Reviews Molecular Cell Biology* 14, 5 (MAY 2013), 283–296.
- [153] SHERIFF, J., BLUESTEIN, D., GIRDHAR, G., AND JESTY, J. High-Shear Stress Sensitizes Platelets to Subsequent Low-Shear Conditions. *Annals of Biomedical Engineering* 38, 4 (Apr 2010), 1442–1450.
- [154] SHNYROV, V., ORLOV, S., ZHADAN, G., AND POKUDIN, N. Thermal Inactivation of Membrane-Proteins, Volume-Dependent Na<sup>+</sup>, K<sup>+</sup>-Cotransport, and Protein-Kinase-C Activator-Induced Changes of the Shape of Human and Rat Erythrocytes. *BIOMEDICA Biochimica Acta* 49, 6 (1990), 445–453.
- [155] SKALAK, R., KELLER, S., AND SECOMB, T. Mechanics of Blood-Flow. *J. of Biomechanical Engineering-Transactions of the ASME* 103, 2 (1981), 102–115.
- [156] SKALAK, R., TOZEREN, A., ZARDA, R., AND CHIEN, S. Strain energy function of red blood cell membranes. *Biophysical J.* 13, 3 (1973), 245 – 264.
- [157] SUCCI, S. *The Lattice Boltzmann Equation for Fluid Dynamics and Beyond (Numerical Mathematics and Scientific Computation)*. Clarendon Press, 2001.
- [158] SUI, Y., CHEW, Y. T., ROY, P., CHENG, Y. P., AND LOW, H. T. Dynamic Motion of red blood cells in simple Shear Flow. *Physics of Fluids* 20, 11 (Nov 2008).
- [159] SUKOP, M., AND THORNE, D. *Lattice Boltzmann Modeling: An Introduction for Geoscientists and Engineers*. Springer, 2007.
- [160] SURESH, S. Mechanical response of human red blood cells in health and disease: Some structure-property-function relationships. *J. of Materials Research* 21 (2006), 1871–1877.
- [161] SUTERA, S., GARDNER, R., BOYLAN, C., CARROLL, G., CHANG, K., MARVEL, J., KILO, C., GONEN, B., AND WILLIAMSON, J. Age-Related-Changes in Deformability of Human-Erythrocytes. *Blood* 65, 2 (1985), 275–282.
- [162] SVELC, T., AND SVETINA, S. Stress-free state of the red blood cell Membrane and the deformation of its skeleton. *Cellular & Molecular Biology Letters* 17, 2 (Jun 2012), 217–227.
- [163] TAHIRI, N., BIBEN, T., EZ-ZAHRAOUY, H., BENYOUSSEF, A., AND MISBAH, C. On the problem of slipper shapes of red blood cells in the microvasculature. *Microvascular Research* 85, 0 (2013), 40 – 45.
- [164] TANG, K., DIMENNA, R., AND BUCKIUS, R. Regions of validity of the geometric optics approximation for angular scattering from very rough surfaces. *International J. of Heat and Mass Transfer* 40, 1 (Jan 1997), 49–59.
- [165] TAYLOR, G.-I. Stability of a Viscous Liquid Contained between Two Rotating Cylinders. *Philosophical Transactions of the Royal Society of London Series A* 223 (1923), 289–343.
- [166] THURSTON, G. Rheological Parameters for the Viscosity Viscoelasticity and Thixotropy of Blood. *Biorheology* 16, 3 (1979), 149–162.



- [167] TOMAIUOLO, G., AND GUIDO, S. Start-up shape dynamics of red blood cells in microcapillary Flow. *Microvascular Research* 82, 1 (Jul 2011), 35–41.
- [168] TOMAIUOLO, G., SIMEONE, M., MARTINELLI, V., ROTOLI, B., AND GUIDO, S. Red blood cell deformation in microconfined Flow. *Soft Matter* 5, 19 (2009), 3736–3740.
- [169] TONG, P., GOLDBURG, W., CHAN, C., AND SIRIVAT, A. Turbulent Transition by Photon-Correlation Spectroscopy. *Physical Review A* 37, 6 (Mar 15 1988), 2125–2133.
- [170] TRANSONTAY, R., NASH, G., AND MEISELMANN, H. Effects of Dextran and Membrane Shear Rate on Red-Cell Membrane Viscosity. *Biorheology* 22, 4 (1985), 335–340.
- [171] TSUBOTA, K.-I., WADA, S., AND LIU, H. Elastic behavior of a red blood cell with the Membrane's nonuniform natural state: equilibrium shape, Motion transition under Shear Flow, and elongation during tank-Treading motion. *Biomechanics and Modeling in Mechanobiology* 13, 4 (Aug 2014), 735–746.
- [172] TURLIER, H., FEDOSOV, D. A., AUDOLY, B., AUTH, T., GOV, N. S., SYKES, C., JOANNY, J.-F., GOMPPER, G., AND BETZ, T. Equilibrium physics breakdown reveals the active nature of red blood cell flickering. *Nat. Phys.* 00, 00 (Jan 2016), 1–8.
- [173] VAN MEER, G., POORTHUIS, B., WIRTZ, K., OPDENKAMP, J., AND VANDEENIEN, L. Transbilayer Distribution and Mobility of Phosphatidylcholine in Intact Erythrocyte-Membranes - Study with Phosphatidylcholine Exchange Protein. *European J. of Biochemistry* 103, 2 (1980), 283–288.
- [174] VARGA-SZABO, D., PLEINES, I., AND NIESWANDT, B. Cell adhesion mechanisms in platelets. *Arteriosclerosis Thrombosis and Vascular Biology* 28, 3 (Mar 2008), 403–412.
- [175] VEERAPANENI, S., GUEYFFIER, D., ZORIN, D., AND BIROS, G. A boundary integral method for simulating the dynamics of inextensible vesicles suspended in a viscous fluid in 2d. *J. of Computational Physics* 228, 7 (2009), 2334 – 2353.
- [176] VERKLEIJ, A., ZWAAL, R., ROELOFSEN, B., COMFURIUS, P., KASTELIJN, D., AND VANDEENIE, L. Asymmetric Distribution of Phospholipids in Human Red-Cell Membrane - Combined Study Using Phospholipases and Freeze-Etch Electron-Microscopy. *Biochimica et Biophysica Acta* 323, 2 (1973), 178–193.
- [177] VIALLAT, A., AND ABKARIAN, M. Red blood cell: from its mechanics to its Motion in Shear Flow. *International J. of Laboratory Hematology* 36, 3, SI (Jun 2014), 237–243.
- [178] VIRTANEN, J., CHENG, K., AND SOMERHARJU, P. Phospholipid composition of the mammalian red cell Membrane can be rationalized by a superlattice model. *Proceedings of the National Academy of Sciences of the United States of America* 95, 9 (Apr 28 1998), 4964–4969.
- [179] WALTER, J., SALSAC, A. V., BARTHES-BIESEL, D., AND LE TALLEC, P. Coupling of finite element and boundary integral methods for a capsule in a Stokes Flow. *International J. for Numerical Methods in Engineering* 83, 7 (Aug 13 2010), 829–850.

- [180] WAN, J., RISTENPART, W. D., AND STONE, H. A. Dynamics of shear-induced atp release from red blood cells. *Proceedings of the National Academy of Sciences* 105, 43 (2008), 16432–16437.
- [181] WANG, J., YAVICH, D., AND LEAL, L. Time-Resolved Velocity-Gradient and Optical Anisotropy in Linear Flow by Photon-Correlation Spectroscopy. *Physics of Fluids* 6, 11 (Nov 1994), 3519–3534.
- [182] WANG, Z., SUI, Y., SPELT, P. D. M., AND WANG, W. Three-dimensional dynamics of oblate and prolate capsules in Shear Flow. *Physical Review E* 88, 5 (Nov 26 2013).
- [183] WATANABE, N., KATAOKA, H., YASUDA, T., AND TAKATANI, S. Dynamic deformation and recovery response of red blood cells to a cyclically reversing Shear Flow: Effects of frequency of cyclically reversing Shear Flow and Shear stress level. *Biophys. J.* 91, 5 (Sep 2006), 1984–1998.
- [184] WEINBAUM, S., TARBELL, J., AND DAMIANO, E. The structure and function of the endothelial glycocalyx layer. *Annual Review of Biomedical Engineering* 9, 1 (2007), 121–167. PMID: 17373886.
- [185] WEISSTEIN, E. W. Oblate spheroid. <http://mathworld.wolfram.com/OblateSpheroid.html>, September 2011. From MathWorld—A Wolfram Web Resource.
- [186] WHITE, F. *Viscous Fluid Flow*. McGraw-Hill series in aeronautical and aerospace engineering. McGraw-Hill, 1974.
- [187] WILLIAMS, A. R., KOO, B.-K., GUNDERT, T. J., FITZGERALD, P. J., AND LADISA, JR., J. F. Local hemodynamic changes caused by main branch stent implantation and subsequent virtual side branch balloon angioplasty in a representative coronary bifurcation. *J. of Applied Physiology* 109, 2 (Aug 2010), 532–540.
- [188] WURZINGER, L., OPITZ, R., AND ECKSTEIN, H. Mechanical blood trauma: an overview. *Angeiologie* 38 (1986), 81–97.
- [189] WURZINGER, L., OPITZ, R., WOLF, M., AND SCHMID-SCHÖNBEIN, H. Shear Induced Platelet Activation - a Critical Reappraisal. *Biorheology* 22, 5 (1985), 399–413.
- [190] YAZDANBAKHSI, K., LOMAS-FRANCIS, C., AND REID, M. Blood groups and diseases associated with inherited abnormalities of the red blood cell membrane. *Transfusion Medicine Reviews* 14, 4 (2000), 364 – 374.
- [191] YAZDANI, A. Z. K., AND BAGCHI, P. Phase diagram and breathing dynamics of a single red blood cell and a biconcave capsule in dilute Shear Flow. *Physical Review E* 84, 2, 2 (Aug 11 2011).
- [192] YURKIN, M., AND HOEKSTRA, A. The discrete-dipole-approximation code adda: Capabilities and known limitations. *J. of Quantitative Spectroscopy and Radiative Transfer* 112, 13 (2011), 2234 – 2247. Polarimetric Detection, Characterization, and Remote Sensing.

- [193] ZARINS, C., GIDDENS, D., BHARADVAJ, B., SOTTIURAI, V., MABON, R., AND GLAGOV, S. Carotid Bifurcation Atherosclerosis Quantitative Correlation of Plaque Localization with Flow Velocity Profiles and Wall Shear-Stress. *Circulation Research* 53, 4 (1983), 502–514.
- [194] ZHANG, T., TASKIN, M. E., FANG, H.-B., PAMPORI, A., JARVIK, R., GRIFFITH, B. P., AND WU, Z. J. Study of Flow-Induced Hemolysis Using Novel Couette-Type Blood-Shearing Devices. *Artificial Organs* 35, 12 (Dec 2011), 1180–1185.
- [195] ZHAO, R., ANTAKI, J., NAIK, T., BACHMAN, T. N., KAMENEVA, M. V., AND WU, Z. J. Microscopic investigation of Erythrocyte deformation dynamics. *Biorheology* 43, 6 (2006), 747–65.
- [196] ZHERNOVAYA, O., SYDORUK, O., TUCHIN, V., AND DOUPLIK, A. The refractive index of Human hemoglobin in the visible range. *Physics in Medicine and Biology* 56, 13 (Jul 7 2011), 4013–4021.
- [197] ZHOU, J., AND FUNG, Y. C. The degree of nonlinearity and anisotropy of blood vessel elasticity. *Proceedings of the National Academy of Sciences* 94, 26 (1997), 14255–14260.
- [198] ZWAAL, R., ROELOFSEN, B., COMFURIUS, P., AND VAN DEENEN, L. Organization of Phospholipids in Human Red-Cell Membranes as Detected by Action of Various Purified Phospholipases. *Biochimica et Biophysica Acta* 406, 1 (1975), 83–96.



# Erklärung

Ich versichere, dass ich die von mir vorgelegte Dissertation selbständig angefertigt, die benutzten Quellen und Hilfsmittel vollständig angegeben und die Stellen der Arbeit - einschließlich Tabellen, Karten und Abbildungen -, die anderen Werken im Wortlaut oder dem Sinn nach entnommen sind, in jedem Einzelfall als Entlehnung kenntlich gemacht habe; dass diese Dissertation noch keiner anderen Fakultät oder Universität zur Prüfung vorgelegen hat; dass sie - abgesehen von unten angegebenen Teilpublikationen - noch nicht veröffentlicht worden ist, sowie, dass ich eine solche Veröffentlichung vor Abschluss des Promotionsverfahrens nicht vornehmen werde. Die Bestimmungen der Promotionsordnung sind mir bekannt. Die von mir vorgelegte Dissertation ist von Prof. Dr. G. Gompper betreut worden.



# Curriculum Vitae

Name:	Mauer
Vorname:	Johannes
Geburtsdatum:	18.10.1987
Geburtsort:	Koblenz
Staatsangehörigkeit:	deutsch

1994 – 2007	Schüler der Grundschule Müden und des Gymnasiums Münstermaifeld
2007 – 2009	Diplom-Student in Physik Universität Karlsruhe (TH)
2009 – 2013	Diplom-Student in Physik Universität Mainz
2013	Diplom <i>Titel der Diplomarbeit: "Competitive Adsorption Processes of Polymers on structured Surfaces"</i>
April 2013 – April 2016	Doktorand im Fach Physik Forschungszentrum Jülich GmbH
Oktober 2014 – Oktober 2016	Promotionsstudent der Physik an der Universität zu Köln